The Proton/Drug Coupling Mechanism of EmrE

By

Nathan E. Thomas

A dissertation submitted in partial fulfillment of

the requirements for the degree of

Doctor of Philosophy

(Biochemistry)

at the

UNVERSITY OF WISCONSIN-MADISON

2021

Date of final oral examination: 07/30/2021

This dissertation is approved by the following members of the Final Oral Committee:

Katherine A. Henzler-Wildman, Professor, Biochemistry
M. Thomas Record, Professor, Biochemistry
Silvia Cavagnero, Professor, Chemistry
Robert Landick, Professor, Biochemistry
Philip A. Romero, Assistant Professor, Biochemistry

Table of Contents

Introduction

EmrE is an integral inner membrane from E. coli that harnesses the proton motive force to efflux toxic hydrophobic cations from the cytoplasm. Due to its small size, ease of purification, and stability, EmrE has been used as a model system to study multidrug recognition and resistance, transporter structure and evolution, and ion-coupled (or *secondary active*) transport[1–9]. Despite its role as a model system, EmrE has proven to be an enigmatic protein to study. EmrE first garnered controversy with the publication of its crystal structure in 2004, which showed that dimeric EmrE adopts an antiparallel topology in the membrane[10]. Such a topology would require random insertion of EmrE protomers into the membrane during synthesis, which was seen as unsavory from a biochemical perspective[11]. Skepticism of the antiparallel topology only increased when the structure was retracted due to a software error, and while the re-solved structure retained the antiparallel topology (Fig. 1), the controversy remained[5,12,13]. The debate was not resolved until nuclear magnetic resonance (NMR) studies in the early 2010s supported the antiparallel topology model[7,14], and subsequent functionally studies confirmed that EmrE was inserted into the membrane with a random topology during synthesis[15]. However, while NMR studies of EmrE helped to resolve one controversy, they initiated another.

When I joined in 2015, the Henzler-Wildman lab had acquired intriguing NMR data that suggested EmrE violated rules thought to be essential for ion-coupled transport. My project was to functionally test these findings, and if possible, to reconcile them with EmrE's well-characterized function of proton-coupled drug efflux. The resulting work challenges many assumptions in the transporter field, but rather than representing something entirely novel, the mechanistic models we propose highlight the significance of early functional and theoretical transporter research.

What is ion-coupled transport, and how does it work?

Transporters constitute a large class of membrane proteins that allow cells to exchange chemicals with their environment and perform crucial roles in enabling cells to maintain homeostasis. While channels and uniporters allow facilitated diffusion of specific chemicals, active transporters expend energy to concentratively acquire nutrients from the environment, extrude toxins and waste from the cell, and maintain electrochemical gradients across the membrane. Primary-active transporters obtain their energy from ATP hydrolysis, while secondary-active (ion-coupled) transporters utilize transport of an ion down an electrochemical gradient to perform uphill transport of a coupled substrate.

While the concept of secondary active transport was proposed as early as the 1940s[16], the subject gained prominence with Peter Mitchell's chemiosmotic hypothesis of oxidative phosphorylation in the 1960s[17–19]. Utilization of energy derived from electrochemical gradients was initially controversial[20], but evidence for ion-coupled transport mounted throughout the 1960s and early 1970s. Predictions made by the chemiosmotic hypothesis, such as a negative correlation between mitochondrial ion permeability and oxidative phosphorylation, were experimentally verified[21,22]. Work on intestinal epithelium cells demonstrated that concentrative uptake of glucose was coupled to sodium flux[23,24]. And concentrative uptake of sugar and amino acids in E. coli membrane vesicles was demonstrated to occur upon the imposition of a membrane potential and in the absence of ATP hydrolysis or respiration, indicating that electrochemical gradients alone were sufficient to drive transport[25,26].

By the late 1970s, active transport driven by electrochemical gradients was generally accepted, marked by the award of 1978 Nobel Prize to Peter Mitchell. At this point, the thermodynamic basis for ion-coupled transport was clear. For the co-transport (symport) of an ion and substrate:

$$(1)\ Ion_{out} + Substrate_{out} \rightleftarrows Ion_{in} + Substrate_{in}$$

The free energy of transport is simply the sum of the chemical potentials of the ion and substrate across the membrane:

$$(2)\ \Delta G_{transport} = \Delta\mu_i + \Delta\mu_s$$

Where the ion and substrate chemical potentials are given by:

$$(3)\ \Delta\mu_i = RT\ln\left(\frac{[Ion]_{in}}{[Ion]_{out}}\right) + z_i F\Delta\Psi$$

$$(4)\ \Delta\mu_s = RT\ln\left(\frac{[Substrate]_{in}}{[Substrate]_{out}}\right) + z_s F\Delta\Psi$$

Similarly, for the exchange (antiport) of an ion and substrate:

$$(5)\ Ion_{out} + Substrate_{in} \rightleftarrows Ion_{in} + Substrate_{out}$$

The free energy of transport is the difference in the ion and substrate chemical potentials:

$$(6)\ \Delta G_{transport} = \Delta\mu_i - \Delta\mu_s$$

How these thermodynamic equations related to mechanism – that is, how the free energy gained from the downhill transport of one ion could be harnessed by a protein to drive the uphill transport of another molecule – was less clear. Due to the technical difficulty of membrane protein biochemistry, progress on the mechanism of ion-coupled transport was slow. Despite the paucity of experimental data, several prescient hypotheses were proposed. The alternating access model provided a structural mechanism to explain how a protein could translocate bound substrates across the membrane (Fig. 1)[27,28]. In this model, the transporter forms a binding pocket for substrates within the plane of the membrane. Conformational change alternates access from the binding pocket to either side of the membrane, and in doing so, allows bound substrates to move from one side of the membrane to the other. Meanwhile, kinetic models were developed to explain the theoretical basis for free energy transduction during ion-coupled transport[29–32]. In addition to

proposing various kinetic mechanisms that could describe coupled transport, this work sought to explain the relationship between the rates of the individual steps in a kinetic mechanism and the thermodynamics of the overall process. Notably, these models frequently included “leak” pathways that could short-circuit coupled transport. While mechanisms including such pathways are less thermodynamically efficient, this early computational work demonstrated that their exclusion was not required for coupled transport.

Gradually, transporter biochemistry began to catch up to transporter theory. The late 1970s saw the first functional reconstitution of purified ion-coupled transporters into lipid vesicles[33–36], and in 1980, LacY was the first ion-coupled transporter to be successfully purified from an overexpression plasmid[37]. Methods were developed to measure transporter stoichiometry and efficiency, including the “static head” or reversal potential experiment[38,39]. Voltage clamp electrophysiology recordings of high turnover transporters gave unprecedented insight into transport kinetics[40,41]. The results of the biochemical data generally agreed with the kinetic models that had been proposed decades earlier. Most transporters had evolved to be highly efficient, but under certain experimental conditions, ion or substrate leak pathways could be observed. Despite these advances, purification of functional transporters remains difficult, and few transporters have sufficiently high turnover rates to be amenable to traditional electrophysiology methods. Consequently, even in 2021, only a handful of ion-coupled transporters have had their mechanisms rigorously biochemically characterized.

In the 2000s, ion-coupled transporter biology entered the structural age[42–44]. Once again, the experimental structural models were in good agreement with the previously proposed theoretical alternating access models[45–48]. For example, LacY consists of a pair of six helix bundles that form a rough V-shape within the membrane. This creates an internal hydrophilic cavity that allows polar substrates (sugars) and ions to bind[49]. The cavity is open to only one side of the membrane at a time, but conformational exchange results in closure of the cavity to one

side of the membrane and opening to the other, transporting bound substrate across the membrane[50]. The emergence of high-resolution structures provided unprecedented insight into the inner workings of ion-coupled transporters, but the emphasis on structural studies did carry some disadvantages. While conformational dynamics are a crucial component of transporter function, highly dynamic proteins produce lower resolution crystal structures and lower quality NMR spectra. As a result, structural studies of transporters often select for slow-dynamics mutants with impaired function[44,51], or transporters with naturally slow dynamics that can be challenging to functionally characterize[52]. Gradually, structural perspectives replaced kinetic perspectives in the transporter mechanism field, and the complex mechanistic models of earlier decades gave way to minimal models that only considered states captured in crystals. Whereas reviews from the early 2000s emphasized the importance of leak pathways to the physiological function of transporters[53], reviews from the early 2010s considered such pathways to be "forbidden"[54–56].

The mechanism of EmrE

When our lab began studying EmrE, it was generally accepted that transporter mechanisms could be described by single cycles with a fixed transport stoichiometry (the number of ions and substrates moved per cycle, Figure 2A,B). Previous mechanistic investigations of EmrE were conducted within this paradigm. Early studies recognized the essential nature of E14[57,58]. As the only charged residue located within the plane of the membrane, E14 serves as a shared binding site for drugs and protons[8]. Competition for this binding site between drugs and protons leads to a simple and elegant coupling mechanism[59,60]. If simultaneous binding of drug and proton is forbidden, and if alternating access is only possible when substrate is bound, then EmrE is restricted to a single transport cycle. As transport of +1 charged drug substrates is electrogenic, it was believed that EmrE's transport stoichiometry was two protons per drug[61]. The

resulting “pure exchange” model (Fig. 2A) was consistent with the antiport mechanisms that dominated the literature in the structural age of transporter biology.

We expected EmrE to adhere to the rules of the pure exchange model, given its widespread acceptance in the field. However, it became apparent that EmrE deviated from the model in several significant ways. First, NMR pH titrations indicated that the two E14 residues of the EmrE dimer are in asymmetric environments, with the E14 on one protomer having a pK_a of 7.0 while the E14 pK_a for the other protomer is 8.3[62]. This means that at physiological pH, a significant population of EmrE is singly protonated in the binding pocket. Moreover, NMR dynamics experiments demonstrated that EmrE could alternate access whether apo-, singly-, or doubly-protonated, despite the fact that alternating access without substrate is forbidden by the pure exchange model. This finding was later confirmed independently by the Traaseth lab using complimentary NMR techniques[63]. Second, NMR studies of drug-bound EmrE demonstrated that while drug binding prevented protonation of one of the E14 residues in the binding pocket, the second E14 residue could still bind proton and that EmrE could alternate access in this state[64]. The pK_a of drug-bound EmrE is reduced relative to the pK_a of drug-free EmrE, indicating that competition for binding remains between drug and proton, but with a measured value of 6.3, its proximity to physiological pH means that the singly-protonated, drug-bound state of EmrE must be accounted for in the transport mechanism. With these findings, it was apparent that EmrE violated the rules thought to govern its coupled antiport mechanism. EmrE could simultaneously bind drug and proton, and EmrE could alternate access in every experimentally observed state.

I joined the Henzler-Wildman lab with the hope of answering the fundamental question raised by this data – how could EmrE couple proton import to drug export while violating the consensus mechanism of coupled antiport? In place of the pure exchange model which comprises the minimum number of states required for antiport, we proposed the free exchange model which comprises the minimum number of states required to explain our NMR data (Fig. 2C). Consistent

with our NMR data, the free exchange model allows every state to alternate access. As a result, in addition to the single 2:1 proton:drug antiport cycle of the pure exchange model, the free exchange model includes cycles for 1:1 proton:drug antiport, proton uniport (leak), drug uniport (leak), and even 1:1 proton:drug symport. My project was to verify the functional predictions of our model and reconcile the proposed existence of these multiple transport cycles with EmrE's proton-drug antiport function.

Transport assays confirmed the existence of multiple transport cycles, providing functional evidence that the free exchange model is a better description of EmrE's transport behavior than the pure exchange model (Chapter 1)[64]. Subsequent mass action kinetic simulations using the alternating access rates measured by NMR confirmed that EmrE can perform proton-coupled concentrative drug efflux with the free exchange model, despite the existence of dissipative leak pathways (Chapter 2)[65]. The kinetically controlled coupled transport exhibited by our model is consistent with early kinetic mechanisms proposed for coupled transport[30]. However, rigorously testing the model's prediction of environmentally dependent transport behavior would require the development of a higher throughput assay. The solid supported membrane electrophysiology (SSME) assay I developed for measuring transporter stoichiometry confirmed that EmrE's transport stoichiometry changes with both pH and drug concentration (Chapter 3). However, functional data contradicts one aspect of the free exchange model – rapid proton transport by EmrE requires the presence of drug, while the model suggests EmrE should leak protons in the absence of drug. Investigations of the conserved C-terminus of EmrE provided a potential explanation for this discrepancy – a gating mechanism not accounted for by either the pure or free exchange models (Chapter 4)[66]. Studies of an EmrE mutant lacking the C-terminal tail confirm its role in reducing uncoupled proton leak (Chapter 5). Finally, we identified a compound that causes a deleterious growth phenotype in cells expressing EmrE by targeting this gating mechanism (Chapter 6).

The work described in this dissertation has contributed to the recent, growing acceptance that many transporters operate according to loosely coupled mechanisms[67–73]. While our lab did not set out to upend the prevailing models of ion-coupled transport, several experimental techniques gave us unprecedented insight into EmrE's function and provided data that challenged assumptions in the transporter field.

The importance of membrane mimetics

The unique chemical environment of the lipid bilayer is a crucial component of integral membrane protein structure and function, but many biochemical techniques require proteins to be removed from their native membranes. As membrane proteins are insoluble in aqueous buffers, membrane mimetics are essential for most biochemical or structural studies. EmrE has been studied using three different membrane mimetics: detergents, liposomes, and bicelles (Fig. 3).

Detergents contain a polar head group and single hydrophobic tail. When aqueous detergent concentrations exceed their critical micelle concentration (CMC), they begin to form micelles – soluble spherical particles with a hydrophilic surface and a hydrophobic core. Detergent micelles are frequently used to solubilize cellular membranes during membrane protein purification. Both decylmaltoside (DM) and dodecylmaltoside (DDM) have been used for this purpose with EmrE. Micelles with a diameter roughly the width of the lipid bilayer (DDM with its longer tail is preferred) can provide a chemical environment similar enough to a native membrane to allow some functional studies of detergent-solubilized proteins. However, it is important to remember that detergent micelles do not perfectly replicate the membrane environment. The lack of lateral pressure provided by the lipid bilayer can disrupt the structure of function of many membrane proteins[74–76]. Several early functional studies of EmrE were performed in detergent[59,77], but EmrE binds drug with orders of magnitude higher affinity in a lipid environment[14].

In many respects, liposomes are the ideal membrane mimetic for studying transporter function, as they preserve the lipid bilayer environment and provide the compartmentalization necessary to perform transport assays. When dry lipids are hydrated in an aqueous buffer, they form multilamellar vesicles (MLVs) – sheets of lipid bilayers stocked on top of each other. Liposomes are formed by the introduction of energy by sonication or extrusion through a filter, which breaks apart the MLVs and ideally, forms unilamellar vesicles such as the one depicted in Fig. 3. Membrane proteins can be reconstituted into proteoliposomes by combining liposomes with detergent-solubilized proteins and subsequently removing the detergent through rapid dilution, dialysis, or the use of hydrophobic beads such as BioBeads or Amberlite XAD-2. Proteoliposomes have been used to study transporter function for over forty years[36,37], but while they carry many advantages over detergents, traditional liposomal transport assays are low throughput. Additionally, the large size of liposomes prevents their use in solution NMR.

Bicelles are flat lipid bilayers capped with detergent or short-chain lipid molecules[78]. Bicelle size can be controlled by the ratio of long chain lipid to short chain lipid, known as the *q* value[79]. When the *q* value is in the correct range ($0.25 < q < 0.4$), bicelles tumble isotropically in solution while retaining a lipid environment for the protein. The use of isotropic bicelles has been essential to our studies of EmrE[80]. Bicelles' lipid environment stabilizes EmrE's dimeric structure and increases the drug binding affinity, allowing for solution NMR studies of drug-saturated EmrE[64,81]. The suitability of the bicelle environment for EmrE's structure and function is further evidenced by the agreement of chemical shifts and alternating access rates measured in bicelles with those measured using solid-state NMR techniques in a full lipid bilayer[63,82]. In addition, the functional data provided by drug binding and proton release experiments performed in bicelles can be compared directly to the structure and dynamics data provided by NMR[62,64–66,83].

NMR as a tool for investigating EmrE's structure and dynamics

NMR is a powerful technique for probing structure/function relationships in proteins, as it can provide structural and dynamics information at functionally relevant experimental temperatures. Systems best suited to NMR investigations are stable, easy to express to high concentrations in E. coli, and relatively small. Thus, the characteristics that made EmrE a model system for biochemical studies also make it an ideal system for NMR.

The vast majority of the NMR experiments included in this dissertation rely on correlations of proton (^{1}H) and nitrogen (^{15}N) chemical shifts. ^{1}H and ^{15}N shifts are highly sensitive to the local electronic environment. ^{1}H-^{15}N correlations of amide groups given by the heteronuclear single quantum coherence (HSQC) experiment are particularly useful, as they provide site-specific chemical probes for each non-proline residue in a protein. The ^{1}H-^{15}N HSQC spectrum of a given protein acts as an NMR thumbprint. Chemical shift perturbations (CSPs) of this thumbprint due to ligand binding, mutation, or a change in the environmental conditions can be quantified to map the effects of these various changes onto the protein structure. Amide nitrogen chemical shifts are primarily affected by hydrogen bonding (including hydrogen bonding to the preceding carbonyl) and the identity, conformation of the preceding amino acid side chain, and backbone torsion angles, while proton chemical shifts are affected by electric fields from charged atoms, ring currents of aromatic groups, magnetic anisotropy around chemical bonds, and nearby paramagnetic groups[84]. Since they report on different things, proton and nitrogen CSPs are mostly uncorrelated and can be combined into a composite CSP:

$$(7)\ d = \sqrt{\delta_H^2 + \alpha \cdot \delta_N^2}$$

Where α is an empirical weighting factor (we use 0.154) to account for the larger range of amide nitrogen chemical shifts.

In addition to the structural information provided by CSPs, ^{1}H-^{15}N HSQC experiments report on protein dynamics. The chemical shift itself is a frequency reported as a fraction (ppm)

of the Larmor frequency – the precession frequency of a nuclei in a given magnetic field. Field strengths of NMR spectrometers are normally described as the Larmor frequency of a proton (750 MHz, 900 MHz, etc.), so a proton chemical shift of 10 ppm corresponds to a frequency of 7500 Hz in a 750 MHz instrument and 9000 Hz in a 900 MHz instrument.

The significance of the chemical shift frequencies comes into play when considering a protein exchanging between two states, such as the alternating access conformational exchange of EmrE (Fig. 1). Each of the 110 amino acids in EmrE's sequence exists in two states in the functional dimer – one protomer with the N- and C- termini on the open side of the protein (conformation A) and one protomer with the N- and C- termini on the closed side (conformation B). The two conformations provide different chemical environments, and thus, the chemical shift of an amino acid in conformation A will be unique from the same amino acid in conformation B. During alternating access, the two protomers swap conformations and each amino acid swaps chemical shifts. The relationship between the rate of exchange and the difference in the chemical shifts has a profound effect on the appearance of the NMR spectrum. The slow exchange regime occurs when the chemical shift difference between the states ($\Delta\omega$) is much larger than the exchange rate between the states (k_{ex}). Under such conditions, each state is visible as a separate peak in the spectrum. The fast exchange regime occurs when k_{ex} is much greater than $\Delta\omega$. This results in a single peak with a chemical shift that is the population-weighted average of the chemical shifts of each state. While both slow and fast exchange regimes can give high quality spectra, intermediate exchange, which occurs when $\Delta\omega$ is similar to k_{ex}, causes broadened peaks and loss of signal to noise (Fig. 4A-C). The alternating access rate of EmrE can span all three exchange regimes, depending on the binding state, mutant, temperature, and field strength of the spectrometer used in a given experiment. As a result, the effect of a certain mutation or substrate on EmrE's function can often be inferred simply from the appearance of the spectrum. Tight-binding substrates or mutations that hinder the alternating access dynamics shift the spectrum

farther into the slow exchange regime with sharp, defined peaks for both conformation A and conformation B, while conditions that increase the alternating access rate (such as protonation) lead to intermediate exchange and line broadening or fast exchange and a single set of peaks.

The exchange regime of peaks in EmrE spectra are affected by substrate binding dynamics as well. In particular, several NMR pH titrations are described in this dissertation. Proton on- and off-rates are generally fast, so the chemical shift of a peak at a given pH is a population-weighted average of the chemical shifts of the protonated and de-protonated states (Fig. 4D). When two protonation events are involved, such as for drug-free EmrE, the population-weighted average of the doubly-, singly-, and de-protonated states can lead to a curved titration of the peak position (Fig. 4F). Fitting the peak position as a function of pH (Fig. 4E,G) can allow for the determination of the pK_a values of various protonatable residues in EmrE (generally E14, but also H110 in Chapter 4).

For residues in the intermediate exchange, quantitative analysis of peak shapes (lineshape analysis) can allow determination of exchange rates[83,85–87], but the highest quality EmrE spectra are in the slow exchange regime. As a result, EmrE's alternating access rate has more commonly been measured using the ZZ-exchange experiment[14,51,62,64,83,88]. ZZ-exchange is similar to a normal HSQC experiment, except with a delay added to the pulse sequence between recording the nitrogen chemical shift and the proton chemical shift. If alternating access occurs during the delay, cross peaks will appear in the spectrum with the nitrogen chemical shift of the original state and the proton chemical shift of the new state (Fig. 5). Fitting the cross peak/auto-peak intensity ratio as a function of the delay time allows for determination of the exchange rate[14].

Solid supported membrane electrophysiology for higher throughput transport assays

While NMR can provide great insight into EmrE's structure and function, it is important to be able to relate the data acquired by NMR to the functional transport behavior of the protein. The

gold standard for functional characterization of transporters are transport assays conducted in proteoliposomes, but these assays are labor and material intensive, limiting the amount of functional characterization that is experimentally practical. Numerous electrophysiology techniques have been developed for more rigorous and/or higher throughput characterization of ion channels and high-flux transporters. These techniques can measure the current across a membrane, or in some cases, through a single channel, but has a lower detection limit of about 1000 s^{-1}, faster than the rate of most transporters.

Solid supported membrane electrophysiology (SSME) was developed to allow electrophysiological characterization of more typical, moderate flux transporters[89–91]. Instead of measuring the current across a single biological or liposomal membrane, thousands of liposomes are adsorbed onto a membrane surface attached to a gold electrode. Capacitive coupling between membranes and the electrode allows detection of the bulk current across all the adsorbed liposomes and observation of transport rates as low as 10 s^{-1} [91,92]. A depiction of the method is shown in Figure 6. One of the primary advantages of SSME over traditional liposomal assays is that sensors are relatively stable once prepared and can be used for dozens of measurements, as perfusion of the original buffer resets the sensor to its initial state. This allows a single sensor containing micrograms of lipid and picomols of protein to be used to screen many different experimental conditions relatively quickly.

While we hoped the technique would be useful when we acquired our first SSME instrument two years ago, we did not foresee just how powerful it would prove to be. In Chapter 3, we develop an SSME assay to measure transport stoichiometry. This assay allowed us to replicate stoichiometry measurements that normally took months of optimization in a matter of days. We further show that it is possible to quantitatively exchange the internal buffer, expanding the range of experiments that can be performed with a single sensor even further. SSME has verified the free exchange model's prediction that EmrE has multiple, environmentally-dependent

transport stoichiometries (Chapter 3 addendum), demonstrated the mechanism of action of the susceptibility substrate harmane (Chapter 5), confirmed that the C-terminal tail is involved with gating proton release (Chapter 6), and verified the functional relevance of a new substrate used for structure determination (Appendix B). SSME will continue to be indispensable as our lab expands into investigating new substrates and new members of the SMR family going forward.

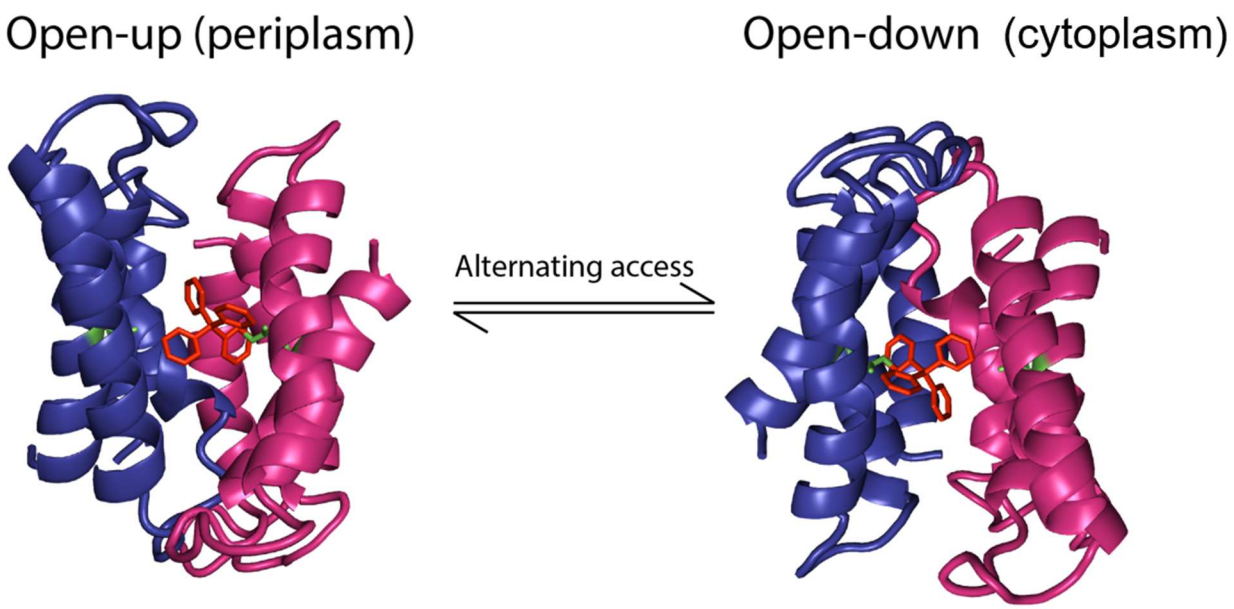

Figure 1 – *Alternating access transport port by EmrE*. Crystal structure of EmrE (3B5D)[5] with bound tetraphenylphosphonium (TPP^+) modeled in red. The critical E14 residue that serves as a shared binding site for drug and proton is shown in green. The subunits swap conformations to alternate access to the binding pocket between either side of the membrane.

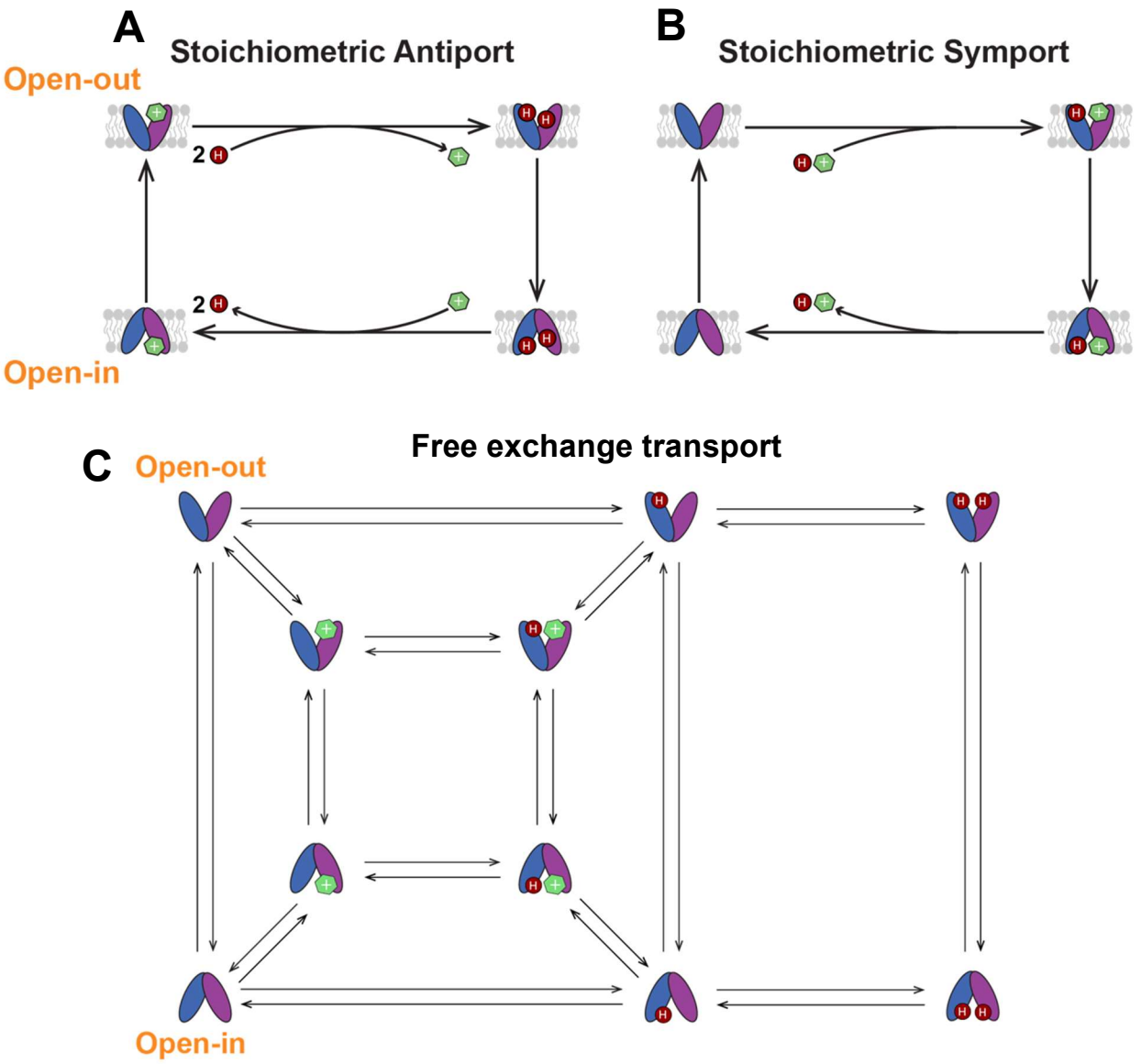

Figure 2 – *Models of coupled transport.* Tightly coupled stoichiometric models for antiport (A) and symport (B) restrict the number of functional states of the transporter, while the loosely coupled free exchange model (C) allows substrate binding and alternating access in a variety of states.

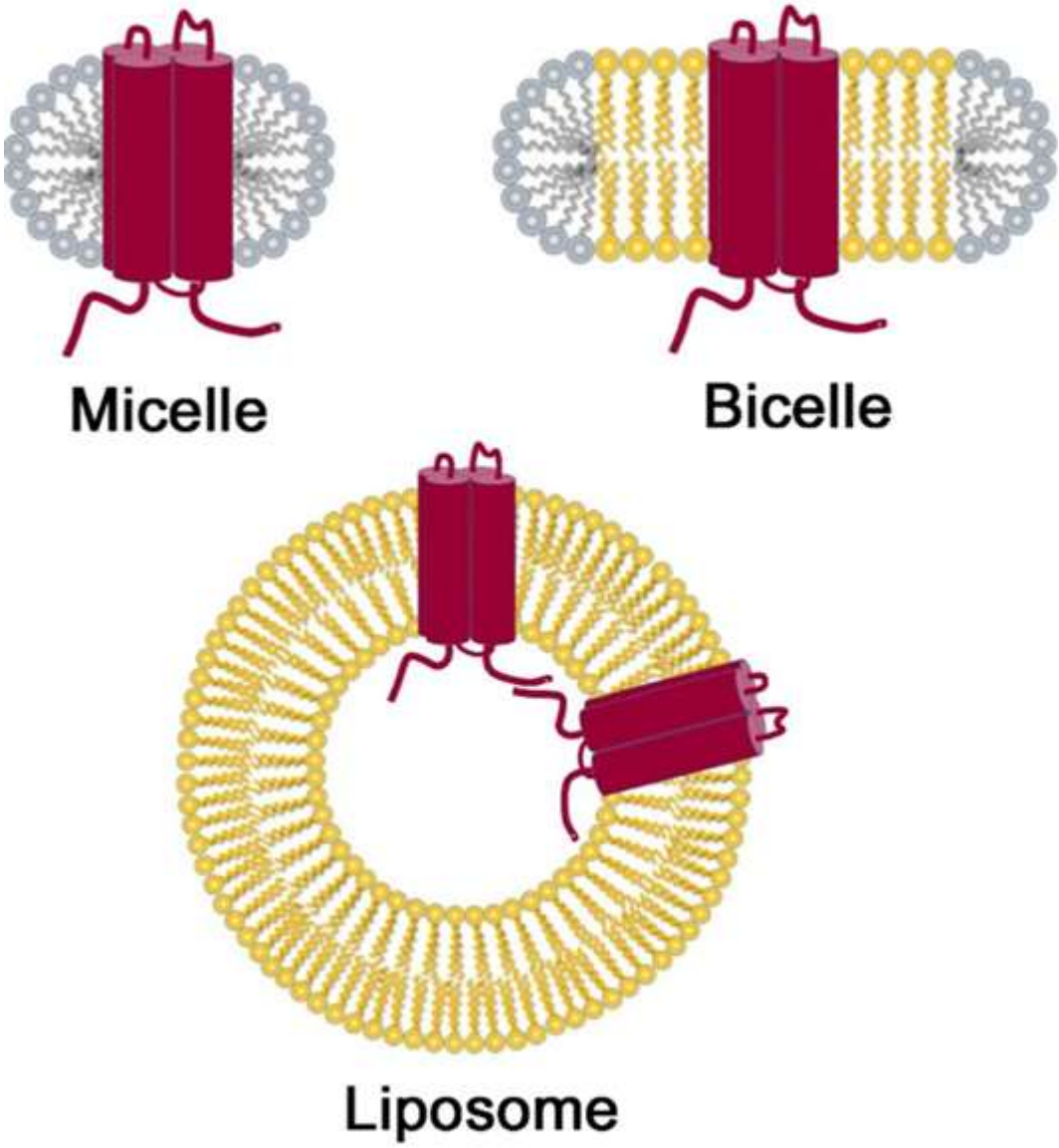

Figure 3 – *Models of common membrane mimetics***.** Reproduced from[93].

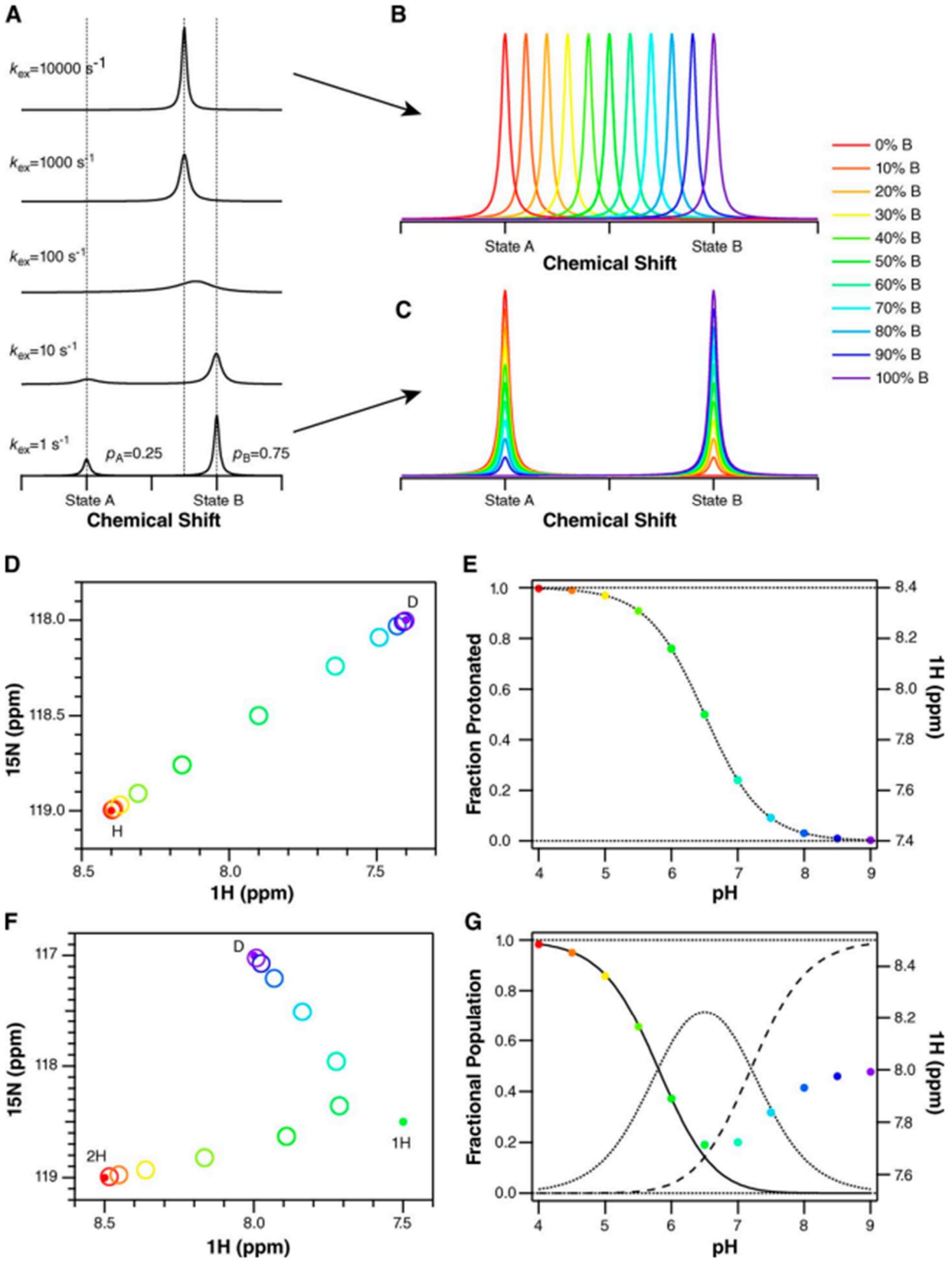
A
k_{ex}=10000 s^{-1}
k_{ex}=1000 s^{-1}
k_{ex}=100 s^{-1}
k_{ex}=10 s^{-1}
k_{ex}=1 s^{-1}
p_A=0.25
p_B=0.75
State A
State B
Chemical Shift
B
State A
State B
Chemical Shift
0% B
10% B
20% B
30% B
40% B
50% B
60% B
70% B
80% B
90% B
100% B
C
State A
State B
Chemical Shift
D
15N (ppm)
1H (ppm)
D
H
E
Fraction Protonated
pH
1H (ppm)
F
15N (ppm)
1H (ppm)
D
2H
1H
G
Fractional Population
pH
1H (ppm)

Figure 4 – *NMR exchange regimes and effect on titration patterns.* Taken from[62]. (A) For a single residue, each unique conformation or state of a protein will have a distinct chemical shift. When these conformations or states are able to exchange, the pattern observed in the NMR spectrum depends on the rate of the exchange process (k_{ex}) relative to the frequency difference between the chemical shifts of the two species ($\Delta\omega$). In A, one-dimensional NMR spectra are simulated for $\Delta\omega$ = 100 Hz. When k_{ex} is much slower than $\Delta\omega$ (bottom, slow-exchange regime), two peaks are observed at the unique chemical shifts of these two conformations or states. The area under each peak reflects the relative population of each, 25%/75% in this example. As the exchange rate increases, the peaks broaden and merge, eventually resulting in a single narrow peak at the population-weighted average chemical shift of the exchanging species (top, fast-exchange regime). NMR spectra are usually reported with axes in units of parts per million (ppm) to remove their dependence on the spectrometer field strength. However, the chemical shift actually corresponds to a frequency. For the spectra presented in[62], acquired on a 700-MHz NMR spectrometer, 1 ppm in proton corresponds to 700 Hz. (B) In the fast-exchange regime, where k_{ex} is fast compared with $\Delta\omega$, titration results in a shift in peak position, from the free to bound state as ligand is added and the relative population of the free and bound states changes. (C) In the slow-exchange regime, the free state disappears, and the bound state appears during the course of a titration as ligand is added and the population shifts from free to bound. Intermediate exchange will result in a combination of peak shifting and broadening. Because proton on/off is generally fast, we expect (and observe) spectra where peaks shift position with pH. (D) In the case of two-state exchange from a protonated state, marked H, to a deprotonated state, marked D, the peak position in a two-dimensional spectrum will move along a line connecting the peaks corresponding to the fully protonated and fully deprotonated states as pH is changed. (E) Plotting the position of the peak (in ppm) as a function of pH will result in a classical binding curve, reflecting the nonlinear dependence of the fraction protonated on pH. Thus, the chemical shift can be analyzed in the same way as any other protein property that is sensitive to protonation-state

changes. (F) If the protein is exchanging between three states (2H, two protons bound; 1H, one proton bound; D, deprotonated, no protons bound), each with unique chemical shifts, then the peak position will reflect the population-weighted average of all three chemical shifts at each pH value. An example is shown for two protonation steps assuming non-interacting sites with pK_a values separated by 1.4 pH units. The averaging of three states results in a curved path of the peak across the spectrum. (G) The fraction doubly protonated (solid line), singly protonated (dotted), and deprotonated (dashed) are shown along with the peak position (in parts per million) as a function of pH. Both transitions are clearly observed in the peak position, although the chemical-shift difference between states 1H and D is smaller along the proton dimension.

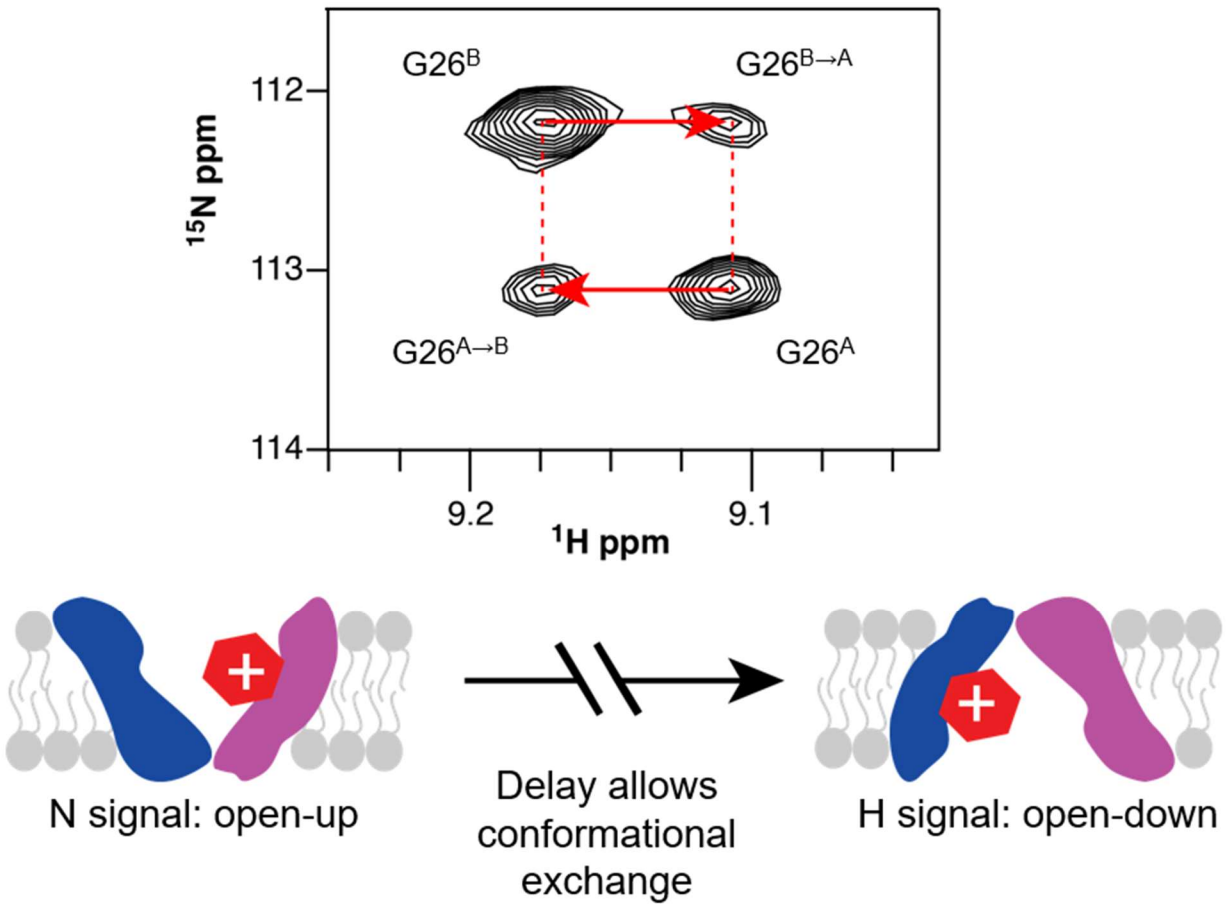

Figure 5 – *ZZ-exchange spectroscopy*. The ZZ-exchange experiment takes a standard ^{1}H-^{15}N HSQC experiment and adds a delay in between recording the nitrogen chemical shift and the proton chemical shift. If conformational exchange occurs during this delay, cross peaks will occur in the spectrum with the ^{15}N chemical shift of the original state and the ^{1}H chemical shift of the new state.

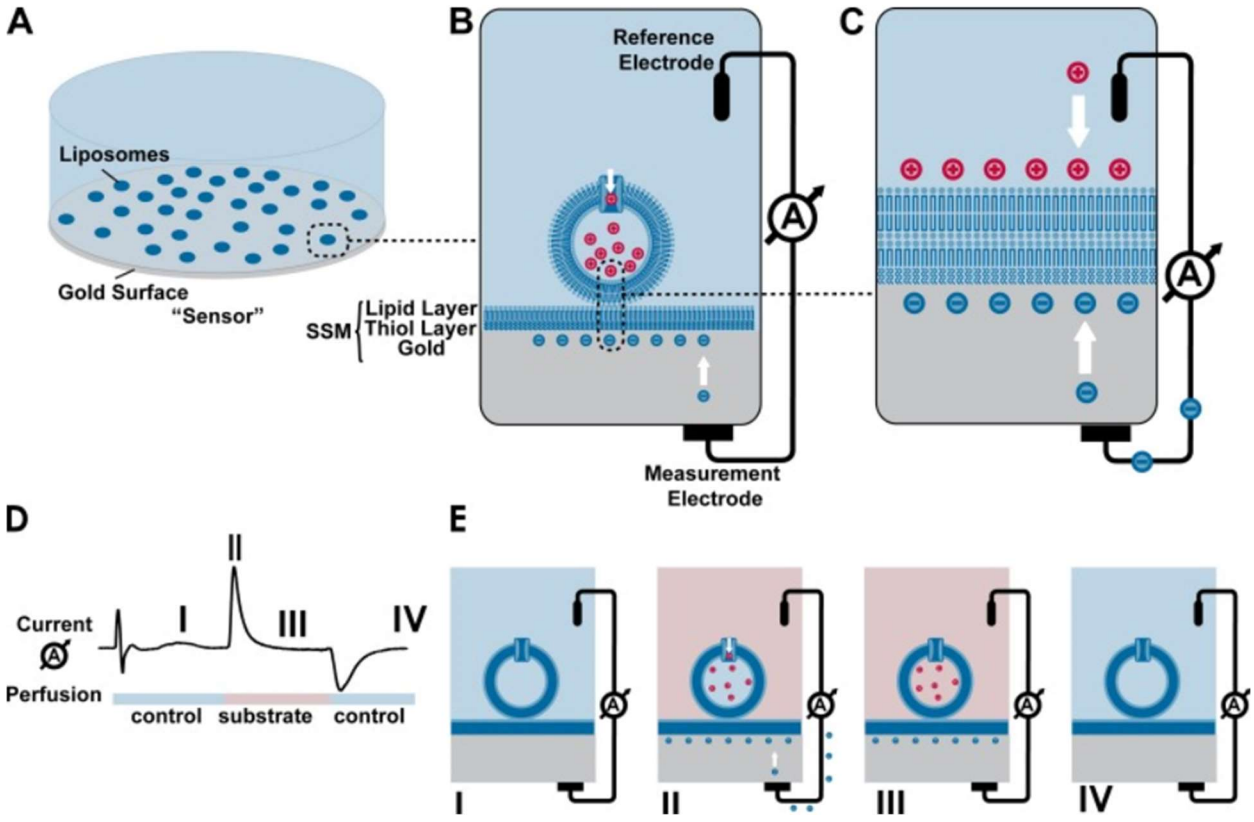

Figure 6 – *Overview of an SSME experiment*. Taken from[94]. (A) Thiolated alkanes are bound to a gold electrode and lipids are added to create the solid supported membrane (SSM). Proteoliposomes are adsorbed onto the membrane to the SSM to create the sensor. (B and C) The liposomal membranes, the SSM, and the electrode are capacitively coupled; current across the liposomal membranes can thus be read by the electrode. (D) Example current trace from an experiment, with a cartoon depiction of the stages shown in (E). During the first stage (I), the internal and external buffer are the same, and buffer perfusion creates a stable baseline. During the second stage, a new activating buffer is perfused to initiate transport – for example, by changing the substrate concentration. The initial current reaches a peak (II) upon full exchange of the buffer. The current quickly decays as the membrane voltage created by transport opposed further transport, eventually reaching a steady state where no additional transport occurs (III). In the final stage, the initial buffer is perfused once again, resetting the sensors and allowing additional experiments to be performed.

References

1. Schuldiner, S. EmrE, a model for studying evolution and mechanism of ion-coupled transporters. *Biochimica et Biophysica Acta (BBA) - Proteins and Proteomics* **1794**, 748–762 (2009).

2. Sharoni, M., Steiner-Mordoch, S. & Schuldiner, S. Exploring the Binding Domain of EmrE, the Smallest Multidrug Transporter. *Journal of Biological Chemistry* **280**, 32849–32855 (2005).

3. Saleh, M., Bay, D. C. & Turner, R. J. Few Conserved Amino Acids in the Small Multidrug Resistance Transporter EmrE Influence Drug Polyselectivity. *Antimicrobial Agents and Chemotherapy* **62**, (2018).

4. Ubarretxena-Belandia, I., Baldwin, J. M., Schuldiner, S. & Tate, C. G. Three-dimensional structure of the bacterial multidrug transporter EmrE shows it is an asymmetric homodimer. *The EMBO Journal* **22**, 6175–6181 (2003).

5. Chen, Y.-J. *et al.* X-ray structure of EmrE supports dual topology model. *PNAS* **104**, 18999–19004 (2007).

6. Lloris-Garcerá, P. *et al.* Antiparallel dimers of the small multidrug resistance protein EmrE are more stable than parallel dimers. *Journal of Biological Chemistry* (2012) doi:10.1074/jbc.M112.357590.

7. Gayen, A., Banigan, J. R. & Traaseth, N. J. Ligand-Induced Conformational Changes of the Multidrug Resistance Transporter EmrE Probed by Oriented Solid-State NMR Spectroscopy. *Angewandte Chemie International Edition* **52**, 10321–10324 (2013).

8. Yerushalmi, H. & Schuldiner, S. A common binding site for substrates and protons in EmrE, an ion-coupled multidrug transporter. *FEBS Letters* **476**, 93–97 (2000).

9. Gayen, A., Leninger, M. & Traaseth, N. J. Protonation of a Glutamate Residue Modulates the Dynamics of the Drug Transporter EmrE. *Nat Chem Biol* **12**, 141–145 (2016).

10. Ma, C. & Chang, G. Structure of the multidrug resistance efflux transporter EmrE from Escherichia coli. *Proceedings of the National Academy of Sciences of the United States of America* **101**, (2004).

11. Schuldiner, S. Controversy Over EmrE Structure. *Science* **317**, (2007).

12. Miller, C. Pretty structures, but what about the data? *Science* **315**, 459 (2007).

13. Schuldiner, S. When biochemistry meets structural biology: the cautionary tale of EmrE. *Trends in Biochemical Sciences* **32**, 252–258 (2007).

14. Morrison, E. A. *et al.* Antiparallel EmrE exports drugs by exchanging between asymmetric structures. *Nature* **481**, 45–50 (2011).

15. Fluman, N., Tobiasson, V. & von Heijne, G. Stable membrane orientations of small dual-topology membrane proteins. *PNAS* **114**, 7987–7992 (2017).

16. Ussing, H. H. Transport of ions across cellular membranes. *Physiological Reviews* **29**, 127–155 (1949).

17. Mitchell, P. Coupling of phosphorylation to electron and hydrogen transfer by a chemi-osmotic type of mechanism. *Nature* **191**, 144–148 (1961).

18. Mitchell, P. Translocations through natural membranes. *Adv Enzymol Relat Areas Mol Biol* **29**, 33–87 (1967).

19. Mitchell, P. & Moyle, J. Chemiosmotic hypothesis of oxidative phosphorylation. *Nature* **213**, 137–139 (1967).

20. Slater, E. C. An evaluation of the Mitchell hypothesis of chemiosmotic coupling in oxidative and photosynthetic phosphorylation. *Eur J Biochem* **1**, 317–326 (1967).

21. Mitchell, P. Aspects of the chemiosmotic hypothesis. *Biochem J* **116**, 5P-6P (1970).

22. Skulachev, V. P. Solution of the problem of energy coupling in terms of chemiosmotic theory. *J Bioenerg* **3**, 25–38 (1972).

23. Bihler, I., Hawkins, K. A. & Crane, R. K. Studies on the mechanism of intestinal absorption of sugars. VI. The specificity and other properties of Na ion-dependent entrance of sugars into intestinal tissue under anaerobic conditions, in vitro. *Biochim Biophys Acta* **59**, 94–102 (1962).

24. Crane, R. K. Hypothesis for mechanism of intestinal active transport of sugars. *Fed Proc* **21**, 891–895 (1962).

25. Hirata, H., Altendorf, K. & Harold, F. M. Role of an Electrical Potential in the Coupling of Metabolic Energy to Active Transport by Membrane Vesicles of Escherichia coli. *PNAS* **70**, 1804–1808 (1973).

26. Hirata, H., Altendorf, K. & Harold, F. M. Energy Coupling in Membrane Vesicles of Escherichia coli: I. ACCUMULATION OF METABOLITES IN RESPONSE TO AN ELECTRICAL POTENTIAL. *Journal of Biological Chemistry* **249**, 2939–2945 (1974).

27. Mitchell, P. A General Theory of Membrane Transport From Studies of Bacteria. *Nature* **180**, 134–136 (1957).

28. Jardetzky, O. Simple Allosteric Model for Membrane Pumps. *Nature* **211**, 969–970 (1966).

29. Hill, T. L. Studies in irreversible thermodynamics. IV. Diagrammatic representation of steady state fluxes for unimolecular systems. *J Theor Biol* **10**, 442–459 (1966).

30. Hill, T. L. & Chen, Y. D. Stochastics of cycle completions (fluxes) in biochemical kinetic diagrams. *PNAS* **72**, 1291–1295 (1975).

31. Hill, T. L. *Free Energy Transduction and Biochemical Cycle Kinetics*. (Academic Press, 1989).

32. Kaback, H. R. Molecular biology and energetics of membrane transport. *J Cell Physiol* **89**, 575–593 (1976).

33. Amanuma, H., Motojima, K., Yamaguchi, A. & Anraku, Y. Solubilization of a functionally active proline carrier from membranes of Escherichia coli with an organic solvent. *Biochem Biophys Res Commun* **74**, 366–373 (1977).

34. Lee, S. H., Cohen, N. S., Jacobs, A. J. & Brodie, A. F. Isolation, purification, and reconstitution of a proline carrier protein from Mycobacterium phlei. *Biochemistry* **18**, 2232–2239 (1979).

35. Kusaka, I. & Kanai, K. Purification and Characterization of Alanine Carrier Isolated from H-Proteins of Bacillus subtilis. *European Journal of Biochemistry* **83**, 307–311 (1978).

36. Hirata, H. Solubilization and purification of alanine carrier from thermophilic bacteria and reconstitution into vesicles capable of transport. *Methods Enzymol* **56**, 430–435 (1979).

37. Newman, M. J. & Wilson, T. H. Solubilization and reconstitution of the lactose transport system from Escherichia coli. *J Biol Chem* **255**, 10583–10586 (1980).

38. Turner, R. J. & Moran, A. Stoichiometric studies of the renal outer cortical brush border membrane D-glucose transporter. *J Membr Biol* **67**, 73–80 (1982).

39. Fukuhara, Y. & Turner, R. J. The static head method for determining the charge stoichiometry of coupled transport systems. Applications to the sodium-coupled D-glucose transporters of the renal proximal tubule. *Biochim Biophys Acta* **770**, 73–78 (1984).

40. Parent, L., Supplisson, S., Loo, D. D. F. & Wright, E. M. Electrogenic properties of the cloned Na+/glucose cotransporter: I. Voltage-clamp studies. *J. Membarin Biol.* **125**, 49–62 (1992).

41. Zerangue, N. & Kavanaugh, M. P. Flux coupling in a neuronal glutamate transporter. *Nature* **383**, 634–637 (1996).

42. Dutzler, R., Campbell, E. B., Cadene, M., Chait, B. T. & MacKinnon, R. X-ray structure of a ClC chloride channel at 3.0 A reveals the molecular basis of anion selectivity. *Nature* **415**, 287–294 (2002).

43. Murakami, S., Nakashima, R., Yamashita, E. & Yamaguchi, A. Crystal structure of bacterial multidrug efflux transporter AcrB. *Nature* **419**, 587–593 (2002).

44. Abramson, J. *et al.* Structure and mechanism of the lactose permease of Escherichia coli. *Science* **301**, 610–615 (2003).

45. Lopez-Redondo, M. L., Coudray, N., Zhang, Z., Alexopoulos, J. & Stokes, D. L. Structural basis for the alternating access mechanism of the cation diffusion facilitator YiiP. *PNAS* **115**, 3042–3047 (2018).

46. Solcan, N. *et al.* Alternating access mechanism in the POT family of oligopeptide transporters. *The EMBO Journal* **31**, 3411–3421 (2012).

47. Ryan, R. M. & Vandenberg, R. J. Elevating the alternating-access model. *Nat Struct Mol Biol* **23**, 187–189 (2016).

48. Zhou, X. *et al.* Structural basis of the alternating-access mechanism in a bile acid transporter. *Nature* **505**, 569–573 (2014).

49. Guan, L., Mirza, O., Verner, G., Iwata, S. & Kaback, H. R. Structural determination of wild-type lactose permease. *Proc Natl Acad Sci U S A* **104**, 15294–15298 (2007).

50. Kumar, H. *et al.* Structure of sugar-bound LacY. *PNAS* **111**, 1784–1788 (2014).

51. Wu, C. *et al.* Identification of an Alternating-Access Dynamics Mutant of EmrE with Impaired Transport. *J Mol Biol* **431**, 2777–2789 (2019).

52. Yamashita, A., Singh, S. K., Kawate, T., Jin, Y. & Gouaux, E. Crystal structure of a bacterial homologue of Na+/Cl--dependent neurotransmitter transporters. *Nature* **437**, 215–223 (2005).

53. Nelson, N., Sacher, A. & Nelson, H. The significance of molecular slips in transport systems. *Nat Rev Mol Cell Biol* **3**, 876–881 (2002).

54. Rudnick, G. How do transporters couple solute movements? *Molecular membrane biology* **30**, 355–9 (2013).

55. Forrest, L. R., Krämer, R. & Ziegler, C. The structural basis of secondary active transport mechanisms. *Biochimica et Biophysica Acta (BBA) - Bioenergetics* **1807**, 167–188 (2011).

56. Boudker, O. & Verdon, G. Structural perspectives on secondary active transporters. *Trends in pharmacological sciences* **31**, 418–26 (2010).

57. Yerushalmi, H. An Essential Glutamyl Residue in EmrE, a Multidrug Antiporter from Escherichia coli. *Journal of Biological Chemistry* **275**, 5264–5269 (2000).

58. Muth, T. R. & Schuldiner, S. A membrane-embedded glutamate is required for ligand binding to the multidrug transporter EmrE. *The EMBO journal* **19**, 234–40 (2000).

59. Soskine, M., Adam, Y. & Schuldiner, S. Direct evidence for substrate-induced proton release in detergent-solubilized EmrE, a multidrug transporter. *The Journal of biological chemistry* **279**, 9951–5 (2004).

60. Schuldiner, S. Competition as a way of life for H(+)-coupled antiporters. *Journal of molecular biology* **426**, 2539–46 (2014).

61. Rotem, D. & Schuldiner, S. EmrE, a Multidrug Transporter from Escherichia coli, Transports Monovalent and Divalent Substrates with the Same Stoichiometry. *J. Biol. Chem.* **279**, 48787–48793 (2004).

62. Morrison, E. A., Robinson, A. E., Liu, Y. & Henzler-Wildman, K. A. Asymmetric protonation of EmrE. *The Journal of General Physiology* **146**, 445–461 (2015).

63. Cho, M.-K., Gayen, A., Banigan, J. R., Leninger, M. & Traaseth, N. J. Intrinsic conformational plasticity of native EmrE provides a pathway for multidrug resistance. *J. Am. Chem. Soc.* **136**, 8072–8080 (2014).

64. Robinson, A. E., Thomas, N. E., Morrison, E. A., Balthazor, B. M. & Henzler-Wildman, K. A. New free-exchange model of EmrE transport. *PNAS* **114**, E10083–E10091 (2017).

65. Hussey, G. A., Thomas, N. E. & Henzler-Wildman, K. A. Highly coupled transport can be achieved in free-exchange transport models. *J. Gen. Physiol.* **152**, (2020).

66. Thomas, N. E. *et al.* The C terminus of the bacterial multidrug transporter EmrE couples drug binding to proton release. *J. Biol. Chem.* **293**, 19137–19147 (2018).

67. Bazzone, A., Zabadne, A. J., Salisowski, A., Madej, M. G. & Fendler, K. A Loose Relationship: Incomplete H+/Sugar Coupling in the MFS Sugar Transporter GlcP. *Biophysical Journal* **113**, 2736–2749 (2017).

68. Bozzi, A. T. *et al.* Structures in multiple conformations reveal distinct transition metal and proton pathways in an Nramp transporter. https://elifesciences.org/articles/41124 (2019) doi:10.7554/eLife.41124.

69. Bozzi, A. T., Bane, L. B., Zimanyi, C. M. & Gaudet, R. Unique structural features in an Nramp metal transporter impart substrate-specific proton cotransport and a kinetic bias to favor import. *J Gen Physiol* **151**, 1413–1429 (2019).

70. Burtscher, V., Schicker, K., Freissmuth, M. & Sandtner, W. Kinetic Models of Secondary Active Transporters. *Int J Mol Sci* **20**, (2019).

71. Bisignano, P. *et al.* A kinetic mechanism for enhanced selectivity of membrane transport. *PLoS Comput Biol* **16**, e1007789 (2020).

72. George, A., Bisignano, P., Rosenberg, J. M., Grabe, M. & Zuckerman, D. M. A systems-biology approach to molecular machines: Exploration of alternative transporter mechanisms. *PLoS Comput Biol* **16**, e1007884 (2020).

73. Grabe, M., Zuckerman, D. M. & Rosenberg, J. M. EmrE reminds us to expect the unexpected in membrane transport. *J Gen Physiol* **152**, (2020).

74. Rouse, S. L. & Sansom, M. S. P. Interactions of lipids and detergents with a viral ion channel protein: molecular dynamics simulation studies. *J Phys Chem B* **119**, 764–772 (2015).

75. Kurauskas, V. *et al.* How Detergent Impacts Membrane Proteins: Atomic-Level Views of Mitochondrial Carriers in Dodecylphosphocholine. *J Phys Chem Lett* **9**, 933–938 (2018).

76. Kurauskas, V. *et al.* Dynamics and interactions of AAC3 in DPC are not functionally relevant. *Nat Struct Mol Biol* **25**, 745–747 (2018).

77. Adam, Y., Tayer, N., Rotem, D., Schreiber, G. & Schuldiner, S. The fast release of sticky protons: Kinetics of substrate binding and proton release in a multidrug transporter. *PNAS* **104**, 17989–17994 (2007).

78. Sanders, C. R. & Schwonek, J. P. Characterization of magnetically orientable bilayers in mixtures of dihexanoylphosphatidylcholine and dimyristoylphosphatidylcholine by solid-state NMR. *Biochemistry* **31**, 8898–8905 (1992).

79. Glover, K. J. *et al.* Structural evaluation of phospholipid bicelles for solution-state studies of membrane-associated biomolecules. *Biophys J* **81**, 2163–2171 (2001).

80. Morrison, E. A. & Henzler-Wildman, K. A. Reconstitution of integral membrane proteins into isotropic bicelles with improved sample stability and expanded lipid composition profile. *Biochimica et biophysica acta* **1818**, 814–20 (2012).

81. Dutta, S., Morrison, E. A. & Henzler-Wildman, K. A. EmrE dimerization depends on membrane environment. *Biochimica et biophysica acta* **1838**, 1817–22 (2014).

82. Shcherbakov, A. A. *et al.* Structure and dynamics of the drug-bound bacterial transporter EmrE in lipid bilayers. *Nat Commun* **12**, 172 (2021).

83. Morrison, E. A. & Henzler-Wildman, K. A. Transported Substrate Determines Exchange Rate in the Multidrug Resistance Transporter EmrE. *J. Biol. Chem.* **289**, 6825–6836 (2014).

84. Williamson, M. P. Using chemical shift perturbation to characterise ligand binding. *Progress in Nuclear Magnetic Resonance Spectroscopy* **73**, 1–16 (2013).

85. Kovrigin, E. L. NMR line shapes and multi-state binding equilibria. *Journal of biomolecular NMR* **53**, 257–70 (2012).

86. Waudby, C. A. *et al.* Two-Dimensional NMR Lineshape Analysis. *Scientific Reports* **6**, 24826 (2016).

87. Rao, B. D. Nuclear magnetic resonance line-shape analysis and determination of exchange rates. *Methods Enzymol* **176**, 279–311 (1989).

88. Li, Y. & Palmer, A. G. TROSY-selected ZZ-exchange experiment for characterizing slow chemical exchange in large proteins. *Journal of biomolecular NMR* **45**, 357–60 (2009).

89. Kelety, B. *et al.* Transporter assays using solid supported membranes: a novel screening platform for drug discovery. *Assay Drug Dev Technol* **4**, 575–582 (2006).

90. Schulz, P., Garcia-Celma, J. J. & Fendler, K. SSM-based electrophysiology. *Methods* **46**, 97–103 (2008).

91. Bazzone, A., Barthmes, M. & Fendler, K. SSM-Based Electrophysiology for Transporter Research. *Meth. Enzymol.* **594**, 31–83 (2017).

92. Garcia-Celma, J. J., Smirnova, I. N., Kaback, H. R. & Fendler, K. Electrophysiological characterization of LacY. *PNAS* **106**, 7373–7378 (2009).

93. Mio, K. & Sato, C. Lipid environment of membrane proteins in cryo-EM based structural analysis. *Biophys Rev* **10**, 307–316 (2017).

94. Barthmes, M., Liao, J., Jiang, Y., Brüggemann, A. & Wahl-Schott, C. Electrophysiological characterization of the archaeal transporter NCX_Mj using solid supported membrane technology. *J Gen Physiol* **147**, 485–496 (2016).

Chapter 1

A new free exchange model of EmrE transport

Anne E. Robinson, Nathan E. Thomas, Emma A. Morrison, Bryan Balthazor and Katherine A. Henzler-Wildman

Preface

In this paper, we describe the NMR results which our inconsistent with canonical models of antiport and propose a new free exchange model to explain EmrE's function. Anne performed experiments and wrote the initial draft of the paper, I performed liposomal transport assays and helped revise the paper, and Emma and Bryan performed additional NMR and ITC experiments.

Abstract

EmrE is a small multidrug resistance transporter found in *E. coli* that confers resistance to toxic polyaromatic cations due to its proton-coupled antiport of these substrates. Here we show that EmrE breaks the rules generally deemed essential for coupled antiport. NMR spectra reveal that EmrE can simultaneously bind and cotransport proton and drug. The functional consequence of this finding is an exceptionally promiscuous transporter: Not only can EmrE export diverse drug substrates, it can couple antiport of a drug to either one or two protons, performing both electrogenic and electroneutral transport of a single substrate. We present a new free exchange model for EmrE antiport that is consistent with these results and recapitulates ΔpH-driven concentrative drug uptake. Kinetic modeling suggests that free exchange by EmrE sacrifices coupling efficiency but boosts initial transport speed and drug release rate, which may facilitate efficient multidrug efflux.

Significance Statement

EmrE facilitates *E. coli* multidrug resistance by coupling drug efflux to proton import. This antiport mechanism has been thought to occur via a pure exchange model which achieves coupled antiport by restricting when the single binding pocket can alternate access between opposite sides

of the membrane. We test this model using NMR titrations and transport assays and find it cannot account for EmrE antiport activity. We propose a new free exchange model of antiport with fewer restrictions that better accounts for the highly promiscuous nature of EmrE drug efflux. This model expands our understanding of proton-coupled transport and has implications for both transporter design and drug development.

Introduction

Secondary active transport moves one substrate across a membrane against its concentration gradient by coupling it to downhill transport of a second substrate, often a proton. This coupled transport process may move both substrates in the same direction (symport) or in opposite directions (antiport). To move molecules across the membrane, the substrate binding site must be alternately accessible to either side of the membrane. Symport or antiport of two substrates is generally explained using models that restrict this alternating access of the transporter to specific states (Fig. 1). These models are appealing because they provide a simple mechanism that efficiently couples transport of the two substrates.

Here we investigate the mechanism of proton/drug antiport by the small multidrug resistance transporter, EmrE. EmrE uses the proton motive force (PMF) across the inner membrane of *E. coli* to drive efflux of toxic polyaromatic cations, conferring resistance to these compounds. The single binding pocket of EmrE is defined by two glutamate 14 residues (1-3), one on each of the two monomers in the asymmetric homodimer (4-7). This binding site can accommodate one drug-substrate or up to two protons. Alternating access of the asymmetric homodimer is achieved by a conformation swap between the two monomers (5) and is necessary for transport activity (8). Traditionally, EmrE antiport has been explained by the pure exchange model (9) in Fig. 1A. Such “pure exchange” of one drug for two protons with no slippage results in tightly coupled stoichiometric antiport. This is achieved by 1) limiting substrate binding such that both substrates never bind simultaneously and 2) limiting in/out exchange (alternating

access) to substrate bound states (fully protonated or drug-bound). Several lines of evidence support this model. Competition between drug and proton binding is demonstrated by substrate-induced proton release (10, 11), a decrease in substrate-binding affinity at low pH (1) and a bell-shaped pH-dependence of transport activity (3). In addition, observation of electrogenic transport of monovalent, but not divalent, substrates is consistent with a 2:1 H^+/drug transport stoichiometry (12). Other transport mechanisms have been considered previously (11), but the traditional pure exchange model has been favored in the absence of compelling data to justify selection of a more complex scheme.

However, the highly dynamic nature of EmrE (13-15), critical for its ability to transport diverse substrates, is hard to reconcile with the strict limitations on alternating access in the pure exchange model. Recent NMR data has provided evidence that EmrE violates at least the second stipulation of the traditional model: protonation of drug-free EmrE is asymmetric (16) such that a singly protonated state exists near neutral pH, and all of the protonation states ($2H^+$-bound, $1H^+$-bound, empty) engage in alternating access (16, 17). These findings suggest the need to develop a new model for EmrE transport activity. In this study, we use NMR spectroscopy and liposomal flux assays to test the pure-exchange model of EmrE antiport. We show that EmrE violates both requirements of pure-exchange antiport and utilizes multiple proton/drug transport stoichiometries. We develop a new “free exchange” EmrE antiport model which reconciles the novel states and unrestricted alternating access behavior of EmrE with its well-established proton-driven drug efflux activity. Our model accounts for previously inexplicable behaviors of EmrE such as the ease of converting the protein to a symporter. Furthermore, our model suggests that a reduced coupling efficiency may be a necessary price for the structural flexibility required to bind and efficiently efflux diverse substrates.

Results

Substrate binding is not exclusive. Competition between drug and proton binding to EmrE is well-established, but the data do not prove mutually exclusive binding, a stipulation of the pure

exchange model (1, 10, 11). The recent demonstration of asymmetry in proton binding (16) led us to reconsider whether EmrE can bind a drug and proton simultaneously. To test this, we performed NMR pH titrations of EmrE saturated with the drug substrate tetraphenylphosphonium (TPP^+) and solubilized in isotropic bicelles. We have previously shown that E14 and H110 are the only residues in EmrE that titrate near neutral pH. Furthermore, titration of E14, but not H110, leads to a global conformational change in the protein that is evident in an NMR pH titration (16). If proton and drug binding are exclusive, as predicted by the traditional model of EmrE antiport, then TPP^+-saturated EmrE should not bind any protons and thus will not titrate globally with pH. However, many peaks in the NMR spectrum do titrate with pH (Figs. 2A and B and S1), demonstrating that protonation does occur when TPP^+ is bound. In contrast to the two protonation events observed for drug-free EmrE (pKa values 7.0 ± 0.1 and 8.2 ± 0.3) (16), the linear movement of the peaks in the TPP^+-bound NMR pH titration is consistent with a single protonation event with a pKa of 6.8 ± 0.1 (Fig. 2C and S2). To test whether this protonation occurs on the critical E14 residue, we repeated the pH titration with TPP^+-saturated E14D-EmrE, which has a lower pKa but still binds TPP^+ (1-3, 16). As expected, we observed a shift in the titration midpoint to lower pH, reflecting the lower pKa of E14D-EmrE (Figs. 2A and B and S3) and confirming we are monitoring protonation of E14 in drug-bound EmrE.

It is well known that TPP^+ and H^+ binding is competitive such that the TPP^+ binding affinity of EmrE is weaker at low pH (1). Thus, it is important to ensure that the pH-dependent chemical shift changes are not due to pH-dependent loss of substrate binding. We used ITC to measure TPP^+ binding at low pH. In isotropic bicelles at 45 °C (matching the NMR sample conditions), the $K_D^{apparent}$ for TPP^+ is 70 ± 9 μM at pH 5.5 (Table S1). With this affinity, >95% of EmrE will remain TPP^+-bound in the NMR sample at pH 5.5. As a second more direct test, we performed an NMR-monitored TPP^+ titration at pH 5.2. As expected, there were no changes in the peak positions with increasing TPP^+ concentrations (Fig. S4), only changes in peak intensity. Therefore, the pH-induced chemical shift changes in the NMR spectra are not due to loss of TPP^+ binding. Loss of

peak intensity with no change in peak position at lower TPP^+ concentrations reflects “slow exchange” on the NMR timescale. In contrast, the change in peak position observed as a function of pH reflects “fast exchange”. This rate difference is not surprising and results in distinct spectral changes in the NMR spectra that allow these two events to be readily distinguished. This NMR data shows that EmrE can simultaneously bind a drug and a proton at physiological pH.

Substrate binding is asymmetric. Mapping the NMR data onto the structure reveals a broad distribution of residues that sense E14 protonation in TPP^+-bound EmrE (Fig. 2D), consistent with protonation-dependent conformational changes in drug-bound EmrE. This is not surprising given the protonation-dependent transport activity of EmrE (3) and the coupled structural and dynamic changes that occur upon protonation in the absence of substrate (16-18). Interestingly, residues corresponding to monomer B in the asymmetric homodimer have much larger chemical shift changes upon pH titration of TPP^+-bound EmrE (Fig. 2D). This implies that TPP^+ interacts asymmetrically with EmrE, associating with the E14 on monomer A such that protonation of this residue is prevented, while the E14 on monomer B remains accessible for protonation. This is further supported by the TPP^+ titration at low pH, which shows that residues in monomer A are more sensitive to TPP^+ binding (Fig. S4). Such asymmetric interaction of the substrate with the two monomers was suggested by the cryoEM structure of TPP^+-bound EmrE (6). It is also consistent with the asymmetric structure of the EmrE homodimer, the unique chemical shifts of the two E14 residues (19) and the asymmetric protonation of the two E14 residues in drug-free EmrE (16).

Drug binding only releases one proton at low pH. To validate this extraordinary finding that an antiporter can simultaneously bind both substrates, we measured TPP^+-induced proton release from EmrE at low pH. According to the pure exchange model, substrate binding is mutually exclusive such that both protons should be released from the EmrE homodimer upon TPP^+ binding at low pH. In contrast, if EmrE is able to bind TPP^+ and a proton simultaneously, TPP^+ binding will only trigger release of a single proton per dimer at low pH. A previous measurement

of TPP^+-induced proton release was inconclusive because the amount of TPP^+ added was insufficient to saturate EmrE at low pH (10). We repeated this measurement with EmrE solubilized in isotropic bicelles using a saturating TPP^+ concentration and observed release of 1.2 ± 0.2 protons per EmrE dimer at pH 5.5 (Fig. S5, 3A). Because the weak buffering required for direct proton detection in this assay results in relatively large errors, we used a second experimental approach to verify the results. By measuring TPP^+ binding with ITC in multiple buffers with different heats of ionization (20) we could determine the number of protons released per TPP^+ binding event and confirm binding saturation (Fig. 3B, Table S1). We again detected 1.2 ± 0.1 protons released per dimer. The ITC data also confirmed the known 1:1 TPP^+/dimer binding stoichiometry remains at low pH. These proton release values are much closer to 1 than 2, consistent with the NMR data demonstrating simultaneous binding of 1 TPP^+ and 1 H^+ to the EmrE dimer at low pH.

EmrE alternates access when bound to both substrates. The ability of EmrE to bind a drug and proton simultaneously will only affect net transport if this state engages in alternating access. For EmrE, the two monomers within the asymmetric homodimer swap conformations to switch between open-in and open-out (alternate access), and this rate can be quantitatively measured using TROSY-selected ZZ exchange NMR experiments (5, 21). We compared the rate of alternating access for TPP^+-saturated EmrE in isotropic bicelles at high pH (only drug bound) and low pH (both drug and proton bound) and found they were nearly identical. (Fig. 4, S6). Thus, EmrE can move both substrates across the membrane at the same time, violating the expected behavior of an antiporter, and requiring the development of a new transport model.

Importantly, chemical shift reflects the unique environment of each nucleus within the three-dimensional structure of the protein. Thus, the peaks in the NMR spectra correspond to the two distinct monomer *conformations* (shapes in Fig. 5A), not monomer identities (colors in Fig. 5A). The asymmetric response of the residues in each monomer to TPP^+ and pH in the NMR

experiments show that TPP^+ interacts more closely with the monomer in *conformation* A, while protonation of E14 can still occur on the monomer in *conformation* B. Since the two monomers swap conformations during alternating access, this means that TPP^+ (and H^+) is (are) swapped back and forth between the two monomers as part of the alternating access process, as illustrated in Fig. 5A. Therefore, although only one E14 is necessary for TPP^+ binding, the swapping of substrate between monomers during alternating access will require both E14 residues for transport. This is consistent with the "functional symmetry" of E14 (22), the observation of TPP^+ binding to mixed WT-E14C EmrE heterodimers (7), and the dominant negative phenotype of E14 mutants *in vivo* and *in vitro* (23).

A new free exchange model for EmrE transport. To accommodate the new states and transitions of EmrE, we expanded the transport scheme (Fig. 5A), removing the restrictions on simultaneous substrate binding and alternating access that are imposed by the pure exchange model. The model predicts that EmrE should have multiple transport pathways, including the well-established 2:1 H+/drug antiport (12) (Fig. 5B) as well as 1:1 antiport, proton leak, uncoupled uniport of drug, and even symport (Fig. 5C). The rates of individual steps in the model are similar, so flux should occur through multiple pathways. Partitioning between the transport pathways will be determined by the relative rates of individual steps, making kinetics an important factor in determining the net stoichiometry of the transport process. Furthermore, because the multiple transport pathways move different net charges across the membrane, they will be driven by distinct thermodynamic driving forces. Kinetics is therefore an important factor controlling net flux, which will vary depending on the precise conditions.

To understand if it is possible to produce the well-established proton/drug antiport activity of EmrE with this scheme we performed mathematical simulations. We can estimate all of the rate constants from our own and others' experimental data (Fig. S7 and Table S2). Rates of alternating access are based on NMR dynamics measurements (5, 16, 17). TPP^+ on- and off-rate estimates

were determined previously for detergent-solubilized EmrE (11). We assumed fast proton on-rates ($\approx 10^{10}$ $M^{-1}s^{-1}$) and used the pKa values determined by NMR (this work and (16)) to estimate off-rates. These are reasonable assumptions given the small size of H^+, the relatively fast on-rates for TPP^+ binding, and the fact that binding affinities of drug-substrates are primarily determined by the off-rate (11).

Numerical simulation of ΔpH-driven transport (Appendix 1) results in rapid concentrative uptake of TPP^+ into liposomes (Fig. 6A, B). A 2-fold pH gradient drives 80-fold concentration of TPP^+, a reduction in coupling efficiency compared to the pure exchange model with a strict $2H^+$:$1TPP^+$ transport stoichiometry. These results clearly demonstrate that ΔpH-driven coupled antiport of TPP^+ can be achieved in our new kinetically-driven model without restricting alternating access or substrate binding.

To better understand how coupled antiport occurs in our new model, we developed a single molecule Gillespie simulation (Appendix 2) (24). Unlike the previous deterministic simulation, this stochastic simulation ignores the finite liposomal volume, but informs on the relative frequency of each transition, which is indicated by arrow thickness in Fig. 6C. Interestingly, TPP^+ is most likely to bind proton-free EmrE but be released subsequent to protonation. Simultaneous proton and TPP^+ binding enhances the release of TPP^+ (Fig. S7), resulting in faster turnover. This mechanism may be advantageous for a multidrug transporter because it allows efficient release of substrates with a wide range of affinities.

While our simulations demonstrate coupled antiport, future work will be needed to test and revise the model. Several rate constants were estimated using simplifying assumptions, and all were measured using solubilized EmrE. Importantly, solubilization results in a symmetric environment rather than the asymmetric conditions experienced in a membrane under a proton motive force. Furthermore, our model does not yet account for a membrane potential, as it remains unclear precisely how a membrane potential affects discrete steps of transport pathways

(25). Because the multiple transport pathways in our model move different net charges across the membrane, the membrane potential will affect the partitioning between pathways in a manner which is currently unaccounted for by our model. Nevertheless, the ability of our simulation to qualitatively recapitulate EmrE antiport is noteworthy because it breaks long-standing assumptions about the mechanism of coupled antiport.

Unlike the pure exchange model, our model allows *free exchange* of the transporter, with alternating access permitted in all states. This has significant functional implications because it allows for *free exchange* of substrates with multiple transport stoichiometries. This differs dramatically from the single antiport stoichiometry achieved with pure exchange of substrates across the membrane. To test our free exchange model, we experimentally investigated two of its key predictions: 1) Does EmrE leak protons? and 2) Is EmrE a strictly-coupled 2:1 H^+/drug antiporter?.

EmrE does not rapidly leak protons. To test whether EmrE leaks protons, we created EmrE proteoliposomes with a negative inside membrane potential. Protons should rapidly enter the liposome under these conditions if EmrE leaks protons, increasing the weakly buffered external pH. However, no significant proton movement was detected (Fig. 7A and B), demonstrating that drug-free EmrE does not rapidly leak protons across the membrane. Addition of a protonophore did result in rapid pH change, confirming the integrity of the assay. These results contrast with the prediction of a rapid proton leak from the NMR exchange rates. However, all of the rates in the free exchange model were measured with symmetric conditions (ΔpH=0, $\Delta\Box$=0). In contrast, this assay is performed in the presence of a membrane potential. Perhaps the asymmetry introduced by the membrane potential alters the structure or dynamics of EmrE in a way that prevents proton leakage.

EmrE does not have a strict 2:1 H^+/drug antiport stoichiometry. To determine whether EmrE can transport drug substrates with different proton coupling stoichiometries as predicted by the

NMR data we performed transport assays. We reconstituted EmrE into 3:1 POPC/POPG liposomes and observed transport by directly detecting proton flux in the weakly buffered solution outside of the liposome. We first performed transport assays using TPP^+ (Fig. S8 and Table S4), but these assays are complicated by the high affinity of TPP^+ for EmrE as well as its hydrophobicity and membrane permeability. We therefore compared ΔpH- and Δ□-driven transport of ethidium (Eth^+), an EmrE substrate that is more well-suited to transport assays due to a weaker binding affinity (K_D at least 1000-fold weaker (26)) and decreased hydrophobicity compared to TPP^+.

We first performed ΔpH-driven transport assays. The proteoliposomes were reconstituted in 100 mM MES, 100 mM KCl, pH6 to create a strongly buffered interior solution. They were then desalted into weak buffer for pH monitoring (0.5 mM MOPS, 100 mM KCl, pH6) and the external pH was adjusted to pH 8 (Fig. 7C and D). Adding drug to the external solution results in EmrE-mediated drug uptake into the liposomes coupled to proton efflux down the pH gradient (Fig. 7D, and Table S3). An electrogenic transport process, such as $2H^+/1Eth^+$ antiport, will proceed under these conditions until the net charge movement creates an opposing membrane potential sufficient to stop further transport. However, due to the relatively large capacitance of the membrane, a significant amount of electrogenic transport can occur before an opposing membrane potential is achieved. Subsequent addition of the potassium ionophore valinomycin, which enables flux of K^+ to relieve any membrane potential, results in additional transport (Fig. 7D and H, and Table S3). This demonstrates that a membrane potential had developed and supports the well-established $2H^+/1drug^+$ antiport activity of EmrE (12). Control experiments confirm that we are observing EmrE-mediated proton efflux and not simply proton-release upon drug binding: (1) DCCD-inactivation of EmrE (3) inhibits the proton release from the proteoliposomes and (2) doubling the number of EmrE dimers per liposome (by doubling the EmrE:lipid ratio) while keeping the total number of liposomes constant results in identical proton-

release from the proteoliposomes (Fig. 7D and H , and Table S3). Binding-related proton release depends on protein concentration and would double, while transport depends only on substrate concentrations and liposome volume, which are the same. Besides establishing the functionality of EmrE, these ΔpH-driven assays demonstrate that Eth^+-bound EmrE does not rapidly leak protons: When the protonophore CCCP is added at the end of the assay, a large pH change is recorded, demonstrating that the pH gradient was maintained throughout the assay. Together with the data in Fig. 7B, this shows that EmrE does not rapidly leak protons in either the drug-free or drug-bound state. Thus, 1:1 antiport combined with uncoupled proton flux cannot account for the observed increase in flux after addition of valinomycin.

Assuming a strict 2:1 antiport stoichiometry, the measured total proton release corresponds to transport of only 38 nmol of Eth^+. Using simple estimates of the liposome internal volume, this corresponds to concentration of Eth^+ inside the liposome by ≈60-70-fold, much less than expected for strict $2H^+/1Eth^+$ antiport driven by ΔpH=2 (see Appendix 3 for detailed calculations). This contradiction could be explained if EmrE transport activity is a mixture of 2:1 and 1:1 antiport stoichiometries. However, because accurate quantitation is difficult (see Appendix 3 for more extended discussion) we turned to Δ□□driven transport assays, which more robustly distinguish different transport stoichiometries.

We compared EmrE transport activity under conditions of positive inside, neutral, and negative inside liposomes (Fig. 7E-H, and Table S5). To generate the membrane potentials (Δ□), we reconstituted EmrE into proteoliposomes with 100-fold K^+ gradients (100 mM KCl versus1 mM KCl + 99 mM NaCl). Upon addition of valinomycin, K^+ diffusion down the gradient creates either a positive-inside (low K^+ inside) or a negative inside (high K^+ inside) membrane potential (Fig. 7A and E). When the internal and external K^+ concentrations are matched, no membrane potential is generated. In all cases, pH≈7.5, ΔpH=0, and the interior was strongly buffered (50 mM MOPS) while the exterior was weakly buffered (0.05 mM MOPS) to allow direct monitoring of H^+ flux.

These assays confirm the previous proton leak assay—addition of valinomycin to generate a membrane potential results in only a slight pH drift (Fig. 7F and G). It does not result in significant pH change, as would occur if H^+ could leak through EmrE in response to the potential. When Eth^+ is added to the external solution of $\Delta\Box$=0 proteoliposomes, the external pH decreases due to coupled influx of Eth^+ and efflux of protons by EmrE (Fig. 7F). This is driven entirely by the Eth^+ gradient since ΔpH and $\Delta\Box$=0 (Fig. 7E). When the assay is repeated with a positive-inside $\Delta\Box$ proton efflux is enhanced (Fig. 7F). Because a positive inside $\Delta\Box$ can only drive electrogenic transport, this data supports 2:1 H^+/drug EmrE antiport activity (Fig. 7E). Such positive-inside-driven EmrE antiport has been observed previously by monitoring drug loading directly (12). Our data confirms that the same result is obtained when monitoring the antiported protons. Control experiments (Fig. 7F) with empty liposomes and an inactive mutant, E14Q-EmrE, show no proton flux, again confirming that the pH changes are due to transport through EmrE.

We then tested the effect of a negative-inside membrane potential (Fig. 7E and G) and obtained an entirely unexpected result. The Eth^+ concentration gradient will always favor Eth^+ influx, and thus H^+ efflux (external pH decrease) due to the coupled antiport activity of EmrE. The negative membrane potential will oppose 2:1 H^+/Eth^+ antiport, just as a positive membrane potential favors it (Fig. 7E). We therefore expected to observe a small decrease in external pH, somewhere between zero and the ΔEth^+-driven transport observed for $\Delta\Box$=0 liposomes. The exact value would depend on the balance between ΔEth^+, $\Delta\Box\Box$ and the net stoichiometry, since 1:1 H^+/Eth^+ antiport would not be inhibited by the membrane potential. Instead, upon addition of Eth^+ to negative-inside proteoliposomes the external pH *increased* indicating proton movement *into* the liposomes (Fig. 7G). Because Eth^+ is only added externally, this means that Eth^+ and H^+ are both moving in the same direction across the membrane (Fig. 7E). This signal was EmrE-dependent as it did not occur with inactive E14Q-EmrE. Coupled transport of two substrates in the same direction, as we observe, is the definition of symport. The free exchange model based

on the NMR data does predict that symport should be possible under the right conditions, since EmrE can simultaneously bind both drug and proton and alternate access with both substrates bound. Symport of Eth^+ and H^+ into the liposome results in a net movement of +2 charges into the liposome and would be strongly favored by a negative inside membrane potential.

EmrE is known as a proton/drug antiporter, not a symporter. Are there any other possible explanations that do not invoke symport? When Eth^+ is added to the negative-inside proteoliposomes (valinomycin has already been added to create the potential), there is an initial lag phase or perhaps even a small release of protons before the large proton uptake occurs. When we reverse the order of addition (Fig. 7G)—adding Eth^+ before valinomycin—we observe proton efflux upon Eth^+ addition. This is the expected behavior for an antiporter, Eth^+ in/H^+ out. There is no membrane potential present at this point, so Eth^+ loading is driven by ΔEth^+. Subsequent addition of valinomycin creates a negative-inside potential and proton *influx* occurs without any lag phase. The net decrease in the concentration of protons on the outside of the liposome could be explained by three other potential processes. 1) EmrE could facilitate uncoupled proton uptake. This explanation is highly unlikely as our assays demonstrate that EmrE does not transport protons in an uncoupled fashion (Fig. 7B, F, G). 2) Uncoupled Eth^+ import is followed by 2:1 H^+/Eth^+ antiport. This second option is also very unlikely since addition of the protonophore CCCP at the end of each experiment demonstrates that a significant membrane potential still remains and uncoupled transport would dissipate the membrane potential (Fig. 7G). 3) EmrE-mediated loading of Eth^+ is followed by EmrE-mediated efflux of Eth^+ with different H^+/Eth^+ stoichiometries. Since the assay begins with no Eth^+ inside, reversing the transport process upon generation of the negative potential can at most pump out all the Eth^+ that has been imported. If import and efflux of Eth^+ occurred via the same stoichiometry, this would result in no net proton flux. However, if Eth^+ is loaded with a 1:1 H^+/Eth^+ antiport stoichiometry and then the membrane potential drives efflux with a 2:1 stoichiometry, twice as many protons would be

imported into the liposome than released from the liposome and the external pH would rise beyond the initial value. However, this is not consistent with the results of the experiment where Eth^+ was added first followed by valinomycin (Fig. 7G). While the data from these transport assays cannot definitively differentiate between this third option or EmrE symport, symport is the most likely explanation for the data. In either case, it is clear that strict 2:1 antiport cannot account for the EmrE-dependent transport activity observed. In fact, the lag phase observed when Eth^+ is added to the negative-inside liposomes is expected if there are multiple transport pathways since the different pathways will have different driving forces and kinetics. Whatever the microscopic pathways, our results indicate net symport of drug and proton into liposomes by EmrE in response to a negative-inside membrane potential. Together with the data from our positive-inside liposome assay demonstrating 2:1 H+/Eth+ antiport activity, these results suggest that EmrE must be able to perform proton-coupled drug transport with multiple transport stoichiometries.

Discussion

Reassessing the mechanism of secondary active transport. Advances in *in vitro* studies of transporter function and structure have expanded our understanding of the range of conformational changes that can produce alternating access (27, 28), and the mechanisms controlling stoichiometry and transport (29). MdfA and $PepT_{ST}$, have different proton/substrate transport stoichiometries when transporting substrates of different size or charge (30, 31) and the stoichiometry of sugar/proton symport by LacY is pH-dependent (32). The ClC transporter performs 2:1 H+/substrate coupled antiport of some anions and uncoupled transport of other anions (33). However, the CLC transport mechanism is not a standard alternating access model—it relies on relatively small movements of amino acid side chains that are easily altered by binding different ions (33, 34). This contrasts with EmrE, where the crystallographic (4), cryoEM (35), and NMR data (5, 8) all support a standard alternating access mechanism with large scale changes in helix orientation. Furthermore, the CLC family evolved to include both channels and

exchangers, and the observed uncoupling and leak behavior appears to shift the protein function along this continuum between transporter and channel for different substrates. In contrast, EmrE never appears to have channel-like behavior: pH gradients and membrane potentials are never fully dissipated in our liposomal assays. Thus, we have described EmrE as having multiple transport stoichiometries due to the multiple transport pathways in the free exchange model, rather than a single transport stoichiometry plus leak or uncoupled transport.

Here we show that EmrE can transport a *single* substrate with multiple proton/substrate transport stoichiometries. This flexibility of transport stoichiometry is achieved by a number of unexpected features. First, TPP^+ binds asymmetrically in the active site, making space for a proton to bind simultaneously. Second, all of the EmrE proton- and/or drug-bound states are capable of engaging in alternating access. These phenomena of mutual binding and unlimited alternating access at first seem to jeopardize EmrE's capacity for coupled antiport, but a closer look reveals the efficacy and benefits of such a mechanism. These features of EmrE are reminiscent of the *de novo* designed transporter, Rocker (36), although EmrE is more efficiently coupled. It suggests that functionally coupled transport can be achieved without the need to invoke significant constraints on the states and transitions of the transporter, perhaps providing new insights for the rational design of *de novo* transporters.

How is antiport driven with these unique parameters? In this free exchange model, the relative rates of the individual steps will determine the efficiency of proton-coupled transport. Although H^+ and TPP^+ can bind simultaneously, their binding is still negatively linked, resulting in differential TPP^+ affinity for the open-in and open-out states of EmrE in the presence of a transmembrane pH gradient. In fact, a pH gradient may even skew the equilibrium between the open-in and open-out states (17). Such differential substrate affinity is important for determining the relative kinetics and efficiency of the transport cycle, particularly in the presence of leak pathways (37). Our new free exchange model relies on both TPP^+/H^+ binding competition and the

thermodynamic and kinetic asymmetry introduced by the PMF to drive productive transport by EmrE. This has an interesting parallel to the finding that the PMF controls the rate of chemiosmotically-driven LacY proton/sugar symport (38).

Exactly how a membrane potential will affect the free exchange model remains unclear. A membrane potential can affect any process involving movement of charge through the potential (39). This includes 1) flux of charged substrates, 2) binding and release of charged substrates if they become occluded from water, 3) alternating access of a charged binding pocket, and 4) structural rearrangements that modify solvent exposure of other charged areas of the protein. In the case of EmrE, all four of these are possible: All substrates are charged, the binding pocket contains two glutamates (1-3, 22) and is thus negatively charged unless protons or cationic substrates are bound, and finally there are other charged residues in the solvent-exposed loops of EmrE which have been implicated in the transport mechanism (18). The impact of each of these components on the transport mechanism is still not well-understood and will likely vary for each transporter (25, 40, 41). Thus, we have not included a membrane potential in our current kinetic simulations of the free exchange model.

The free exchange model based on the NMR-detected states and transitions of EmrE predicts that EmrE should leak protons. However, we do not experimentally detect leak in any liposomal assays: Protons do not rapidly flow into or out of EmrE proteoliposomes when a membrane potential is generated, and the transport processes saturate without fully dissipating the membrane potential or ΔpH in all transport assays. It is important to remember that high-resolution kinetic and structural data are almost always obtained from studies of membrane proteins solubilized in membrane mimetic environments. This data can provide great insight into the detailed molecular mechanisms. However, it must be carefully interpreted because it is not obtained in the asymmetric environment created by the proton motive force, which is necessary to drive active transport. In contrast, transport assays provide information on the effect of

asymmetric gradients on net transport, but these assays cannot be performed under the solubilized protein conditions used for structural studies. Thus, when building a model from a combination of structural and transport data, it is important to remember the variety of conditions used to collect disparate data sets. Our results highlight the need to develop structural biology tools capable of experimentally determining the effect of a PMF on protein structure and dynamics.

Our transport assays confirm that EmrE does not have a single 2:1 H+/drug antiport stoichiometry, but additional experiments will be needed to understand why EmrE does not leak protons as predicted by the NMR data, determine the transport stoichiometry as a function of different conditions to understand how ΔpH and Δ□ affect the coupling stoichiometry, and to revise the free exchange model.

Biological implications of the new mechanism. The free exchange model has an elegant simplicity of its own, placing no structural or dynamic constraints upon EmrE. This is functionally relevant because the highly dynamic nature of EmrE is important for its promiscuous multidrug recognition (13-15). Our model suggests that simultaneous drug and proton binding may even be advantageous, speeding up the release of tight binding substrates (Fig. S7) that would otherwise compromise EmrE's ability to rapidly pump toxic molecules out of *E. coli*. The free exchange model allows for extreme adaptability in a minimalistic protein, sacrificing coupling efficiency for increased transport speed. Interestingly, reduced coupling efficiency was previously proposed as a necessary compromise for multisubstrate specificity (42, 43), and reduced efficiency may be an acceptable tradeoff in the context of a bacterial cell that continuously regenerates the PMF, similar to futile ATP hydrolysis by P-glycoprotein (44, 45).

The possibility of multiple transport pathways for a single substrate also offers mechanistic flexibility for promiscuous transport of diverse substrates with different charge (+1 or +2) and binding affinities (which vary over 5 orders of magnitude for known EmrE substrates) (26). In the

free exchange model partitioning between transport pathways depends on the relatives of rates of binding and release of each substrate to/from EmrE in the specific environment (pH, substrate concentration) on each side of the membrane, as well as the rate of alternating access in each drug- and/or proton-bound state. Different transport pathways may be faster for different substrates or different environmental conditions, resulting in different coupling stoichiometry. The coupling stoichiometry will determine the net charge movement and how strongly transport will be driven by ΔpH or Δ□. This may be advantageous since pH changes the relative contribution of ΔpH and Δ□ to the PMF. Thus, mechanistic flexibility provides favorable transport mechanisms for a broader set of substrates and in a diverse set of conditions.

Pure exchange models are appealing due to their apparent simplicity, tight coupling and stoichiometric antiport. However, even a simple shared-carrier model, which allows for alternating access of the apo transporter, will give rise to coupled antiport (9). The data presented here takes this one step further, demonstrating that the promiscuous transporter, EmrE, can move both substrates across the membrane simultaneously. This has been assumed to be behavior indicative of a symporter, and not possible for an antiporter. The flexibility inherent in our free exchange model accommodates the observed ease of converting SMR transporters from antiporters to symporters (46-48) and suggests that this mechanism may be common across the SMR family. This kinetically-controlled model relies upon the relative rates of substrate binding and alternating access to determine partitioning among possible transport pathways and net coupling stoichiometries. In fact, our data, while not conclusive, suggest that under the proper conditions, EmrE may favor symport rather than antiport of the same substrate. Since the transported substrate determines the rate of alternating access (26), it may be possible to design novel substrates which could favor SMR symport rather than antiport under physiological conditions. Such a compound would be actively imported by *E. coli*, rather than effluxed. The pH-dependent stoichiometry of LacY proton/sugar symport (49) as well as the variability in coupling

efficiency for CLC exchangers, $PepT_{ST}$, and MdfA provide precedent for the idea that substrate identity could be a significant factor in defining the coupling stoichiometry.

In fact, a single transporter acting as both a symporter and antiporter of different substrates has been reported for W63G-EmrE (46). W63G-EmrE performs proton-coupled antiport of erythromycin but symport of bis-tris-propane *in vitro* and *in vivo*, conferring resistance to erythromycin but performing concentrative uptake of bis-tris-propane into *E. coli* to toxic levels (46). This unusual phenotype cannot be explained by the classical models of proton-coupled transport, which place mutually exclusive requirements on alternating access of the drug-free transporter (Fig. 1). However, the behavior of W63G-EmrE is readily explained with our kinetically-driven free exchange model. Negative linkage between proton and erythromycin binding will favor independent binding of the two substrates and antiport via a shared-carrier model. On the other hand, positive linkage between bis-tris-propane and proton binding will favor simultaneous drug and proton binding and symport. In our kinetic simulations, switching the negative linkage between drug and proton binding observed for WT EmrE to positive linkage by altering both the proton and drug on- and off-rates can switch WT EmrE from an antiporter to a (relatively inefficient) symporter (Fig. 5). A similar process could be occurring in our negative inside transport assay: the negative inside membrane potential along with the Eth^+ gradient may produce conditions which favor simultaneous Eth^+ and H^+ binding and symport. Future experiments will be needed to more thoroughly test whether robust symport can be achieved. This will likely vary with each SMR because the interplay between the relative rates of all the microscopic steps will be important for the efficiency and efficacy of either antiport or symport.

In an era when antibiotic resistance and drug-delivery pose a serious challenge, our results suggest a novel strategy. If an MDR efflux pump can indeed function as both a symporter and antiporter, and this balance can be shifted by properties of the transported substrate, perhaps it can be subverted to drive drugs *in* to bacteria, providing a new route for drug delivery. Despite

decades of study, EmrE continues to reveal its surprising complexity and expand our understanding of basic transport mechanisms and multidrug efflux.

Methods

EmrE was expressed in *E. coli* BL21(DE3), purified, and reconstituted into proteoliposomes and bicelles as described previously (5, 50). NMR samples contained 0.5-1.0 mM EmrE monomer in DLPC/DHPC (q = 0.33) isotropic bicelles in 20 mM acetate, 100 mM MOPS, 100 mM bicine. All NMR spectra were collected on a 700 MHz Varian Inova spectrometer equipped with a room temperature probe, processed with NMRPipe (51), and analyzed in CcpNmr analysis (52). The pH was measured at the experimental temperature just prior to acquiring ^{1}H-^{15}N BEST-TROSY-HSQC spectra (53, 54). TROSY-selected ZZ exchange spectra (21) were acquired and analyzed as described previously, with error determined by jackknife analysis of individual residue fits (5, 55).

Proton release upon TPP^{+} addition to EmrE in isotropic bicelles was monitored in real time as in (10) and quantitated with a known addition of NaOH. Assays were performed in 20 mM NaCl, pH 7 with 3, 5, and 10 nmol EmrE in triplicate and 0.9 mM TPP^{+} was added. ITC experiments were performed as described previously (26). 5 mM TPP^{+} was titrated into 835 µM EmrE in isotropic bicelles in a TA Instruments Low Volume Nano calorimeter at 45 °C. The number of protons released was determined using the method of (20). Buffer was 20 mM buffer (cacodylate, MES, or piperazine) and 20 mM NaCl.

The kinetic simulation of EmrE transport (Fig. 4A, and Table S2) was run in Berkeley Madonna (version 9.0, Kagi shareware, Berkeley, CA) using the code in Appendix 1. A Gillespie simulation using Octave (24) was performed using the code in Appendix 2.

Proton leak was monitored by diluting EmrE proteoliposomes (50mM sodium phosphate, 100 mM KCl, pH 7) into weakly buffered outside buffer (75 µM Phenol Red, 99 mM NaCl, 1 mM KCl, pH 7) to a final EmrE concentration of 0.8 µM. Valinomycin (1 µg/mL final) was added to

create a membrane potential (negative inside). FCCP (1μg/mL final) was added as a positive control. 10 nmol HCl was added at the end of the assay.

For proton transport assays, EmrE was reconstituted into proton-tight liposomes with EmrE:lipid mole ratios between 1:400 and 1:1000. For ΔpH-driven assays, the interior was strongly-buffered pH 6 and the exterior weakly buffered pH 8 with high potassium on both sides. For $\Delta\Psi$-driven assays, the interior was strongly-buffered pH 7.5 with either 1 mM KCl and 99 mM NaCl (for positive inside liposomes) or 100 mM KCl (for negative inside liposomes). The exterior was weakly buffered at pH 7.5, and either 100 mM KCl (for positive inside liposomes) or 1 mM KCl and 99 mM NaCl (for negative inside liposomes). External pH was quantitated with addition of known quantities of NaOH or HCl and recorded with a microelectrode in real-time. 1 μg/ml valinomycin or 1 μg/ml protonophore were added as indicated. EmrE was inactivated with N,N'-dicyclohexylcarbodiimide (DCCD). Full experimental details can be found in the Supporting Information.

Acknowledgments

We thank Geoff Chang for the EmrE expression plasmid. We thank Eric Galburt and John Robinson for assistance in developing the Gillespie transport model. This work was supported by the National Institutes of Health (1R01GM095839), NSF graduate research fellowships to E.M. and A.R. (DGE-1143954), and a Mr. and Mrs. Spencer T. Olin Fellowship for Women in Graduate Study to A.R.

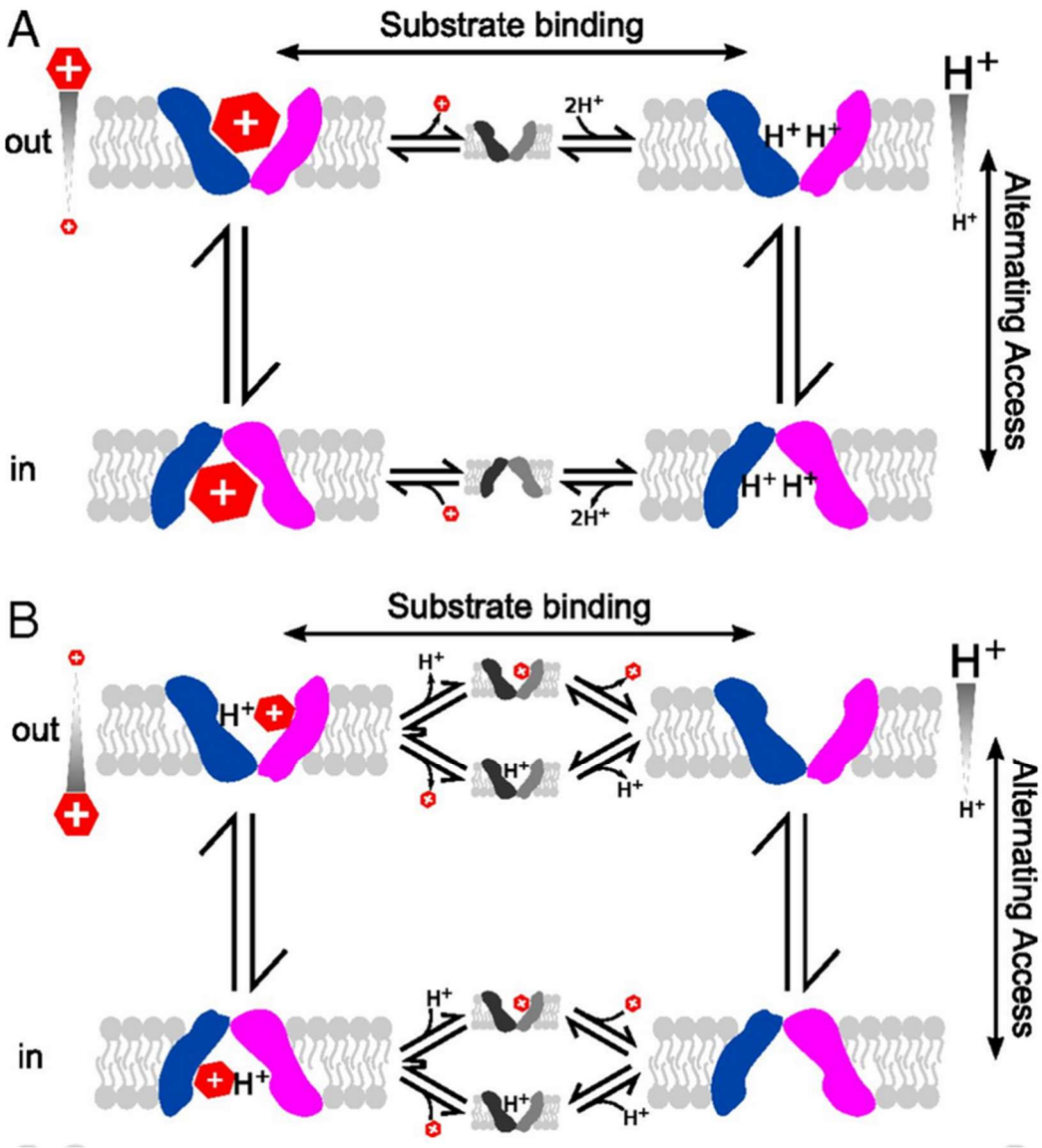

Fig. 1. Models of tightly-coupled secondary transport. (A) The pure exchange model of coupled antiport applied to EmrE (red hexagon, TPP^+). The asymmetric homodimer of EmrE is represented by the distinct shapes of the two conformations, and the two monomers are colored blue and magenta. (B) General model for proton-coupled symport illustrating the differences in which states participate in alternating access. Grey structures represent intermediates which are restricted from alternating access in these models.

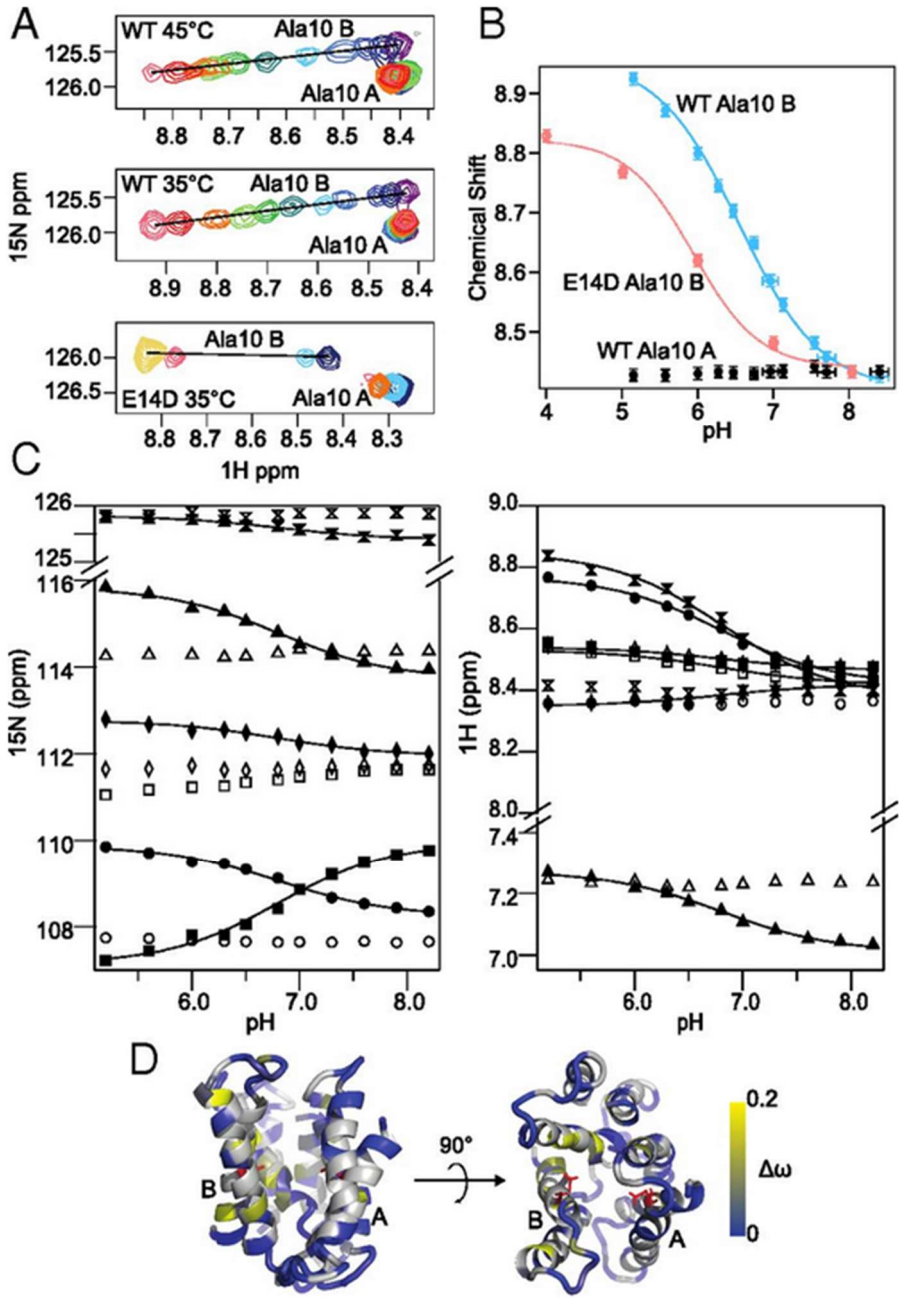

Fig. 2. EmrE can bind drug and proton simultaneously. (A) NMR pH titrations of TPP^+-bound $^2H/^{15}N$- WT (45 °C and 35 °C) and E14D (35 °C) EmrE shown for residue Ala10, a well-resolved residue near E14 (Full spectra in Fig. S1 and S3). pH values range from 5.2 (pink) to 8.3 (purple) for WT and 4.0 (yellow) to 8.0 (navy) for E14D-EmrE. (B) Chemical shifts of Ala10 plotted versus

pH highlight the difference between WT and E14D-EmrE and the asymmetric response of monomer A and B. Lines represent global pKa fit. (C) Global fitting of the pH-dependent chemical shifts from monomer B residues near E14 (solid symbols) yields a single pKa of 6.8 ± 0.1 at 45 °C. Monomer A residues (open symbols) have relatively pH-independent chemical shifts. Error bars are smaller than the symbols. (D) Plotting the chemical shift changes (Δω) between pH 5.6 and 7.6 onto the structure of TPP^+-bound EmrE (PDB 3B5D) highlights the localization of pH-dependent effects in monomer B (grey, residues not resolved at both pH values). E14 is shown as red sticks.

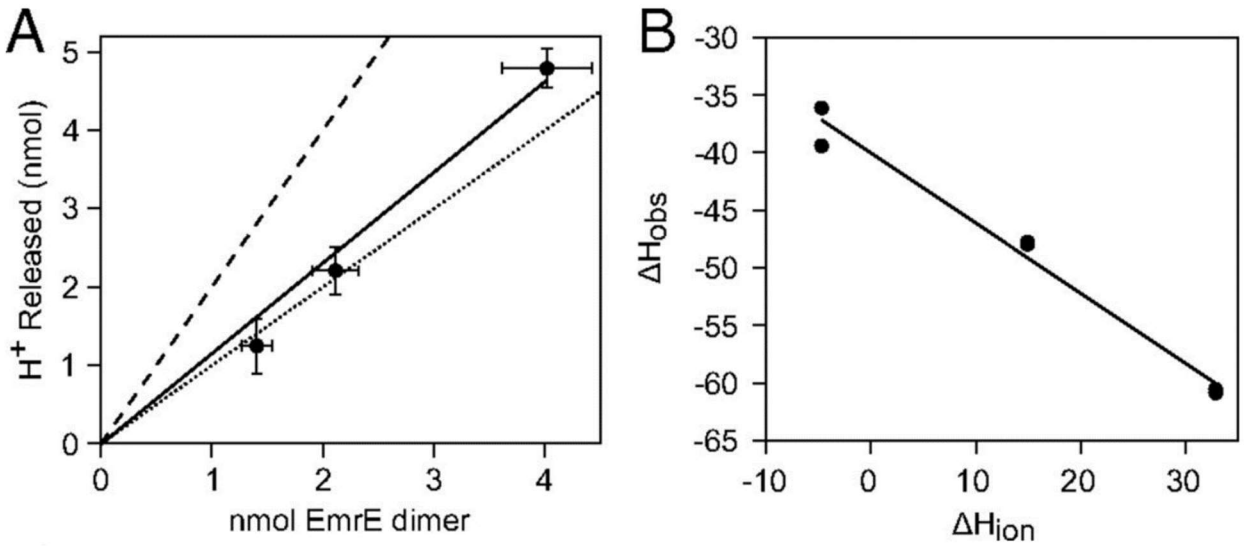

Fig. 3. TPP^+-induced proton release at low pH. (A) Direct pH measurement of the nmoles H^+ released upon addition of saturating TPP^+ as a function of EmrE concentration yields a slope of 1.2 H^+ released per EmrE dimer. Dotted and dashed lines show expected behavior if 1 or 2 protons are released per dimer, respectively. The estimated error in the protein concentration was 10%. Vertical error bars represent standard error determined from replicates. (B) ITC was used to characterize TPP+ binding to EmrE in buffers with different ionization enthalpies (ΔH_{ion}). The relationship between ΔH_{obs} (per EmrE monomer) from each ITC experiment and ΔH_{ion} of each buffer is linear with a slope of 1.2 H^+ released per dimer.

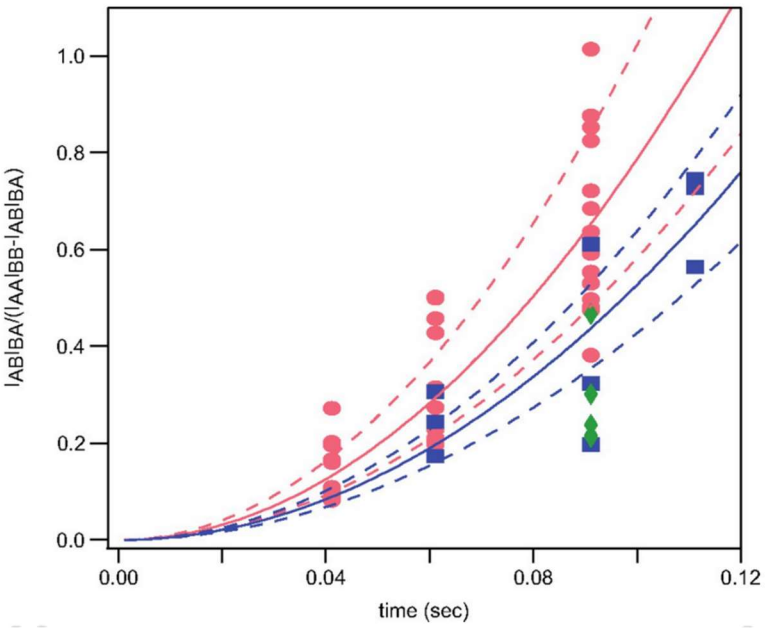

Fig. 4. All EmrE substrate-bound states engage in alternating access. The composite peak ratio from ^{1}H-^{15}N TROSY-selected ZZ-exchange NMR experiments is shown for multiple residues at pH 5.2 (pink circles), pH 7.0 (green diamonds), and pH 8.0 (blue squares). Global fits yield alternating access rates of 8.9 ± 1.2 s^{-1} at pH 5.2 (TPP^{+}/H^{+} both bound) and 7.3 ± 0.7 s^{-1} at pH 8.0 (only TPP^{+} bound). Error was estimated with jackknife analysis of individual residue fits (dotted lines).

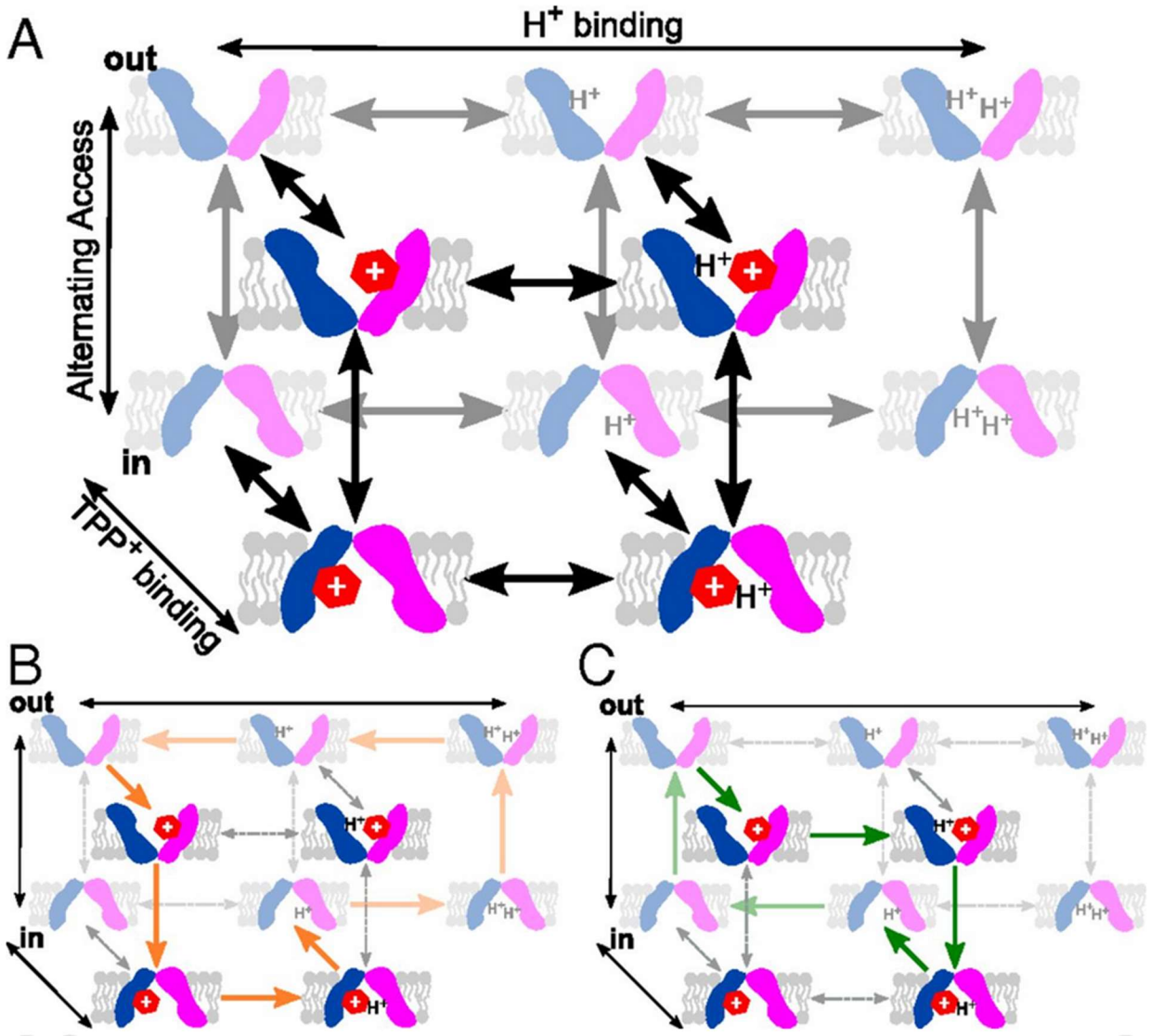

Fig. 5. Free exchange model for EmrE transport. (A) Three-dimensional transport scheme including all known states and transitions of EmrE based on NMR and biophysical assays. (B) Orange arrows highlight a 2:1 H^+/Eth^+ antiport pathway in the direction observed during liposomal transport assays. (C). Green arrows highlight the possibility of 1:1 H^+/Eth^+ symport under the liposomal assay conditions.

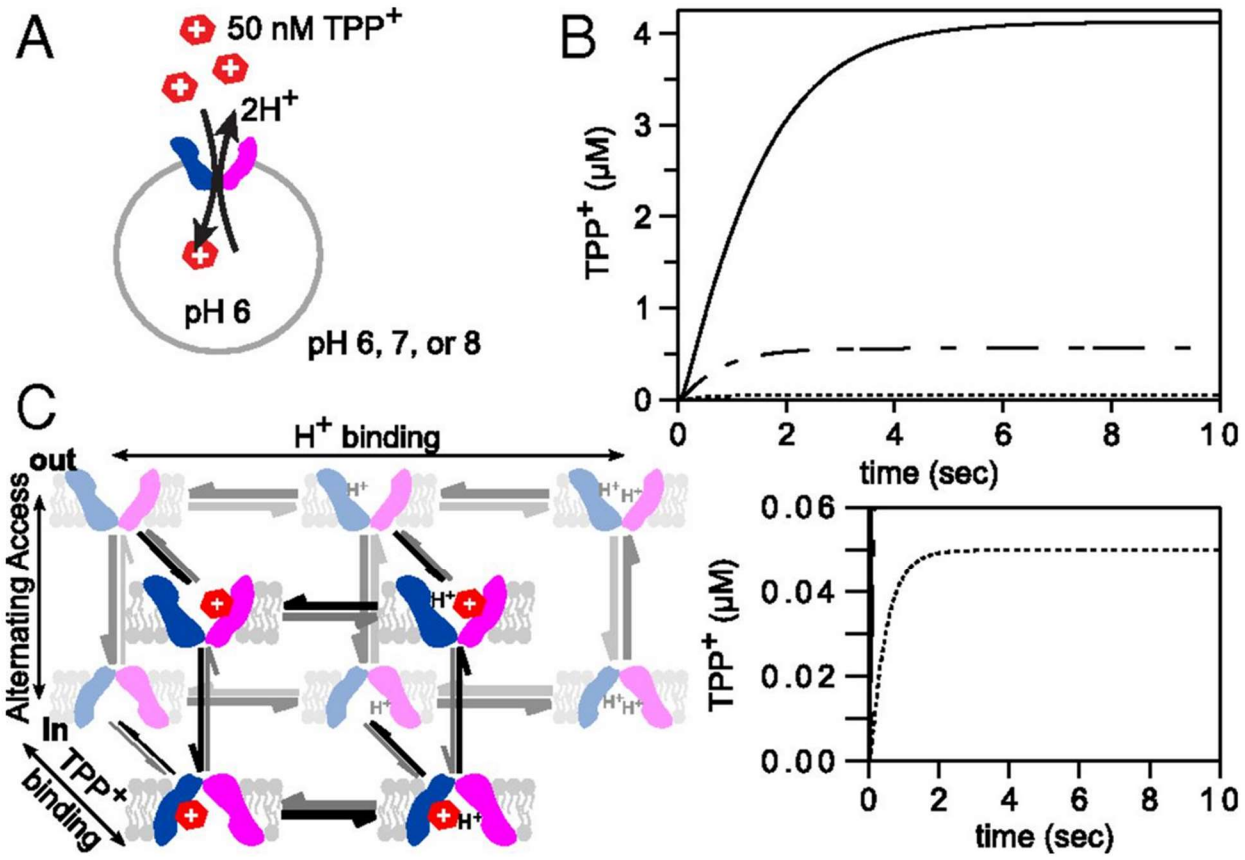

Fig. 6. Simulation of the kinetically-driven free exchange model. (A) Cartoon illustrates the ΔpH-driven liposomal loading that was modeled. (B) Kinetic simulation of TPP^+ uptake into liposomes using the rate constants in Fig. S7 and Table S2 results in proton-driven concentrative uptake of TPP^+ into EmrE proteoliposomes (pH 6 inside) when ΔpH=1 (pH 7 outside, dashed lines) or ΔpH=2 (pH 8 outside, solid lines). When ΔpH=0 (dotted line, expanded below), 50 nM TPP^+ rapidly equilibrates. (C) Arrow line weights on the transport scheme reflect the relative frequency of each transition during the Gillespie simulation (pH 8 out, pH 6 in, 50 nM TPP^+ outside); darker lines indicate higher frequency.

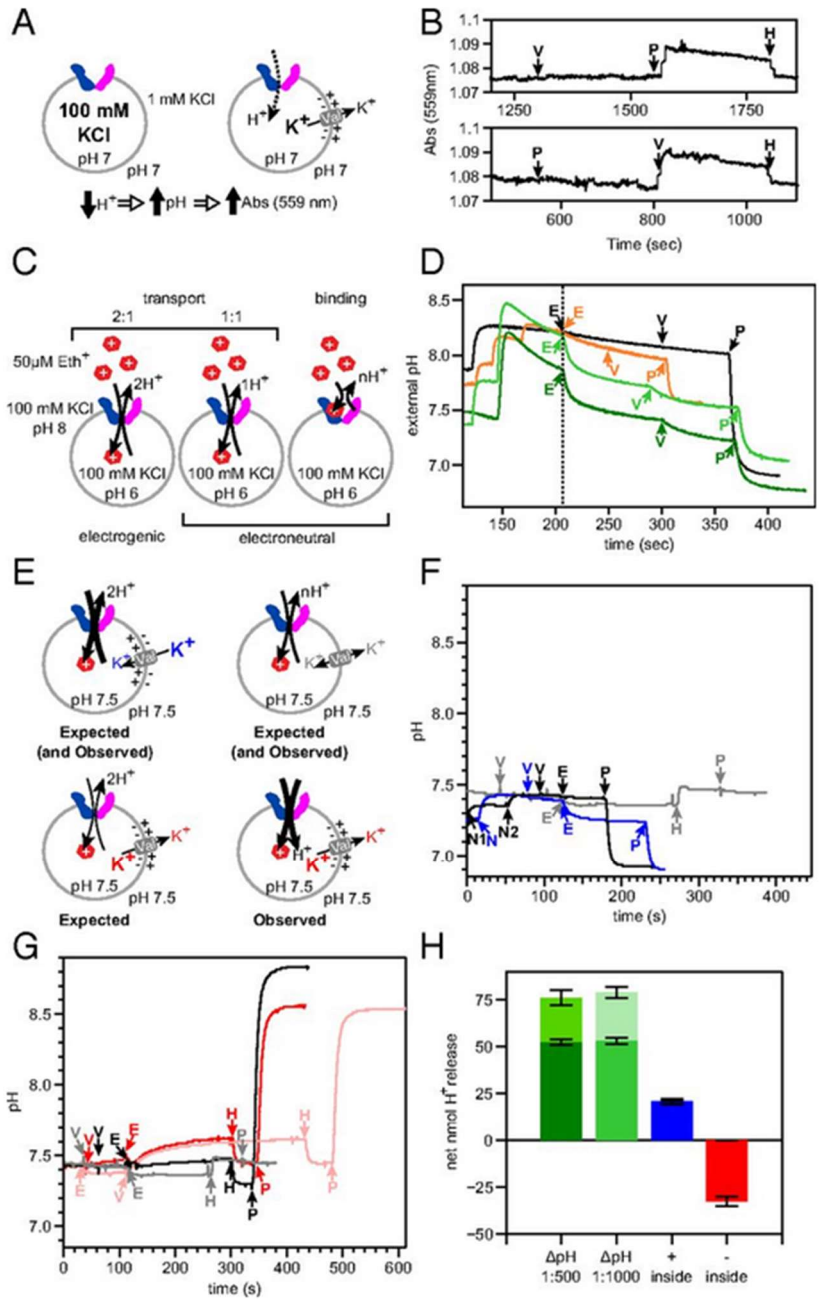

Fig. 7. EmrE does not leak H^+ but transports Eth^+ with multiple H^+/drug stoichiometries. (A) Cartoon for the proton leak assay showing key conditions. EmrE is reconstituted into 3:1 POPC/POPG proteoliposomes with a 100-fold potassium gradient. Addition of valinomycin (*V*) generates a negative inside membrane potential and creates a driving force for protons to enter the liposome. (B) pH is directly monitored in the weakly-buffered external solution using the pH

indicator phenol red. The phenol red absorbance at 559 nm will go up if external pH increases, as expected if EmrE leaks protons (dotted line in A). This is not observed. Proton flux in the expected direction is detected upon subsequent addition of a protonophore (*P*) that allows direct proton movement across the membrane. 10 nmol HCl (*H*) was added at the end of each assay for reference. Representative traces are shown, n=3. (C) Cartoons illustrate the potential sources of proton release upon ΔpH-driven drug uptake into EmrE proteoliposomes. (D) ΔpH-driven drug uptake. pH is directly monitored in the weakly-buffered outside buffer. In the presence of a pH gradient, addition of 50 μM Eth^+ (*E*) outside results in a sudden release of protons prior to addition of valinomycin. Proton release is EmrE-dependent as demonstrated by DCCD inactivation of EmrE (orange) and empty liposomes (black). The same proton release is observed for 1:500 (dark green) and 1:1000 (light green) EmrE:lipid mole ratios, showing that proton release is due to transport and not binding. Addition of a protonophore confirms the proton gradient was maintained. Proton release was quantified using the observed pH shift upon addition of a known aliquot of NaOH. (E) Cartoons showing expected (assuming pure 2:1 antiport) and observed outcomes for ΔΨ-driven drug uptake into EmrE proteoliposomes. ΔΨ is created with potassium gradients and valinomycin as in (A). Low potassium inside and high potassium outside yields positive-inside liposomes (blue) while reversing the potassium gradient creates negative-inside liposomes (red). Equal potassium concentrations results in neutral liposomes (grey). (F) ΔΨ-driven (positive inside) drug uptake. External pH is monitored as in (D). Addition of valinomycin generates a positive inside ΔΨ and no pH change is detected, confirming that EmrE does not rapidly leak protons. Subsequent addition of Eth^+ results in proton release from positive-inside EmrE proteoliposomes (blue trace) that is larger than observed for neutral EmrE proteoliposomes (gray trace). This confirms Δ□-driven 2:1 H^+/Eth^+ antiport by EmrE. Positive-inside E14Q-EmrE proteoliposomes show no proton flux upon addition of Eth^+, confirming EmrE-dependent transport (black trace). Addition of a protonophore allows protons to move in response to the membrane potential, confirming the membrane potential was maintained in the expected direction. H^+ release

was quantified by comparison to addition of known amounts of HCl (50 nmol) or NaOH (*N*, 40 nmol; N1, 15 nmol; N2, 20 nmol). (G) ∆Ψ-driven (negative inside) drug uptake. External pH is monitored as in (D). Addition of Eth^+ to negative-inside EmrE proteoliposomes results in proton uptake (negative inside, red trace). This is apparent net symport since Eth^+ must also move into the liposomes. Transport requires active EmrE since no flux occurs using negative-inside E14Q-EmrE proteoliposomes (black trace). Addition of a protonophore confirms the negative-inside membrane potential. Reversing the order of addition (pink trace) results in an initial release of H^+ similar to the proton flux in neutral proteoliposomes (grey trace), followed by substantial H^+ uptake upon addition of valinomycin to create a negative-inside membrane potential. H^+ release was quantified by comparison to addition of known amounts of HCl (50 nmol). (H) Net nmol H^+ released for distinct driving forces are compared. The stacked bars for the ∆pH-driven assays indicate the subsequent H^+ release following valinomycin addition. Error bars represent standard deviation, n =3. Representative traces (see Tables S3 and S5 and Fig. S5 for additional replicates, controls, and quantitation).

Supporting Information

SI Methods

EmrE expression and purification

EmrE was expressed in *E. coli* BL21(DE3) and purified as described previously (5) using a pET15b vector with an N-terminal 6x His tag kindly provided by G. Chang. For $^{2}H/^{15}N$-labelled EmrE, the M9 media contained 1 g $^{15}NH_4Cl$, 2 g glucose, 0.5 g ^{15}N,D Isogro (Sigma, St. Louis, MO), and 1 multivitamin per liter D_2O. Purification was via Ni-NTA chromatography followed by size exclusion chromatography with a Superdex 200 column equilibrated in either NMR buffer (for bicelle NMR samples) or the appropriate inside buffer (for liposomal reconstitution and transport assays), each with 10 mM decyl maltoside (DM, Anatrace, Maumee, OH).

NMR sample preparation and data acquisition

EmrE in NMR buffer (20 mM acetate, 100 mM MOPS, 100 mM bicine) with 10 mM DM was reconstituted into DMPC (1,2-dimyristoyl-*sn*-glycero-3-phosphocholine, Avanti Polar Lipids, Alabaster, AL) at 75:1 lipid:EmrE monomer mole ratio following the protocol in (50). EmrE proteoliposomes were collected by ultracentrifugation (100,000 g, 2 hr, 6 °C) and resuspended in NMR buffer with DHPC (1,2-dihexanoyl-*sn*-glycero-3-phosphocholine, Avanti Polar Lipids, Alabaster, AL) and freeze-thawed 3 times to create q=0.33 (56) bicelles. Final NMR samples contained 0.5-1.0 mM EmrE monomer, 10% D_2O, 0.05% NaN_3, 2 mM TCEP (*tris*(2-carboxyethyl)phosphine), 2 mM EDTA (Ethylenediaminetetraacetic acid), and 2 mM DSS (4,4-dimethyl-4-silapentane-1-sulfonic acid). EmrE concentration was determined using the extinction coefficient reported previously (38370 l mol^{-1} cm^{-1}) (5).

The pH of NMR samples was measured at the experimental temperature in a water bath with a pH electrode calibrated at the same temperature and adjusted by step-wise addition of

weak HCl or NaOH. When possible, pH titrations were performed with two samples at high and low pH that were mixed to titrate pH.

All NMR spectra were collected on a 700 MHz Varian Inova spectrometer equipped with a room temperature probe. ^{1}H chemical shifts were referenced with DSS, ^{15}N chemical shifts were referenced indirectly, and temperature was calibrated using ethylene glycol. pH titrations were collected with ^{1}H-^{15}N BEST-TROSY-HSQC pulse sequences (53, 54). The TROSY-selected ZZ exchange experiment (21) was modified and run as previously described (5). All data were processed with NMRPipe (51) and analyzed in CcpNmr analysis (52). pKa values were determined by fitting proton and nitrogen chemical shifts as a function of pH to the following equation (57):

$$\delta = \frac{\delta_H 10^{-pH} + \delta_D 10^{-pK_A}}{10^{-pH} + 10^{-pK_A}} \quad (1)$$

ZZ-exchange rates were determined by globally fitting a composite ratio of the auto and cross peak intensities for all residues with well-resolved cross- and auto-peaks in the ZZ-exchange spectra, with error determined by jackknife analysis of individual residue fits, as described previously (5, 55):

$$\Xi = \frac{I_{AB} I_{BA}}{I_{AA} I_{BB} - I_{AB} I_{BA}} = k^2 t^2 \quad (2)$$

ITC experiments

EmrE was reconstituted into DLPC/DHPC isotropic bicelles with effective q-values of 0.33 and a minimum ratio of 100:1 DLPC:EmrE. Additional lipid was added to low-concentration samples to keep the total lipid concentration above 40 mM and preserve bicellar morphology (56). EmrE is fully dimeric at all protein:lipid ratios used(58).

Titrations of TPP^+ into EmrE were carried out in multiple buffers (Table S1) with a range of ionization enthalpies. Both TPP^+ and EmrE solutions contained matching concentrations of isotropic bicelles, 20 mM buffer and 20 mM NaCl. 5 mM TPP^+ was titrated into 835 μM EmrE in a TA Instruments Low Volume Nano calorimeter using the ITCRun software (TA Instruments,

Lindon, UT) with 2.5 µL injections, stirring at 350 rpm at 45 °C. Sample pH was checked at 45 °C before and after each experiment. Data is reported in Table S1.

Buffer ionization enthalpies (59) were adjusted to 45 °C using the reported standard molar heat capacity change at 25 °C. Each titration was analyzed independently, confirming the 1 TPP^+:EmrE dimer binding stoichiometry under all conditions. Plots of ΔH°_{obs} (determined by ITC) vs ΔH^{i}_{b} (ΔH of buffer ionization) have a slope of nH^+, regardless of how complex a mechanistic model is considered, as shown below (eqns. 4,7,10).

Assuming that only two protons or one drug molecule can bind at a time (model in Fig. 1A), the simplifying condition of independent sites (no linkage) can be made. Following the notation of (20), for two independent and identical proton-binding sites, the system is represented by:

$$K_{obs} = K_{int}\frac{1}{\left(1+K_p^f a_{H+}\right)^2} \quad (3)$$

$$\Delta H^o_{obs} = \frac{-2\Delta H_p^f K_p^f a_{H+}}{1+K_p^f a_{H+}} + \Delta H^o_{int} + n_{H+}\Delta H_b^i \quad (4)$$

$$n_{H+} = \frac{-2K_p^f a_{H+}}{1+K_p^f a_{H+}} \quad (5)$$

where K_{obs} is the observed TPP^+ binding affinity and ΔH^{o}_{obs} is the observed enthalpy change upon TPP^+ binding as measured experimentally with ITC. n_{H+} is the change in the number of protons bound by EmrE upon TPP^+ binding, a_{H+} is the proton activity (10^{-pH}), K_{int} is the TPP^+-association constant for apo EmrE, K_p^f is the H^+ binding constant for apo EmrE (10^{pKa}), ΔH^{o}_{int} is the enthalpy change for TPP^+ binding to apo EmrE, ΔH_p^f is the enthalpy of protonation of apo EmrE and ΔH^{i}_{b} is the ionization enthalpy of the buffer.

For two independent and non-identical proton-binding sites, as reported for EmrE (16), the system is represented by:

$$K_{obs} = K_{int}\frac{1}{\left(1+K_{1,p}^f a_{H+}\right)\left(1+K_{2,p}^f a_{H+}\right)} \quad (6)$$

$$\Delta H^o_{obs} = \frac{-\Delta H^f_{1,p} K^f_{1,p} a_{H+}}{1+K^f_{1,p} a_{H+}} - \frac{\Delta H^f_{2,p} K^f_{2,p} a_{H+}}{1+K^f_{2,p} a_{H+}} + \Delta H^o_{int} + n_{H+} \Delta H^i_b \quad (7)$$

$$n_{H+} = \frac{-K^f_{1,p} a_{H+}}{1+K^f_{1,p} a_{H+}} - \frac{K^f_{2,p} a_{H+}}{1+K^f_{2,p} a_{H+}} \quad (8)$$

where $K_{1,p}{}^f$ and $K_{2,p}{}^f$ are the H^+ binding constants for binding the first and second protons by apo EmrE (10^{pKa1}, 10^{pKa2}) and $\Delta H_{1,p}{}^f$ and $\Delta H_{2,p}{}^f$ similarly represent the enthalpy of the first and second protonation steps for apo EmrE.

If, however, one proton and one drug molecule can bind simultaneously, the mechanism becomes more complex (Fig. 4A). In the case that EmrE can bind two protons at independent non-identical sites, one drug molecule, or a single proton and a drug molecule, the system is represented by:

$$K_{obs} = K_{int} \frac{1+K^c_p a_{H+}}{\left(1+K^f_{1,p} a_{H+}\right)\left(1+K^f_{2,p} a_{H+}\right)} \quad (9)$$

$$\Delta H^o_{obs} = \frac{\Delta H^c_p K^c_p a_{H+}}{1+K^c_p a_{H+}} - \frac{\Delta H^f_{1,p} K^f_{1,p} a_{H+}}{1+K^f_{1,p} a_{H+}} - \frac{\Delta H^f_{2,p} K^f_{2,p} a_{H+}}{1+K^f_{2,p} a_{H+}} + \Delta H^o_{int} + n_{H+} \Delta H^i_b \quad (10)$$

$$n_{H+} = \frac{K^c_p a_{H+}}{1+K^c_p a_{H+}} - \frac{K^f_{1,p} a_{H+}}{1+K^f_{1,p} a_{H+}} - \frac{K^f_{2,p} a_{H+}}{1+K^f_{2,p} a_{H+}} \quad (11)$$

where $K_p{}^c$ is the H^+-binding constant for TPP^+-bound EmrE and $\Delta H_p{}^c$ is the enthalpy of protonation for TPP^+-bound EmrE. The NMR data presented in Fig. 2 do not show any indication that EmrE can bind TPP^+ and 2 H^+ simultaneously, so we did not consider more complex scenarios.

Proton release measurements

EmrE was prepared in q=0.33 DLPC:DHPC isotropic bicelles as described above, but the final steps of isotropic bicelle preparation were performed with unbuffered solutions (20 mM NaCl, pH 7) to create a final sample with weak buffering capacity. Assays were performed with 3, 5, and 10 nmol EmrE and 80 mM total lipid in triplicate. The pH was monitored in real-time using a Biotrode micro pH electrode as a saturating concentration of TPP^+ (0.9 mM) was added to the sample as determined from ITC measurements of the binding affinity. 10 nmol of NaOH was

added at the end of the assay for quantitation. pH was recorded before TPP^+ addition, after TPP^+ addition and after HCl addition in order to fit a linear baseline to each segment to account for pH drift occurring in the weakly buffered solution. The number of protons released was calculated from the slope of a plot of the protons released versus the EmrE concentration. Error was propagated through each of the linear fitting steps to estimate the error in the number of protons released.

Proteoliposome reconstitution for transport assays

POPE, POPC, or POPG polar lipids (Avanti Polar Lipids, Alabaster, AL) in chloroform were dried under nitrogen and rinsed twice with pentane or lyophilized overnight to remove residual chloroform. Dry lipids were hydrated at 20 mg/ml for 1 hr in the appropriate inside buffer for the desired assay (see below), extruded 21 times through a 0.2μm filter (Avanti Polar Lipids, Alabaster, AL) and permeabilized with 0.5% octyl-glucoside for 15 min at room temperature. Purified EmrE in 10 mM DM was added to obtain a 1:64 or 1:50 w/w protein:lipid mole ratio for ethidium or TPP^+ transport assays, respectively, resulting in ≈1:1000 or ≈1:800 EmrE:lipid mole ratio. A second set of samples was reconstituted with twice the protein:lipid ratio for control experiments, and empty liposomes were prepared by adding 10 mM DM without protein. After 20 min incubation, detergent was removed with amberlite (Sigma, St. Louis, MO) as in NMR sample preparation. 8 ml of proteoliposomes were then dialyzed (Slide-A-Lyzer Dialysis Cassettes, 2K MWCO, Thermo Fisher Scientific, Waltham, MA) against 1 L inside buffer for 24 hours twice to remove any residual detergent. Final liposomes were aliquoted, flash frozen in liquid nitrogen and stored at -80°C until use. Empty liposomes were prepared in the same way, with 10 mM DM added to simulate the reconstitution process.

Proton leak assay

1.8 mL of weakly buffered low potassium outside buffer (75 μM Phenol Red, 99 mM NaCl, 1 mM KCl, pH 7) was added to a quartz cuvette. pH was monitored in real- time from the absorbance of phenol red at 595nm using using an Agilent Cary spectrophotometer with slow

stirring and peltier temperature control at 25 °C. pH was adjusted to a constant starting value for each replicate. EmrE proteoliposomes (3:1 POPC:POPG) with high potassium inside buffer (50mM sodium phosphate, 100 mM KCl, pH 7) were thawed at 45°C, freeze/thawed 3x, re-extruded through a 0.2 µm filter and then diluted 20-fold into outside buffer in the cuvette. The final EmrE monomer concentration in the cuvette was 0.8 µM. Once equilibrated, the potassium ionophore valinomycin (1 mg/mL in DMSO) was added to a final concentration of 1 µg/mL to create a membrane potential (negative inside). The protonophore carbonyl cyanide p-trifluoromethoxyphenylhydrazone (FCCP) (1mg/mL in DMSO) was added to 1 µg/mL as a positive control to detect proton movement. As a reference, 10 nmol HCl was added at the end of the assay. Experiments were run in triplicate with two independently prepared batches of proteoliposomes.

Proton transport assays

For ΔpH-driven assays, EmrE was reconstituted into 3:1 POPE/POPG liposomes (TPP^+ transport) or 3:1 POPC:POPG liposomes (ethidium$^+$ transport) in strongly buffered high-potassium inside buffer (20 mM potassium phosphate, 300 mM KCl, pH 6 for TPP^+ transport, or 100 mM MES, 100 mM KCl, pH 6 for ethidium$^+$ transport) as described and extruded 21x through a 0.4 µm filter (TPP^+ transport) or 0.2 µm filter (ethidium$^+$ transport). Proteoliposomes were passed over two 10 mL Sephadex G25 desalting columns equilibrated with weakly buffered outside buffer (1 mM potassium phosphate, 300 mM KCl, pH 6 for TPP^+ transport, or 0.5 mM MOPS, 300 mM KCl, pH 6 for ethidium$^+$ transport). 1.2-1.4 ml total volume was used directly for each TPP^+ transport assay. 1 mL of proteoliposomes was diluted with 0.5 mL outside buffer for each ethidium$^+$ transport assay.

For $\Delta\Psi$-driven assays, wt-EmrE or E14Q-EmrE was reconstituted into 3:1 POPC:POPG liposomes in 50 mM MOPS at pH 7.5 with either 1 mM KCl and 99 mM NaCl (for positive inside liposomes) or 100 mM KCl (for negative inside liposomes), and extruded 21x through a 0.2 µm

filter. Proteoliposomes were passed over two 10 mL Sephadex G25 desalting columns equilibrated with weakly buffered outside buffer (50 μM MOPS, 100 mM KCl, pH 7.5 for positive inside liposomes, or 50 μM MOPS, 1 mM KCl, 99 mM NaCl, pH 7.5 for negative inside liposomes). 1 mL of proteoliposomes was diluted with 0.5 mL outside buffer for each assay.

The external pH of the proteoliposome solution was recorded with a microelectrode using an analog pH meter, digitized with a DataQ data logger and recorded in real-time. External pH was adjusted with small aliquots of NaOH or HCl to the desired external starting pH and then substrate was added from a stock solution (38.5 mM TPP^+ or 25 mM ethidium$^+$) at the same external pH. The potassium ionophore valinomycin was added to 1 μg/ml to eliminate any charge build up due to electrogenic transport (for ΔpH-driven assays) or to create a membrane voltage (for $\Delta\Psi$-driven assays), either before or after addition of drug. The protonophore (carbonyl cyanide m-chlorophenyl hydrazine (CCCP) for Eth^+ transport and carbonyl cyanide-p-trifluoromethoxyphenylhydrazone (FCCP) for TPP^+ transport) was added to 1μg/ml to allow full pH equilibration at the end of the assay. A subset of EmrE proteoliposomes was inhibited by incubation with 0.5 mM N,N'-dicyclohexylcarbodiimide (DCCD) (300 mM stock in ethanol) at room temperature for 2 hr prior to use in the transport assay as a negative control. EmrE concentration was checked by A280 measurement using bicelles created by adding 4 mg DHPC to 1 ml proteoliposome stock followed by 3 freeze-thaw cycles.

Building a Kinetic Simulation

We developed a system of non-linear differential equations to simulate EmrE transport activity based upon the schematic model presented in Fig. 4A. All rates were determined from experimental data presented in this and previous studies, as denoted in Table S2, except for the rate of proton binding and release. We assumed a diffusion-limited on-rate (10^{10} $M^{-1}s^{-1}$) for all proton-binding steps and used this assumption and our measured pKa values to calculate proton off-rates. This is a significant assumption, since the highly shifted pKa values demonstrate that

E14 is not located in a typical environment exposed to bulk water. The model was simulated in Berkeley Madonna (version 9.0, Kagi shareware, Berkeley, CA) to model the amount of TPP^+ loaded into the liposome over time under different conditions using the code in Appendix 1.

To appreciate the relative frequencies of each transition, the system of equations was modified to run a Gillespie simulation (24) using Octave (60) (Appendix 2). Here, total TPP^+ accumulation was not counted or factored in. Rather, infinite inside and outside volumes were assumed (TPP^+ concentrations were locked) and the frequency of each transition was recorded. Rates and terminology are defined in Table S2.

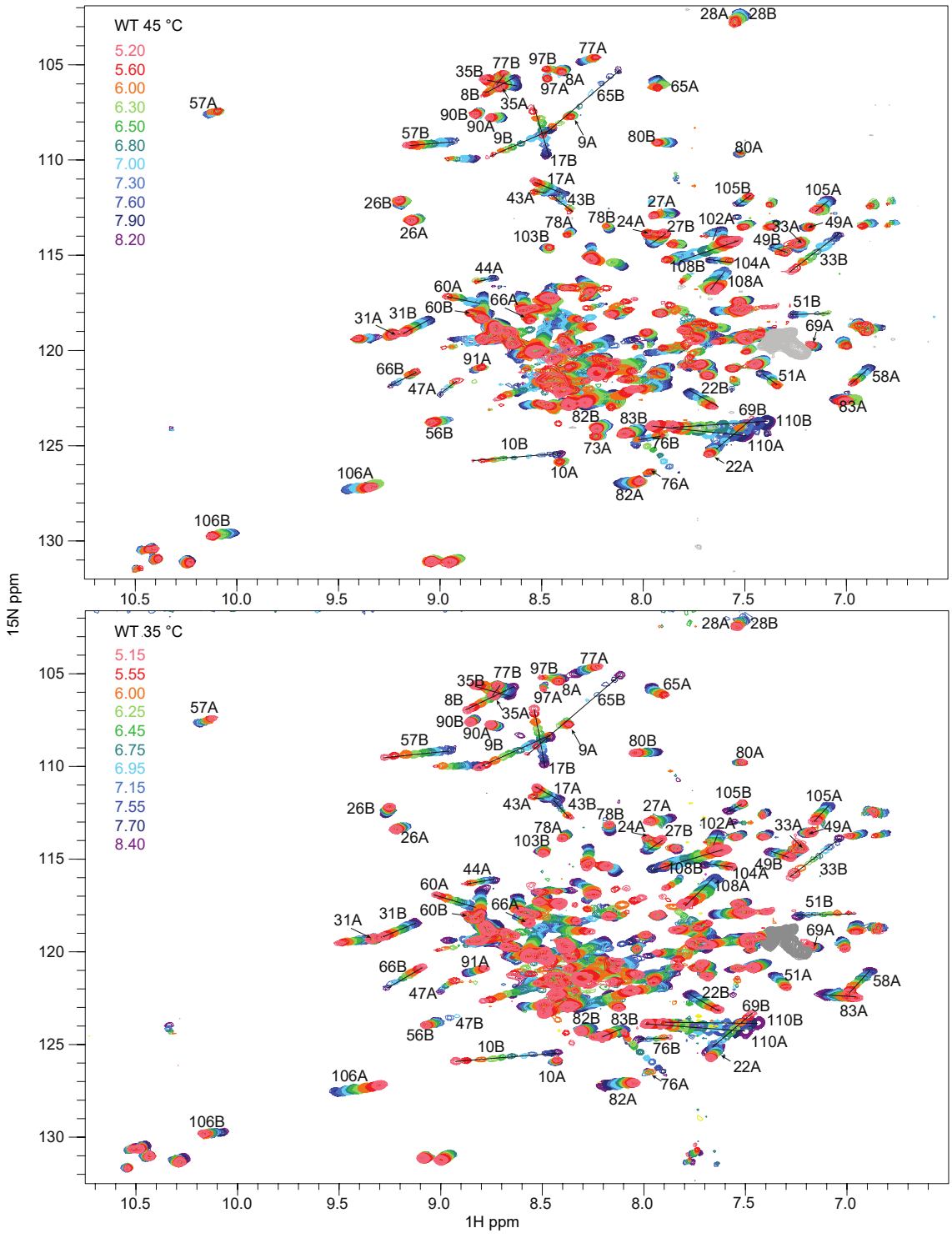

Fig. S1.

Full spectra show the global response of TPP$^+$-bound WT EmrE to protonation. 1H-15N BEST-TROSY spectra of WT TPP$^+$-bound EmrE collected at a range of pH values at 45 °C (top) and 35 °C (bottom). Lines are drawn to help follow the titration-induced shifts of individual residues. In all the spectra, negative contours are shown in grey.

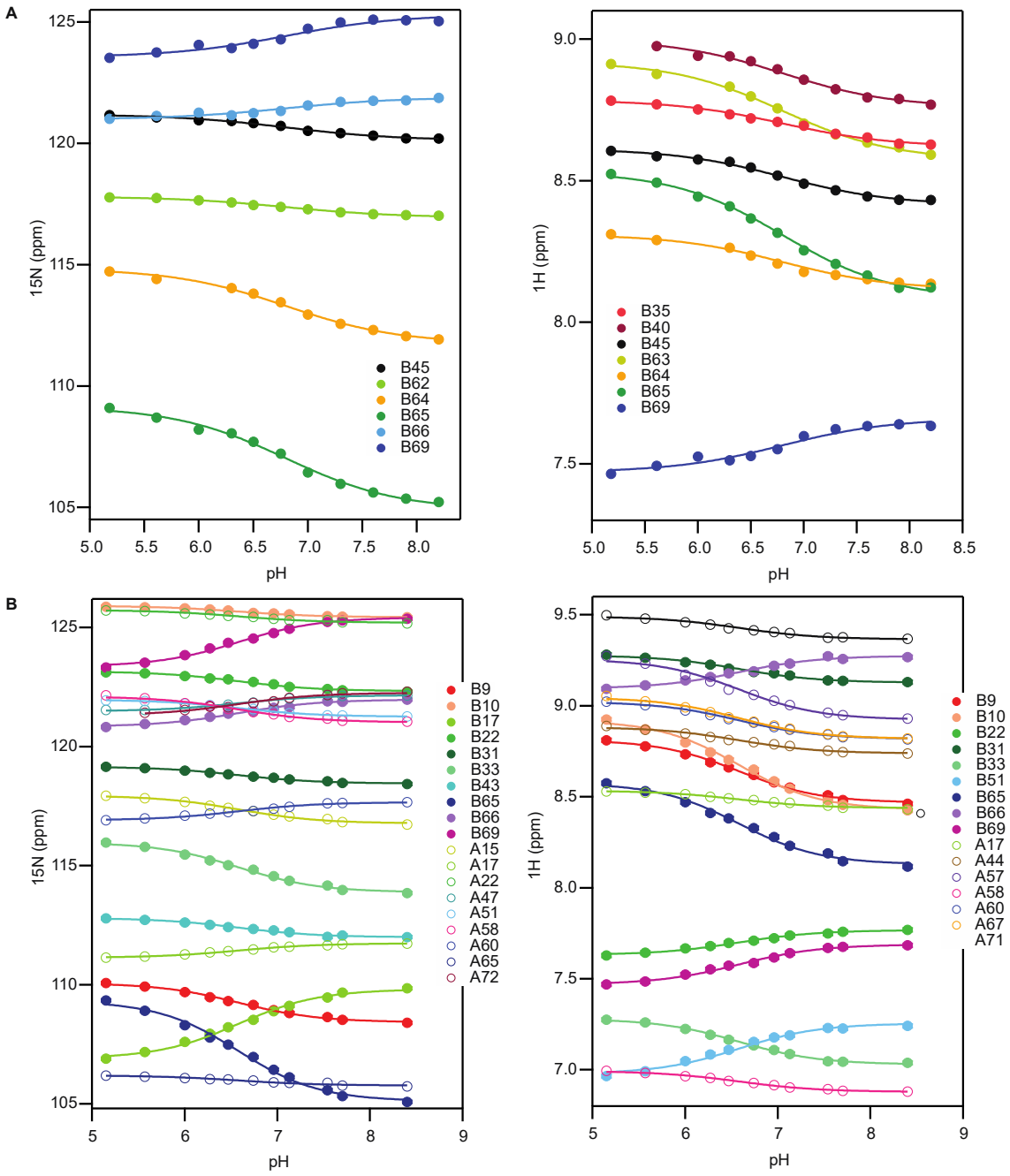

Fig. S2.

All resolved residues in TPP$^+$-bound WT EmrE can be globally fit to a single pKa value. A) At 45 °C, additional residues are fit to the same single pKa value of 6.8 ± 0.1 determined from sites in close proximity to E14 (Fig. 2). B) At 35 °C, the same residues (9, 10, 17, 33, 43) are globally fit using Equation 1, resulting in a single pKa value of 6.6 ± 0.1, and all other residues are also well-fit with this same value. As for drug-free EmrE (16), the pKa values have only minor temperature dependence.

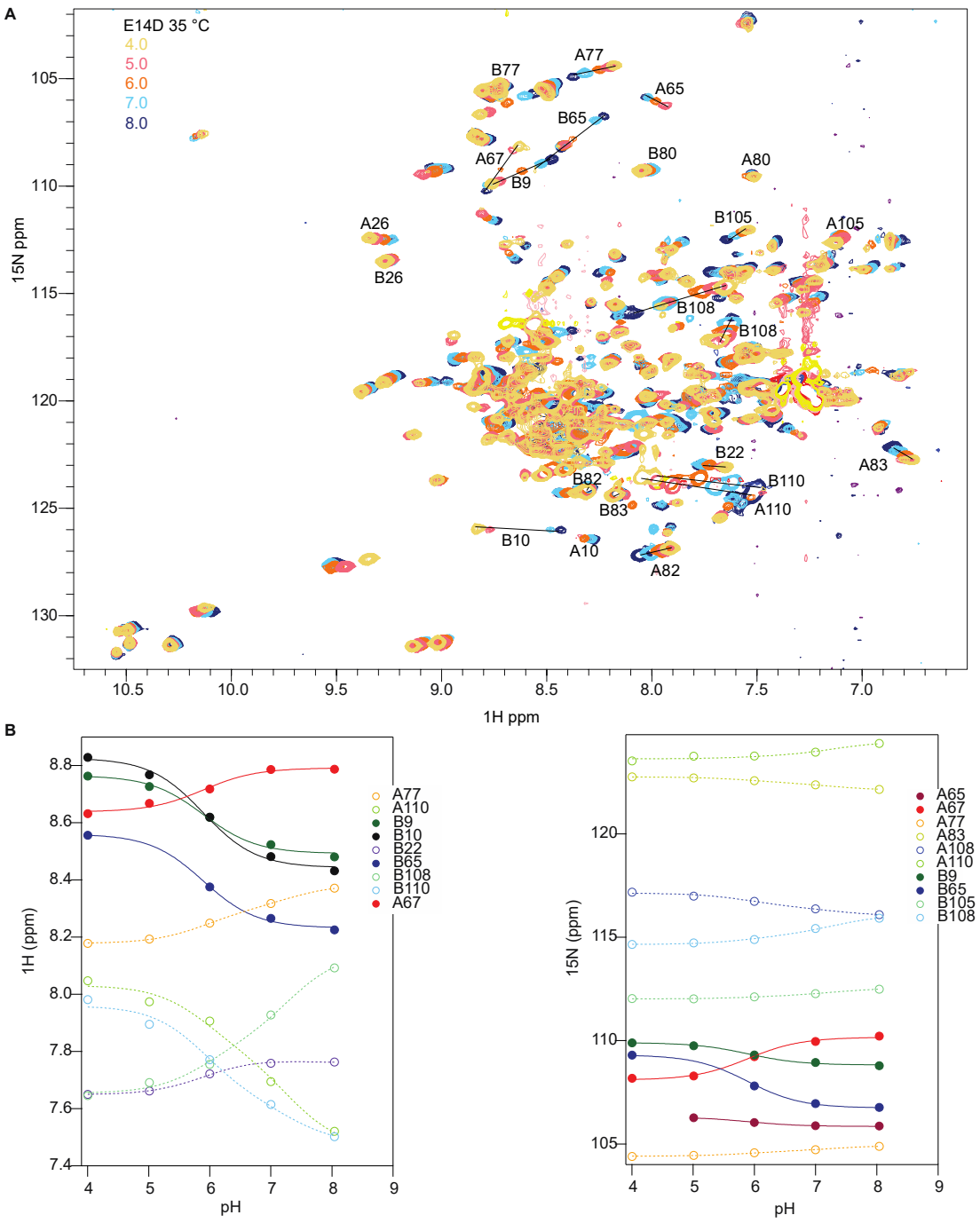

Fig. S3.

Full spectra show the global response of TPP⁺-bound E14D EmrE to protonation. A) pH titration of bicelle-solubilized, TPP⁺-bound E14D-EmrE followed by 1H-15N BEST-TROSY spectra. B) Fits of the pH titration according to Equation 1 result in a pKa value of 5.9 ± 0.1 for TPP⁺-bound E14D-EmrE. Only residues in close proximity to E14 (solid symbols and lines) were used to determine the pKa, although all resolved residues are well fit by this pKa value (open symbols and dotted lines).

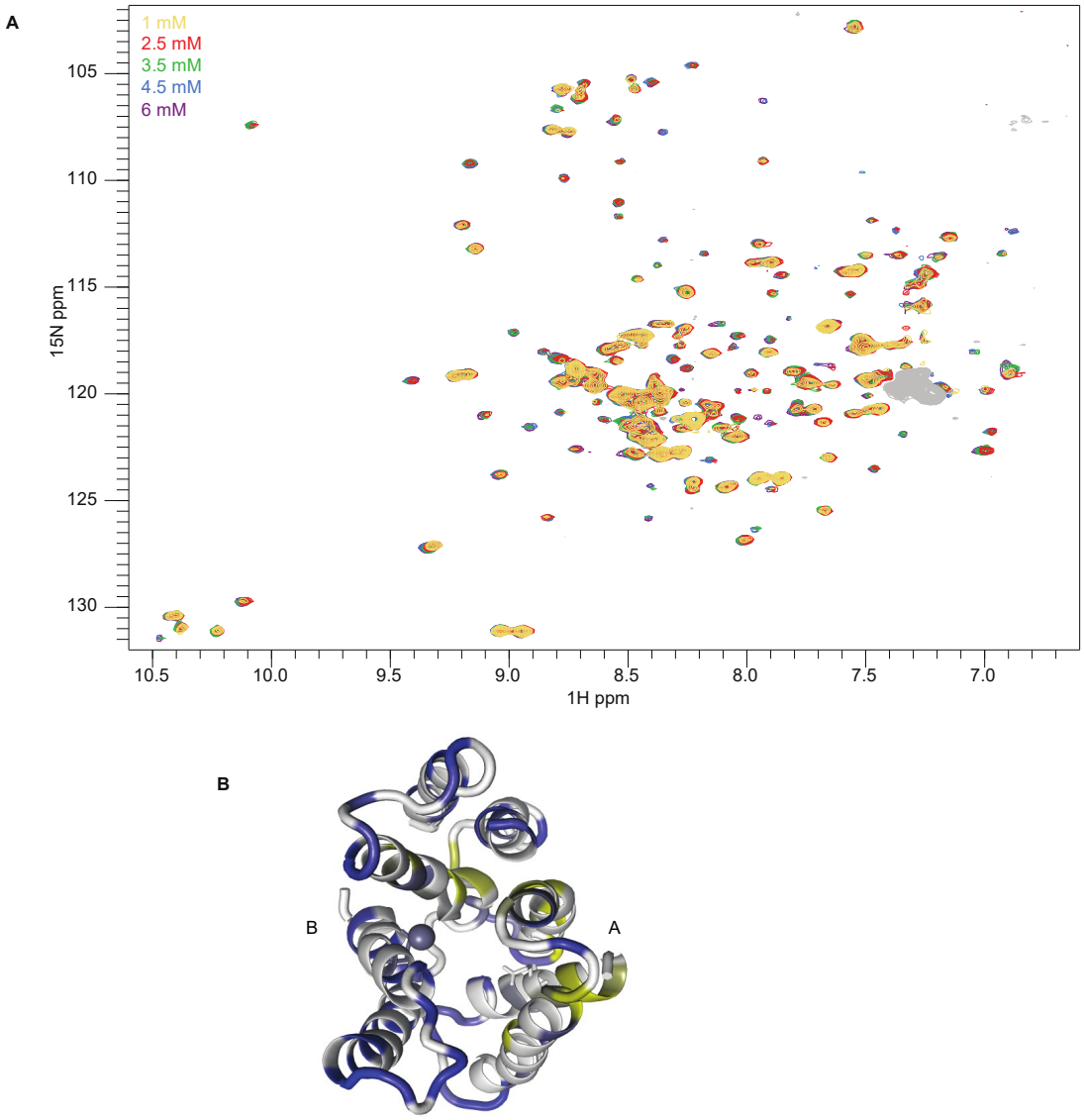

Fig. S4.

EmrE remains saturated with TPP⁺ throughout the pH titration. A) 1H-15N BEST-TROSY spectra of WT EmrE at pH 5.2 with increasing concentrations of TPP⁺ as indicated in colored text on the spectra. All negative contours are grey. Note that peaks do not move in response to changing TPP⁺ concentrations but some peaks are broadened and even missing at sub-saturating TPP⁺ concentrations. This contrasts with the pH-dependent shift in peak position, consistent with proton on/off rates being faster than TPP⁺ on/off rates. B) The effect of increasing TPP⁺ concentrations on peak intensity are mapped onto the low-resolution crystal structure (PDB 3B5D) with a blue-yellow color scale where yellow indicates residues most sensitive to TPP⁺ concentration and blue corresponds to residues with no change in peak intensity. Grey residues are not resolved. Note that peaks in monomer A are more strongly affected by TPP⁺ binding (E14 in monomer A is shown in light grey sticks), while monomer B titrated with pH (grey ball represents the protonatable E14 side-chain in monomer B).

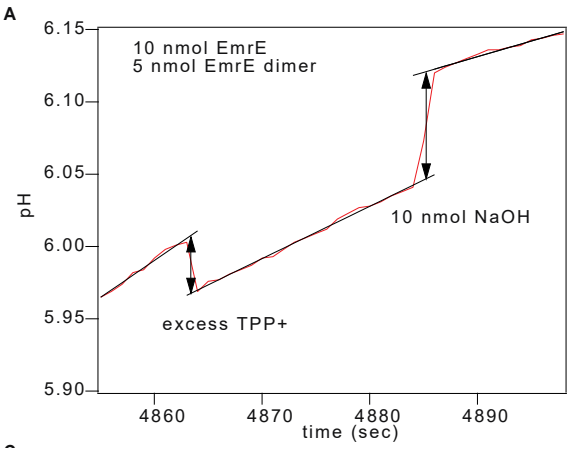

Fig. S5.

Proton release upon TPP^+ binding. Proton release from bicelle-solubilized EmrE upon TPP^+ binding was measured directly in a weakly buffered solution at 25 °C. The pH drifted gradually over time due to the limited buffering capacity, so a baseline was fit to each region to more accurately determine the pH change upon addition of a saturating amount of TPP^+. A known aliquot of base was added to quantitate the proton release in the assay. This measurement was repeated in triplicate at multiple EmrE concentrations in order to determine the number of protons released per EmrE dimer upon TPP^+ binding.

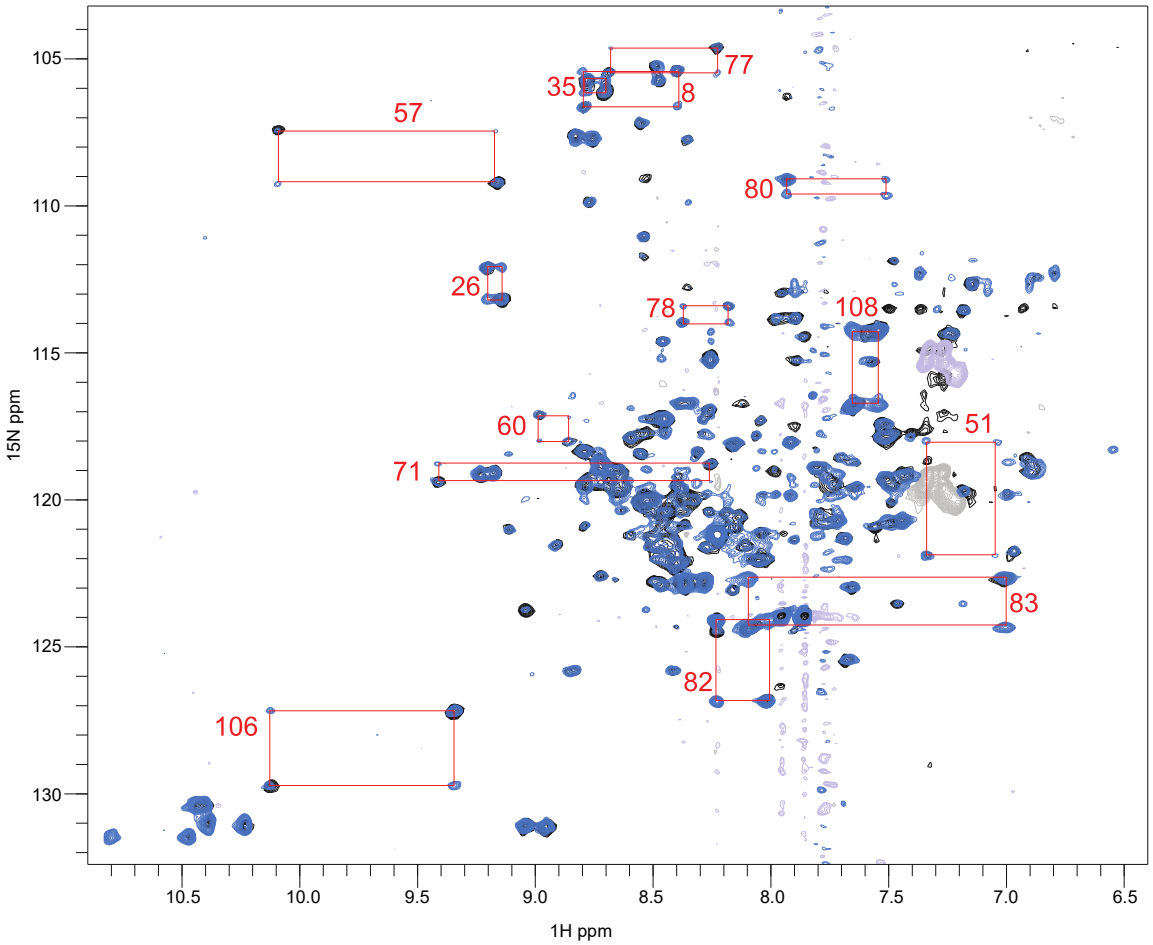

Fig. S6.

Determination of the open-in/open-out exchange rate for drug-and-proton-bound EmrE. The TROSY-selected ZZ exchange spectrum with an 80 msec mixing time (blue) is overlaid with the 1H-15N TROSY-HSQC (black), both collected at pH 5.2 for EmrE solubilized in isotropic bicelles at 45 °C and saturated with TPP^+. Crosspeaks appear throughout the ZZ exchange spectrum, connecting the two peaks corresponding to the same residue in each monomer, as highlighted by the red boxes for several residues. Lighter colors (pale blue and grey, respectively) indicate negative contours.

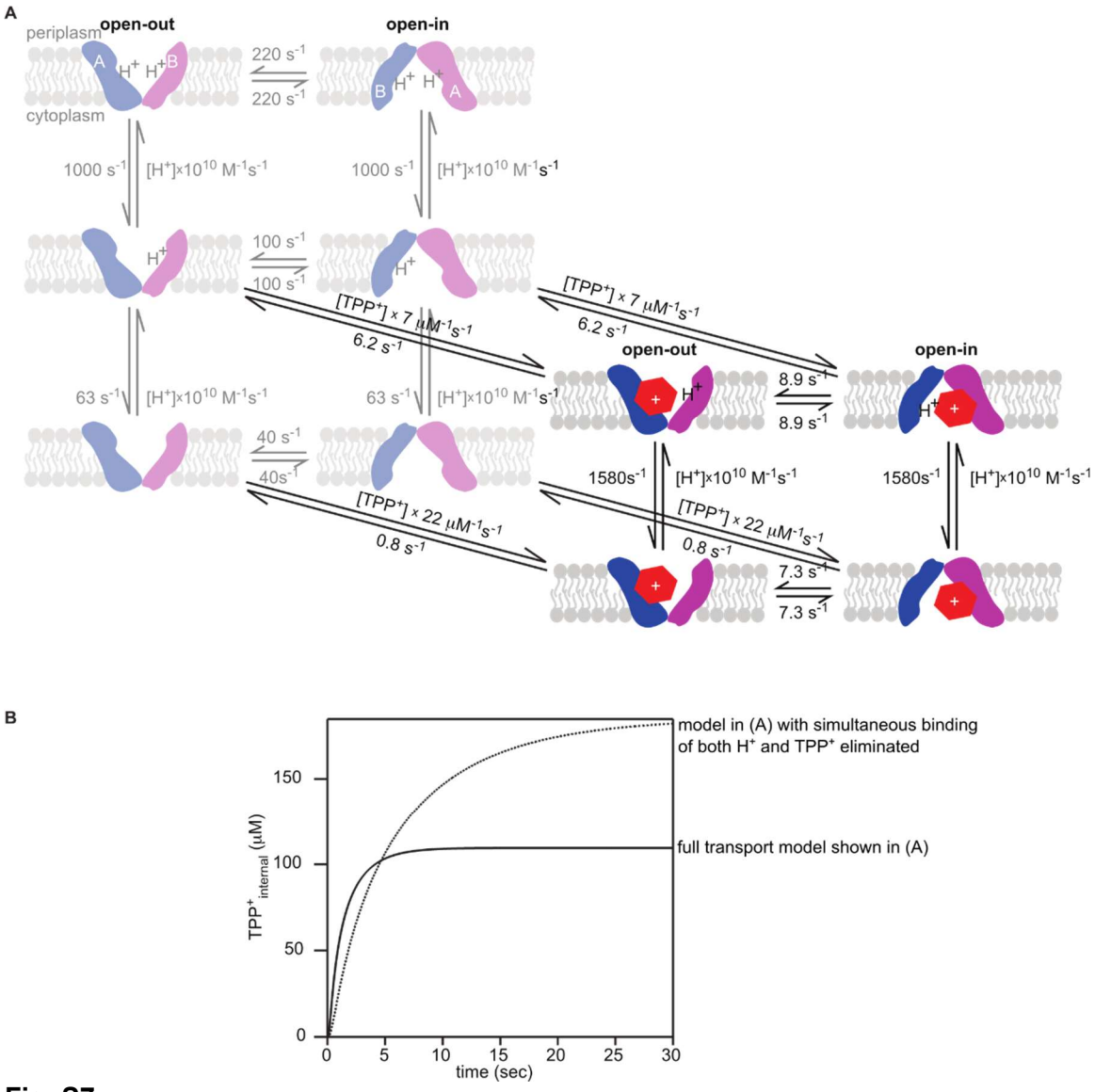

Fig. S7.

Annotated transport figure showing the variables used in the kinetic simulations. A) Kinetically-driven free exchange transport model including all known states of EmrE with estimates for each transition rate constant (Table S2). B) Kinetic simulation of TPP^+ uptake into liposomes shows that the ability of EmrE to simultaneously bind drug and proton reduces the coupling efficiency, as expected, but also increases the initial rate of drug transport (pH 6 inside, pH 8 outside, 1μM TPP^+ outside at time 0).

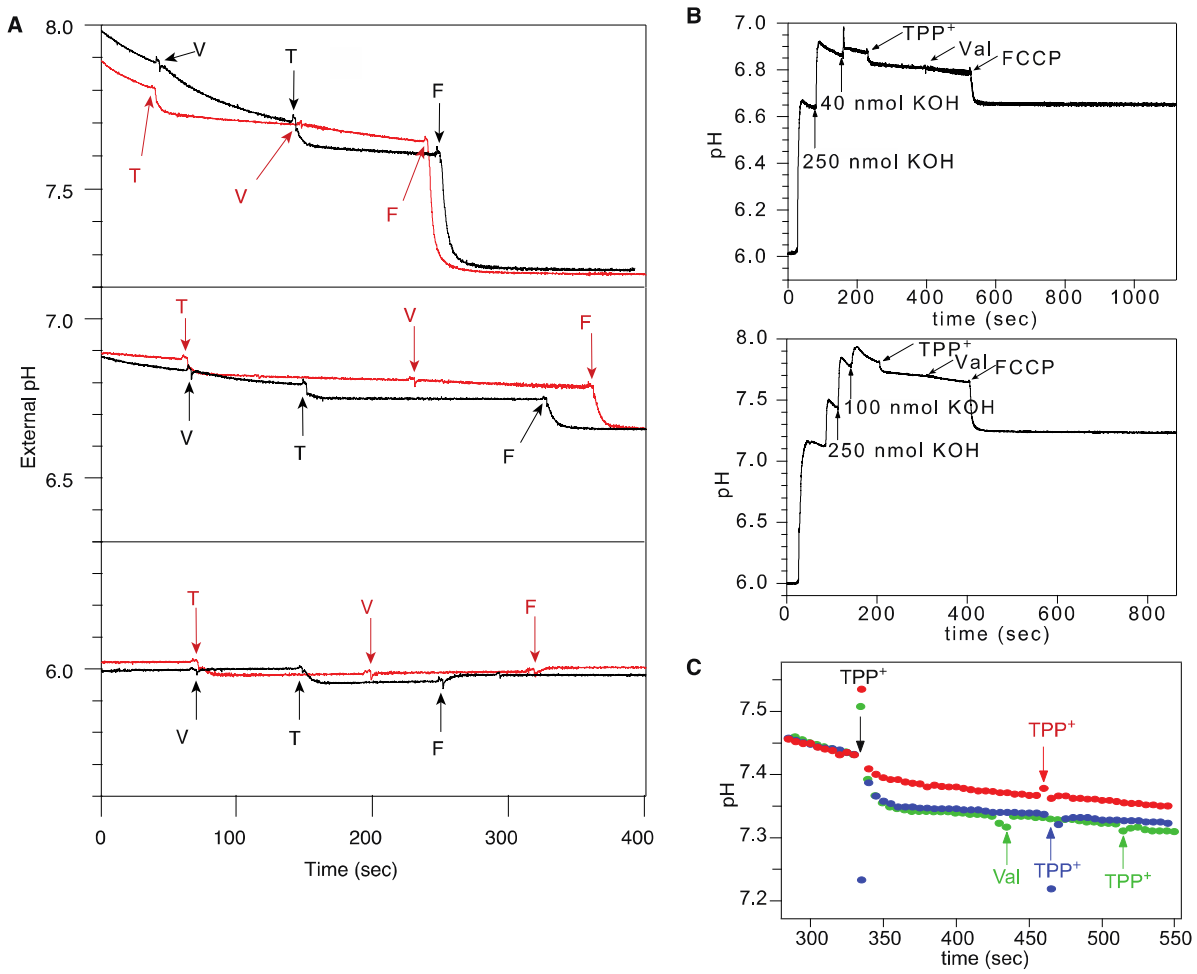

Fig. S8.

TPP⁺ transport pH dependence, quantitation and controls. A) Both proton release upon TPP⁺ binding and 1:1 antiport are electroneutral processes. To distinguish them, we determined the effect of external pH on the number of protons released. Increasing external pH increases ΔpH, and thus the driving force for 1:1 antiport. Therefore, proton efflux coupled to TPP⁺ uptake (1:1 antiport) will be *greater* at higher $pH_{external}$. However, proton release upon drug binding will *decrease* at higher $pH_{external}$ (1) since fewer protons are bound to EmrE initially. More protons are liberated at higher external pH (greater ΔpH): 46 ± 2 nmol H^+/ml at pH 7.7_{ext}, ΔpH=1.7 versus 31 ± 2 nmol H^+/ml at pH 7.0_{ext}, ΔpH=1 (Table S4). Unlike with Eth⁺, addition of valinomycin following addition of substrate does not result in additional proton release (Fig. 5C). TPP⁺ is a high affinity ligand (26). 1:1 transport likely yields a $TPP^+_{internal}$ concentration that is sufficient to saturate open-in EmrE such that no additional net flux can occur. B) To quantitate proton release from liposomes upon TPP⁺ uptake, we used the same approach as for direct measurement of proton-release upon TPP⁺ binding to solubilized EmrE. Since the external buffer pH was initially adjusted by adding small aliquots of base, these known KOH additions were used for quantitation. Addition of the protonophore FCCP at the end demonstrates that the proton gradient was not fully dissipated, even after addition of TPP⁺ and valinomycin. Indeed, the pH is very steady after addition of TPP⁺, demonstrating that there is not significant proton leak with TPP⁺ present. Thus proton leak cannot be the cause of the increased proton release

from the proteoliposomes with larger ΔpH. C) DCCD inactivation of EmrE significantly suppresses the H^+-release signal upon TPP^+ addition (red dots), confirming that it is due to H^+ release from EmrE. When not pre-treated with DCCD, this batch of proteoliposomes behaves the same way: addition of TPP^+ after (blue dots) or before (green dots) valinomycin results in the same H^+ release. The traces are aligned at the first TPP^+ addition (black arrow) to aid comparison. Other additions are noted in the same color as the relevant trace. Addition of a second aliquot of TPP^+ causes little further H^+ release, confirming that the slight pH difference between the TPP^+ stock and outside buffer is not the source of the observed pH change.

Table S1. ITC Experimental Data

pH	Buffer	Buffer ΔH (kJ/mol)*	[EmrE] (μM)[#]	[TPP$^+$] (μM)	K_a^{obs} (1/M)	ΔH (kJ/mol)	n[#]	K_d^{obs} (M)	Blank (μJ)
5.5	Cacodylate	-4.72	664	2810	1.50E+04	-39.4	0.55	6.69E-05	-5.8
5.5	Cacodylate	-4.72	835	4890	1.28E+04	-36.1	0.53	7.81E-05	-3.8
5.5	MES	14.90	808	4560	1.25E+04	-47.9	0.56	8.03E-05	-10.5
5.5	MES	14.90	802	4610	1.38E+04	-47.7	0.57	7.25E-05	-13.7
5.5	Piperazine	32.83	792	4870	1.71E+04	-60.5	0.57	5.84E-05	-12.5
5.5	Piperazine	32.83	801	4980	1.60E+04	-60.8	0.56	6.24E-05	-12.6

All ITC experiments were performed at 45 °C.

*Buffer data taken from (59) and adjusted for temperature as described in the methods.

[#][EmrE] listed is the monomer concentration, *n* is therefore the stoichiometry of TPP$^+$ bound per EmrE monomer, confirming that 1 TPP$^+$ binds per dimer. All replicates are shown.

Table S2. The variables and rates used in each model.

Process	Variable - B*	Variable - G*	Rate	Notes
EH -> EH2	kOnH2	k2, k9	10000 μM^{-1} s^{-1}	1
EH2 -> EH	kOffH2	k1, k10	1000 s^{-1}	2, using pKa of 7.0
E -> EH	kOnH	k4, k7	10000 μM^{-1} s^{-1}	1
EH -> E	kOffH	k3, k8	63 s^{-1}	2, using pKa of 8.2
EH -> ETH	kOnHT	k15, k30	7 μM^{-1} s^{-1}	3
ETH -> EH	kOffHT	k16, k29	6.2 s^{-1}	4
E -> ET	kOnT	k17, k26	22 μM^{-1} s^{-1}	3
ET -> E	kOffT	k18, k25	0.8 s^{-1}	4
ET -> ETH	kOnTH	k20, k27	10000 μM^{-1} s^{-1}	1
ETH -> ET	kOffTH	k19, k28	1580 s^{-1}	2, using pKa of 6.8
EH2ext <-> EH2int	kEH2io, kEH2oi	k12, k11	220 s^{-1}	5
EHext <-> EHint	kEHio, kEHoi	k14, k13	100 s^{-1}	5
Eext <-> Eint	kEio, kEoi	k5, k6	40 s^{-1}	5
ETHext <-> ETHint	kETHio, kETHoi	k23, k24	8.9 s^{-1}	6
EText <-> ETint	kETio, kEToi	k21, k22	7.3 s^{-1}	6

*Variable names used in the Berkeley Madonna simulation (B) or Gillespie simulation (G)

1 We assume fast proton on-rates of $10^{10} M^{-1} s^{-1}$

2 Proton off-rates are estimated from the pKa values and on-rate. The pKa values of drug-free EmrE (16) and TPP^+-bound EmrE (Fig. 2B and S2) were determined by NMR.

3 TPP^+ on-rates are from Model A in fig. S10 of a stopped-flow study of drug-binding to EmrE that considered multiple EmrE protonation states with two pKa values for drug-free EmrE (11).

4 TPP^+ off-rates are calculated from the pH dependent K_D (ITC data in this paper and (26)) and the on-rates.

5 Open-in/open-out conformational exchange rates were determined by NMR for apo and doubly-protonated EmrE and the rate for the singly protonated species is estimated between these values based on the pH-dependence of the conformational exchange rate in drug-free EmrE (15-17).

6 Open-in/open out exchange rates for TPP^+-bound EmrE, both with and without H^+ bound, were determined by NMR (Fig. 3).

Table S3. Proton-detected Transport Assay for ∆pH-driven Ethidium$^+$ Uptake

	EmrE dimer (nmol)*	Ethidium$^+$ (nmol)*	H^+ released after ethidium$^+$ addition (nmol)$^{\#}$	H^+ released upon valinomycin addition (nmol)$^{\#}$	Initial external pH before ethidium$^+$ addition	∆pH (out-in)†
	6.5	49	54	28	8.0	2.0
	6.5	49	51	23	7.8	1.8
	6.5	49	52	20	7.9	1.9
avg	**6.5**	**49**	**52**	**24**	**7.9**	**1.9**
	3.2	48	54	29	7.8	1.8
	3.2	47	51	23	8.2	2.2
	3.2	47	54	26	7.8	1.8
avg	**3.2**	**47**	**53**	**26**	**7.9**	**1.9**

*nmol of EmrE *dimer* or ethidium$^+$ normalized to a 1 ml assay volume. Thick lines separate different experimental conditions. All assays included the same total lipid concentration. The protein:lipid ratio was halved to decrease the protein concentration in the second data set.

$^{\#}$nmol of H^+ released per 1 ml assay calculated by comparison with ∆pH upon addition of a known quantity of NaOH.

†Inside pH was constant at pH6 for all proton-monitored transport assays.

Table S4. Proton-detected Transport Assay for ∆pH-driven TPP^+ Uptake

	EmrE dimer (nmol)*	TPP^+ (nmol)*	H^+ released (nmol)[#]	Initial external pH before TPP^+ addition[†]	∆pH (out-in)[†]
	16	39	32	6.8	0.8
	16	39	30	6.7	0.7
avg	**16**	**39**	**31**	**6.8**	**0.8**
	16	39	45	7.8	1.8
	16	39	48	7.8	1.8
	12	39	49	7.7	1.7
	12	39	43	7.8	1.8
	12	39	46	7.6	1.6
	12	39	43	7.6	1.6
	14	39	46	7.8	1.8
avg	**13**	**39**	**46**	**7.7**	**1.7**
	27[‡]	39	63	7.9	1.9
	27[‡]	39	63	7.9	1.9
	27[‡]	39	60	8	2.0
avg	**27[‡]**	**39**	**62**	**7.9**	**1.9**

*nmol of EmrE *dimer* or TPP^+ normalized to a 1 ml assay volume. Thin lines separate independently prepared batches of proteoliposomes. Thick lines separate different experimental conditions. All assays included the same total lipid concentration. The protein:lipid ratio was doubled to increase the protein concentration in the third data set. These conditions correspond to 39 µM TPP^+ and 24-54 µM EmrE *monomer* in the assay, well above the K_D at all pH values.

[#]nmol of H^+ released per 1 ml assay calculated by comparison with ∆pH upon addition of a known quantity of KOH.

[†]Inside pH was constant at pH6 for all proton-monitored transport assays.

[‡]To confirm that the signal is not solely a result of TPP^+ binding, we repeated the assay with twice the protein:lipid ratio. This will not change net transport, and thus the difference in H^+ release will be due to binding. With this doubled ratio, we observe an increase of 1.2 nmol H^+ released per dimer, from 2.3 nmol H^+ released per dimer to 3.5 nmol H^+ released per dimer. This demonstrates that although there is measurable binding-induced proton release (1.2 nmol H^+ per dimer) when using the tight-binding TPP^+ for transport assays, it does not account for the total number of protons liberated from the liposomes upon TPP^+ addition and 1:1 transport must occur.

Table S5. Proton-detected Transport Assay for ΔΨ-driven Ethidium$^+$ Uptake

EmrE dimer (nmol)*	Ethidium$^+$ (nmol)*	H$^+$ released after ethidium$^+$ addition (nmol)$^\#$	Internal K$^+$ concentration (mM)	External K$^+$ concentration (mM)	Direction of ΔΨ
4.6	33	19	1	100	Positive inside
4.6	33	22	1	100	Positive inside
4.6	33	21	1	100	Positive inside
avg 4.6	**33**	**21**	**1**	**100**	
4.6	33	-30	100	1	Negative inside
4.6	33	-33	100	1	Negative inside
4.6	33	-35^	100	1	Negative inside
avg 4.6	**33**	**-33**	**100**	**1**	

*nmol of EmrE *dimer* or ethidium$^+$ normalized to a 1 ml assay volume. Thick lines separate different experimental conditions. All assays included the same total lipid concentration.

$^\#$nmol of H$^+$ released per 1 ml assay calculated by comparison with ΔpH upon addition of a known quantity of NaOH.

†Inside pH was constant at pH6 for all proton-monitored transport assays.

^For this sample, ethidium was added before valinomycin ($\Delta\Psi = 0$), leading to an initial efflux of 11 nmol/mL protons from the liposomes (decrease in pH). Upon addition of valinomycin and the creation of negative-inside ΔΨ, 46 nmol/mL protons went back into the liposomes (pH increased). H$^+$ released was calculated from the total net proton transport out of the liposomes (11 nmol/mL − 46 nmol/mL = -35 nmol/mL).

Appendix 1 Berkeley Madonna simulation code

```
{Units are:
concentration in micromolar
time in seconds
surface area in square microns
2D concentration in molecules/square micron
volume in mL}
METHOD RK4

STARTTIME = 0
STOPTIME=100
DT = 0.0001

{Rate equations defining 9 of the 10 EmrE states, state 10 is defined from conservation
equation and constant Etot.}

d/dt (Eext) = - kEoi*Eext+kEio*Eint+kOffH*EHext-kOnH*Hext*Eext-
kOnT*Text*Eext+kOFFT*EText

d/dt (Eint) = + kEoi*Eext-kEio*Eint+kOffH*EHint-kOnH*Hint*Eint-
kOnT*Tint*Eint+kOffT*ETint

d/dt (EHext) = - kEHoi*EHext+kEHio*EHint+kOffH2*EH2ext-kOnH2*Hext*EHext+
kOnH*Hext*Eext- kOffH*EHext-kOnHT*Text*EHext+kOffHT*ETHext

d/dt (EHint) = + kEHoi*EHext-kEHio*EHint+kOffH2*EH2int-kOnH2*Hint*EHint+
kOnH*Hint*Eint- kOffH*EHint-kOnHT*Tint*EHint+kOffHT*ETHint

d/dt (EH2ext) = - kEH2oi*EH2ext+kEH2io*EH2int-kOffH2*EH2ext+kOnH2*Hext*EHext

{d/dt (EH2int) = + kEH2oi*EH2ext-kEH2io*EH2int-kOffH2*EH2int+kOnH2*Hint*EHint}

d/dt (EText) = - kEToi*EText+kETio*ETint+kOffTH*ETHext-
kOnTH*Hext*EText+kOnT*Text*Eext-kOFFT*EText

d/dt (ETint) = + kEToi*EText-kETio*ETint+kOffTH*ETHint-
kOnTH*Hint*ETint+kOnT*Tint*Eint-kOffT*ETint

d/dt (ETHext) = - kETHoi*ETHext+kETHio*ETHint-
kOffTH*ETHext+kOnTH*Hext*EText+kOnHT*Text*EHext-kOffHT*ETHext

d/dt (ETHint) = + kETHoi*ETHext-kETHio*ETHint-kOffTH*ETHint+kOnTH*Hint*ETint-
kOffHT*ETHint+kOnHT*Tint*EHint{Total EmrE given in molecules per square micron.
Dimer concentration times 48548 molecules per square micron.}
Etot=.04*48548
EH2int=Etot-EH2ext-EHint-EHext-Eint-Eext-ETHint-ETHext-ETint-EText

{Liposome and volume definitions. Smem is surface area, Vint is internal volume, this factor
converts from molecules per square micron to concentration of molecules in micromolar.}
Smem=1.24e10
Vint=2.64e-7
```

```
Vtot=0.001
Vext=Vtot-Vint

{Rate equation to define build-up of TPP on the inside of the liposome.}
d/dt (Tint)=- kOnT*Tint*Eint* Smem/(Vint*6.02e17)- kOnHT*Tint*EHint*
Smem/(Vint*6.02e17)+kOffHT*ETHint*Smem/(Vint*6.02e17)+kOffT*ETint*Smem/(Vint*6.02
e17)

{TPP concentration given in micromolar.}
Text=Ttot-(Tint*Vint/Vtot)-(EText+ETint+ETHext+ETHint)*Smem/(Vtot*6.02e17)
Ttot=0.05

{pH, given in micromolar concentrations of H. Assuming pH 7 inside and out in this
iteration.}
Hext=0.1
Hint=0.1

{Initial conditions.}
init Eint=Etot/2
init Eext=Etot/2
init EHext=0
init EHint=0
init EH2ext=0
init EText=0
init ETint=0
init ETHext=0
init ETHint=0
init Tint=0

{Rates, measured or estimated from experiment as listed in Table 2}
kEoi=40
kEio=40
kOffH=63
kOnH=10000
kEHoi=100
kEHio=100
kOffH2=1000
kOnH2=10000
kEH2oi=220
kEH2io=220
kOnT=22
kOffT=0.8
kOffHT=6.2
kOnHT=7
kEToi=7.3
kETio=7.3
kOffTH=1580
kOnTH=10000
kETHoi=8.9
kETHio=8.9
```

Appendix 2 Gillespie simulation code

```
page_screen_output(0);

page_output_immediately(1);


T = 0.05; %TPP concentration in uM

Tint = T; %TPP concentration inside liposome

Text = T; %TPP concentration outside liposome

Hint = 1.0; %proton concentration inside liposome, in uM

Hext = 0.01; %proton concentration outside liposome, in uM


% invariant rate constants

k1 = 1000; %koffH2

k2 = 10000; %konH2

k3 = 63; %koffH

k4 = 10000; %konH

k5 = 40; %kEoi

k6 = 40; %kEio

k7 = 10000; %konH

k8 = 63; %koffH

k9 = 10000; %konH2

k10 = 1000; %koffH2

k11 = 220; %kEH2io

k12 = 220; %kEH2oi

k13 = 100; %kEHio

k14 = 100; %kEHoi

k15 = 7; %konHT

k16 = 6.2; %koffHT

k17 = 22; %konT

k18 = 0.8; %koffT

k19 = 1580; %koffTH
```

```
k20 = 10000; %konTH

k21 = 7.3; %kEToi

k22 = 7.3; %kETio

k23 = 8.9; %kETHoi

k24 = 8.9; %kETHio

k25 = 0.8; %koffT

k26 = 22; %konT

k27 = 10000; %konTH

k28 = 1580; %koffTH

k29 = 6.2; %koffHT

k30 = 7; %konHT

rates = {[k1 k12] [k2*Hext k3 k14 k15*Text] [k4*Hext k5 k17*Text] [k6 k7*Hint k26*Tint] [k8
k9*Hint k13 k30*Tint] [k10 k11] [k16 k19 k23] [k18 k20*Hext k21] [k22 k25 k27*Hint] [k24
k28 k29]};

moves = {[2 6] [1 3 5 7] [2 4 8] [3 5 9] [4 6 2 10] [5 1] [2 8 10] [3 7 9] [8 4 10] [7 9 5]};

% ---- Now we actually run the simulation ----


time = zeros(1000,1); states = zeros(1000,1); prevState = 0;

transitions = zeros(length(moves), length(moves));

t = 0; state = 1;

tEnd = 5000; % simulation length in seconds

n = 1; pct = 0;

printf("0%%...");

while t < tEnd

    time(n) = t;

    states(n) = state;

    prevState = state;

    %pick time from distribution of total out-rates

    t = t + -log(1-rand)/sum(rates{state});

    %pick direction

    number = rand;
```

```
    if (number < rates{state}(1)/sum(rates{state}))
        state = moves{state}(1);
    elseif (number < (rates{state}(1)+rates{state}(2))/sum(rates{state}))
        state = moves{state}(2);
    elseif (number < (rates{state}(1)+rates{state}(2)+rates{state}(3))/sum(rates{state}))
        state = moves{state}(3);
    else
        state = moves{state}(4);
    endif

    % record state transition
    transitions(prevState, state)++;
    n = n + 1;
    % Print out percent simulation completed
    prop = floor(t/tEnd*10);
    if (prop > pct) % if we've completed another 10%
        pct = prop;
        printf("%d%%...", pct*10);
    endif
endwhile
printf("Done!\nSaving files...\n");
% save data to files
csvwrite("states.csv", states);
csvwrite("times.csv", time);
csvwrite("transitions.csv", transitions);
```

Appendix 3 Quantitative analysis of the ΔpH-driven transport assay

In the ethidium uptake assay, we directly measure a total of 76 nmol H+ efflux from the EmrE proteoliposomes per ml of assay volume. Only 53 nmol ethidium+ per ml was added to this assay. The table below shows the transport calculations for pure 2:1 or pure 1:1 antiport stoichiometry.

Antiport Stoichiometry (H+/Eth+)	nmol Eth+ uptake into liposome	nmol Eth+ remaining outside	Eth+ concentration gradient*
1:1	76	-23	Pure 1:1 antiport cannot explain the data: 76 nmol H+ effluxed is more than the total 53 nmol Eth+ added to the assay.
2:1	38	15	64:1

*The internal and external liposome volumes were estimated using the equations below to be 0.038 ml and 0.96 ml, respectively, per 1 ml assay volume. The internal and external Eth+ concentrations were calculated using these volumes and the nmol Eth+ uptake into the liposome (internal) or remaining outside (external).

First the surface area, volume, and number of lipids per liposome were estimated as in (61).

$$SA_{liposome} = 4\pi\left\{\left(\frac{d}{2}\right)^2 + \left(\frac{d}{2} - l\right)^2\right\}$$

$$V_{liposome} = \frac{4}{3}\pi\left(\frac{d}{2} - l\right)^3$$

$$\#lipids/liposome = \frac{SA_{liposome}}{SA_{lipid}}$$

$SA_{liposome}$ = surface area of one liposome

d = diameter of the liposome, 0.2 μm

l = lipid bilayer thickness, 0.005 μm

$V_{liposome}$ = internal volume of one liposome

SA_{lipid} = surface area of one lipid, 0.64 nm^2, 0.64 * 10^{-6} μm^2

The total lipid in the assay was calculated from the final protein concentration (measured using absorbance at 280 nm by adding DHPC to break the liposomes up into bicelles) and the protein:lipid ratio used during reconstitution. This method assumes that any losses during reconstitution and proteoliposome extrusion equally affect protein and lipid. This is a reasonable assumption based on our NMR studies of EmrE in bicelles. For NMR experiments, EmrE is reconstituted into liposomes in exactly the same manner as used for the transport assays. The liposomes are then broken up into bicelles by addition of a known quantity of the short-chain lipid, DHPC. At these high concentrations, a 1D 1H NMR spectrum can be acquired and the peaks corresponding to the terminal methyl of the lipid acyl chains integrated to quantitatively determine the relative concentrations of the DHPC and the long-chain lipid derived from the liposomes for comparison with the protein concentration. These measurements show reconstitution efficiency of 85-90% for both EmrE and lipid.

$$n_{lipids} = [EmrE]\left(\frac{L}{P}\right)N_A(10^{-6})$$

$$n_{liposome} = \frac{n_{lipids}}{\#lipids/liposome}$$

$$SA_{tot} = n_{liposome}SA_{liposome}$$

$$V_{internal} = n_{liposome}V_{liposome}$$

$$V_{external} = (1\ ml) - \ n_{liposome}\left(\frac{4}{3}\pi\left(\frac{d}{2}\right)^3\right)$$

n_{lipids} = number of lipids in 1 ml assay

$[EmrE]$= EmrE concentration in mM

$\left(\frac{L}{P}\right)$ = lipid/protein mole ratio

N_A = Avogadro's number

$n_{liposome}$ = number of liposomes in 1 ml assay

SA_{tot} = total surface area of liposomes in 1 ml assay

$V_{internal}$ = total internal volume of liposomes in 1 ml assay

$V_{external}$ = external volume outside liposomes in 1 ml assay

These results also suggest that EmrE does not perform solely 2:1 H+/drug+ antiport. The thermodynamic driving force provided by a pH gradient is

$$ln\left(\frac{H_i^+}{H_o^+}\right)^n = ln\left(\frac{Eth_i^+}{Eth_o^+}\right)$$

for antiport of *n*H^+ per Eth^+, where the subscripts indicate the inside (i) or outside (o) concentration of each substrate. This assumes that valinomycin has been added to dissipate the membrane potential. It predicts a 10,000-fold gradient in Eth^+ from the initial ∆pH=2 assuming a strict 2:1 antiport stoichiometry. This assumes that the strong buffering inside the liposome prevents any pH drift as the external pH is raised rapidly to pH 8 by addition of NaOH. However, even if internal pH drifts 0.5 pH units and ∆pH is only 1.5, this equation predicts a 1000-fold gradient in Eth^+, well above the 64-fold gradient estimated above.

These calculations are not quantitatively accurate, relying on round-number estimates of lipid bilayer thickness, surface area per lipid in the POPC/POPG bilayer, liposome diameter after extrusion, and accurate protein and lipid concentration. Furthermore, they assume that all liposomes are unilamellar. However, these calculations should provide a rough estimate. The driving force provided from ∆pH should drive orders of magnitude more transport than observed, suggesting that strict 2:1 antiport cannot account for the observed transport activity of EmrE.

References

1. Muth TR, Schuldiner S (2000) A membrane-embedded glutamate is required for ligand binding to the multidrug transporter EmrE. *EMBO J* 19(2):234–240.

2. Yerushalmi H, Mordoch SS, Schuldiner S (2001) A single carboxyl mutant of the multidrug transporter EmrE is fully functional. *J Biol Chem* 276(16):12744–12748.

3. Yerushalmi H, Schuldiner S (2000) An essential glutamyl residue in EmrE, a multidrug antiporter from Escherichia coli. *J Biol Chem* 275(8):5264–5269.

4. Chen YJ, et al. (2007) X-ray structure of EmrE supports dual topology model. *Proc Natl Acad Sci USA* 104(48):18999–19004.

5. Morrison EA, et al. (2011) Antiparallel EmrE exports drugs by exchanging between asymmetric structures. *Nature* 481(7379):45–50.

6. Ubarretxena-Belandia I, Baldwin JM, Schuldiner S, Tate CG (2003) Three-dimensional structure of the bacterial multidrug transporter EmrE shows it is an asymmetric homodimer. *EMBO J* 22(23):6175–6181.

7. Rotem D, Sal-man N, Schuldiner S (2001) In vitro monomer swapping in EmrE, a multidrug transporter from Escherichia coli, reveals that the oligomer is the functional unit. *J Biol Chem* 276(51):48243–48249.

8. Dutta S, Morrison EA, Henzler-Wildman KA (2014) Blocking Dynamics of the SMR Transporter EmrE Impairs Efflux Activity. *Biophys J* 107(3):613–620.

9. Stein WD (1986) *Transport and diffusion across cell membranes* (Academic Press, Inc.).

10. Soskine M, Adam Y, Schuldiner S (2004) Direct evidence for substrate-induced proton release in detergent-solubilized EmrE, a multidrug transporter. *J Biol Chem* 279(11):9951–9955.

11. Adam Y, Tayer N, Rotem D, Schreiber G, Schuldiner S (2007) The fast release of sticky protons: kinetics of substrate binding and proton release in a multidrug transporter. *Proc Natl Acad Sci USA* 104(46):17989–17994.

12. Rotem D, Schuldiner S (2004) EmrE, a multidrug transporter from Escherichia coli, transports monovalent and divalent substrates with the same stoichiometry. *J Biol Chem* 279(47):48787–48793.

13. Korkhov VM, Tate CG (2008) Electron crystallography reveals plasticity within the drug binding site of the small multidrug transporter EmrE. *J Mol Biol* 377(4):1094–1103.

14. Amadi ST, Koteiche HA, Mishra S, McHaourab HS (2010) Structure, dynamics, and substrate-induced conformational changes of the multidrug transporter EmrE in liposomes. *J Biol Chem* 285(34):26710–26718.

15. Cho M-K, Gayen A, Banigan JR, Leninger M, Traaseth NJ (2014) Intrinsic conformational plasticity of native EmrE provides a pathway for multidrug resistance. *J Am Chem Soc* 136(22):8072–8080.

16. Morrison EA, Robinson AE, Liu Y, Henzler-Wildman KA (2015) Asymmetric protonation of EmrE. *J Gen Physiol* 146(6):445–461.

17. Gayen A, Leninger M, Traaseth NJ (2016) Protonation of a glutamate residue modulates the dynamics of the drug transporter EmrE. *Nat Chem Biol*. doi:10.1038/nchembio.1999.

18. Dastvan R, Fischer AW, Mishra S, Meiler J, McHaourab HS (2016) Protonation-dependent conformational dynamics of the multidrug transporter EmrE. *Proc Natl Acad Sci USA* 113(5):1220–1225.

19. Lehner I, et al. (2008) The key residue for substrate transport (Glu14) in the EmrE dimer is asymmetric. *J Biol Chem* 283(6):3281–3288.

20. Baker BM, Murphy KP (1996) Evaluation of linked protonation effects in protein binding reactions using isothermal titration calorimetry. *Biophys J* 71(4):2049–2055.

21. Li Y, Palmer AG (2009) TROSY-selected ZZ-exchange experiment for characterizing slow chemical exchange in large proteins. *J Biomol NMR* 45(4):357–360.

22. Weinglass AB, et al. (2005) Exploring the role of a unique carboxyl residue in EmrE by mass spectrometry. *J Biol Chem* 280(9):7487–7492.

23. Yerushalmi H, Lebendiker M, Schuldiner S (1996) Negative dominance studies demonstrate the oligomeric structure of EmrE, a multidrug antiporter from Escherichia coli. *J Biol Chem* 271(49):31044–31048.

24. Gillespie DT (1976) A general method for numerically simulating the stochastic time evolution of coupled chemical reactions. *J Comp Phys* 22(4):403–434.

25. Forrest LR, Krämer R, Ziegler C (2011) The structural basis of secondary active transport mechanisms. *ACTA-BIOENERG* 1807(2):167–188.

26. Morrison EA, Henzler-Wildman KA (2014) Transported substrate determines exchange rate in the multidrug resistance transporter EmrE. *J Biol Chem* 289(10):6825–6836.

27. Reyes N, Ginter C, Boudker O (2009) Transport mechanism of a bacterial homologue of glutamate transporters. *Nature* 462(7275):880–885.

28. Basilio D, Noack K, Picollo A, Accardi A (2014) Conformational changes required for H(+)/Cl(-) exchange mediated by a CLC transporter. *Nat Struct Mol Biol* 21(5):456–463.

29. Picollo A, Malvezzi M, Houtman JCD, Accardi A (2009) Basis of substrate binding and conservation of selectivity in the CLC family of channels and transporters. *Nat Struct Mol Biol* 16(12):1294–1301.

30. Parker JL, Mindell JA, Newstead S (2014) Thermodynamic evidence for a dual transport mechanism in a POT peptide transporter. *eLife* 3:e04273.

31. Fluman N, Adler J, Rotenberg SA, Brown MH, Bibi E (2014) Export of a single drug molecule in two transport cycles by a multidrug efflux pump. *Nat Commun* 5:4615.

32. Ramos S, Kaback HR (1977) The elctrochemical proton gradient in Escherichia coli membrane vesicles. *Biochemistry* 16(5):848–854.

33. Nguitragool W, Miller C (2006) Uncoupling of a CLC Cl-/H+ exchange transporter by polyatomic anions. *J Mol Biol* 362(4):682–690.

34. Accardi A, Picollo A (2010) CLC channels and transporters: proteins with borderline personalities. *Biochim Biophys Acta* 1798(8):1457–1464.

35. Tate CG, Kunji ER, Lebendiker M, Schuldiner S (2001) The projection structure of EmrE, a proton-linked multidrug transporter from Escherichia coli, at 7 A resolution. *EMBO J* 20(1-2):77–81.

36. Joh NH, et al. (2014) De novo design of a transmembrane Zn2+-transporting four-helix bundle. *Science* 346(6216):1520–1524.

37. Stein WD, Honig B (1977) Models for the active transport of cations ··· The steady-state analysis. *Mol Cell Biochem* 15(1):27–44.

38. Kaback HR (2015) A chemiosmotic mechanism of symport. *Proc Natl Acad Sci USA* 112(5):1259–1264.

39. Reynolds JA, Johnson EA, Tanford C (1985) Incorporation of membrane potential into theoretical analysis of electrogenic ion pumps. *Proc Natl Acad Sci USA* 82(20):6869–6873.

40. Garcia-Celma JJ, Smirnova IN, Kaback HR, Fendler K (2009) Electrophysiological characterization of LacY. *Proc Natl Acad Sci USA* 106(18):7373–7378.

41. Bianchi F, et al. (2016) Asymmetry in inward- and outward-affinity constant of transport explain unidirectional lysine flux in Saccharomyces cerevisiae. *Sci Rep* 6(1):31443.

42. Krupka R (1998) Channelling free energy into work in biological processes. *Exp Physiol* 83(2):243–251.

43. Krupka RM (1999) Limits on the tightness of coupling in active transport. *J Membr Biol* 167(1):35–41.

44. Al-Shawi MK, Polar MK, Omote H, Figler RA (2003) Transition state analysis of the coupling of drug transport to ATP hydrolysis by P-glycoprotein. *J Biol Chem* 278(52):52629–52640.

45. Krupka RM (1999) Uncoupled Active Transport Mechanisms Accounting for Low

Selectivity in Multidrug Carriers: P-Glycoprotein and SMR Antiporters. *J Membr Biol* 172(2):129–143.

46. Brill S, Falk OS, Schuldiner S (2012) Transforming a drug/H+ antiporter into a polyamine importer by a single mutation. *Proc Natl Acad Sci USA* 109:16894–16899.

47. Brill S, Sade-Falk O, Elbaz-Alon Y, Schuldiner S (2015) Specificity determinants in Small Multidrug Transporters. *J Mol Biol* 427:468–477.

48. Son MS, et al. (2003) Mutagenesis of SugE, a small multidrug resistance protein. *Biochem Biophys Res Commun* 312(4):914–921.

49. Ramos S, Kaback HR (1977) pH-dependent changes in proton:substrate stoichiometries during active transport in Escherichia coli membrane vesicles. *Biochemistry* 16(19):4270–4275.

50. Morrison EA, Henzler-Wildman KA (2012) Reconstitution of integral membrane proteins into isotropic bicelles with improved sample stability and expanded lipid composition profile. *Biochim Biophys Acta* 1818(3):814–820.

51. Delaglio F, et al. (1995) NMRPipe: a multidimensional spectral processing system based on UNIX pipes. *J Biomol NMR* 6(3):277–293.

52. Vranken WF, et al. (2005) The CCPN data model for NMR spectroscopy: development of a software pipeline. *Proteins* 59(4):687–696.

53. Favier A, Brutscher B (2011) Recovering lost magnetization: polarization enhancement in biomolecular NMR. *J Biomol NMR* 49(1):9–15.

54. Lescop E, Kern T, Brutscher B (2010) Guidelines for the use of band-selective radiofrequency pulses in hetero-nuclear NMR: Example of longitudinal-relaxation-enhanced BEST-type (1)H-(15)N correlation experiments. *J Magn Reson* 203(1):190–198.

55. Miloushev VZ, et al. (2008) Dynamic properties of a type II cadherin adhesive domain: implications for the mechanism of strand-swapping of classical cadherins. *Structure* 16(8):1195–1205.

56. Glover KJ, et al. (2001) Structural evaluation of phospholipid bicelles for solution-state studies of membrane-associated biomolecules. *Biophys J* 81(4):2163–2171.

57. McIntosh LPL, et al. (2011) Dissecting electrostatic interactions in Bacillus circulans xylanase through NMR-monitored pH titrations. *J Biomol NMR* 51(1-2):5–19.

58. Dutta S, Morrison EA, Henzler-Wildman KA (2014) EmrE dimerization depends on membrane environment. *Biochim Biophys Acta* 1838(7):1817–1822.

59. Goldberg RN, Kishore N, Lennen RM (2002) Thermodynamic Quantities for the Ionization Reactions of Buffers. *J Phys Chem Ref Data* 31(2):231–370.

60. Eaton JW, Bateman D, Hauberg S (2007) *GNU Octave version 3.0. 1 manual: a high-level interactive language for numerical computations*.

61. Nilsson T, et al. (2016) Lipid-mediated Protein-protein Interactions Modulate Respiration-driven ATP Synthesis. *Sci Rep* 6(1):24113.

Chapter 2

Highly coupled transport can be achieved in free exchange transport models

Grant A. Hussey, Nathan E. Thomas, Katherine A. Henzler-Wildman

Department of Biochemistry, University of Wisconsin at Madison, Madison, WI 53706, USA.

Preface

Secondary active transport mechanisms often depict a limited number of states and transitions, although recent research suggests alternative “leak” pathways are not always minor. Here, we numerically simulate a fully unrestricted model and demonstrate that highly-efficient transport can be achieved despite the existence of multiple leak pathways. Grant created and ran the simulations and wrote the first draft of the manuscript. I helped to supervise and design experiments, analyze the results, and edit the manuscript.

Abstract

Secondary active transporters couple the transport of an ion species down its concentration gradient to drive the uphill transport of another substrate. Despite the importance of secondary active transport to multidrug resistance, metabolite transport, and nutrient acquisition among other biological processes, the microscopic steps of the coupling mechanism are not well understood. Often, transport models illustrate coupling mechanisms through a limited number of “major” conformations or states, yet recent studies have indicated that at least some transporters violate these models. The small multidrug resistance transporter EmrE has been shown to couple proton influx to multidrug efflux via a mechanism that incorporates both “major” and “minor” conformational states and transitions. The resulting free exchange transport model includes multiple leak pathways and theoretically allows for both exchange and co-transport of ion and substrate. To better understand how coupled transport can be achieved in

such a model, we numerically simulate a free-exchange model of transport to determine the step-by-step requirements for coupled transport. We find that only moderate biasing of rate constants for key transitions produce highly-efficient net transport approaching a perfectly-coupled, stoichiometric model. We show how a free exchange model can enable complex phenotypes, including switching transport direction with changing environmental conditions or substrates. This research has broad implications for synthetic biology as it demonstrates the utility of free exchange transport models and the fine-tuning required for perfectly-coupled transport.

Abbreviations

E. coli, Escherichia coli; NMR, nuclear magnetic resonance; WT, wild-type; Ext, external; Int, internal; TPP, tetraphenyl phosphonium; MDR, multidrug resistance; ATP, adenosine triphosphate; ΔΨ, transmembrane voltage

Introduction

Secondary active transporters use the energetically favorable flux of one ion down its electrochemical gradient in order to drive transport of a second substrate in the same (symport) or opposite (antiport) direction. Despite the importance of these integral membrane proteins for nutrient acquisition, metabolite transport, and toxin efflux, the mechanistic details of ion-substrate coupling are still not fully understood (Zhang et al., 2019; Yazaki et al., 2008; Amaral et al., 2014; Silverman, 2002). Frequently, transport mechanisms are depicted by models which include only the minimum number of states and transitions needed to explain transport [5–11] (Figure 1). Through restricting transport to a single pathway, these models lead to perfect energetic coupling between substrate and ion. Occasional “slippage”, or transport through pathways apart from those prescribed by perfect coupling, is expected but assumed to be a relatively minor contributor to net flux. Although net transport stoichiometry is challenging to

measure accurately, it has been measured via reversal potential for several transporters [12–14], and stoichiometric or near-stoichiometric transport was observed, as expected. Together with crystals structures [15,16] that have captured a finite number of states for individual transporters and families, this has led to the widespread representation of such models in the literature.

However, it is becoming clear that deviations from ideal coupled transport may be common for some transporters, and that "slippage" pathways may even become the dominant transport pathway under certain conditions. For example, $GlcP_{Se}$, a sugar transporter from *Staphyloccocus epidermidis,* can perform sugar/proton symport, sugar uniport, and proton uniport based upon pH conditions, indicating it is possible for a single protein to engage in both coupled and uncoupled transport pathways [17]. Some transporters engage in multiple transport regimes or stoichiometries based on substrate identity. Examples include Nramp, a metal ion transporter that performs proton-coupled symport of manganese and uniport of cadmium [18], or NIS, the classical sodium-iodide symporter that performs 2:1 Na^+/I^+ symport but also 1:1 perchlorate symport [19]. Additionally, single point mutations of LacY result in a variety of leaky phenotypes while still performing net import of sugar molecules [8,20,21]. In these examples, "slippage" pathways significantly influence net flux. Thus, a mechanistic model that explicitly considers all possibilities for ion-coupled transport is required.

Our lab uses EmrE, a proton-coupled multidrug efflux pump from *E. coli* [22,23], to investigate the requirements for ion-coupled transport. Since the proton motive force is inwardly-directed in *E. coli*, EmrE confers resistance to toxic polyaromatic cations through proton/drug antiport. EmrE's small size, stability, and ease-of-purification makes it a model system to study by nuclear magnetic resonance (NMR) spectroscopy. This powerful technique can simultaneously provide structural, thermodynamic, and kinetic information, giving unprecedented insight into the transport cycle of an ion-coupled transporter [24–27]. Strikingly, NMR reveals that EmrE adopts states and performs transitions nominally "forbidden" for an

antiporter: it can both bind drug and proton simultaneously [24] and alternate access in every available state [24,25,28]. In light of this evidence, we proposed a “free-exchange” model of transport for EmrE that incorporates all experimentally observed states and transitions (Figure 2) [24]. The free-exchange model includes multiple leak pathways, yet WT EmrE demonstrates sufficient coupling to confer resistance to a wide array of toxic compounds in its native *E. coli*.

Here, we investigate the requirements for coupled transport using mass action kinetics to simulate the free-exchange model of transport [29]. Using a bottom-up approach, we first model the simplest implementation of free exchange, the 8-state model (equation 1, Figure 3), before investigating the 10-state model (equation 2, Figure 2) needed to describe EmrE transport [24]. We base our simulations on EmrE because it is one of the few secondary active transporters for which the rate constants are experimentally measured or estimated for all of the microscopic steps in the transport cycle. We demonstrate that only modest biasing of rates is necessary to achieve reasonably well-coupled transport, a result which has broad implications both for synthetic biology and for our understanding of the fundamental nature of active transport.

Methods

Numerical simulations of transport. We model EmrE-mediated drug transport into/out of a virtual proteoliposome in a simulated liposomal-flux assay (Figure 4). We use the default parameters in ODE15s in MATLAB to numerically solve the following coupled nonlinear differential equations to determine evolution of transport over time for the generic 8-state model (Figure 3),

$$\frac{d}{dt}EH_{ext} = k_1E_{ext} - k_2EH_{ext} - k_{13}EH_{ext}\frac{Drug_{ext}}{VolFactExt} + k_{14}EHD_{ext} + k_{17}EH_{int} - k_{18}EH_{ex}$$

$$\frac{d}{dt}EH_{int} = k_3E_{int} - k_4EH_{int} - k_{15}EH_{int}\frac{Drug_{int}}{VolFactInt} + k_{16}EHD_{int} - k_{17}EH_{int} + k_{18}EH_{ext}$$

$$\frac{d}{dt}E_{ext} = -k_1E_{ext} + k_2EH_{ext} - k_9E_{ext}\frac{Drug_{ext}}{VolFactExt} + k_{10}ED_{ext} + k_{19}E_{int} - k_{20}E_{ext}$$

$$\frac{d}{dt}E_{int} = -k_3E_{int} + k_4EH_{int} - k_{11}E_{int}\frac{Drug_{int}}{VolFactInt} - k_{12}ED_{int} - k_{19}E_{int} + k_{20}E_{ext}$$

$$\frac{d}{dt}EHD_{ext} = k_5ED_{ext} - k_6EHD_{ext} + k_{13}EH_{ext}\frac{Drug_{ext}}{VolFactExt} - k_{14}EHD_{ext} + k_{23}EHD_{int} - k_{24}EHD_{ext}$$

$$\frac{d}{dt}EHD_{int} = k_7ED_{int} - k_8EHD_{int} + k_{15}EH_{int}\frac{Drug_{int}}{VolFactInt} - k_{16}EHD_{int} - k_{23}EHD_{int} + k_{24}EHD_{ext}$$

$$\frac{d}{dt}ED_{ext} = -k_5ED_{ext} + k_6EHD_{ext} + k_9E_{ext}\frac{Drug_{ext}}{VolFactExt} - k_{10}ED_{ext} + k_{21}ED_{int} - k_{22}ED_{ext}$$

$$\frac{d}{dt}ED_{int} = -k_7ED_{int} + k_8EHD_{int} + k_{11}E_{int}\frac{Drug_{int}}{VolFactInt} - k_{12}ED_{int} - k_{21}ED_{int} + k_{22}ED_{ext}$$

$$\frac{1}{VolFactExt}\frac{d}{dt}Drug_{ext} = -k_5ED_{ext} + k_6EHD_{ext} + k_9E_{ext}\frac{Drug_{ext}}{VolFactExt} - k_{10}ED_{ext}$$

$$+k_{21}ED_{int} - k_{22}ED_{ext}$$

$$\frac{1}{VolFactExt}\frac{d}{dt}Drug_{int} = -k_7ED_{int} + k_8EHD_{int} + k_{11}E_{int}\frac{Drug_{int}}{VolFactInt} - k_{12}ED_{int}$$

$$-k_{21}ED_{int} + k_{22}ED_{ext} \quad (1)$$

and the EmrE-based 10-state model (Figure 2),

$$\frac{d}{dt}EH_{ext} = k_1E_{ext} - k_2EH_{ext} - k_{13}EH_{ext}\frac{Drug_{ext}}{VolFactExt} + k_{14}EHD_{ext} + k_{17}EH_{int} - k_{18}EH_{ext}$$

$$\frac{d}{dt}EH_{int} = k_3E_{int} - k_4EH_{int} - k_{15}EH_{int}\frac{Drug_{int}}{VolFactInt} + k_{16}EHD_{int} - k_{17}EH_{int} + k_{18}EH_{ext}$$

$$\frac{d}{dt}E_{ext} = -k_1E_{ext} + k_2EH_{ext} - k_9E_{ext}\frac{Drug_{ext}}{VolFactExt} + k_{10}ED_{ext} + k_{19}E_{int} - k_{20}E_{ext}$$

$$\frac{d}{dt}E_{int} = -k_3E_{int} + k_4EH_{int} - k_{11}E_{int}\frac{Drug_{int}}{VolFactInt} - k_{12}ED_{int} - k_{19}E_{int} + k_{20}E_{ext}$$

$$\frac{d}{dt}EHD_{ext} = k_5ED_{ext} - k_6EHD_{ext} + k_{13}EH_{ext}\frac{Drug_{ext}}{VolFactExt} - k_{14}EHD_{ext} + k_{23}EHD_{int} - k_{24}EHD_{ext}$$

$$\frac{d}{dt}EHD_{int} = k_7ED_{int} - k_8EHD_{int} + k_{15}EH_{int}\frac{Drug_{int}}{VolFactInt} - k_{16}EHD_{int} - k_{23}EHD_{int} + k_{24}EHD_{ext}$$

$$\frac{d}{dt}ED_{ext} = -k_5ED_{ext} + k_6EHD_{ext} + k_9E_{ext}\frac{Drug_{ext}}{VolFactExt} - k_{10}ED_{ext} + k_{21}ED_{int} - k_{22}ED_{ext}$$

$$\frac{d}{dt}ED_{int} = -k_7 ED_{int} + k_8 EHD_{int} + k_{11} E_{int} \frac{Drug_{int}}{VolFactInt} - k_{12} ED_{int} - k_{21} ED_{int} + k_{22} ED_{ext}$$

$$\frac{d}{dt}EHH_{ex} = k_{25} EHH_{int} - k_{26} EHH_{ext} + k_{27} EH_{ext} - k_{28} EHH_{ext}$$

$$\frac{d}{dt}EHH_{int} = -k_{25} EHH_{int} + k_{26} EHH_{ext} + k_{29} EH_{int} - k_{30} EHH_{int}$$

$$\frac{1}{VolFactExt}\frac{d}{dt}Drug_{ext} = -k_5 ED_{ext} + k_6 EHD_{ext} + k_9 E_{ext} \frac{Drug_{ext}}{VolFactExt} - k_{10} ED_{ext}$$
$$+k_{21} ED_{int} - k_{22} ED_{ext} - k_{25} EHH_{int} + k_{26} EHH_{ext} + k_{29} EH_{int}$$
$$-k_{30} EHH_{int}$$

$$\frac{1}{VolFactInt}\frac{d}{dt}Drug_{int} = -k_7 ED_{int} + k_8 EHD_{int} + k_{11} E_{int} \frac{Drug_{int}}{VolFactInt} - k_{12} ED_{int}$$
$$-k_{21} ED_{int} + k_{22} ED_{ext} - k_{25} EHH_{int} + k_{26} EHH_{ext} + k_{29} EH_{int}$$
$$-k_{30} EHH_{int} \quad (2)$$

where the species are labeled as in Figures 2 and 3 and the rate constants (k_1 - k_{30}) are defined in Table 1. *VolFactInt* and *VolFactExt* represent conversion factors between the units of the EmrE species (molecules/decimeters^2) within the 2-dimensional surface of the liposome and the interior/exterior aqueous drug concentration (M). We ran sets of simulations using different combinations of rate constants as described for each experiment in Table 3 and the initial

conditions listed in Table 2. All simulations were run until the system reached steady state, as determined when the internal drug concentration changed by less than 1 in 1000 over the final 5% of the run.

Parameters, such as liposome size, protein:lipid ratio, and surface area of the membrane, are based on our previously-published liposomal-flux assays [24]. The initial conditions were also set to mimic those experimental transport assays with the pH gradient set to higher $[H]^+_{int}$ (lower pH_{int}), providing an outward driving force of protons. We set initial drug concentrations inside/outside the liposome to be identical ($[Drug]_{ext} = [Drug]_{int}$) and then assessed net transport by monitoring which direction the drug moved in response to the pH gradient and other conditions in each simulation. Net transport is reported using the final value of the parameter T_r,

$$T_r = \frac{[Drug]_{int}}{[Drug]_{ext}} \qquad (3)$$

where $[drug]_{ext}$ and $[drug]_{int}$ represent the free drug concentrations inside/outside the virtual proteoliposome once steady state was reached. EmrE-bound drug is excluded from the T_r calculation. T_r starts at 1, and a value of $T_r > 1$ (< 1) indicates net movement of drug into (out of) the liposome during the simulation. Since the pH gradient drives outward H^+ movement, $T_r > 1$ reflects net antiport of H^+/drug, while $T_r < 1$ reflects net symport of H^+/drug.

Constraints and simplifying assumptions. In buffered drug-monitored liposomal transport assays [30] and in live cells[31], the proton motive force remains relatively constant. Therefore, we make the simplifying assumption of infinite buffering, such that internal/external proton concentration remains constant throughout the simulation.

The model is also simplified by thermodynamic principles and assumptions we make based on experimental data for EmrE. In the 8-state (Figure 3) and 10-state models (Figure 2), there are a total of 24 and 30 rate constants, respectively (Table 3). The thermodynamic cycle

constrains drug and proton binding ($pK_a^1 + pK_d^2 = pK_d^1 + pK_a^D$), reducing the number of independent rate constants.

We imposed three additional constraints based on experimental observations for EmrE: (1) rate constants for substrate-on and proton-on are diffusion-limited and uniformly constant (Figure 5.A) [25,32], (2) all on- and off-rate constants are identical for open-in and open-out conformations, which is true for EmrE due to its unique antiparallel topology and identical open-in and open-out structures (Figure 5.B) [26], and (3) rate constants for alternating-access are equal for open-in to open-out and open-out to open-in (Figure 5.C) [25,26,28]. It is important to note that these rate constants were all measured for EmrE in the absence of any proton gradient or transmembrane voltage, and the last two constraints may not reflect the behavior of EmrE in the presence of transmembrane gradients. Altogether, these thermodynamic and EmrE-based constraints reduce the total free parameters to 8 for the 8-state model and 10 for the 10-state model, simplifying this initial exploration of the free exchange model.

Investigating the requirements for coupled symport and antiport in the 8-state model. To test how much changing the value of the alternating-access rates alone could bias transport toward symport or antiport, we varied the alternating-access rate constants from 1 s^{-1} to 100 s^{-1} while holding the proton-off rate-constants at 1000 s^{-1} and drug-off rate-constants at 1 s^{-1} (Table 3, column 1). We defined a ratio for alternating-access rate constants (Figure 6.A) to determine the degree of bias towards antiport or symport,

$$R_{AA} = \frac{k_{AA}^{Antiport}}{k_{AA}^{Symport}} \qquad (4)$$

Where

$$k_{AA}^{Antiport} = k_{AA}^{EH} = k_{AA}^{ED} \qquad (5)$$

$$k_{AA}^{Symport} = k_{AA}^{E} = k_{AA}^{EHD} \qquad (6)$$

R_{AA} < 1 favors flux through the E and EHD states and thus symport, while R_{AA} > 1 favors flux through the EH and ED states and thus antiport. To reduce the number of parameters, a single antiport alternating access rate was used for both antiport states, and a single symport alternating access rate was used for both symport states according to simplify parameter space. This coupling of the antiport and symport rates results in the best-case scenario for drug and proton coupling at a given R_{AA}.

To test how much changing the value of the substrate-off rate constants alone could favor symport or antiport phenotypes, we varied proton-off rate constants from 1 - 1,000,000 s^{-1} and drug-off rate constants from 0.01 – 10,000 s^{-1} (such that pK_a values ranged between 4.0 - 10.0 and K_d values ranged from nM to mM, respectively) while holding alternating-access rate constants uniformly constant at 1, 10, or 100 s^{-1} such that R_{AA} = 1 (Table 3, column 2). To maximize coupling efficiency and reduce the dimensionality of the parameter space within the constraints of the thermodynamic cycles, we imposed k_{off}^{ED} / $k_{off\ D}^{EHD}$ = k_{off}^{EH} / k_{offH}^{EHD} (Figure 6.B) and defined this ratio as R_{off}:

$$R_{off} = \frac{k_{off}^{ED}}{k_{off\ D}^{EHD}} = \frac{k_{off}^{EH}}{k_{off\ H}^{EHD}} \qquad (7)$$

R_{off} > 1 favors flux through E and EHD states and thus symport, while R_{off} < 1 favors flux through EH and ED states and thus antiport.

Finally, to test whether off-rate constants and alternating-access rate constants were additive or synergistic, we varied both R_{off} and R_{AA} (Table 3, column 3). Alternating-access rate constants were set at 1, 2, 3, 4, or 5 s^{-1} to span 0.125 ≤ R_{AA} ≤ 5.

Modeling the effect of a second protonation event. The liposomal assay simulations were repeated using the 10-state model, which includes a second protonation event. Since protonation is sequential, this model includes an additional constraint that the first proton binds

with higher affinity than the second proton, $pK_a^1 \geq pK_a^2$. This negative linkage between two proton binding events is expected for two protonation sites in close proximity within a hydrophobic environment, as observed for EmrE [25]. We again varied substrate-off rate constants, with simulations performed for 6 values of pK_a^2 (Table 3, column 4). All alternating-access rate constants were held constant at 1 s^{-1}.

Investigating influence of environmental pH on transport. Our initial simulations all utilized an inverted-physiological pH parameter with lower pH on the inside of the membrane to mimic our liposomal flux assays [24]. However, to explore how pH affects transport under conditions more closely aligned to the environment of a transporter in the bacterial inner membrane, we performed additional simulations holding pH_{int} = 7.4 while varying pH_{ext} ±2 units (pH_{ext} = 5.4 - 9.4). This was tested in both the 8-state model and 10-state model to see if the extent of drug transport drug differed depending on the number of proton binding events. For the 8-state model, we used an antiport configuration with R_{AA} = 10 and R_{off} = 0.1 (Table 3, column 5); for the 10-state model, we used rates estimated for EmrE interacting with the substrate TPP^+ (Table 3, column 6) [24].

Investigating how a single transporter can act as both an antiporter and a symporter. For these simulations, we varied the drug-dependent rate constants while holding constant the protein-specific rate constants. Rate constants that vary with the identity of the transported drug include drug-off (k_{off}^{ED}, $k_{off\ D}^{EHD}$), proton-off for the drug-bound state ($k_{off\ H}^{EHD}$), and alternating-access rate constants in the ED and EHD states (k_{AA}^{ED}, k_{AA}^{EHD}). Protein-specific variables are invariant to drug identity and include alternating-access rate constant in the apo, singly-, and doubly-protonated states (k_{AA}^{E}, k_{AA}^{EH}, k_{AA}^{EH}) as well as proton-off rate constants (k_{off}^{EH}, k_{off}^{EHH}, which dictate pK_a^1 and pK_a^2, respectively). We ran simulations scanning through physiological ranges for k_{off}^{ED}, k_{off}^{EHD}, k_{AA}^{ED}, and k_{AA}^{EHD} for two different pK_a combinations: pK_a^1 = 8.2 and pK_a^2 = 7.0, representing WT EmrE (Table 3, column 7), and pK_a^1 = 7.0 and pK_a^2 = 5.0, representing a

mutant with pK_a values downshifted toward more typical glutamate pK_a values (Table 3, column 8). T_r was used to assess whether the downshifted mutant permitted both antiport and symport upon changes to drug-dependent rates. These experiments followed pH conditions for liposomal transport assays.

Supplemental information

The supplemental information includes the matrix form of the differential equations (equations 1 and 2) as well as the MATLAB files for the kinetic model. All of the MATLAB files needed to run the kinetic simulations, including the specific parameters used to produce each of the figures in this paper are deposited on github at https://github.com/granthussey/EmrE-Modeling.git.

Results

Building mass-action kinetic models of free exchange. Our 8-state model includes all states required to describe both coupled antiport and coupled symport of one proton and one drug (Figure 3.B and 3.C), while our 10-state model includes the experimentally observed states required to describe two-proton-coupled transport by EmrE (Figure 2). Both models contain three types of rate constants that determine net transport phenotype: substrate-on rate constants, substrate-off rate constants, and alternating-access rate constants. These are constrained three different ways based on observations of EmrE. First, we assume that (1) substrate on-rates are diffusion-limited [32] (Figure 5.A). For EmrE, all drug-substrates studied in detail have similar on-rates and the off-rate determines each binding affinity, which ranges over five orders of magnitude [32,33]. Similarly, we assume that proton on-rate is uniformly constant and diffusion-limited, and off-rate determines pK_a [25,32]. Next, since EmrE has an antiparallel topology that results in identical open-in and open-out conformations [25], we assume that (2) binding affinities (and thus on- and off-rates) are identical for open-in and open-out states (Figure 5.B) and that (3) alternating-access rates are equal in both directions (Figure 5.C) [25,26,28]. As a result,

substrate-off rate constants and alternating-access rate constants are the two groups of rate constants that are variable parameters in our simulations.

We model EmrE reconstituted in a virtual proteoliposome with infinite buffering both inside and outside, resulting in constant pH throughout the simulation. Each simulation is run using a particular set of rate constants (see Table 1) for the microscopic steps in the transport mechanism. The same initial conditions are used unless otherwise noted, with pH lower inside than outside to creating a pH gradient that will drive protons out of the liposome (see Table 2). Each simulation continues until steady state is reached, as assessed by monitoring the change in $[Drug]_{int}$ over time. Different experiments comprise sets of simulations (Table 3) that probe the influence of pH, alternating-access rates, and substrate off-rates on the final drug gradient achieved at steady state. The direction and extent of the drug gradient is assessed using the ratio of , T_r (Equation 3), where $T_r < 1$ represents movement of drug out of the liposome (net symport) while $T_r > 1$ represents movement of drug into the liposome (net antiport). For perfectly-coupled stoichiometric transport, the steady state T_r is empirically calculated from the initial proton gradient and the integer coupling stoichiometry constant *n* [14]:

$$T_r^{max} = \left(\frac{[H_{int}]^+}{[H_{ext}]^+}\right)^n \qquad (8)$$

In our model, T_r at steady state is determined by ΔpH and the relative values of the rate constants. It is independent of the exact value of the initial drug concentration, which affects the *rate* at which steady state is achieved but not the steady state T_r. Comparing the T_r for each simulation to T_r^{max} provides insight on how tightly coupled the net transport process is. We defined transport as "highly-coupled" if the T_r for that simulation was at least 80% of T_r^{max}. For example, for the 8-state model with $n = 1$, T_r^{max} would be 10.0 (0.1) for antiport (symport), with highly coupled transport defined as T_r greater than 8 (antiport) or less than 0.125 (symport).

Requirements for highly-coupled transport of one H^+ and one substrate. Figure 3 depicts the antiport and symport pathways within the 8-state model. While multiple pathways exist for both modes of transport, each contain key transitions that couple proton and drug flux across the membrane: alternating access in the EH and ED states for antiport, or the E and EHD states for symport. For a complete cycle of antiport, EH must alternate access to translocate bound proton in one direction while ED must alternate access to translocate drug in the opposite direction. Similarly, a complete cycle of symport requires alternating access of EHD to simultaneously translocate bound drug and proton in one direction before alternating access of E returns the empty transporter to the opposite side. These are exactly the states where alternating access occurs in the single-pathway, tightly-coupled transport models shown in Fig. 1.

If all rate constants in the free exchange model are equal, all pathways are equally likely, and the transporter simply facilitates downhill diffusion of both proton and drug. To achieve coupled transport, rate constants must be skewed to tip the balance between transport regimes by increasing the relative flux through the key transitions for antiport or symport. We hypothesized that this could be accomplished through manipulating the rates for substrate-off and/or alternating access. Varying the alternating-access rate constants will directly impact the relative frequency of these transitions that are critical for moving substrate across the membrane. On the other hand, varying substrate-off rate constants alters the partitioning between futile substrate binding and release and productive movement of molecules across the membrane via the key alternating-access transitions. We explored the independent and combined effects of substrate-off rates and alternating-access rate through three experiments to explore the transport behavior of the free-exchange model.

In the first set of simulations, alternating-access rate constants were varied around a physiological range while holding proton off-rate constants at 1000 s^{-1} and drug off-rates constants at 1 s^{-1} for all states of the transporter (Table 3, column 1). Alternating-access rate

constants were grouped according their contribution to antiport or symport and covaried to reduce the number of free variables within the model. We examined how shifting the ratio R_{AA} (Equation 4) of the key alternating-access rate constants (Equations 5 and 6) affected T_r. For values of $R_{AA} > 1$, the key antiport states alternate access faster, while for $R_{AA} < 1$ this is true for the key symport states. Figure 7.A shows the relationship between R_{AA} and T_r. To reach the 80% T_r^{max} benchmark for highly-coupled transport, the alternating-access rates need to be skewed 25-fold in either direction: $R_{AA} \geq 25$ for antiport or $R_{AA} \leq 1/25$ for symport. This reveals the expected symmetry within the 8-state free-exchange model—whatever degree of biasing is required for highly-coupled antiport is the inverse of what is required for highly-coupled symport.

In the second set of simulations, we varied substrate off-rate constants across the range of values observed for EmrE substrates while holding alternating-access rates constants uniformly at 1, 10, or 100 s^{-1}, resulting in a single k_{AA} value for all alternating access transitions (Table 3, column 2). To minimize the number of free variables needed for simulation, we varied the substrate off-rate constants critical to either antiport (k_{off}^{EH} and k_{off}^{ED}) or symport ($k_{off\,H}^{EHD}$ and $k_{off\,D}^{EHD}$) such that $k_{off}^{ED} / k_{off\,D}^{EHD} = k_{off}^{EH} / k_{off\,H}^{EHD}$ (Figure 6.B). We then examined how shifting the ratio of these rate constants (R_{off}, Equation 7) affected transport. For $R_{off} < 1$, the antiport-critical states have slower off-rates and higher stability than the symport-critical states, indicating competitive binding between drug and proton as expected for antiport. For $R_{off} > 1$, this is inverted, and drug and proton bind cooperatively. Similar to the R_{AA} experiment, T_r was calculated for each value of R_{off} (Figure 7.B). Although $R_{AA} = 1.0$ and neither symport nor antiport is directly favored by the alternating access steps in the transport cycle, alternating-access rates *do* affect transport behavior when they are the same order of magnitude as drug and proton off-rates. If alternating access is fast, then alternating access is less likely to result in coupled movement of molecules across the membrane. This is particularly important for symport, where both substrates must bind on one side of the membrane and be released on the

other side. Thus, at faster alternating access rates (Fig 7.B, orange and yellow lines), the antiport and symport phenotypes are no longer symmetric (inverting R_{off} does not result in inverted T_r), as symport is less well-coupled. At slower alternating access rates, this symmetry is restored. When k_{AA}=1 s^{-1}, 80% T_r^{max} is achieved by 630-fold off-rates bias in either direction ($R_{off} \leq 1/630$ for antiport or $R_{off} \geq 630$ for symport).

In the third set of simulations, we varied both R_{off} and R_{AA}. Figure 7.C shows T_r as a function of R_{off} similar to the second set of simulations, however each curve now represents a different R_{AA} value (Table 3, column 3). With 5-fold skewing of alternating-access rate constants (Figure 7.C, green line), only a 23-fold difference in the substrate off-rate constants is needed to achieve 80% T_r^{max}, much less than the 630-fold-difference required if alternating-access rates are uniformly held at 1 s^{-1} (Figure 7.B). This result demonstrates that the combined effects of alternating-access and substrate off-rates synergize non-linearly such that robust proton-coupled transport phenotypes can be achieved without the need for highly skewed rates. In other words, highly-coupled transport does not require states or pathways to be excluded from the transport model. Only relatively modest biasing of rate constants channels the majority of flux through key pathways and achieves relatively well-coupled transport.

Modeling the transport cycle of EmrE. EmrE requires a more complex transport mechanism due to its ability to perform two-proton coupled antiport (Figure 2). Since there is no evidence that EmrE can simultaneously transport drug and two protons, the 10-state model introduces an asymmetry. Whereas the 8-state model possesses a maximum of 1 coupled proton per drug (*n* = 1, Equation 8) for both antiport and symport, the 10-state model increases *n* for antiport to *n* = 2, while symport remains at *n* = 1. In other words, an initial 1.0 pH unit gradient can now drive a maximum 100-fold drug gradient (T_r = 100) via antiport but can still only drive a maximum 10-fold drug (T_r = 1/10) gradient via symport. In effect, this extra protonation event creates a new

key antiport state, EHH, that cannot contribute to symport. We explored how this asymmetry affects the distribution of transport outcomes.

Since the second protonation event introduces an additional proton off-rate (k_{off}^{EHH}) we repeated the experiment varying R_{off} (Figure 7.B, blue trace) but over six different values of this newly-introduced proton off-rate (Figure 8). Proton on-rates are assumed to be diffusion limited and constant at 10^{10} s^{-1}, so this is recapitulated as six curves of different pK_a^2 values for the second protonation event (Table 3, column 4). Protonation appears to be sequential in EmrE, thus requiring $pK_a^1 \geq pK_a^2$ [25]. This restricts the parameter space, resulting in the gray portion of Figure 8 (for example, if $pK_a^2 = 9$, pK_a^1 can only range from 9 – 10). At low pK_a^2 values, the second protonation event is rare, and the 10-state model greatly resembles the 8-state model (Figure 8, overlapping orange and blue lines). However, as the value of pK_a^2 rises above 7, the EHH state becomes populated and transitions through this state contribute to net flux, resulting in increasing domination of antiport phenotypes. In fact, as pK_a^2 approaches 9, the system starts to resemble a stoichiometric transport model, where perfect competition yields perfectly coupled antiport. Thus, the second protonation event biases the transporter toward antiport under these particular conditions with only ΔpH and no membrane potential.

Effect of pH on steady state transport phenotypes. Next, we examined the influence of environmental conditions on net transport. In our simulations, the energy required to drive coupled transport is stored in the proton gradient. For perfectly-coupled stoichiometric transport, a given ΔpH will drive a set substrate gradient according to Equation 8. However, in free-exchange transport, the degree of proton/drug coupling is inherently influenced by the exact internal and external pH values. As proton on-rates depend on both the proton-on rate constant and the proton concentration, a change in pH affects the distribution of the key states and the partitioning between different pathways. Thus, even for a constant ΔpH, a change in mean pH alters the balance of antiport, symport, and uncoupled uniport.

To investigate this phenomenon, we ran simulations in the 8-state and the 10-state model, holding the rate constants while varying pH. The rate constants were chosen to favor antiport using EmrE-like rates for both models (Table 3, column 5 and 6, for the 8- and 10-state model, respectively). Internal pH was held at physiological levels (pH_{int} = 7.4) while external pH was varied either 2 units higher or lower. Figure 9 shows how the two models diverge in behavior. Once again, the 8-state model displays symmetric behavior, with an inverted pH gradient leading to an inverted T_r. Interestingly, this is not the case for the 10-state model, which drives a much larger drug gradient with an acidic external environment (drug efflux, left-hand side of Figure 9) than with a basic external environment (drug uptake, right-hand side of Figure 9). This reveals that a 10-state transporter is a better antiporter under physiological conditions than it is with an unnatural inverted pH gradient, providing a possible failsafe to resist backflow of drug into a cell when the cell is exposed to a basic external environment.

How an antiporter can become a symporter. The W63G point mutation of EmrE abolishes classical WT substrate specificity and replaces it with resistance to macrolide antibiotics like erythromycin. However, it also confers concentrative uptake of aliphatic polyamines into *E. coli* [34]. This combination of erythromycin export and polyamine import means that W63G-EmrE must switch transport direction based on substrate identity alone. While it is not experimentally resolved whether the polyamine import phenotype is the result of proton-coupled symport or results from uniport with positively charged polyamines driven into the cell by the negative-inside membrane potential, here we explore how a single transporter may switch between coupled antiport and coupled symport using the 10-state model.

For EmrE, the identity of the bound drug can change the alternating-access rate over nearly two orders of magnitude [33]. Additionally, EmrE can bind drug with affinities ranging over five orders of magnitude, with drug binding affinity determined by off-rate for those substrates that have been studied in detail [32], and the drug off-rate varies with protonation state of the

transporter [24]. Thus, we completed simulations varying all drug-dependent rate constants (k_{AA}^{ED}, k_{AA}^{EHD}, k_{off}^{ED}, $k_{off\,H}^{EHD}$, and $k_{off\,D}^{EHD}$) over reasonable physiological ranges around the known values for EmrE. Since pK_a^2 must be lower than 7 to allow for symport in the 10-state model, we ran two simulations (Table 3, columns 7 and 8): one with values estimated for WT EmrE (Figure 10.A, pK_a^1 = 8.2 and pK_a^2 = 7) and one with lower pK_a values (Figure 10.B, pK_a^1 = 7.0, pK_a^2 = 5.0) closer to what is expected for a glutamate residue in aqueous solution. These figures are graphed in 2-D space by collapsing alternating-access rates and drug/proton off-rates as ratios. As expected, no combination of drug-induced rates can drive symport when using values estimated for WT EmrE (Figure 10.A) under these conditions. However, with sufficient lowering of both pK_a values, coupled antiport and symport *can* coexist in a single transporter (Figure 10.B). This simple scheme allows for the identity of transported drug to determine the type proton-coupled transport, a striking result.

Discussion

Transporters have been traditionally classified as either antiporters, symporters, or uniporters. Mechanistic models of transporters generally reflect these strict classifications, and only include pathways that allow for stoichiometric coupled transport [5,7,11]. Recently, improved experimental methods applied to a broader set of transporters have revealed that some transporters cross these boundaries and do not fit cleanly within a single class [14,17–19,24]. In light of this, a new generalized model of transport is required that can simultaneously accommodate all transport modes. We initially developed an unrestricted “free-exchange model” to account for all the observed states and transitions of EmrE [24]. The free exchange model theoretically allows this proton-coupled drug efflux pump to perform antiport, symport, and uniport. Here, we have shown that such an unrestricted model can describe the antiport phenotype seen in EmrE (Figure 10.A), and in fact the second proton binding event favors antiport (Fig. 8) and enhances the efficiency of antiport relative to symport under these simple ΔpH-only conditions (Fig. 9).

These simulations can also recapitulate the curious phenotype of W63G [34], a point mutant of EmrE in which transport direction reverses based on the identity of the transported drug (Figure 10.B).

Most importantly, we have shown that both highly coupled transport can be achieved in the free-exchange model with minimal biasing of rate constants (Figure 7, 8). The simulations also show that the particular combination of rate constants may result in a transporter that has robust behavior that does not change under different environmental conditions or may switch transport behavior with changing environmental conditions (Fig. 9). This demonstrates the utility of a free-exchange model for systems requiring consideration of “minor” states/transitions and demystifies how substrate and ion can be coupled without restrictions on transporter states and transitions. Nevertheless, free exchange transport is inherently less energetically efficient than stoichiometric transport mechanisms. Here, we consider the potential benefits of a free-exchange model in comparison with a traditional tightly-coupled mechanism to begin to understand why some transporters appear to follow each type of mechanism.

Evolution. Evolution selects for coupling tailored to the needs of a particular biological system [35]. For example, mammals regulate sugar availability at the organismal level. Consequently, the mammalian GLUT family of hexose transporters function as sugar uniporters, with a few tissue-specific exceptions. In contrast, microbes often have to survive in environments with unpredictable nutrient availability. Thus, many microbial homologs of the GLUT transporters appear to be tightly coupled sugar/proton symporters, allowing efficient concentrative sugar import [36–38]. Interestingly, the GLUT homolog GlcP from *Staphylococcus epidermidis* appears to represent an intermediate case. It employs a free exchange mechanism to perform both proton-coupled sugar symport and sugar uniport depending on external pH [17]. These examples of sugar transporters demonstrate how each have likely evolved to maintain the degree of coupling sufficient for their function in the host organism.

While sugar symporters represent an instance where imperfect coupling is sufficient, loose coupling may be required for multidrug antiporters. Observations of ATP-driven multidrug transporters reveal that futile cycles of ATP-hydrolysis occur between productive drug efflux events, and that this may be a trade-off required to achieve multidrug recognition [39,40]. Thus, it was predicted that proton-driven multidrug transporters may also sacrifice efficiency to achieve multidrug recognition [41,42]. The ability to export diverse toxic substrates is critical to ensure survival, and thus would be favored evolutionarily, even at the expense of perfect efficiency. A second potential advantage of a free exchange mechanism involves efficient substrate release. Multidrug transporters recognize and transport chemically diverse molecules, and the binding affinities (and thus off-rates) can range over five orders of magnitude in the case of EmrE [33]. This presents an issue for tight binding substrates, where slow off-rates may cause tight binding substrates to become “stuck” on the transporter if not for the ability to simultaneously bind proton, which reduces the affinity and enhances the drug off-rate. This idea is supported by Gillespie simulations of EmrE that can resolve the exact pathways for transport [24]. This flexibility is not possible in pure-exchange models of transport (Figure 1) but is possible within the free exchange (Figure 2.B, 3), and may be a property that is selected for by evolution, by enabling continued efficient transport of toxins out of the cell.

Even for transporters with apparently perfect stoichiometric transport like LacY, single point mutations can produce leak pathways [8,20,21]. The fine-tuning required to achieve stoichiometric transport in naturally occurring transporters may help to explain the relatively loose coupling exhibited by the *de novo* designed zinc/proton exchanger Rocker [43]. However, this suggests there may be a low barrier for evolution from a tightly- to a loosely-coupled transport regime, and thus, tightly-coupled systems could become “scaffolding” to design new free-exchange transporters. In fact, this appears to have happened naturally in the small multidrug resistance transporter family [13].

Voltage in the proton-motive force. The proton motive force which drives proton-coupled transport *in vivo* includes both the proton gradient (ΔpH) and the transmembrane voltage (ΔΨ). Indeed, coupled antiport in EmrE can be driven by either ΔpH or ΔΨ alone or in combination [23,44,45]. One limitation of the current free-exchange model is that we only consider ΔpH and not ΔΨ. This choice was based on the availability of experimental measurements of rates for EmrE at different pH values, allowing us to more reliably model the effect of ΔpH. However, since alternating access moves both charged substrates and charged residues of EmrE across the membrane, alternating-access rates are certainly impacted by ΔΨ. In addition, the binding of charged substrates can be affected by voltage as well, if the binding process effectively moves a charged substrate partway down the voltage gradient [46]. Unfortunately, despite the ability of voltage gradients to drive transport, the effect of voltage on individual steps in the transport cycle is unclear [8]. New research probing the effect of voltage on all steps in the transport cycle is needed to elucidate how voltage influences the microscopic rate constants required to model transport.

Overall, modeling voltage presents new possibilities to predict transport under more conditions and explain some phenotypes of EmrE. For example, WT EmrE has been seen to move proton and drug in the same direction under voltage alone, suggesting the ability to reverse the flux of traditionally antiported substrates [24]. Voltage may also enhance the efficiency of electrogenic coupled transport by further biasing relative flux throughout certain pathways. For example, the negative-inside potential could speed up proton on-rates and slow proton off-rates on the periplasmic side of the membrane, resulting in faster turnover of drug. Overall, more complex phenotypes may occur when both ΔΨ and ΔpH are present. This is the subject of future effort in our lab to acquire the necessary kinetic data to expand the model to include voltage in a biologically relevant manner.

Conclusions

Research into free exchange models of transport has broad implication for protein design. By understanding the requirements for different transport regimes, and how to switch between them, researchers can design *de novo* transporters or manipulate existing transporters to switch behavior under different pH, drug, or other environmental conditions. Overall, our understanding of mechanisms not as a singular pathway but as a superposition of many possible outcomes allows us to further investigate the boundaries of transporters, understand the physiological behavior of these important proteins, and engineer novel systems.

Supplementary Materials

Code used for all numerical simulations is freely available on Github (https://github.com/granthussey/EmrE-Modeling).

Acknowledgements

This work was supported by NIH Grant R01GM0958339 to K.H.W., the Hilldale Undergraduate Research Fellowship to G.A.H., and NIH National Research Service Award T32 GM007215 to N.E.T. Additionally, we thank Hallie Hanson for assisting writing the code.

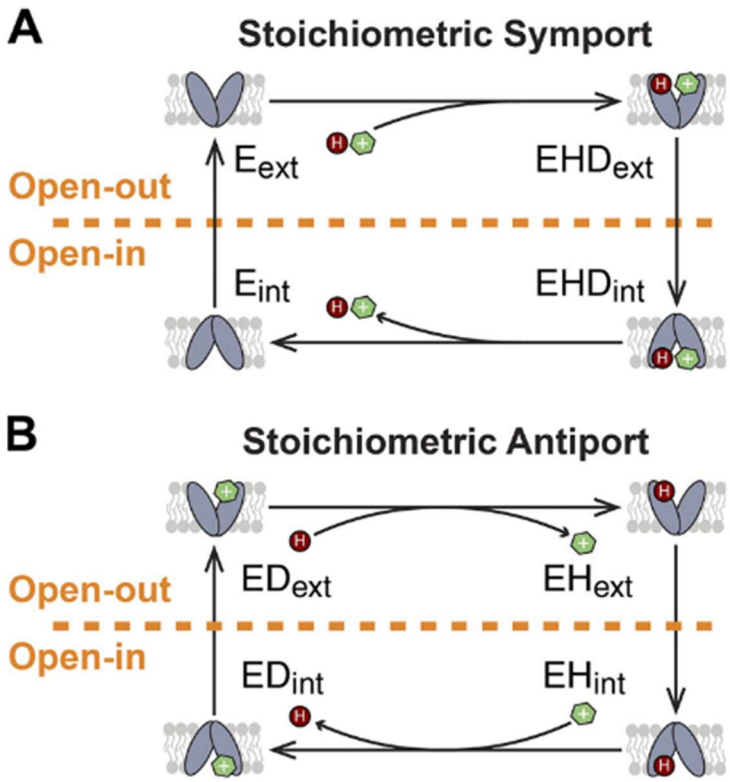

Figure 1: Stoichiometric models for secondary-active transport. Mechanistic descriptions of transport often depict only the major states and transitions contributing to stochiometric coupled transport of substrate and ion. Here, the transported substrate is represented as a cationic drug (green hexagon) and the driving ion is proton (dark red circle), while the transporter is shown in pale blue. (A) For symport, the transporter binds both drug and proton cooperatively and alternating access occurs in both this doubly-bound state and in the apo state. (B) For antiport, drug and proton cannot bind simultaneously and alternating access only occurs when the transporter is bound to either substrate (drug) or ion (proton).

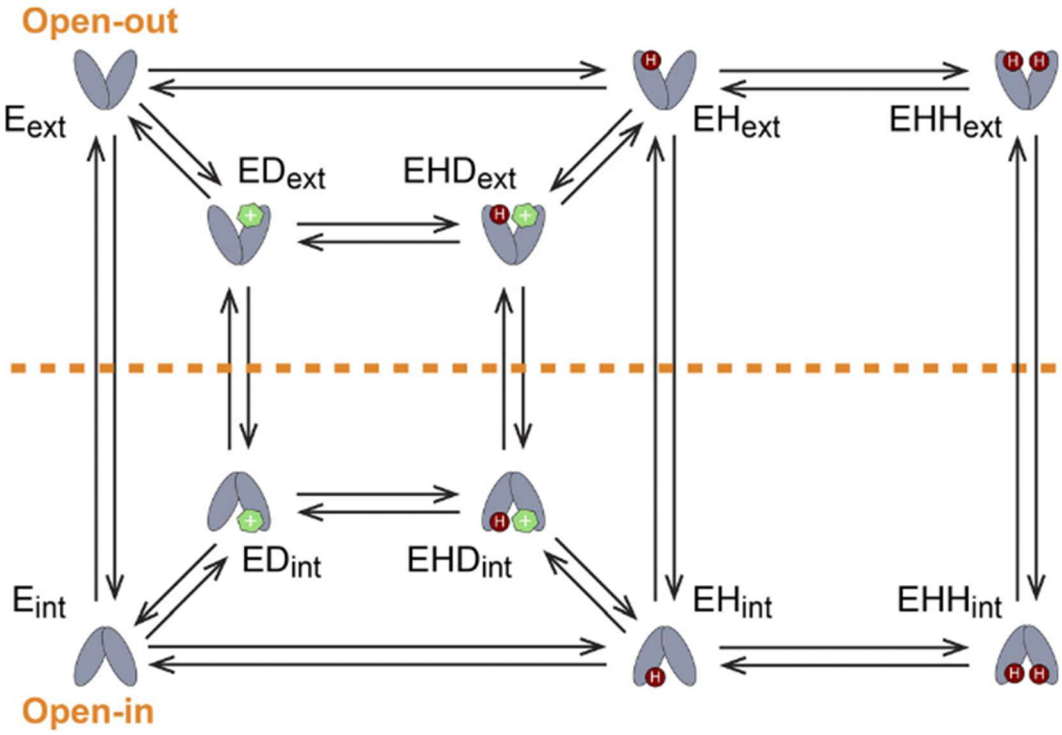

Figure 2: The 10-state free-exchange model of EmrE transport. All states and transitions observed for EmrE are incorporated into one unified model. Multiple pathways exist for proton-coupled antiport (2:1 or 1:1 proton/drug stoichiometry), proton-coupled symport, as well as uncoupled drug transport and uncoupled proton transport (leak). Colors are as in Fig. 1 and states are labeled (apo, E; proton-bound, EH; double-proton-bound, EHH; drug-bound, ED; and proton/drug-bound, EHD). The membrane is not shown for clarity due to the complexity of this model, but the states of the transporter open to either side of the membrane are separated by the orange dotted line and labeled with ext or int for open-out and open-in, respectively.

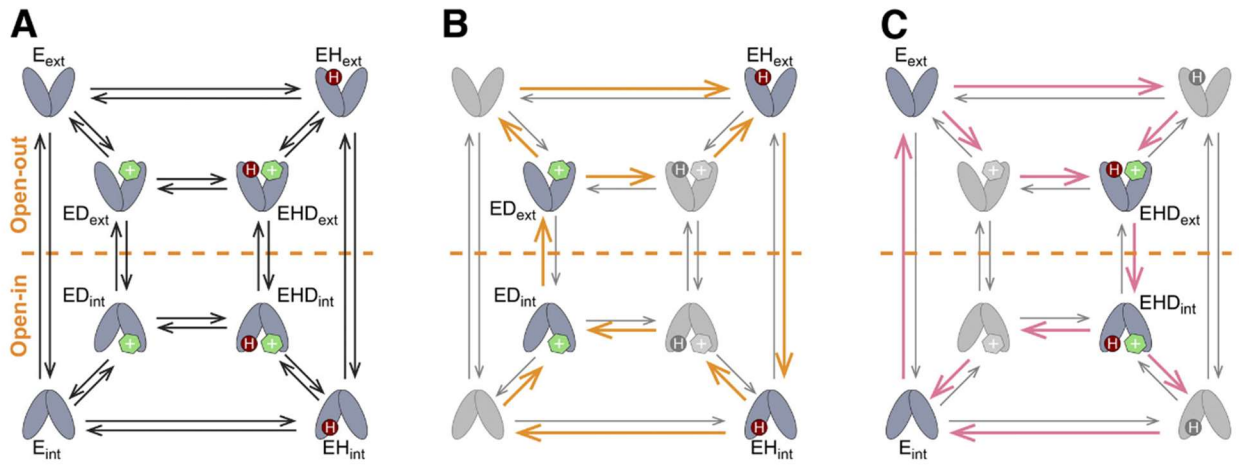

Figure 3: The 8-state free-exchange model of generalized transport. The transporter can assume four different binding states (apo, E; proton-bound, EH; drug-bound, ED; and proton/drug-bound, EHD). All states can perform alternating access. The pathways leading to antiport or symport are shown in B and C, respectively. In either case, proton and drug can bind in any order. However, different pairs of key states must alternate access to achieve coupled antiport (ED and EH) or coupled symport (E and EHD). Colors and labeling are as in Figures 1 and 2.

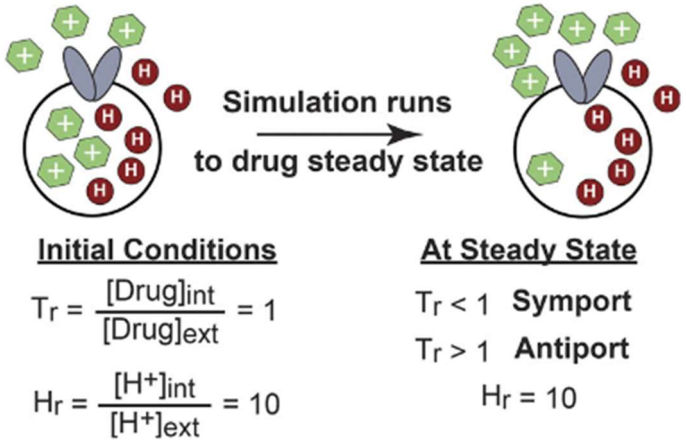

Figure 4: Simulated liposomal flux assay. Simulations are conducted as virtual liposomal flux assays. The simulation begins with a $_{10\text{-fold}}$ proton gradient and identical drug concentration inside and outside the proteoliposome. We assume infinite buffering capacity so the proton gradient, represented as H_r, remains constant throughout the simulation. Unless otherwise indicated, H_r is set at 10. The simulation is then run until the drug concentration reaches steady-state. Transport outcome is assessed by T_r, or the ratio of internal to external drug concentration at steady-state ($T_r = [Drug]_{int} / [Drug]_{ext}$).

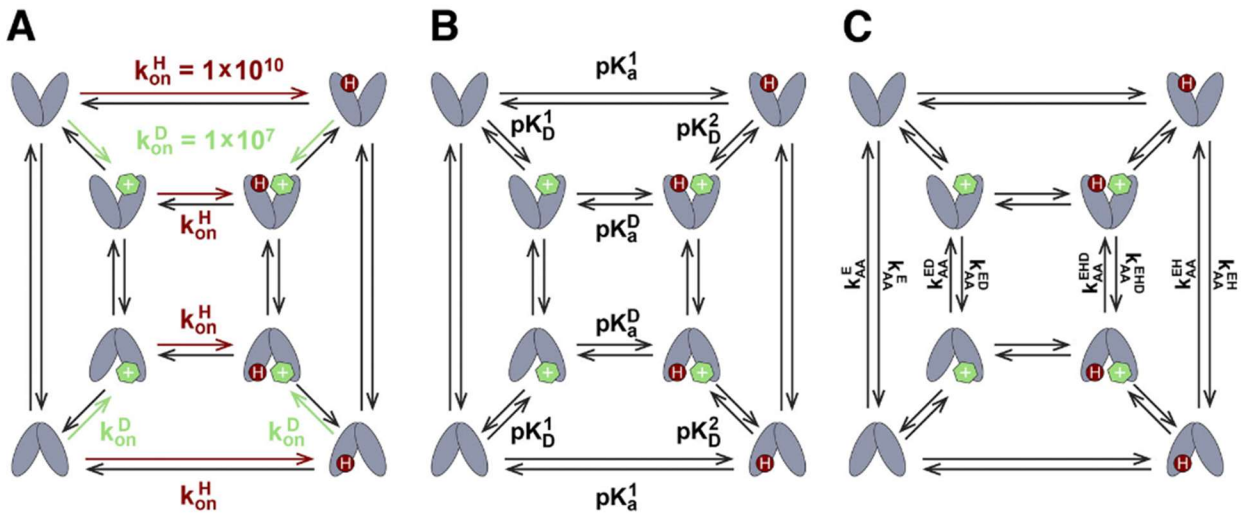

Figure 5: Constraints used in modeling transport. These constraints are based on experimental observations for EmrE. (A) Both drug- and proton-on rates are diffusion-limited and constant. (B) Binding affinities are the same for open-in and open-out conformations of the transporter. Additionally, these four values are constrained by the thermodynamic cycle (pK_a^1 + pK_D^2 = pK_D^1 + pK_a^D). (C) All alternating access rates are equal going in either direction. Colors are as in Figures 1, 2, and 3.

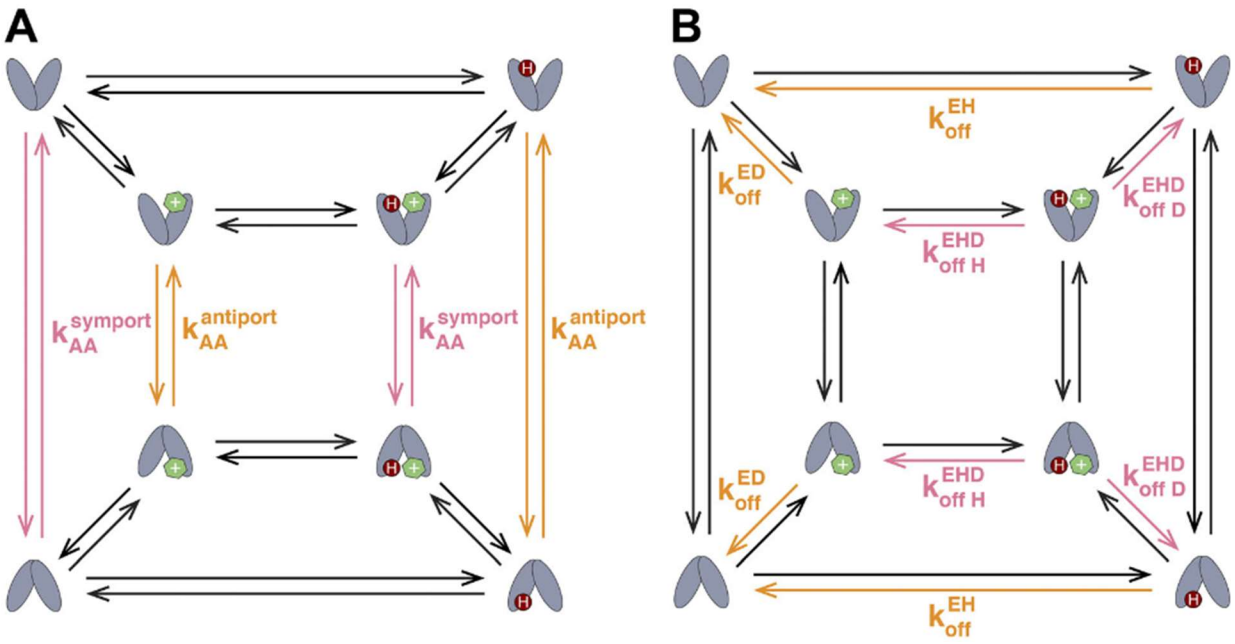

Figure 6: Certain key transitions predict dominance of transport phenotype. Free exchange includes all possible transport pathways in one model. To tip the balance of transport towards a single type of proton-coupled transport, rate constants need to favor one pathway over the others. (A) Alternating access rates directly influence coupling if the key transitions for antiport or symport pathways are faster. (B) Substrate off-rates indirectly influence transport by altering the partitioning between futile binding/release on one side of the membrane and productive transport of molecules through key alternating access transitions. Colors are as in Figures 1, 2, 3, and 5.

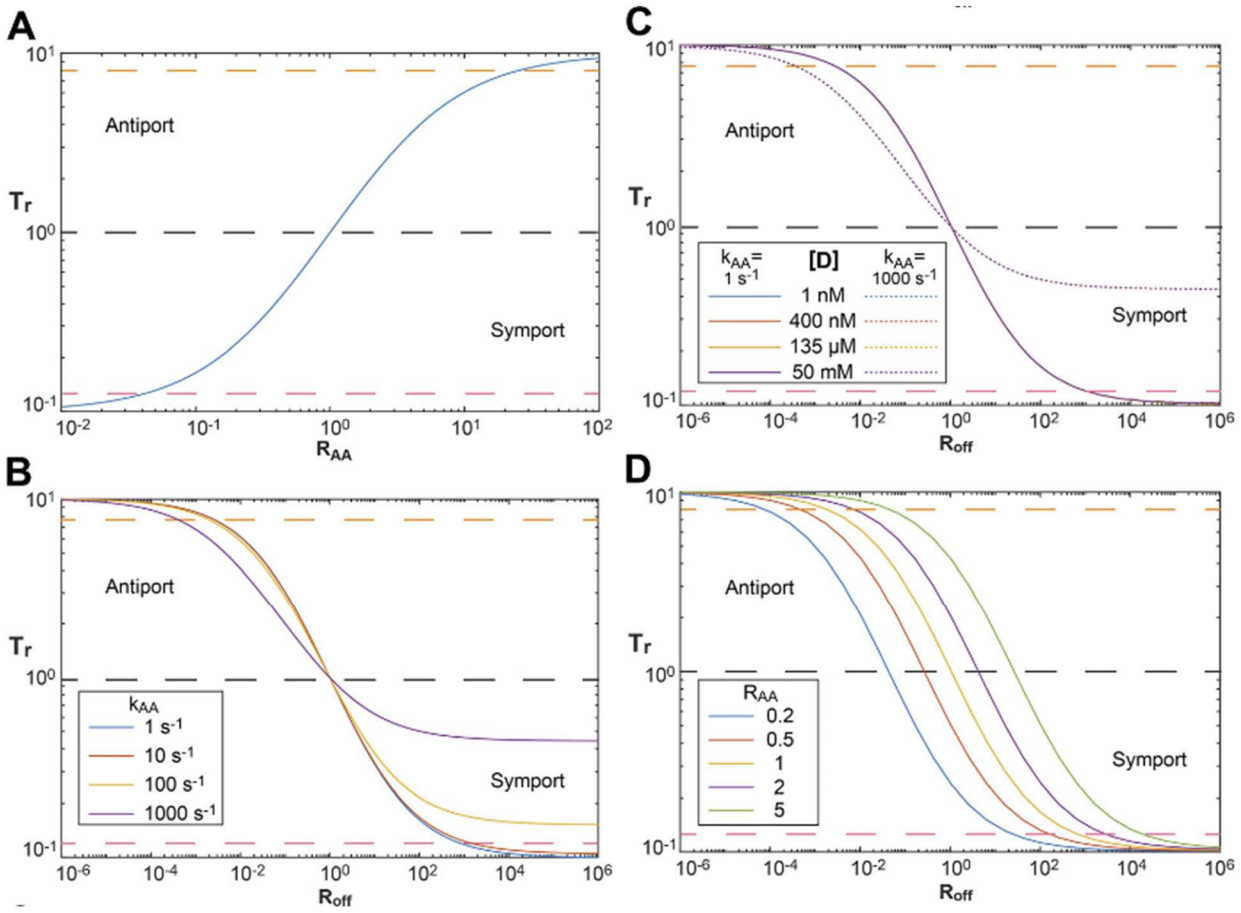

Figure 7. Rate bias is sufficient to achieve coupled transport in the 8-state model. Four sets of simulations explore the independent and combined effects of substrate off-rates and alternating access rates on drug gradient (T_r) observed at steady-state with a driving force ΔpH = 1. In the 8-state model, perfectly coupled transport will result in a 10-fold drug gradient at steady-state: T_r = 10 in the case of antiport and T_r = 0.1 in the case of symport. The orange dashed line represents 80% of the maximum coupling efficiency for antiport while the pink dashed line represents 80% of the maximum coupling efficiency for symport. (A) When only alternating access rates are varied, skewing the relative rates of alternating access in the states critical for symport or antiport pathways by 25-fold (R_{AA} = 25 for antiport and 1/25 for symport) achieves ~80% of the maximum coupling efficiency. R_{AA} is defined in Eqn. 4. (B) When only substrate off-rates are varied, skewing the relative substrate off-rates for symport- and antiport-

critical states by 630-fold (R_{off} = 630 for symport, 1/630 for antiport) is needed to achieve ~80% of the maximum coupling efficiency if the alternating access rates are sufficiently slow ($k_{AA} \leq 1\ s^{-1}$, blue line). If the uniformly constant alternating access rates are faster than about 10 s^{-1} (orange, yellow, purple lines), transport is less efficient and the antiport/symport phenotypes diverge in behavior. R_{off} is defined in Eqn. 7. (C) Steady-state transport phenotypes are independent of drug-concentration, regardless of alternating access rate. Lines for drug concentrations ranging from 1 nM to 50 mM lie on top of each other. (D) When both R_{off} and R_{AA} are varied simultaneously, less skewing of the relative rates is needed to achieve highly-coupled transport. The colored lines reflect the effect of varying R_{off} at different values of R_{AA} (R_{AA} = 0.2, blue; R_{AA} = 0.5, orange; R_{AA} = 1.0, yellow; R_{AA} = 2.0, purple; R_{AA} = 5.0, green). For all simulations, $k_{AA} = 1\ s^{-1}$. With R_{AA} = 5.0 favoring antiport (green), 80% of the maximum coupling efficiency is achieved with a ratio of off-rates of only R_{off} = 1/23.

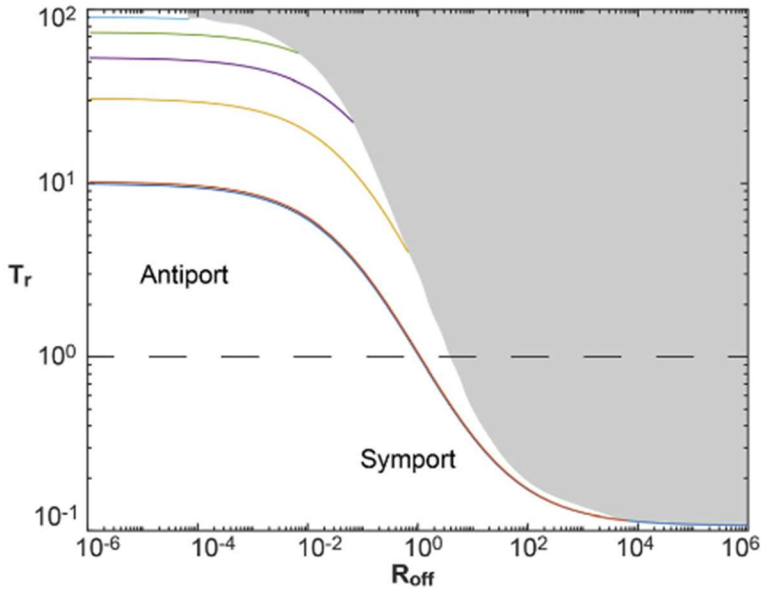

Figure 8. The 10-state model is biased towards antiport when driven solely by a pH gradient. We varied the second protonation value, pK_a^2, to examine how this parameter affects transport in the 10-state model. Here, pK_a^2 = 4, blue; 5, orange (overlapped with blue); 7, yellow; 7.5, purple; 8, green; and 9, cyan. Unlike the 8-state model, where inverting the rates for an efficient antiporter can produce an equally-efficient symporter, the 10-state model is asymmetric. The requirement that EmrE sequentially bind protons, requiring $pK_a^2 \leq pK_a^1$, restricts the sample space (gray area excluded). Although the blue and orange traces (pK_a^2 = 4 and 5, respectively) retain the behavior of the 8-state model, symport is not observed for $pK_a^2 \geq$ 7.0 for any value of R_{off} and the transporter approaches stoichiometric transport at high values of pK_a^2, reflecting a strong bias towards antiport for the 10-state model under these particular conditions and constraints.

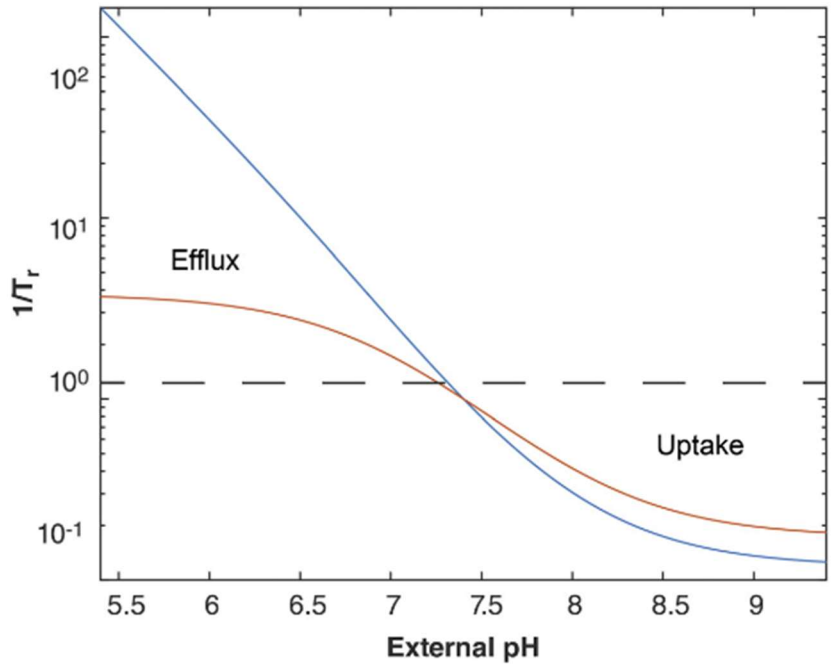

Figure 9. The 10-state model drives more efficient efflux than uptake under physiological conditions. Unlike other simulations, internal pH was held constant at a physiological value (pH_{int} = 7.4) while external pH was varied. For the 8-state model (orange trace, EmrE-like rates, Table 3), symmetric transport behavior is observed for external pH values above and below the internal pH of 7.4. In the 10-state model (blue trace, EmrE-like rates, Table 3), a much larger drug gradient is achieved when external pH is lower than internal pH.

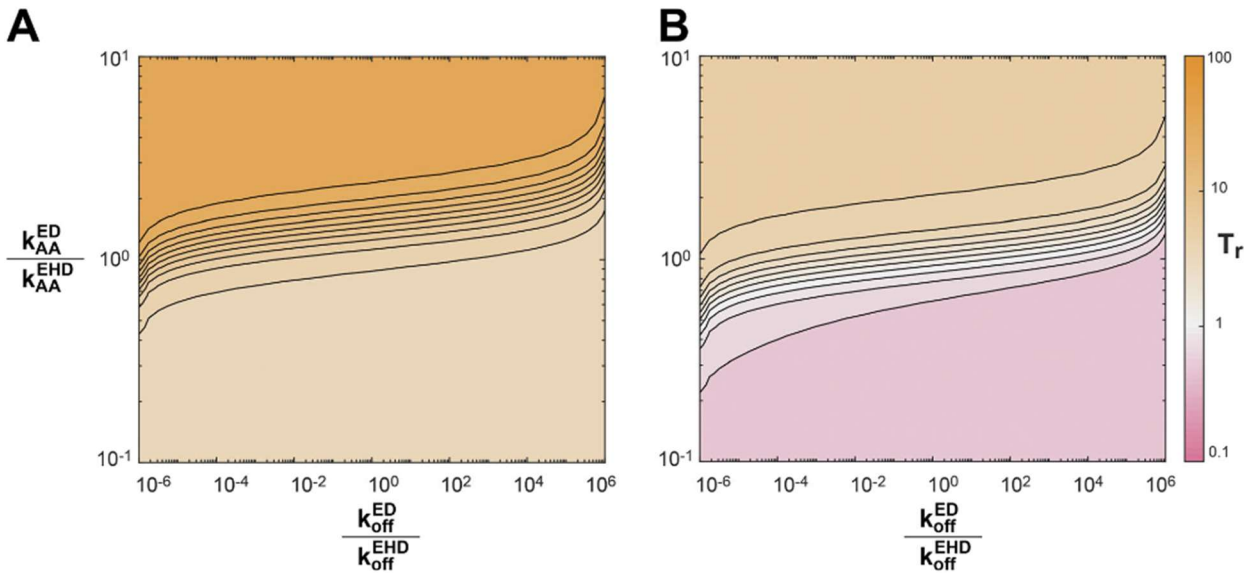

Figure 10. Drug identity can trigger a switch from efflux to influx. Four rate constants may vary depending on the identity of the transported drug (k_{off}^{ED}, k_{off}^{EHD}, k_{AA}^{ED}, and k_{AA}^{EHD}). We varied these rate constants over a physiological range to explore whether different combinations of these parameters (to mimic transport of different drugs) can induce both symport (T_r < 1, pink) and antiport (T_r > 1, orange) of different drugs by the same transporter. (A) Using pK_a values estimated for WT EmrE (pK_a^1 = 8.2 and pK_a^2 = 7), antiport dominates the parameter space regardless of drug-dependent rate constants when transport is driven by a pH gradient alone. (B) By lowering the pK_a values (pK_a^1 = 7.0, pK_a^2 = 5.0) for proton binding by the transporter, different values of the drug-dependent rate constants can result in either symport or antiport even though the transporter-specific parameters are held constant, reflecting the potential for a single transporter to perform both proton-coupled antiport and symport of different substrates.

Tables

Table 1. Rate constant definitions for the free-exchange model simulations.

Parameter (Unit)	Transition	Side of Membrane	Process	Physiological Value/Range
k1 (M^{-1} s^{-1})	Eext -> EHext	External	Proton-on*	1 x 10^{10}
k2 (s^{-1})	Eext <- EHext	External	Proton-off	1 - 1,000,000
k3 (M^{-1} s^{-1})	Eint -> EHint	Internal	Proton-on*	1 x 10^{10}
k4 (s^{-1})	Eint <- EHint	Internal	Proton-off	1 - 1,000,000
k5 (M^{-1} s^{-1})	EDext -> EHDext	External	Proton-on*	1 x 10^{10}
k6 (s^{-1})	EDext <- EHDext	External	Proton-off	1 - 1,000,000
k7 (M^{-1} s^{-1})	EDint -> EHDint	Internal	Proton-on*	1 x 10^{10}
k8 (s^{-1})	EDint <- EHDint	Internal	Proton-off	0.01 – 10,000
k9 (M^{-1} s^{-1})	Eext -> EDext	External	Drug-on**	1 x 10^{7}
k10 (s^{-1})	Eext <- EDext	External	Drug-off	0.01 – 10,000
k11 (M^{-1} s^{-1})	Eint -> EDint	Internal	Drug-on**	1 x 10^{7}
k12 (s^{-1})	Eint <- EDint	Internal	Drug-off	0.01 – 10,000
k13 (M^{-1} s^{-1})	EHext -> EHDext	External	Drug-on**	1 x 10^{7}
k14 (s^{-1})	EHext <- EHDext	External	Drug-off	0.01 – 10,000
k15 (M^{-1} s^{-1})	EHint -> EHDint	Internal	Drug-on**	1 x 10^{7}
k16 (s^{-1})	EHint <- EHDint	Internal	Drug-off	0.01 – 10,000
k17 (s^{-1})	EHint -> EHext	-	Alternating Access	1 - 100
k18 (s^{-1})	EHint <- EHext	-	Alternating Access	1 - 100
k19 (s^{-1})	Eint -> Eext	-	Alternating Access	1 - 100
k20 (s^{-1})	Eint <- Eext	-	Alternating Access	1 - 100
k21 (s^{-1})	EDint -> EDext	-	Alternating Access	1 - 100
k22 (s^{-1})	EDint <- EDext	-	Alternating Access	1 - 100
k23 (s^{-1})	EHDint -> EHDext	-	Alternating Access	1 - 100
k24 (s^{-1})***	EHDint <- EHDext	-	Alternating Access	1 - 100
k25 (s^{-1})***	EHHint -> EHHext	-	Alternating Access	1 - 100
k26 (s^{-1})***	EHHint <- EHHext	-	Alternating Access	1 - 100
k27 (M^{-1} s^{-1})***	EHext -> EHHext	External	Proton-on*	1 x 10^{10}
k28 (s^{-1})***	EHext <- EHHext	External	Proton-off	1 – 1,000,000
k29 (M^{-1} s^{-1})***	EHint -> EHHint	Internal	Proton-on*	1 x 10^{10}
k30 (s^{-1})***	EHint <- EHHint	Internal	Proton-off	1 – 1,000,000

* Proton on-rates are assumed to be diffusion-limited and constant as observed for EmrE [32].

** Drug on-rates are assumed to be diffusion-limited and slower than proton on-rates as observed for EmrE [24,32].

*** Only used in 10-state model.

Table 2. Initial conditions for simulations of liposomal-flux assays.*

Parameter (Unit)	Meaning	Estimated Values
Hint (M)	Interior [H] (constant)	$10^{-6.5}$ (pH = 6.5)
Hext (M)	Exterior [H] (constant)	$10^{-7.5}$ (pH = 7.5)
Dint (M)	Initial internal [drug]	25×10^{-9}
Dext (M)	Initial external [drug]	25×10^{-9}

* Due to the fully reversible system, initial conditions of EmrE species do not impact final steady state drug concentration (T_r) [47].

Table 3. Rate constants used in each experiment.

	Independent and combined effects of alternating-access rates and substrate off-rates on transport outcome			Simulating the 10-state model	Understanding the effects of ΔpH on Transport in the 8- and 10-state model		Understanding how drug-induced rate constants may drive antiport vs symport	
Parameter (Unit)	Figure 7.A	Figure 7.B	Figure 7.C	Figure 8	Figure 9 (8-State)	Figure 9 (10-State)	Figure 10.A	Figure 10.B
k1 (M^{-1} s^{-1})	1 x 10^{10}	1 x 10^{10}	1 x 10^{10}	1 x 10^{10}	1 x 10^{10}	1 x 10^{10}	1 x 10^{10}	1 x 10^{10}
k2 (s^{-1})	1000	1 - 1,000,000	1 - 1,000,000	1 - 1,000,000	63.1	63.1	63.1	1000
k3 (M^{-1} s^{-1})	1 x 10^{10}	1 x 10^{10}	1 x 10^{10}	1 x 10^{10}	1 x 10^{10}	1 x 10^{10}	1 x 10^{10}	1 x 10^{10}
k4 (s^{-1})	1000	1 - 1,000,000	1 - 1,000,000	1 - 1,000,000	63.1	63.1	63.1	1000
k5 (M^{-1} s^{-1})	1 x 10^{10}	1 x 10^{10}	1 x 10^{10}	1 x 10^{10}	1 x 10^{10}	1 x 10^{10}	1 x 10^{10}	1 x 10^{10}
k6 (s^{-1})	1000	1 - 1,000,000	1 - 1,000,000	1 - 1,000,000	1584	1584	6.3 x 10^{-5} – 6.3 x 10^{7}*	0.001 - 1 x 10^{9}*
k7 (M^{-1} s^{-1})	1 x 10^{10}	1 x 10^{10}	1 x 10^{10}	1 x 10^{10}	1 x 10^{10}	1 x 10^{10}	1 x 10^{10}	1 x 10^{10}
k8 (s^{-1})	1000	0.01 – 10,000	0.01 – 10,000	0.01 – 10,000	1584	1584	6.3 x 10^{-5} – 6.3 x 10^{7}*	0.001 - 1 x 10^{9}*
k9 (M^{-1} s^{-1})	1 x 10^{7}	1 x 10^{7}	1 x 10^{7}	1 x 10^{7}	1 x 10^{7}	1 x 10^{7}	1 x 10^{7}	1 x 10^{7}
k10 (s^{-1})	1	0.01 – 10,000	0.01 – 10,000	0.01 – 10,000	0.631	0.631	0.01 – 10,000	0.01 – 10,000
k11 (M^{-1} s^{-1})	1 x 10^{7}	1 x 10^{7}	1 x 10^{7}	1 x 10^{7}	1 x 10^{7}	1 x 10^{7}	1 x 10^{7}	1 x 10^{7}
k12 (s^{-1})	1	0.01 – 10,000	0.01 – 10,000	0.01 – 10,000	0.631	0.631	0.01 – 10,000	0.01 – 10,000
k13 (M^{-1} s^{-1})	1 x 10^{7}	1 x 10^{7}	1 x 10^{7}	1 x 10^{7}	1 x 10^{7}	1 x 10^{7}	1 x 10^{7}	1 x 10^{7}
k14 (s^{-1})	1	0.01 – 10,000	0.01 – 10,000	0.01 – 10,000	10	10	0.01 – 10,000	0.01 – 10,000
k15 (M^{-1} s^{-1})	1 x 10^{7}	1 x 10^{7}	1 x 10^{7}	1 x 10^{7}	1 x 10^{7}	1 x 10^{7}	1 x 10^{7}	1 x 10^{7}
k16 (s^{-1})	1	0.01 – 10,000	0.01 – 10,000	0.01 – 10,000	10	10	0.01 – 10,000	0.01 – 10,000
k17 (s^{-1})	1 - 100	1, 10, 100	1, 2, 3, 4, 5	1	100	100	100	100
k18 (s^{-1})	1 - 100	1, 10, 100	1, 2, 3, 4, 5	1	100	100	100	100
k19 (s^{-1})	1 - 100	1, 10, 100	1, 2, 3, 4, 5	1	40	40	40	40
k20 (s^{-1})	1 - 100	1, 10, 100	1, 2, 3, 4, 5	1	40	40	40	40
k21 (s^{-1})	1 - 100	1, 10, 100	1, 2, 3, 4, 5	1	7.3	7.3	1 - 100	1 - 100
k22 (s^{-1})	1 - 100	1, 10, 100	1, 2, 3, 4, 5	1	7.3	7.3	1 - 100	1 - 100
k23 (s^{-1})	1 - 100	1, 10, 100	1, 2, 3, 4, 5	1	8.9	8.9	1 - 100	1 - 100
k24 (s^{-1})	1 - 100	1, 10, 100	1, 2, 3, 4, 5	1	8.9	8.9	1 - 100	1 - 100
k25 (s^{-1})	-	-	-	1	-	220	220	220
k26 (s^{-1})	-	-	-	1	-	220	220	220

k27 (M^{-1} s^{-1})	-	-	-	1×10^{10}	-	1×10^{10}	1×10^{10}	1×10^{10}
k28 (s^{-1})	-	-	-	10, 100, 316.2, 1,000, 100,000, 1,000,000	-	1,000	1000	100,000
k29 (M^{-1} s^{-1})	-	-	-	1×10^{10}	-	1×10^{10}	1×10^{10}	1×10^{10}
k30 (s^{-1})	-	-	-	10, 100, 316.2, 1,000, 100,000, 1,000,000	-	1,000	1000	100,000

***** This number is solved to complete the thermodynamic cycle. These pK_a values range from 1 – 14.2.

References

1. Zhang, Y., Zhang, Y., Sun, K., Meng, Z. & Chen, L. The SLC transporter in nutrient and metabolic sensing, regulation, and drug development. *J. Mol. Cell Biol.* **11**, 1–13 (2019).

2. Yazaki, K., Sugiyama, A., Morita, M. & Shitan, N. Secondary transport as an efficient membrane transport mechanism for plant secondary metabolites. *Phytochem. Rev.* **7**, 513–524 (2008).

3. Amaral, L., Martins, A., Spengler, G. & Molnar, J. Efflux pumps of Gram-negative bacteria: what they do, how they do it, with what and how to deal with them. *Front. Pharmacol.* **4**, (2014).

4. Silverman, J. A. Multidrug-Resistance Transporters. in *Membrane Transporters as Drug Targets* (eds. Amidon, G. L. & Sadée, W.) 353–386 (Springer US, 2002). doi:10.1007/0-306-46812-3_13.

5. Oh, S. & Boudker, O. Kinetic mechanism of coupled binding in sodium-aspartate symporter GltPh. *eLife* **7**,.

6. Luo, P. *et al.* Inward-facing conformation of l -ascorbate transporter suggests an elevator mechanism. *Cell Discov.* **4**, 35 (2018).

7. Lolkema, J. S. & Slotboom, D. J. Models to determine the kinetic mechanisms of ion-coupled transporters. *J. Gen. Physiol.* **151**, 369–380 (2019).

8. Forrest, L. R., Krämer, R. & Ziegler, C. The structural basis of secondary active transport mechanisms. *Biochim. Biophys. Acta BBA - Bioenerg.* **1807**, 167–188 (2011).

9. Quistgaard, E. M., Löw, C., Guettou, F. & Nordlund, P. Understanding transport by the major facilitator superfamily (MFS): structures pave the way. *Nat. Rev. Mol. Cell Biol.* **17**, 123–132 (2016).

10. Feng, L., Campbell, E. B. & MacKinnon, R. Molecular mechanism of proton transport in CLC Cl^-/H^+ exchange transporters. *Proc. Natl. Acad. Sci. U. S. A.* **109**, 11699–11704 (2012).

11. Stein, W. *Transport and Diffusion Across Cell Membranes.* (Academic, San Diego, CA, 1986).

12. Fitzgerald, G. A., Mulligan, C. & Mindell, J. A. A general method for determining secondary active transporter substrate stoichiometry. *eLife* https://elifesciences.org/articles/21016 (2017) doi:10.7554/eLife.21016.

13. Kermani, A. A., Macdonald, C. B., Gundepudi, R. & Stockbridge, R. B. Guanidinium export is the primal function of SMR family transporters. *Proc. Natl. Acad. Sci.* **115**, 3060–3065 (2018).

14. Nguitragool, W. & Miller, C. Uncoupling of a CLC Cl-/H+ exchange transporter by polyatomic anions. *J. Mol. Biol.* **362**, 682–690 (2006).

15. Chen, Y.-J. *et al.* X-ray structure of EmrE supports dual topology model. *Proc. Natl. Acad. Sci.* **104**, 18999–19004 (2007).

16. Iancu, C. V., Zamoon, J., Woo, S. B., Aleshin, A. & Choe, J. Crystal structure of a glucose/H+ symporter and its mechanism of action. *Proc. Natl. Acad. Sci.* **110**, 17862–17867 (2013).

17. Bazzone, A., Zabadne, A. J., Salisowski, A., Madej, M. G. & Fendler, K. A Loose Relationship: Incomplete H+/Sugar Coupling in the MFS Sugar Transporter GlcP. *Biophys. J.* **113**, 2736–2749 (2017).

18. Bozzi, A. T., Bane, L. B., Zimanyi, C. M. & Gaudet, R. Proton co-transport and voltage dependence enforce unidirectional metal transport in an Nramp transporter. *bioRxiv* 402412 (2018) doi:10.1101/402412.

19. Dohán, O. *et al.* The Na+/I− symporter (NIS) mediates electroneutral active transport of the environmental pollutant perchlorate. *Proc. Natl. Acad. Sci. U. S. A.* **104**, 20250–20255 (2007).

20. Guan, L. & Kaback, H. R. Lessons from Lactose Permease. *Annu. Rev. Biophys. Biomol. Struct.* **35**, 67–91 (2006).

21. Varela, M. F. & Hastings Wilson, T. Molecular biology of the lactose carrier of Escherichia coli. *Biochim. Biophys. Acta BBA - Bioenerg.* **1276**, 21–34 (1996).

22. Purewal, A. S. Nucleotide sequence of the ethidium efflux gene from Escherichia coli. *FEMS Microbiol. Lett.* **82**, 229–231 (1991).

23. Yerushalmi, H., Lebendiker, M. & Schuldiner, S. EmrE, an Escherichia coli 12-kDa multidrug transporter, exchanges toxic cations and H+ and is soluble in organic solvents. *J. Biol. Chem.* **270**, 6856–63 (1995).

24. Robinson, A. E., Thomas, N. E., Morrison, E. A., Balthazor, B. M. & Henzler-Wildman, K. A. New free-exchange model of EmrE transport. *Proc. Natl. Acad. Sci.* **114**, E10083–E10091 (2017).

25. Morrison, E. A., Robinson, A. E., Liu, Y. & Henzler-Wildman, K. A. Asymmetric protonation of EmrE. *J. Gen. Physiol.* **146**, 445–461 (2015).

26. Morrison, E. A. *et al.* Antiparallel EmrE exports drugs by exchanging between asymmetric structures. *Nature* **481**, 45–50 (2011).

27. Thomas, N. E. *et al.* The C terminus of the bacterial multidrug transporter EmrE couples drug binding to proton release. *J. Biol. Chem.* **293**, 19137–19147 (2018).

28. Gayen, A., Leninger, M. & Traaseth, N. J. Protonation of a Glutamate Residue Modulates the Dynamics of the Drug Transporter EmrE. *Nat. Chem. Biol.* **12**, 141–145 (2016).

29. Horn, F. & Jackson, R. General mass action kinetics. *Arch. Ration. Mech. Anal.* **47**, 81–116 (1972).

30. Robinson, A. E., Henderson, J. P. & Henzler-Wildman, K. A. A mass spectrometry based transport assay for studying EmrE transport of unlabeled substrates. *Anal. Biochem.* **549**, 130–135 (2018).

31. Bakker, E. P. & Mangerich, W. E. Interconversion of components of the bacterial proton motive force by electrogenic potassium transport. *J. Bacteriol.* **147**, 820–826 (1981).

32. Adam, Y., Tayer, N., Rotem, D., Schreiber, G. & Schuldiner, S. The fast release of sticky protons: Kinetics of substrate binding and proton release in a multidrug transporter. *Proc. Natl. Acad. Sci.* **104**, 17989–17994 (2007).

33. Morrison, E. A. & Henzler-Wildman, K. A. Transported Substrate Determines Exchange Rate in the Multidrug Resistance Transporter EmrE. *J. Biol. Chem.* **289**, 6825–6836 (2014).

34. Brill, S., Falk, O. S. & Schuldiner, S. Transforming a drug/H+ antiporter into a polyamine importer by a single mutation. *Proc. Natl. Acad. Sci.* **109**, 16894–16899 (2012).

35. Henderson, R. K., Fendler, K. & Poolman, B. Coupling efficiency of secondary active transporters. *Curr. Opin. Biotechnol.* **58**, 62–71 (2019).

36. Walmsley, A. R., Barrett, M. P., Bringaud, F. & Gould, G. W. Sugar transporters from bacteria, parasites and mammals: structure-activity relationships. *Trends Biochem. Sci.* **23**, 476–481 (1998).

37. Wilson-O'Brien, A. L., Patron, N. & Rogers, S. Evolutionary ancestry and novel functions of the mammalian glucose transporter (GLUT) family. *BMC Evol. Biol.* **10**, 152 (2010).

38. Mueckler, M. & Thorens, B. The SLC2 (GLUT) Family of Membrane Transporters. *Mol. Aspects Med.* **34**, 121–138 (2013).

39. Al-Shawi, M. K., Polar, M. K., Omote, H. & Figler, R. A. Transition State Analysis of the Coupling of Drug Transport to ATP Hydrolysis by P-glycoprotein. *J. Biol. Chem.* **278**, 52629–52640 (2003).

40. Sharom, F. J., Yu, X., Chu, J. W. & Doige, C. A. Characterization of the ATPase activity of P-glycoprotein from multidrug-resistant Chinese hamster ovary cells. *Biochem. J.* **308**, 381–390 (1995).

41. Krupka, R. M. Uncoupled Active Transport Mechanisms Accounting for Low Selectivity in Multidrug Carriers: P-Glycoprotein and SMR Antiporters. *J. Membr. Biol.* **172**, 129–143 (1999).

42. Krupka, R. M. Limits on the Tightness of Coupling in Active Transport. *J. Membr. Biol.* **167**, 35–41 (1999).

43. Joh, N. H. *et al.* De novo design of a transmembrane Zn2+-transporting four-helix bundle. *Science* **346**, (2014).

44. Rotem, D. & Schuldiner, S. EmrE, a Multidrug Transporter from Escherichia coli, Transports Monovalent and Divalent Substrates with the Same Stoichiometry. *J. Biol. Chem.* **279**, 48787–48793 (2004).

45. Robinson, A. E., Henderson, J. P. & Henzler-Wildman, K. A. A mass spectrometry based transport assay for studying EmrE transport of unlabeled substrates. *Anal. Biochem.* **549**, 130–135 (2018).

46. Garcia-Celma, J. J., Smirnova, I. N., Kaback, H. R. & Fendler, K. Electrophysiological characterization of LacY. *Proc. Natl. Acad. Sci.* **106**, 7373–7378 (2009).

47. Craciun, G. & Feinberg, M. Multiple Equilibria in Complex Chemical Reaction Networks: II. The Species-Reaction Graph. *SIAM J. Appl. Math.* **66**, 1321–1338 (2006).

Chapter 3

An SSM Electrophysiology Assay for Efficient Characterization of Ion-Coupled Transport

Nathan E. Thomas[1], Wei Feng[2], and Katherine A. Henzler-Wildman[1*]

[1]Department of Biochemistry, University of Wisconsin-Madison

[2]Department of Molecular and Cellular Physiology, Stanford University School of Medicine

**Email address: henzlerwildm@wisc.edu*

Preface: The free exchange model predicts that EmrE should transport drug with multiple transport stoichiometries using multiple transport pathways. The relative contributions of these pathways should depend on the environmental conditions, such as the concentration of the transported substrates. Measuring EmrE's transport stoichiometry under different experimental conditions would provide a great test of the free exchange model, but the traditional methods for performing these experiments are prohibitively expensive in both time and material. Here, we develop a new, higher throughput method for measuring transport stoichiometry using solid supported membrane electrophysiology, providing proof of principle for the method with two well-characterized transporters. I developed the assay, performed experiments, and wrote the initial draft of the manuscript while Wei expressed and purified CLC-ec1, provided input on assay conditions, and edited the manuscript.

Abstract:

Transport stoichiometry determination can provide great insight into the mechanism and function of ion-coupled transporters. Traditional reversal potential assays are a reliable, general method for determining the transport stoichiometry of ion-coupled transporters, but the time and material costs of this technique hinder investigations of transporter behavior under multiple experimental conditions. Here, we develop a new technique for measuring transport stoichiometry with greatly

improved throughput using solid supported membrane electrophysiology (SSME). Using this technique, we are able to verify the recent report of a fixed 2:1 stoichiometry for the proton:guanidinium antiporter Gdx, reproduce the $1H^+$:$2Cl^-$ antiport stoichiometry of CLC-ec1, and confirm loose proton:nitrate coupling for CLC-ec1. Our SSME method requires small amounts of transporter and provides a fast, easy, general method for measuring transport stoichiometry, which will facilitate future mechanistic and functional studies of ion-coupled transporters.

Introduction

Ion-coupled transporters utilize energy stored in electrochemical gradients to drive uphill substrate transport across cellular membranes. These transporters are essential to numerous physiological processes, from nutrient uptake to neural signaling, and are common drug targets, but successful therapeutic design is limited by our understanding of these integral membrane proteins' structures, functions, and mechanisms[1,2]. Transport stoichiometry – the number of ions and substrates moved per transport cycle – is a function of the transporter's mechanism and is a crucial determinant of the direction of driven transport, the energy spent per substrate transported, and the maximum substrate gradient that can be maintained at equilibrium. Generally, ion-coupled transporters have been assumed to operate according to tightly coupled mechanisms with a single, set transport stoichiometry. This understanding has led to the traditional classification of transporters as either antiporters, symporters, or uniporters. However, there is growing evidence that many ion-coupled transporters operate through complex mechanisms that violate the assumption of stoichiometric transport, engaging in behavior that cannot be cleanly classified as antiport, symport, or uniport[3–8]. In light of these findings, there is a pressing need for detailed mechanistic investigations of a greater variety of transporters.

The emergence of high-resolution structures of membrane proteins has revealed specific substrate binding sites on transporters, which together with biochemical assays, have significantly advanced our understanding of transporter:substrate binding stoichiometry[9–12]. However, it is

important to distinguish binding stoichiometry from transport stoichiometry[13]. At times, ions or substrates can bind as allosteric effectors without being transported[14]. This is especially difficult to untangle in the case of proton-coupled transporters with multiple protonatable side chains[15,16]. Furthermore, establishing that substrate bound at a specific site can be transported is insufficient to establish that its transport is obligatory to the mechanism, as loosely coupled transporters may be able to transport one substrate without co-transport of the coupled ion or substrate [3,17]. Thus, measuring a transporter's coupling stoichiometry not only sheds light on its biological function, but also provides crucial information about the transport mechanism.

The only way to reliably determine transport stoichiometry is through transport assays. Reversal potential assays have emerged as the method of choice for electrogenic transporters, as they are applicable to a variety of systems and allow for model-independent determination of the transport stoichiometry[18–22]. In brief, these assays follow transport as a function of membrane voltage for a set initial substrate and/or ion gradient. The reversal potential, the membrane voltage where there is no net transport, can be used to determine the transport stoichiometry. In theory, this method can be applied to any electrogenic transporter, but there are several important limitations. First, transport must be able to be monitored. Several eukaryotic transporters are amenable to patch clamp electrophysiology[23–25], but this technique is generally only suitable for high-flux transporters that can be highly expressed in eukaryotic cells, which excludes many structurally characterized prokaryotic transporters. Assays of purified protein in proteoliposomes allow for characterization of the widest range of transporters but require an appropriate readout of transport activity. Ideally, liposomal transport is observed through real-time probes such as fluorophores. However, fluorophores are not available for every coupling ion. Radioactive transport assays may be used instead[22] but do not offer real-time monitoring, significantly increasing the time and effort required to collect data for the multiple time points and conditions needed to determine transport stoichiometry. A second issue with traditional liposomal assays is that intraliposomal contents

cannot easily be changed after reconstitution. This increases the difficulty of screening a wide range of assay conditions and can make it difficult to accurately establish internal ion and substrate concentrations. A third issue is that liposomal assays often require a large amount of purified transporter, depending on the sensitivity of the detection method and the number of conditions that must be tested. Finally, for many of the reasons listed above, traditional liposomal transport assays are low throughput and require significant time and effort, even if the material costs can be kept to a minimum. As a consequence, transport stoichiometry has been measured for only a small fraction of structurally characterized transporters[22,26]. A method for routine measurements of transport stoichiometry would greatly facilitate functional and mechanistic studies of ion-coupled transporters.

Here we present a new approach for measuring coupling stoichiometry by adapting reversal-potential assays to solid-supported membrane-based electrophysiology (SSME), a technique developed over the last two decades to allow electrophysiological characterization of lower flux transporters[27,28]. SSME carries several advantages over traditional liposomal transport assays. By directly measuring transported charge, SSME allows real-time monitoring of electrogenic transport without the need for fluorophores or radiolabeled substrates. In addition, its sensitivity requires only picomole amounts of protein to achieve sufficient signal. Finally, dozens of conditions can be tested on a single sensor without the need for separate reconstitutions, greatly increasing the throughput of the assay. We demonstrate the utility of this method using *E. coli* Gdx, whose 2:1 proton:guanidinium antiport stoichiometry was recently established using traditional reversal potential measurements[29], and CLC-ec1, which has been shown to engage in both tightly-coupled and loosely-coupled proton:anion transport[21]. With our SSME assay, we confirmed these results, using less than 2 nmol total protein to perform 400 transport assays in under a week of measurement time. In addition, we demonstrate that it is possible to change the internal ion and substrate concentrations using the SSME setup, expanding the number of

experimental conditions that can be tested on a single protein sample. This assay is fast, easy, and accurate, requires a minimal amount of sample, and is broadly applicable to electrogenic transporters, regardless of coupling ion or transported substrate.

Results

An SSME transport reversal assay

Reversal potential assays rely on the thermodynamic reversibility of coupled transport. That is, transport of an ion down a large electrochemical gradient can drive transport of another substrate uphill against its electrochemical gradient, and conversely, transport of a substrate down a large gradient can drive transport of an ion up its electrochemical gradient. When the electrochemical gradients are balanced, no net transport occurs, allowing for calculation of the transport stoichiometry (see *Materials and Methods* for equations and derivations). Our assay adapts this principle to SSME.

In an SSME experiment, proteoliposomes are adsorbed onto a membrane-coated gold electrode, creating the sensor. To initiate an experiment, buffer is run over the sensor in three stages[27]. First, a “non-activating” buffer containing the same solution as inside the liposomes is flowed over the sensor to ameliorate artifacts due to buffer perfusion. Second, an “activating” buffer is flowed over the sensor to initiate transport. Capacitive coupling between the liposomal membrane and the surface-supported membrane on the electrode allows for measurement of currents across the membrane (“on-currents”). Transport proceeds until a steady state is obtained where sufficient membrane potential opposes further net transport. Third, the non-activating buffer is reapplied, and the reverse transport process returns the sensor to its initial state. During this phase, “off-current” transport proceeds in the opposite direction of the on-current, driven by both chemical and electrical gradients.

Fig. 1 shows representative traces from our assay for all three stages of the experiment. First, non-activating buffer equilibrates the liposomes with a known concentration of proton and guanidinium. In the second stage, the activating buffer sets a 2-fold proton gradient to initiate transport. In Fig. 1A, the guanidinium concentration is not changed, so there is no guanidinium gradient and the outward-facing proton gradient should drive guanidinium into the liposomes. The negative on-current indicates that charge is moving out of the liposome, consistent with the expected $2H^+$(out):$1Gdm^+$(in) antiport[29]. In Fig. 1B, the activating buffer simultaneously sets an 8-fold outward-facing guanidinium gradient in addition to the 2-fold outward-facing proton gradient. Under these conditions, the large guanidinium gradient drives uphill proton transport into the liposomes and reverses the direction of net charge movement. In the third and final stage, current flux in the opposite direction from the on-currents is observed when non-activating buffer is re-applied to the sensor. While the off-currents in our experiments behave as expected qualitatively, we use only the on-currents for analysis following general practice in SSME data analysis[27].

Both chemical gradients and transmembrane voltage contribute to the total electrochemical potential driving transport. In a traditional reversal potential assay, chemical gradients are kept constant, and transport is observed as a function of applied membrane voltage. In contrast, there is no applied membrane voltage in our assays, and instead, chemical gradients are varied[30]. Thus, we plot the observed transport (integrated on-current) as a function of the applied chemical gradients, denoted as the ratio of the initial substrate and ion chemical potentials ($\Delta\mu_s/\Delta\mu_i$). Null transport at a given $\Delta\mu_s/\Delta\mu_i$ chemical potential ratio should correspond to an ion:substrate transport stoichiometry of the same value (see Methods for derivation). For Gdx's $2H^+$:$1Gdm^+$ transport stoichiometry, null transport should occur at a $\Delta\mu_{Gdm^+}/\Delta\mu_{H^+}$ ratio of 2. We chose chemical potential ratios corresponding to a variety of plausible H^+:Gdm^+ stoichiometries (Table 1) to determine the extent to which different stoichiometries can be distinguished by our method.

SSME can measure Gdx transport stoichiometry

Before proceeding to our analysis, we performed several critical controls. To assess the magnitude of signal due to solution exchange, we ran the assay using sensors prepared with two negative controls: proteoliposomes reconstituted with the non-functional mutant E13Q-Gdx and "empty" liposomes reconstituted without transporters. Signals for both negative controls were of similar magnitude and small compared to transport signals for WT-Gdx (Fig.1C and Fig. S3). As an additional control, we prepared sensors from liposomes with different lipid to protein ratios (LPR) but with the same total amount of lipid. Altering the protein concentration in this manner will not alter the thermodynamics of transport but will affect transport kinetics as well as pre-steady state currents related to electrogenic partial reactions, such as substrate binding or protein gating[27]. Since we are interested in transport stoichiometry, it is important to check that the currents reflect the full transport cycle and not just a partial reaction. Integrated currents for WT-Gdx are independent of LPR (Fig. 1D), as expected if the currents correspond to transport.

Having confirmed that the currents reflect transport with the appropriate controls, we plotted transported charge as a function of chemical potential ratio. For both concentrations of WT-Gdx, null transport occurs at the expected 2:1 $\Delta\mu_{Gdm^+}/\Delta\mu_{H^+}$ ratio (Fig.1D). This result is unchanged when either the empty liposome or E13Q controls are subtracted. This confirms that our assay accurately measures the transport stoichiometry of Gdx.

Quantitative exchange of internal conditions

One key advantage of SSME over traditional liposomal assays is that one single SSM sensor allows dozens of measurements, drastically reducing sample requirements. Furthermore, it is well established that a single sensor can be used to screen different activating (external) buffers over several experiments[27,31]. We wished to test whether it was possible to reliably change the *internal* buffer solution of the liposomes adsorbed to the sensors, which would greatly expand the number of conditions that could be tested on a single sensor and further increase the throughput of this method. We prepared sensors at pH 7.00 with 1 mM guanidinium in the same manner as in the

experiments in Fig. 1. We then performed a series of rinses with pH 6.70, 1 mM guanidinium buffer while monitoring the current. After about 3 mL of total rinse volume, the currents stabilized near zero (Fig. 2A). We then proceeded to perform the assay with a nominal internal pH of 6.70 and activating buffers at pH 7.00. The integrated current was plotted against chemical potential, assuming that the transmembrane pH gradient matched the nominal value. The graph once again yielded a transport stoichiometry of $2H^+$:Gdm^+ (Fig. 2C,E), confirming that the internal pH was 6.70, as intended. This demonstrates that a single sensor can be used to test multiple internal pH conditions.

We then tested whether it is also possible to change the internal substrate concentrations. After preparing sensors with pH 7, 1 mM guanidinium buffer, we performed a series of three 1 mL rinses with pH 7.00, 500 µM guanidinium buffer, each separated by about ten minutes, while monitoring the current. Several sensors required a fourth 1 mL rinse, but eventually, currents on all sensors stabilized near zero. Once the rinse currents stabilized at zero, we proceeded with the assay. The observed signal was lower overall, possibly the result of using lipids stocks that were 18 months old by the time of the experiment. Nevertheless, the signal trends were consistent with previous experiments, and once again, null transport occurred at the gradient ratio corresponding to $2H^+$:Gdm^+ antiport (Fig. 2D,F). This confirms that the internal Gdm^+ was quantitatively exchanged on the sensor. These results provide evidence that internal substrate concentrations can be quantitatively exchanged on an SSME sensor, greatly expanding the possible range of experiments that can be performed using a single reconstitution of proteoliposomes.

CLC-ec1 stoichiometry can be determined despite background signal

To determine whether the results of our assay with Gdx are generally applicable to other transporters, we next turned to CLC-ec1. This well characterized transporter has previously been studied by SSME and is known to produce robust transport currents[32,33]. CLC-ec1's canonical function is tightly coupled $1H^+$:$2Cl^-$ antiport, but interestingly, it is also capable of transporting other

anions with varying degrees of proton coupling[21]. To test whether our SSME assay can accurately probe the effect of varied experimental conditions on transport stoichiometry, we performed a series of four reversal experiments with CLC-ec1 sensors (Table 2). Sensors with liposomes prepared from an identical reconstitution process without protein were used as negative controls.

In the first set of experiments, the internal buffer matched the conditions of the reconstitution – pH 4.84 and 150 mM chloride. The external buffer was set to pH 5.24 and the external chloride concentration was varied to cover a range of possible proton:chloride stoichiometries (Fig. 3A and Table 2, row 1). Despite CLC-ec1's high turnover rate, the observed signal did not reach a clear steady state under several experimental conditions. Instead, after an initial fast transport process, a slow but steady decrease could be observed in the integrated current traces (Fig. 3C). This decrease became more significant with larger chloride gradients, a phenomenon which was also observed with the empty liposome negative controls (Fig. 3E). This indicates that unlike with Gdx, a non-transporter-mediated process has a significant contribution to the signal, which must be taken into account when analyzing the data. Fortunately, the empty liposome control allows this signal to be isolated. Once isolated, background signals can be subtracted from sample signals to reveal the transporter-mediated signals in reversal potential assays[18] (see Supplementary Information for further discussion). When the signal in the empty liposome samples is subtracted from the signal in the CLC-ec1 samples, it is clear that CLC-ec1-mediated transport reaches steady state in fractions of a second (Fig. 3G), with null transport observed at the expected $1H^+/2Cl^-$ antiport stoichiometry (Fig. 3G, J).

For the second set of experiments, the internal chloride concentration was reduced from 150 mM to 3 mM by successive washes of the desired internal buffer, as described above for Gdx (Fig. S5). We then proceeded with the second reversal experiment with inwardly directed proton and/or chloride gradients (Fig. 4B and Table 2, row 2). Once again, background signal was observed when chloride gradients were present (Fig. 3D,F), but subtracting this signal from the signal of

the CLC-ec1 sensors unambiguously yielded a $1H^+$:$2Cl^-$ stoichiometry (Fig.3H, J). These results demonstrate the utility of our assay for a second system, even in the presence of significant background signal.

Reduced proton:nitrate coupling by CLC-ec1 is due to nitrate leak

For the final two sets of reversal experiments, we rinsed the sensors to replace the chloride with 15 mM nitrate. CLC-ec1 transports nitrate with reduced proton coupling compared to chloride. Published reversal potentials are consistent with a transport stoichiometry between 7 and 10 nitrates per proton, but as Nguitragool and Miller noted, it is difficult to imagine a mechanism that could account for tightly coupled $7(+)NO_3^-$:$1H^+$ antiport[21]. Subsequent computational and experimental studies on CLC-ec1 taken together support the suggestion that the increased nitrate:proton stoichiometry is due to presence of an uncoupled nitrate uniport pathway in parallel to the coupled nitrate:proton antiport pathway[33–36]. Nevertheless, tightly coupled transport has not been rigorously ruled out by published experimental data.

We performed nitrate reversal potential assays under two sets of conditions (Table 2) – first with inward-facing proton and nitrate gradients (Fig. 4A, C-J orange) and second with outward facing proton and nitrate gradients (Fig. 4B, D-J purple). If our assay is capable of detecting the reduced nitrate:proton coupling, then the direction of transported charge should require a smaller anion gradient to reverse with nitrate than with chloride. Furthermore, if the reduced coupling is due to a combination of nitrate leak and coupled antiport and not tightly coupled nitrate:proton antiport with a large stoichiometry, we would expect the apparent stoichiometry to change as the experimental substrate and proton concentrations are altered[6,21,37] (see SI and Fig. S6 for a more detailed explanation).

Our data shows that CLC-ec1 indeed transports nitrate with reduced proton coupling. When no nitrate gradient is present, the proton gradient dictates the direction of transported charge (Fig. 4

grey traces), but a relatively small nitrate gradient is sufficient for charge to be transported in the opposite direction of the proton gradient (Fig. 4 orange and purple traces) indicating a large apparent transport stoichiometry. However, our data is less clear on the question of whether this is due to tight coupling or nitrate leak. Any difference in the reversal point between the conditions is within the error of the measurement (Fig. 4I,J). While the magnitude and direction of the gradients varied between the two conditions, both conditions had identical internal proton and nitrate concentrations. It is possible that these conditions were too similar to each other to distinguish the relative transport rates, so we adapted our assay to quickly survey a wider range of experimental conditions.

We performed a series of measurements with a constant inward-facing proton gradient ($\Delta\mu_{H^+}$) and matched internal and external chloride or nitrate concentrations (setting $\Delta\mu_{anion}$ to zero) while varying the absolute value of the nitrate or chloride concentration (Fig. 5). If transport is tightly coupled, the amount of transport should be independent of the absolute anion concentration. On the other hand, anion leak should increase with increasing anion concentration[37]. If anion leak is possible, anions will leak in the opposite direction of the electrochemical gradients created by proton:anion antiport, resulting in a decrease in observed transport. The observed signal was independent of chloride concentration between 1 and 150 mM, consistent with tightly coupled antiport of $1H^+$:$2Cl^-$ by CLC-ec1. However, very different behavior was observed for nitrate transport. The observed signal decreased as the nitrate concentration increased, consistent with an increased prevalence of anion leak at higher nitrate concentrations. This provides clear evidence that the CLC-ec1's reduced proton coupling with nitrate is due to nitrate leak rather than a higher order nitrate:proton stoichiometry.

Discussion

As a key determinant of transporter function, accurate determination of transport stoichiometry provides great insight into transporter mechanism. Currently available methods for measuring

transport stoichiometry are time consuming and technically difficult, and as a consequence, transport stoichiometry is rarely quantitatively measured during structural or functional characterization of transporters. Among transporters that have had their transport stoichiometry characterized, many have been tested at a single experimental condition, which can lead to an assumption of a single transport stoichiometry that may not always be true[13,21]. Our SSME assay addresses several key technical obstacles for stoichiometry determination and in doing so, will facilitate measurement of transport stoichiometry for more transporters under a broader array of experimental conditions.

In addition to generalized signal detection and improvements to throughput, SSME also allows for fast and easy confirmation of the internal contents of the liposome. All that is required is to rinse the sensor with the desired internal buffer while recording. If the internal ion and substrate concentrations differ from the intended concentrations, a transport current will be evident (Fig. 2A and S5, blue traces) but no current will occur if the internal concentrations are matched to the known external buffer (Fig. 2, red traces and Fig. S5, yellow traces). This property can further be exploited to change the internal concentrations of the liposomes and test a wider variety of experimental conditions on the same sample, as demonstrated here for proton (Fig. 2), guanidinium (Fig. 2), chloride (Fig. 3 and 5), and nitrate (Fig. 4 and 5). It should be noted that both proton and chloride are relatively membrane permeable[38,39]. Nevertheless, while the timescale of the internal buffer equilibration may increase for other molecules, recording the currents of successive rinses of internal buffer provides a robust method for ensuring that the internal buffer has indeed been exchanged.

The linear dependence of transported charge on ion/substrate potential hints at another advantage of our assay. In SSME, transport proceeds until sufficient membrane voltage is produced to oppose further transport – in effect, the reversal potential. While this reversal potential is not quantified directly by SSME, it is directly proportional to the total amount of transported

charge. The linearity of the graphs in Figs. 1-4 further indicates that the reversal potential is directly set by the ion and substrate concentration gradients (see Supplementary Information for further discussion). This facilitates experiments such as the one in Fig. 5 that rely on the accurate analysis of transport potentials under different experimental conditions. In principle, similar experiments could be performed by running traditional liposomal transport assays to their endpoint, but such experiments are often rendered impractical due to the time they require or the presence of ion or substrate leaks[18]. In contrast, the transport currents observed by SSME approach steady-state in a fraction of a second, allowing rapid and accurate analysis of transport potentials.

As with any method, the reliability of this assay requires proper controls and assay conditions. SSME is sensitive enough to detect charge displacement due to conformational changes of proteins in the membrane[40], ion-transporter binding events[41,42], and solution exchange artifacts[27]. To control for non-transport currents, sensors can be prepared with different LPRs, changing the protein concentration but keeping the lipid concentration constant. Currents due to binding or conformational changes will change with protein concentration, but integrated transport currents will not, as they depend only on the chemical potentials set by buffer exchange. In our Gdx results, there was no significant difference between the integrated currents for sensors prepared from LPRs of 150 and 400. As CLC-ec1 has previously been demonstrated to produce large transport currents by SSME[32], we did not perform assays with different CLC-ec1 LPRs. Furthermore, since CLC-ec1 concentrations were approximately an order of magnitude lower than the Gdx concentrations in our assay and since binding currents are proportional to protein concentration, it is reasonable to conclude that the currents in our CLC-ec1 assays are due to transport. Negative controls should be used to estimate background current due to solution exchange artifacts. For Gdx, it is possible to abolish transport activity through a single mutation (E13Q), but transport-dead mutants are not available for every transporter. In such cases, “empty” liposomes which

have undergone a simulated reconstitution process without protein may be used instead. The simulated reconstitution process is crucial, as the addition and subsequent removal of detergent can greatly affect the integrity of the lipid bilayer. Empty liposomes that have undergone such a process can serve as quantitatively accurate negative controls, even in the presence of significant background signal, as shown in our chloride transport data for CLC-ec1.

While this assay holds many improvements over traditional reversal potential assays, there are limits to the types of transport that it can measure. The most basic requirement is that the transport process must be electrogenic, though this is also a requirement of traditional reversal potential experiments, as otherwise, changing the membrane potential will not affect the thermodynamics of the transport process. A second limitation is that while SSM electrophysiology can detect much smaller currents than traditional electrophysiological methods, currents from transporters with turnover rates below 1 per second may still be inaccessible through SSME[27,28]. We attempted to perform the assay with VcINDY but were unable to detect transport currents by SSME, perhaps unsurprisingly, given the reported turnover for VcINDY of 0.3 per *minute*[43]. Signal from low-turnover transporters can be increased by lowering the LPR[44], but there is a limit to how much the concentration of protein can be increased while maintaining the integrity of the membrane. For transporters with turnover rates as low as VcINDY, the sensitivity provided by radioactivity may be necessary to observe reversal[22].

As our appreciation for the complexity of transporter mechanisms grows[3,15–17], it is increasingly important to be able to measure transport stoichiometry. The SSME assay reported here addresses several key limitations of traditional reversal potential assays for measuring the stoichiometry of transporters. By directly measuring transported charge, this assay's detection method is broadly applicable to electrogenic transporters that can be functionally reconstituted into liposomes. By allowing repeated measurements of the same sample, this assay reduces sample requirements and vastly increases throughput. And finally, by enabling quantitative

exchange of internal substrate concentrations, this assay facilitates investigations of transporter behavior under a variety of experimental conditions. Taken together, these improvements will help to make transporter stoichiometry determination more routine, providing powerful tools for in-depth characterization of transporter mechanism and function.

Materials and Methods

Sample Preparation

WT- and E13Q-Gdx were expressed in *E. coli* from a pET15b vector and purified as previously described for the homolog EmrE [45]. Briefly, cells were lysed after overnight induction, and the protein was solubilized in 40 mM decylmaltoside (DM). Solubilized protein was run over a Ni^{2+}-affinity column and eluted in 400 mM imidazole. The N-terminal hexahistidine tag was removed by overnight thrombin cleavage, and cleaved protein was further purified using size-exclusion chromatography. To minimize solution exchange artifacts, the buffers used for size exclusion chromatography, reconstitution, and electrophysiology steps had the same salt composition: 50 mM MES, 50 mM MOPS, 50 mM bicine, 100 mM NaCl, and 2 mM $MgCl_2$. Buffer pH values were carefully adjusted using only NaOH to ensure that internal and external Cl^- concentrations were identical for all measurements.

WT-Gdx or E13Q-Gdx was reconstituted into POPC proteoliposomes at a lipid to protein mole ratio of either 150:1 or 400:1 Gdx monomer (300:1 or 800:1 per functional dimer) in a pH 7.0 buffer. As an additional negative control, POPC liposomes were put through a simulated reconstitution process without protein. Detergent was removed with Amberlite XAD-2. Reconstituted liposomes were aliquoted and flash frozen. Immediately prior to measurements, liposome samples were thawed, diluted 2-fold in pH 7.00 buffer containing 2 mM guanidinium, and briefly sonicated. 10 µL of liposomes at a lipid concentration of 1.4 µg/µL were then used to prepare sensors for each sample condition.

CLC-ec1 was purified as previously described [33,46] and reconstituted into E. coli polar lipids (Avanti) in a pH 4.8 buffer containing 100 mM sodium citrate, 150 mM sodium chloride, 150 mM sodium isethionate, and 5 mM magnesium sulfate at a lipid to protein weight ratio of 50:1 (around 3300:1 mole ratio, assuming an average lipid molecular weight of 750). As a negative control, E. coli polar lipids were put through a simulated reconstitution process without protein. Detergent was removed by dialysis with four changes of the pH 4.8 buffer containing 100 mM sodium citrate, 150 mM sodium chloride, 150 mM sodium isethionate, and 5 mM magnesium sulfate.

3mm gold electrode sensors were prepared according to the standard previously described protocol [27]. Briefly, sensors were incubated for at least 30 minutes in an octadecane thiol solution, then rinsed thoroughly with isopropanol and water. The SSM was prepared by pipetting 1.5 µL of diphytanoyl phosphatidylcholine dissolved in n-decane onto the electrode surface, followed by 60 µL of an aqueous buffer. Immediately prior to measurements, liposome samples were thawed and briefly sonicated. 10 µL of liposome sample was pipetted onto each SSM sensor and samples were adsorbed by centrifugation at 2500g for 30 minutes.

Transport Buffer Preparation

Transport buffers were prepared by mixing buffer stock solutions. For the Gdx transport assays, buffer stocks were prepared at pH 6.7, 7.0, and 7.3 with either 2 mM HCl or 2 mM guanidinium-HCl for a total of six buffer stocks. Each buffer stock contained 50 mM MES, 50 mM MOPS, 50 mM bicine, 100 mM NaCl, and 2 mM $MgCl_2$ and was adjusted to the desired pH with sodium hydroxide. To prepare transport buffers for each guanidinium concentration, the 2 mM guanidinium stock buffer was mixed with the 2 mM HCl stock buffer at the desired pH to ensure a constant chloride concentration.

For the CLC-ec1 transport assays, a total of nine buffer stocks were prepared: 300 mM stocks of either sodium chloride, sodium nitrate, or sodium isethionate at either pH 4.2, 4.8, or 5.2. In

addition to the 300 mM sodium salt, each stock contained 100 mM citric acid and 5 mM magnesium sulfate. Stocks of each of the salts were adjusted to the desired pH values with sodium hydroxide. To prepare transport buffers of the desired substrate concentration, the 300 mM sodium isethionate stock was mixed with either the 300 mM sodium chloride stock or the 300 mM sodium nitrate stock at the desired pH to ensure a constant sodium and total anion concentration. Buffer conditions for each data point can be found in Tables 1 and 2 for Gdx or CLC-ec1, respectively.

SSME Data Acquisition and Analysis

All electrophysiology measurements were recorded on a Surfe2r N1 solid-supported membrane-based electrophysiology instrument from Nanion Technologies GmbH (Munich, Germany). Prior to recording any transport measurements, sensors were rinsed with at least 1 mL of non-activating (internal) buffer while recording currents to ensure a flat baseline. Transport recordings occurred in three one-second stages according to Figure 1 with 200 µL/s buffer perfusion. After each transport measurement, sensors were again rinsed with 1 mL of non-activating buffer to ensure equilibration of the internal buffer before the next measurement.

Initial data analysis was performed using the Surfe2r N1 instrument-specific analysis software from Nanion. The final 200 ms of non-activating buffer perfusion was averaged to obtain the baseline. Both peak current and integrated current data were obtained solely from the activating buffer perfusion. For transport currents with both positive and negative components (e.g., the 250 µM trace in Fig. S3A and B), the peak with the largest absolute value was recorded as the peak current. The entire stage of activating perfusion was integrated to obtain the integrated current values.

At least three sensors were prepared for each sample. While total current varied between sensors, transport behavior was highly consistent between sensors (Fig. S1 and S2). Reported

peak and integrated currents consist of the average of at least three sensors, normalized to the average total peak or integrated current observed on each sensor. Total current was determined by summation of the absolute value of the peak or integrated current observed on a sensor across all conditions tested. Y-error bars represent the standard error of the mean. X-error bars were calculated by propagation from Equation 8, assuming either a 1% (for CLC-ec1 buffers) or 2% (for Gdx buffers) error in substrate concentration and a 2% error in proton concentration.

Derivation of transport equations

We assume that transport proceeds according to a stoichiometric transport reaction:

$$(1)\ nIon_{out} + mSubstrate_{out} \rightleftarrows nIon_{in} + mSubstrate_{in}$$

If *n* and *m* are the same sign, this equation describes symport while if *n* and *m* are opposite signs, the equation describes antiport. Note that if *n* and *m* are opposite signs, Equation 1 can be rearranged to give an equation for antiport with positive stoichiometric coefficients:

$$(2)\ nIon_{in} + mSubstrate_{out} \rightleftarrows nIon_{out} + mSubstrate_{in}$$

The chemical potential of ion and substrate across the membrane is given by:

$$(3)\ \Delta\mu_i = RT\ln\left(\frac{[Ion]_{in}}{[Ion]_{out}}\right) + z_{Ion}F\Delta\Psi$$

$$(4)\ \Delta\mu_s = RT\ln\left(\frac{[Substrate]_{in}}{[Substrate]_{out}}\right) + z_{Substrate}F\Delta\Psi$$

At time zero in our SSME assay, there is no membrane voltage. Thus, the chemical potentials of the ion and substrates are described completely by their respective gradients:

$$(5)\ \Delta\mu_i = RT\ln\left(\frac{[Ion]_{in}}{[Ion]_{out}}\right)$$

$$(6)\ \Delta\mu_s = RT\ln\left(\frac{[Substrate]_{in}}{[Substrate]_{out}}\right)$$

The free energy for the coupled transport reaction is given by:

$$(7)\ \Delta G = n\Delta\mu_i + m\Delta\mu_s$$

When $\Delta G = 0$,

$$(8)\ -\frac{n}{m} = \frac{\Delta\mu_s}{\Delta\mu_i} = \frac{RT\ln\left(\frac{[Substrate]_{in}}{[Substrate]_{out}}\right)}{RT\ln\left(\frac{[Ion]_{in}}{[Ion]_{out}}\right)}$$

Thus, plotting transported charge against $\Delta\mu_s/\Delta\mu_i$ gives an x-intercept at $-n/m$, allowing determination of the transport stoichiometry. For more complete mathematical descriptions of transport equations, see previous publications [18,47,48]

Acknowledgements

We thank Dr. Maria Barthmes and Dr. Andre Bazzone for their support of the assay development, Dr. Joe Mindell for the vcINDY plasmid and purification protocol, and Dr. Merritt Maduke for helpful feedback on manuscript clarity. Funding was provided by National Institutes of Health Grant 1R01GM095839 (NET and KHW), NIH National Research Service Award T32 GM007215 (NET), and Stanford Bridge Funding (FW). All data needed to evaluate conclusions of the manuscript are present in the paper and/or supplementary materials. Requests for the data should be submitted to KHW. The authors declare that they have no competing interests.

Figure and Tables

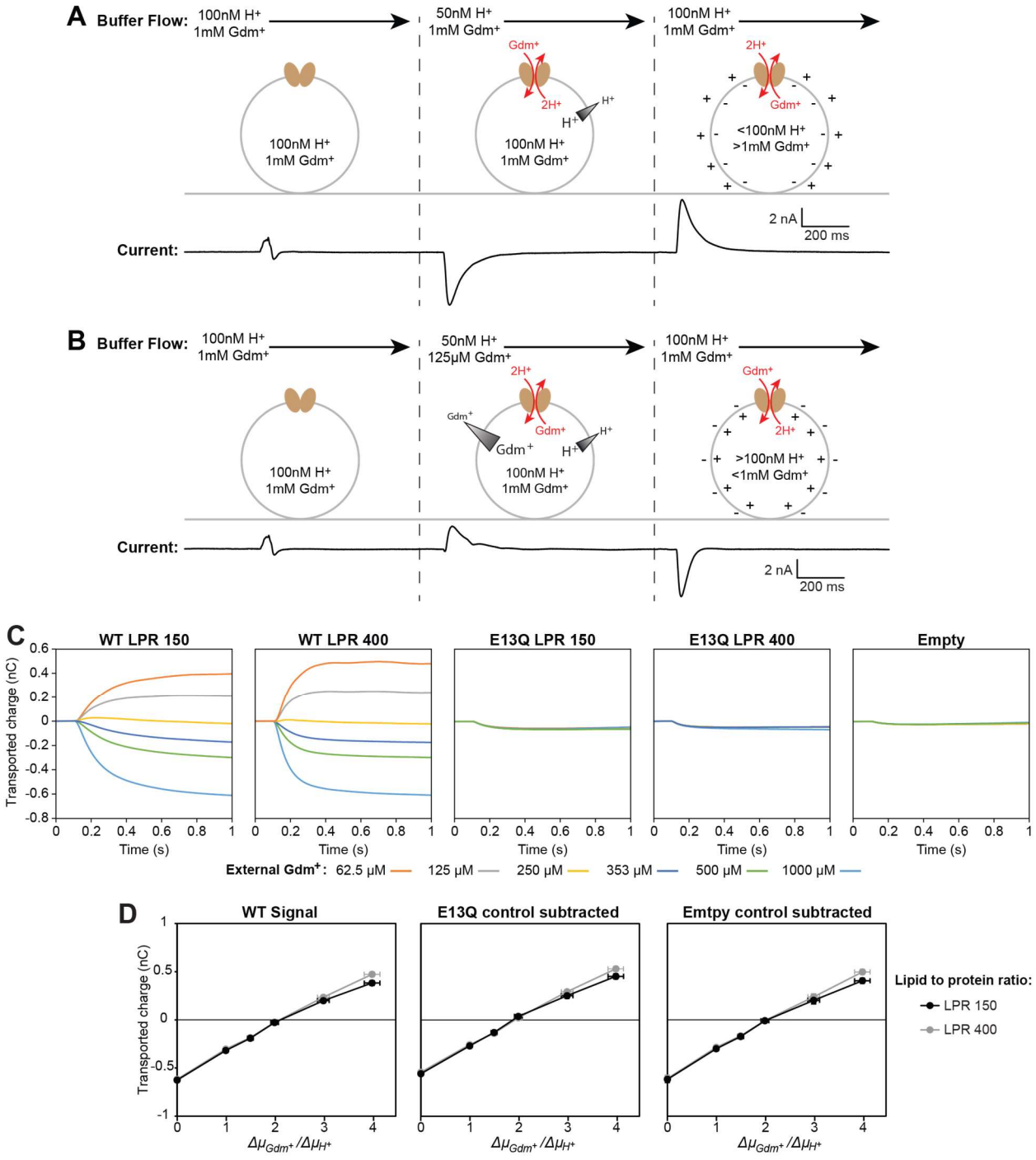

Fig. 1 – SSME reversal assay with Gdx. Each assay consists of three stages of buffer perfusion. In the first stage, the “non-activating” buffer is identical to the internal buffer of the liposomes. In the second stage, the “activating” buffer sets a proton gradient and the guanidinium gradient is

varied, leading to the transport on-current. In the third stage, “non-activating” buffer is reintroduced, and the transport off-current is observed as the liposomes return to their initial state. **(A)** The activating buffer sets a two-fold proton gradient but no guanidinium gradient. The proton gradient drives guanidinium transport into the liposomes in exchange for two protons. Net charge is transported out of the liposomes, creating a negative on-current. **(B)** The activating buffer sets a two-fold proton gradient and an eight-fold guanidinium gradient. The guanidinium gradient drives uphill proton transport into the liposomes, creating a positive on-current. **(C)** For stoichiometry analysis, the on-current is integrated to observe transported charge. **(D)** Plotting integrated on-current as a function of imposed gradient ratios yields null transport at the published $2H^+/Gdm^+$ stoichiometry, regardless of subtraction of background signal. Data points represent average normalized values obtained from four sensors for each (proteo)liposome sample. Y-error bars represent standard error of the mean, propagated where necessary, and X-error bars are calculated by propagation assuming a 2% error in substrate and ion concentrations. Complete buffer conditions can be found in Table 1.

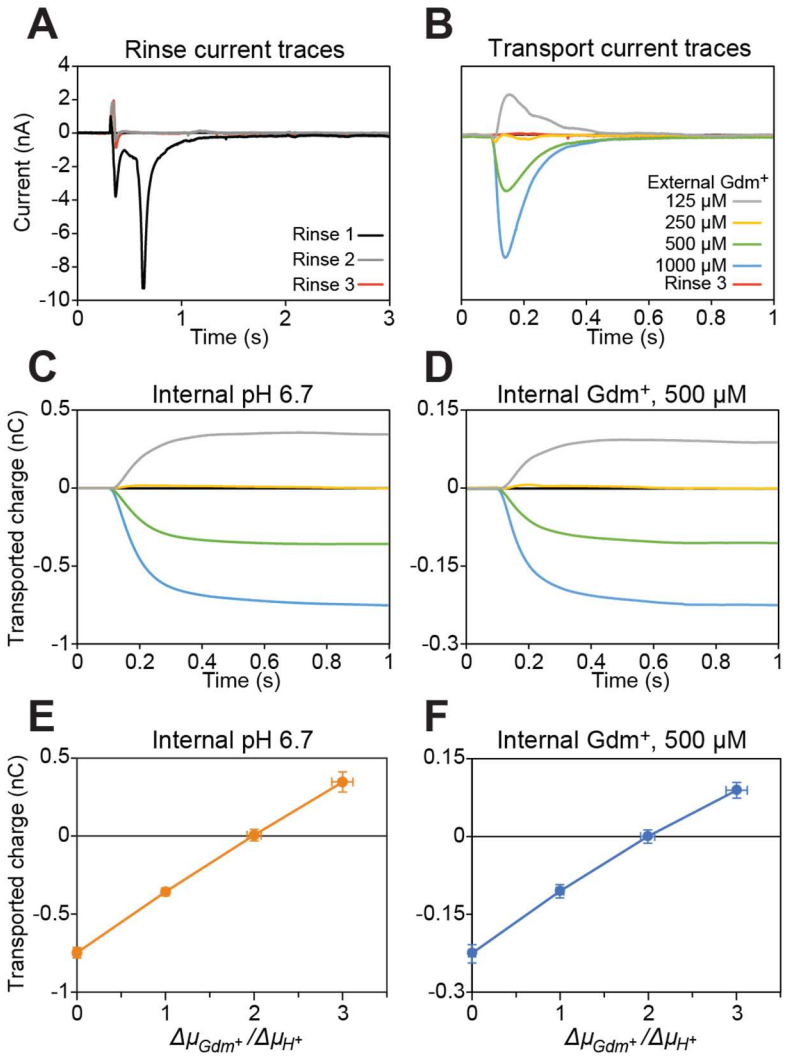

Fig. 2 – Internal concentrations can be quantitatively changed on the sensor. (A) Plots of currents of successive rinses to change the internal buffer pH 7.00 and 1 mM guanidinium to pH 6.70 and 1 mM guanidinium. **(B)** Representative current traces for transport at the low pH condition compared with current from the final rinse. **(C)** and **(D)** Average integrated current traces for each internal buffer condition with signal from E13Q sensors subtracted. **(E)** and **(F)** Plots of transported charge vs. potential ratios for an internal buffer conditions, with signal from E13Q sensors subtracted. Complete buffer conditions can be found in Table 1. Data points represent average normalized values obtained from four sensors for each sample condition. Y-error bars

represent propagated standard error of the mean and X-error bars are calculated by propagation assuming a 2% error in substrate and ion concentrations.

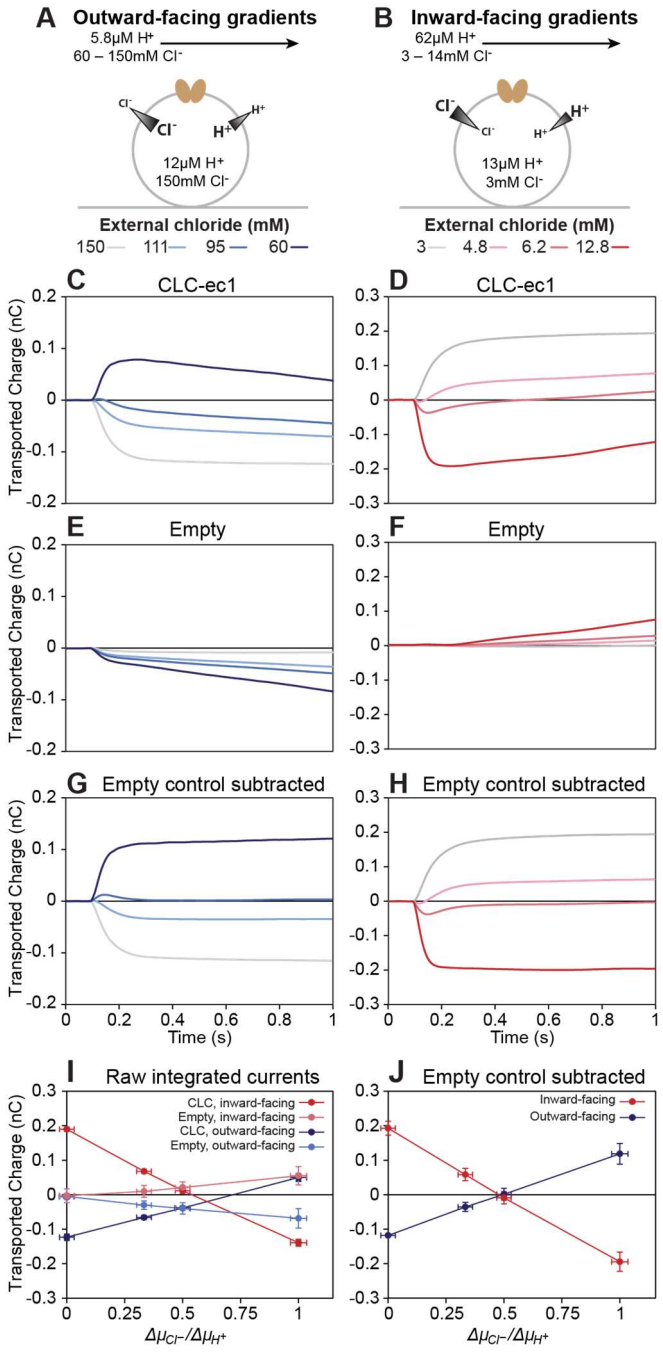

Fig. 3 – CLC-ec1 chloride reversal assay. The SSME reversal assay was performed with CLC-ec1 sensors with both outward-facing and inward-facing proton and chloride gradients. **(A)** and **(B)** Depiction of the internal and external buffer conditions during the on-current stage of the

SSME assay. **(C)** and **(D)** Average integrated current traces for CLC-ec1 sensors. **(E)** and **(F)** Average integrated current traces for sensors prepared with empty liposomes. **(G)** and **(H)** Average integrated current traces with signal from empty liposomes subtracted. **(I)** Plots of transported charge vs. chemical potential ratios for CLC-ec1 and empty liposomes with either outward-facing or inward-facing gradients. Empty liposome negative controls measured significant signal as the chloride gradient increased. **(J)** Correct stoichiometry of $1H^+/2Cl^-$ is obtained after subtracting the negative control signal from the sample signal. For **(I)** and **(J)**, data points represent average normalized values obtained from four sensors for each (proteo)liposome sample. Y-error bars represent standard error of the mean, propagated where necessary, and X-error bars are calculated by propagation assuming a 1% error in chloride concentrations and 2% error in proton concentrations. Complete buffer conditions can be found in Table 2.

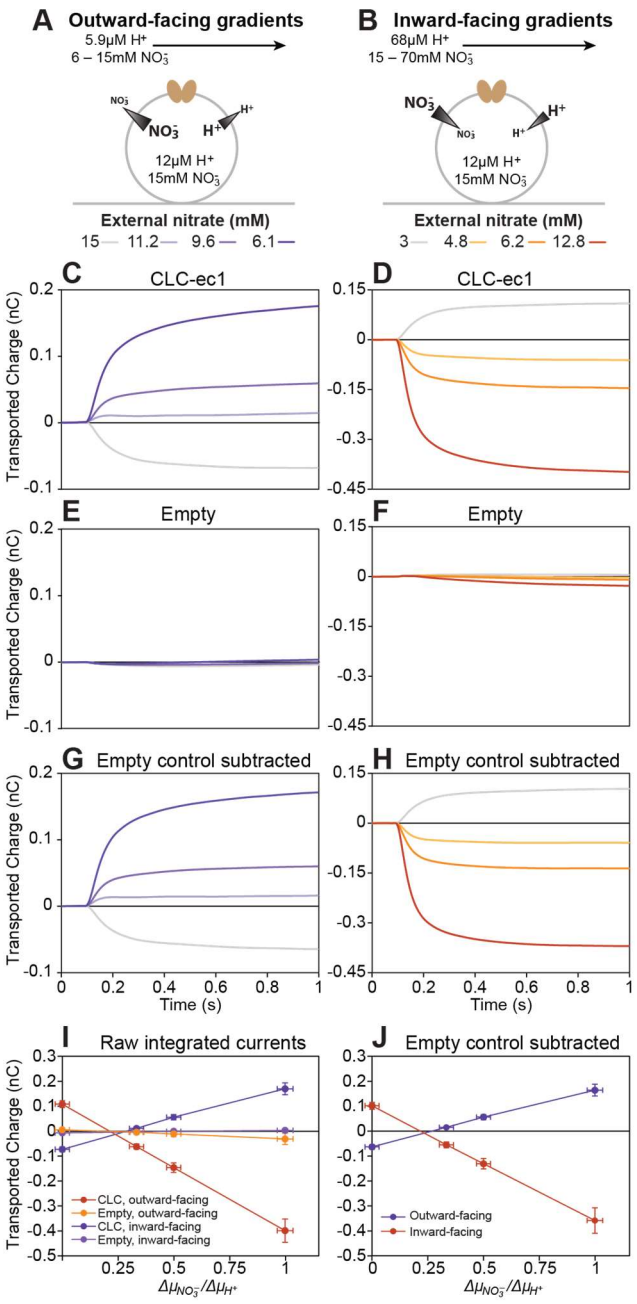

Fig. 4 – CLC-ec1 nitrate reversal assay. The SSME reversal assay was performed with CLC-ec1 sensors with both outward-facing and inward-facing proton and nitrate gradients. **(A)** and **(B)** Depiction of the internal and external buffer conditions during the on-current stage of the SSME assay. **(C)** and **(D)** Average integrated current traces for CLC-ec1 sensors. **(E)** and **(F)** Average integrated current traces for sensors prepared with empty liposomes. **(G)** and **(H)** Average integrated current traces with signal from empty liposomes subtracted. **(I)** Plots of transported

charge vs. chemical potential ratios for CLC-ec1 and empty liposomes with either inward-facing or outward-facing gradients. **(J)** Plots of integrated nitrate transport currents vs. chemical potential ratios with the signal from empty liposomes subtracted. Reversal occurs at a potential ratio below 0.5, indicating that CLC-ec1 transports nitrate with decreased proton coupling compared to chloride, but the reversal point is too similar between the two conditions to distinguish between tightly coupled and loosely coupled transport. For **(I)** and **(J)**, data points represent average normalized values obtained from three sensors for each (proteo)liposome sample. Y-error bars represent standard error of the mean, propagated where necessary, and X-error bars are calculated by propagation assuming a 1% error in nitrate concentrations and 2% error in proton concentrations. Complete buffer conditions can be found in Table 2.

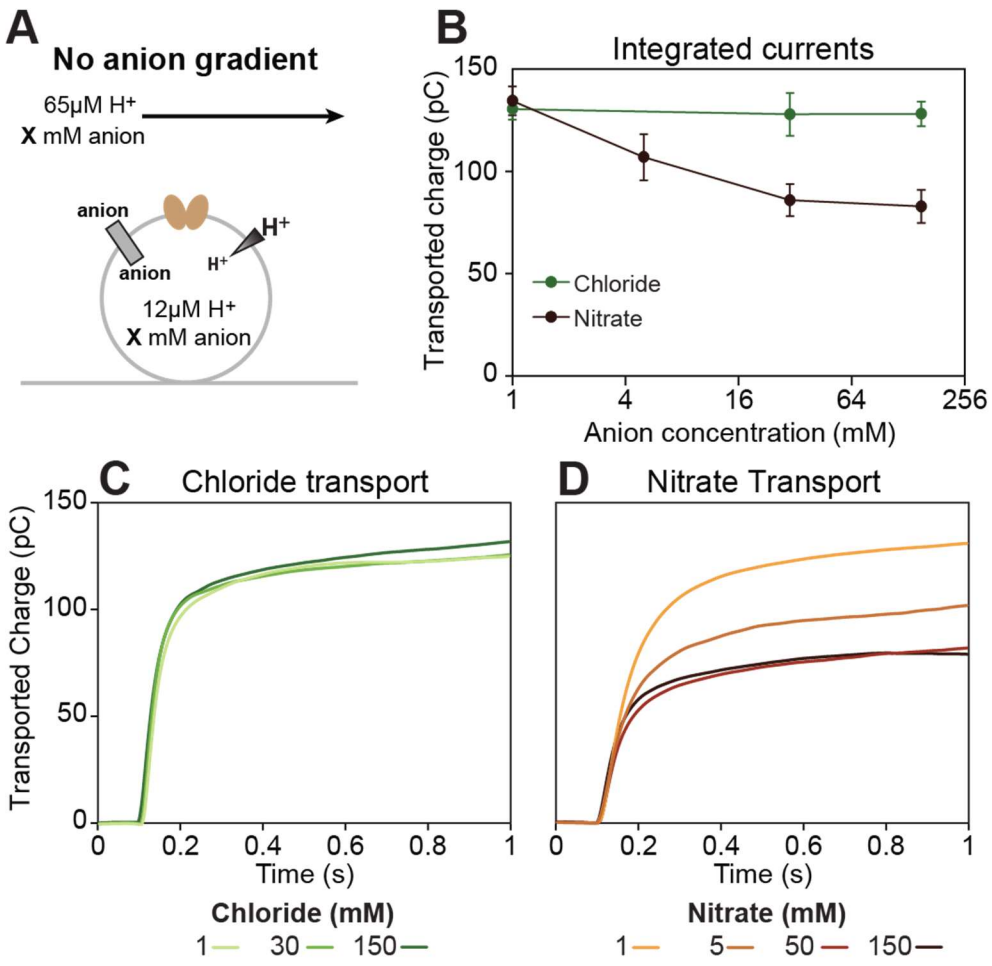

Fig. 5 – CLC-ec1 transports nitrate with reduced proton coupling due to nitrate leak. Sensors were successively equilibrated at seven different anion concentrations: 150mM, 30mM and 1mM chloride, and then 1mM, 30mM, 150mM, and 5mM nitrate. For each data point, the external buffer was set to create an inward-facing proton gradient, but no anion gradient **(A)**. With these conditions, the chemical potentials of the transported substrates are constant. Thus, if transport is tightly coupled, the amount of observed transport should not change with changing anion concentrations. If substrate leak is possible, it will occur in the opposite direction of the electrochemical gradients created by proton:anion antiport, reducing the signal. **(B)** Integrated current does not change as a function of chloride concentration but decreases as nitrate concentration increases. This confirms that chloride transport is tightly coupled and indicates that nitrate's reduced proton coupling is due to nitrate leak. Data points represent average normalized values obtained from three sensors, with signal from empty sensors subtracted. Error bars indicate the standard error of the mean. **(C)** Average integrated current traces for chloride transport, with signal from empty liposome controls subtracted. **(D)** Average integrated current traces for nitrate transport, with signal from empty liposome controls subtracted.

Table 1 – Gdx reversal assay conditions

Fig.	Internal Conditions	External Conditions					
1	pH 7.0 1 mM Gdm^+	pH 7.3 1 mM Gdm^+	pH 7.3 500 µM Gdm^+	pH 7.3 353 µM Gdm^+	pH 7.3 250 µM Gdm^+	pH 7.3 125 µM Gdm^+	pH 7.3 62.5 µM Gdm^+
2B,C,E	pH 6.7 1 mM Gdm^+	pH 7.0 1 mM Gdm^+	pH 7.0 500 µM Gdm^+		pH 7.0 250 µM Gdm^+	pH 7.0 125 µM Gdm^+	
2D,F	pH 7.0 500 µM Gdm^+	pH 7.35 500 µM Gdm^+	pH 7.35 223 µM Gdm^+		pH 7.35 100 µM Gdm^+	pH 7.35 44 µM Gdm^+	
Chemical potential ratio ($\Delta\mu_{Gdm^+}/\Delta\mu_{H^+}$)		0	1	3/2	2	3	4

Table 2 – CLC-ec1 reversal assay conditions

Fig.	Internal Conditions	External Conditions			
3, blue	pH 4.84 150 mM chloride	pH 5.24 150 mM chloride	pH 5.24 111 mM chloride	pH 5.24 95 mM chloride	pH 5.24 60 mM chloride
3, red	pH 4.88 3 mM chloride	pH 4.21 3 mM chloride	pH 4.21 5 mM chloride	pH 4.21 6.5 mM chloride	pH 4.21 14 mM chloride
4, orange	pH 4.84 15 mM nitrate	pH 4.17 15 mM nitrate	pH 4.17 25 mM nitrate	pH 4.17 32 mM nitrate	pH 4.17 70 mM nitrate
4, purple	pH 4.84 15 mM nitrate	pH 5.23 15 mM nitrate	pH 5.23 11.2 mM nitrate	pH 5.23 9.6 mM nitrate	pH 5.23 6.1 mM nitrate
Chemical potential ratio ($\Delta\mu_{anion}/\Delta\mu_{H^+}$)		0	1/3	1/2	1

Supporting Information

A note on replicates and reproducibility

As we collected our data, we observed several trends which impacted our subsequent data analysis. All Gdx data were collected using four sensors per sample condition (LPR150, LPR400, etc.). Each sensor was then used to record two traces per chemical potential ratio, which allowed us to assess the reproducibility of the data both from different recordings on the same sensor and from recordings of the same conditions across different sensors. Different traces from the same sensor overlay strikingly well (Fig. S1A), but there is variability in the amount of signal observed across different sensors (Fig. S1B). This is not surprising, as the amount of signal depends on the number of liposomes that are adsorbed to the electrode surface during sensor preparation. Nevertheless, the signal trends across sensors are consistent (Figs. S1C, S1E, and S2). Normalizing the signal observed on a given sensor to the average total signal from that sensor accounts for the variation between different sensors (Fig. S1 D,F), and thus, data normalization was performed for all samples.

Analysis of integrated current vs. analysis of peak current

We analyzed the results of changing the applied proton and substrate gradient on observed current using two methods: peak on-current (Fig. S3 and S4) and integrated on-current (Fig. 1). Peak on-current is a parameter related to the turnover rate of the transporter and is a commonly quantified for SSME experimental analysis[27,28,49–51]. However, peak current is ultimately a kinetic parameter, while transport stoichiometry is a thermodynamic quantity. We therefore considered a second parameter by analyzing the integrated current, representing the total net charge movement, as a function of the chemical potential ratio.

The peak current reverses near the expected potential, but changes with both protein concentration and the type of negative control (Fig. S4B). This renders it difficult to distinguish

between the previously reported $2H^+$:$1Gdm^+$ antiport stoichiometry and a less likely but still theoretically possible $3H^+$:$2Gdm^+$ antiport stoichiometry. However, plotting the integrated on-current as a function of chemical potential ratio clearly and precisely yields the published $2H^+$:$1Gdm^+$ transport stoichiometry (Fig. 1D). This result is unchanged when either the empty liposome or E13Q controls are subtracted. This confirms that the thermodynamic parameter of integrated current is the better metric for determining transport stoichiometry in this assay.

Effect of experimental conditions on transport stoichiometry

Untangling transporter-mediated leak from coupled transport is a different proposition than separating coupled transport from a background signal, as transporter-mediated leak cannot be isolated with negative controls. Instead, it is helpful to consider the relationship between the kinetic mechanism and the transport thermodynamics of a loosely coupled system. Figure S6 shows simple kinetic models for both tightly coupled (Fig. S6A) and loosely coupled (Fig. S6B) transporters. In a tightly coupled system, there is only one transport pathway, setting a single transport stoichiometry that is invariant across experimental conditions. In contrast, the loosely coupled model allows both coupled antiport (red cycle) and leak (blue cycles). The apparent transport stoichiometry in such a system is a function of the relative flux through the coupled and uncoupled (leak) pathways, which depends on the relative rates of substrate binding, substrate release, and alternating access. Changing the proton or substrate concentrations will change the substrate binding rates, altering the partitioning between pathways, the net flux through leak and transport cycles, and the apparent net stoichiometry[6,21,37].

Goldman-Hodgkin-Katz reversal potential and subtracting background signal

The ability to quantitatively exchange the internal liposomal contents indicates that the integrity of the lipid bilayers in our samples are imperfect. While this property is not unique to SSME (no lipid bilayer is completely impermeable to ions), it is important to consider the implications that ion leak

currents have on our assays. In SSME, charge transport proceeds until the membrane voltage reaches the reversal potential[32]. The Goldman-Hodgkin-Katz (GHK) voltage equation (Eq. S1) describes the reversal potential in terms of the relative flux of permeant ions[47]. For monovalent ions, the equation can be written:

$$\text{(S1)}\ E_{rev} = \frac{RT}{F} ln\left(\frac{\sum_i^n P_{C_i^+}\left(C_i^+\right)_{out} + \sum_j^m P_{A_j^-}\left(A_j^-\right)_{in}}{\sum_i^n P_{C_i^+}\left(C_i^+\right)_{in} + \sum_j^m P_{A_j^-}\left(A_j^-\right)_{out}}\right)$$

Where E_{rev} is the reversal potential, R is the universal gas constant, F is Faraday's constant, C and A are monovalent cations and anions, respectively, and P is the relative permeability of each ion. This equation holds true as long as the concentrations of the permeable ions are constant. While transport must change ion concentrations to some extent, the relative linearity of the graphs of transported charge against substrate potential (Fig. 1D, 2E, 2F, 3J, and 4J) indicates that the equilibrium voltage is a direct, linear function of the initial chemical gradients. Thus, the concentrations must not change significantly during the one second that transport is measured, and the GHK equation can be applied.

The relevant takeaway from the GHK equation for our assay is that ion permeability through the lipid bilayer should have a predictable impact on the amount of observed transport. If bilayer permeability is much slower than permeability through the transporter, the observed transport at a given condition will be a function only of the stoichiometry of the transporter. This is what we observe with Gdx, where currents in the negative controls are minimal compared to currents in samples containing active transporter. At the other extreme, if bilayer permeability is fast relative to coupled transport, then leak currents will dominate and transport currents will be unobservable. This explains why stoichiometry determination using our SSME assay fails for low turnover transporters such as VcINDY. In between these two extremes are examples such as CLC-ec1, where transport is faster than leak, but leak currents are still observable on the timescale of the measurements. The GHK equation indicates that signal from the coupled transport process can

still be determined under these conditions, as long as the signal due to bilayer permeability can be isolated and subtracted. This is precisely what we observe with CLC-ec1. Subtracting the empty liposome signal from the CLC-ec1 signal unambiguously yields CLC-ec1's $2Cl^-$:$1H^+$ antiport stoichiometry.

Additional experimental conditions can help determine when leak currents can be subtracted versus when they are too large to be dealt with effectively. Changing permeant ion concentrations while maintaining the ion gradient ratios will change the relative rates of transport and leak currents and thus, change the GHK reversal potential. While the thermodynamics of the system will be altered, the thermodynamics of a tightly coupled transport process will be constant. Once again, this is borne out by the CLC-ec1 data. When only the CLC-ec1 liposome signals are considered, the null transport point varies significantly between the outward-facing (150 mM internal chloride, Fig. 3I, dark blue) and inward-facing (3 mM internal chloride, Fig. 3I, dark red) gradient conditions. However, the empty liposome controls allow the background signal to be isolated, and the difference between conditions disappears when the empty liposome signals are subtracted (Fig. 3J).

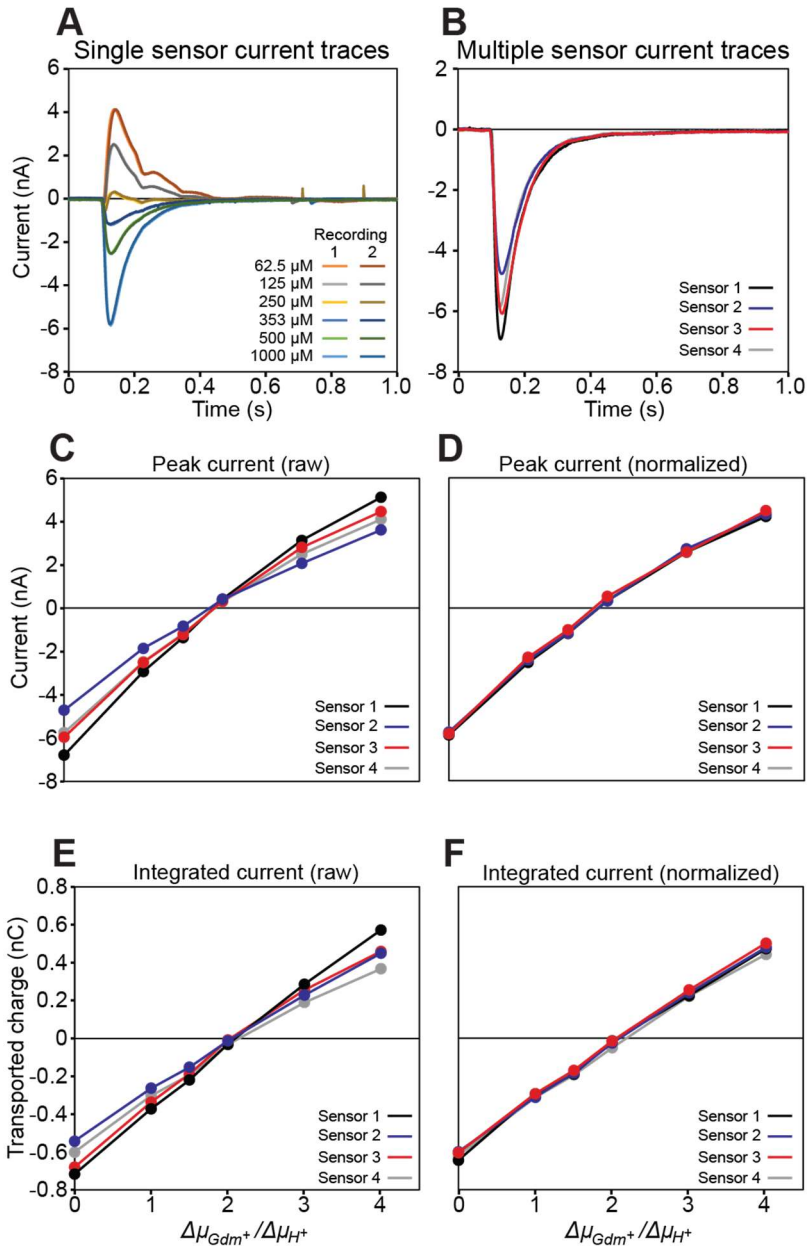

Fig. S1 – Examples of replicates and data normalization. (A) Representative current traces showing two recordings of a single sensor for each external buffer condition. Current traces for the same condition overlay nearly perfectly, indicating that little variability is introduced from repeated recordings on a single sensor. **(B)** Current traces for a single condition (1 mM Gdm+, pH 7.3 external) for four different sensors indicate that there is variability in signal intensity across different sensors. Nevertheless, each sensor exhibits the same trends in both peak current **(C)**

and integrated current **(D)** across the different experimental conditions. Normalizing the total signal observed on each sensor to the average total signal observed across sensors accounts for most of the variability observed between sensors in both peak **(E)** and integrated **(F)** currents. All data shown is for WT-Gdx LPR 400 liposomes. The same trends in data reproducibility were observed for all sample conditions.

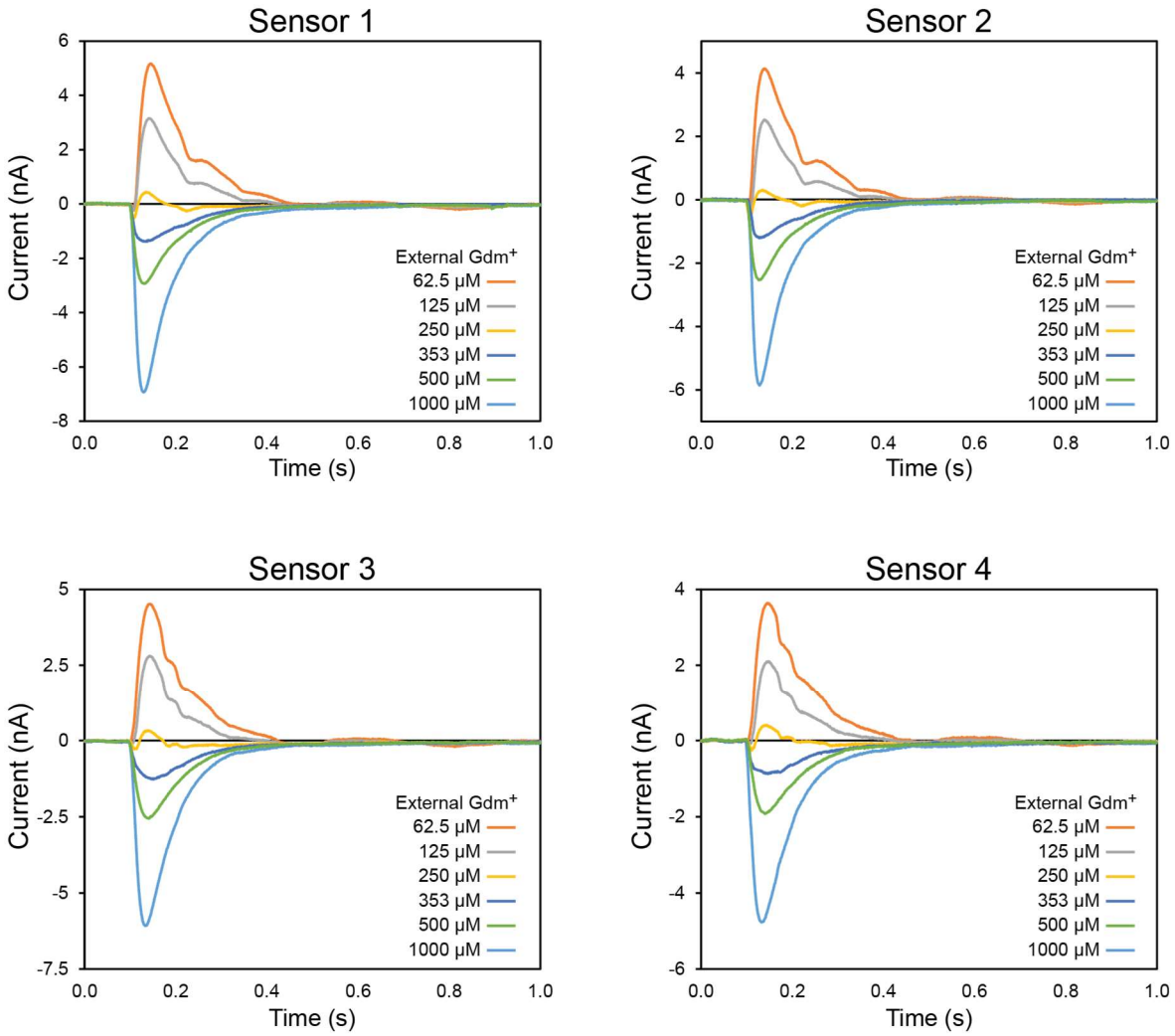

Fig. S2 – *Current traces from all WT Gdx LPR 400 sensors*. Amount of transport varied across sensors(note the variation in the scale of the y-axis), but signal trends across different external buffer conditions is consistent from sensor to sensor.

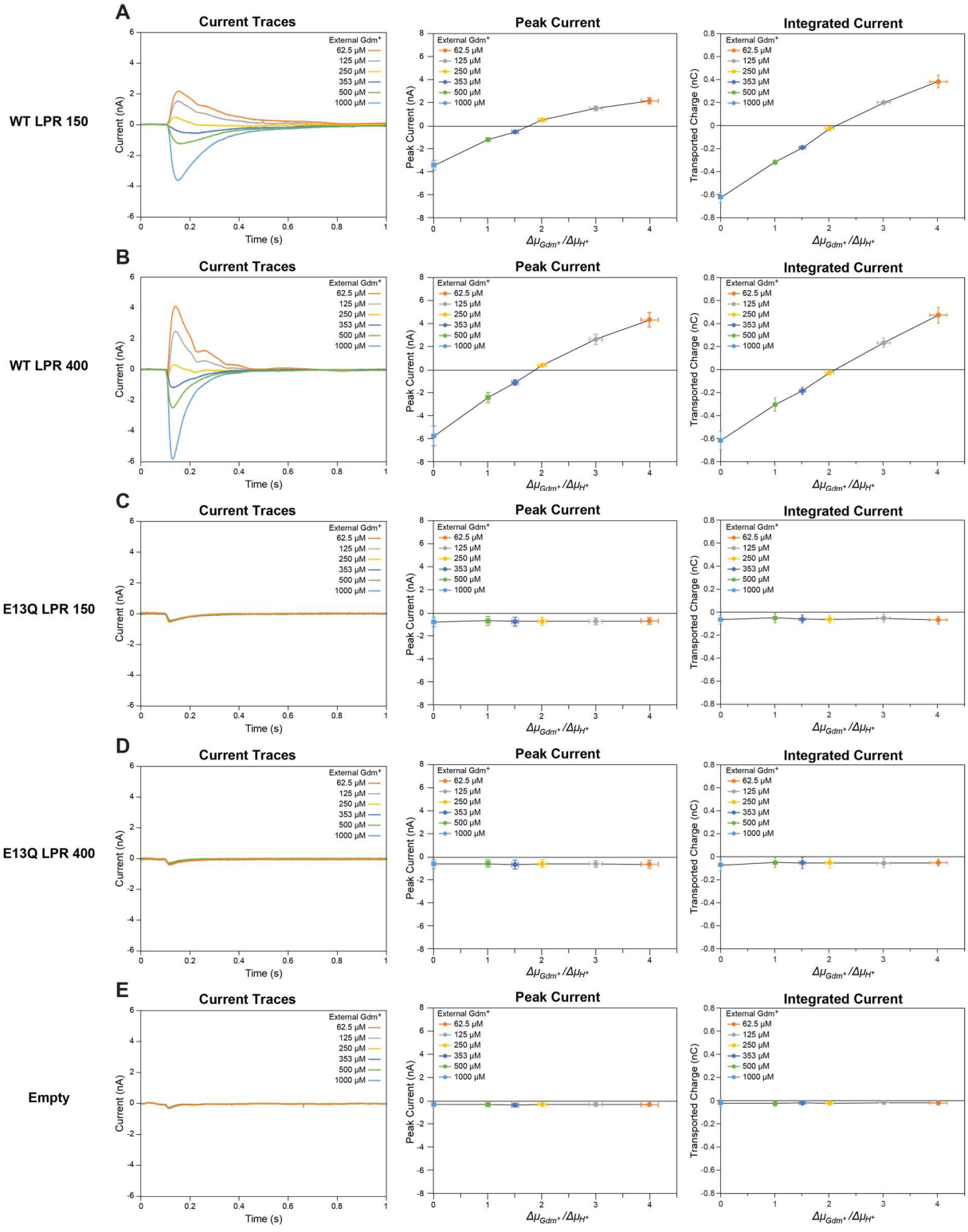

Fig. S3 – Reversal assay data across sample conditions. Representative current traces (*left column*), average peak current (*middle column*), and average integrated current (*right column*) for

each external guanidinium concentration are shown for WT-Gdx proteoliposomes with an LPR of 150 **(A)** and an LPR of 400 **(B)**, E13Q-Gdx proteoliposomes with an LPR of 150 **(C)** and an LPR of 400 **(D)**, and empty liposomes **(E)**. Data points represent average values obtained from four sensors for each (proteo)liposome sample. Y-error bars represent standard error of the mean and X-error bars are calculated by propagation assuming a 2% error in substrate and ion concentrations. Complete buffer conditions can be found in Table 1.

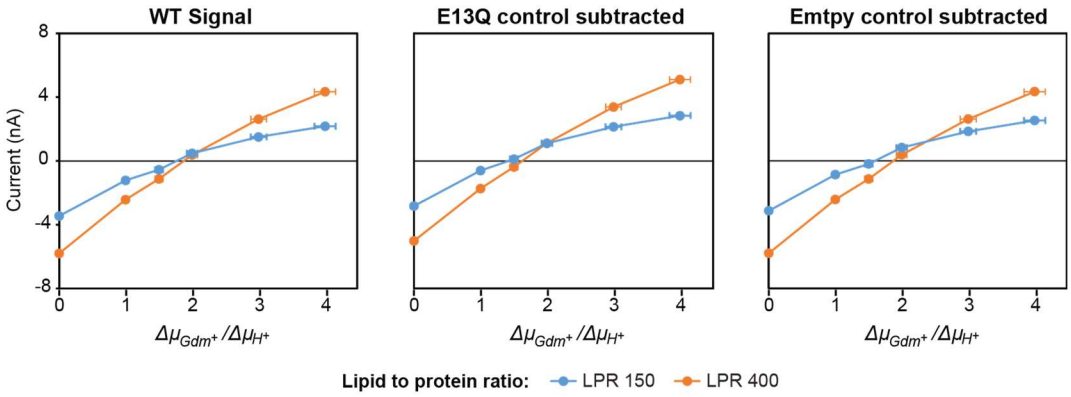

Fig. S4 – Peak current analysis yields the correct stoichiometry. Plots of peak currents against the imposed chemical potential ratio with the indicated data treatment. Peak current analysis yields a null current at a stoichiometry between 1.5 and $2H^+/Gdm^+$, depending on the LPR and on which control (if any) is subtracted. Data points represent average normalized values obtained from four sensors for each (proteo)liposome sample. Y-error bars represent standard error of the mean, propagated where necessary, and X-error bars are calculated by propagation assuming a 2% error in substrate and ion concentrations. Complete buffer conditions can be found in Table 1.

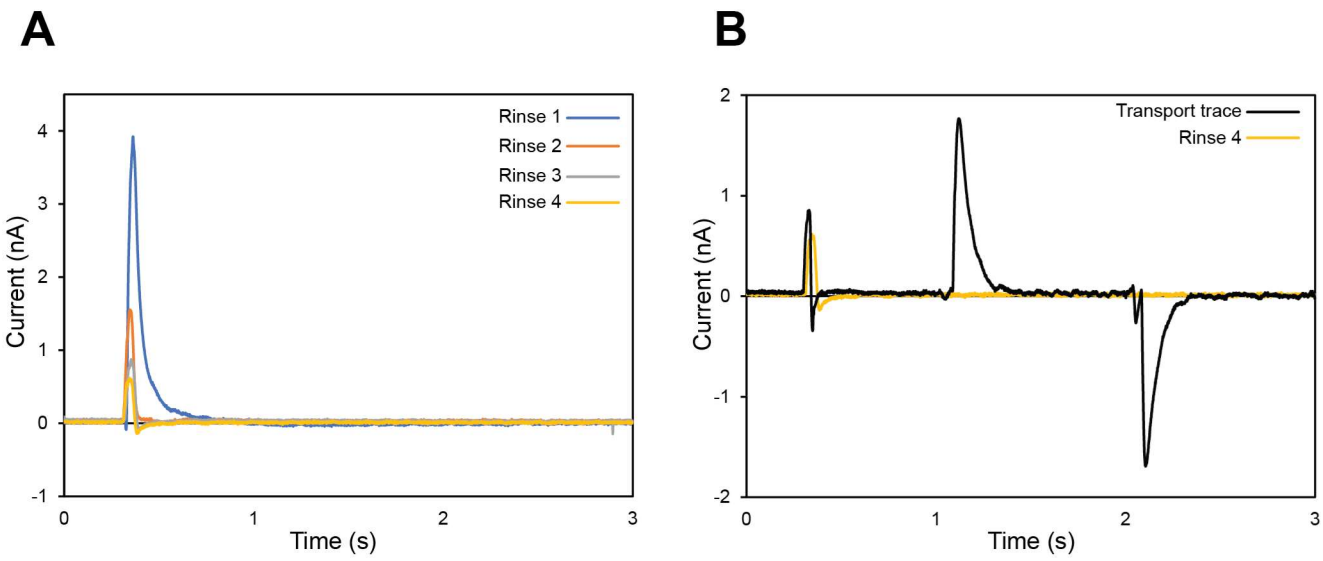

Fig. S5 – Representative current traces of internal buffer exchange. (A) Observed current reaches a baseline level after a sensor previously equilibrated with 150 mM chloride buffer undergoes four successive 600 µL rinses of 30 mM chloride buffer. **(B)** Overlay of the final buffer rinse and the subsequent transport current trace.

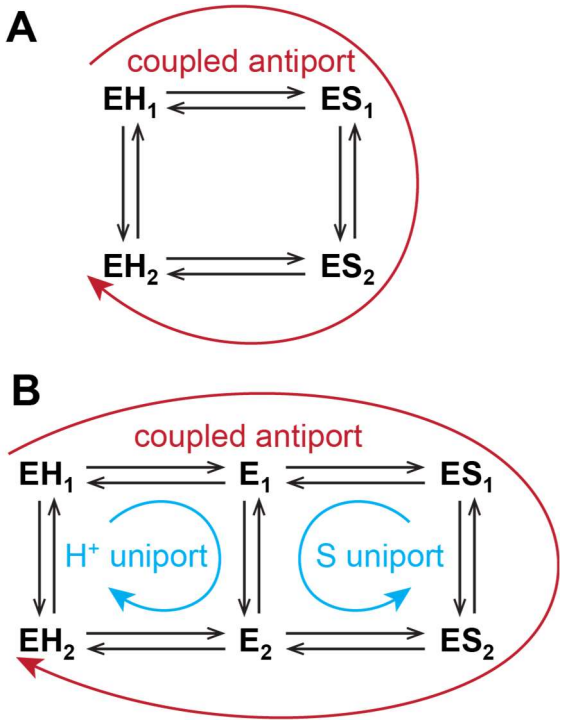

Fig. S6 – Transport models. Depictions of simple kinetic models for tightly coupled **(A)** or loosely coupled **(B)** transport, where EH is proton-bound transport, ES is substrate-bound transporter, E is empty transporter, and the subscript indicates the orientation of the transporter with respect to the membrane. In **(A)**, only one transport cycle is available, setting a single transport stoichiometry. In **(B)**, coupled antiport is still possible (red cycle), but alternating access of the empty transporter can short-circuit transport, leading to proton and substrate leak cycles (blue).

Chapter 3 Addendum

Apart from a general desire to develop a better method of measuring transport stoichiometry, our motivation for developing the assay described in this chapter was to use it to test the function of EmrE under a variety of experimental conditions. Like CLC-ec1 with nitrate transport, the free exchange model predicts that EmrE should transport drug with different stoichiometries at different experimental conditions[6,17]. The data included here is preliminary (only one replicate is shown, though qualitatively, results have been consistent across multiple technical and biological replicates), but initial SSME reversal assays are consistent with our hypothesis.

We tested the effects of varying both the drug concentration and the proton concentration on EmrE's stoichiometry. Under all conditions, the size of the proton gradient was constant – 2-fold and inwardly directed. To test the effect of the drug concentration, we equilibrated sensors at pH 7.3 and perfused pH 7.0 buffer with either 10 μM or 40 μM methyltriphenylphosphonium ($MeTPP^+$) for the low or high drug concentration experiments, respectively. The internal drug concentration was varied to give the indicated chemical potential ratios (Addendum Figure 1A). At low drug concentrations, the signal reversed with an apparent stoichiometry of just over 2 protons per drug. However, at high drug concentrations, the signal no longer reversed, even when the 2-fold proton gradient was combined with a 16-fold drug gradient, indicating that EmrE's transport stoichiometry is dependent on drug concentration.

We then tested the effect of the proton concentration by repeating the assay with 10 μM external $MeTPP^+$, but with varied internal and external proton concentrations, with the internal pH value 0.3 units higher than the external value. At average pH values of 7.15, 6.85, or 6.55, transport direction reversed with an identical apparent stoichiometry of just over 2 protons per drug. At pH values below or above this range, the apparent stoichiometry increased, indicating an increased prevalence of a proton leak pathway in addition to the coupled antiport pathway.

At the most alkaline conditions (average pH values of 7.75 and 8.05), transport never reversed direction, even with a 16-fold drug gradient.

Taken together, these initial results suggest that the loosely coupled free exchange model effectively describes EmrE's drug transport behavior. EmrE is most efficient at neutral or slightly acidic pH, as expected given the pH environment across the inner membrane of *E. coli*. EmrE's loss of efficiency at high drug concentrations is less readily explained, but once again, is better understood in a physiological context. EmrE is just one of a large network of multidrug efflux pumps that work together to rid *E. coli* of toxic compounds[52]. The AcrAB-TolC complex actively removes drugs from the periplasm and pumps them across the outer membrane, reducing the effective drug concentration that EmrE must manage. Furthermore, the loss of proton-coupling efficiency at higher drug concentrations does not necessarily imply a loss of drug efflux efficacy. At high drug concentrations, it may be more important for EmrE to be able to quickly remove drug from the cytoplasm than to do so with peak thermodynamic efficiency. While these experiments will need to be replicated for publication, these results indicate that EmrE is finely tuned to function in its native physiological environment.

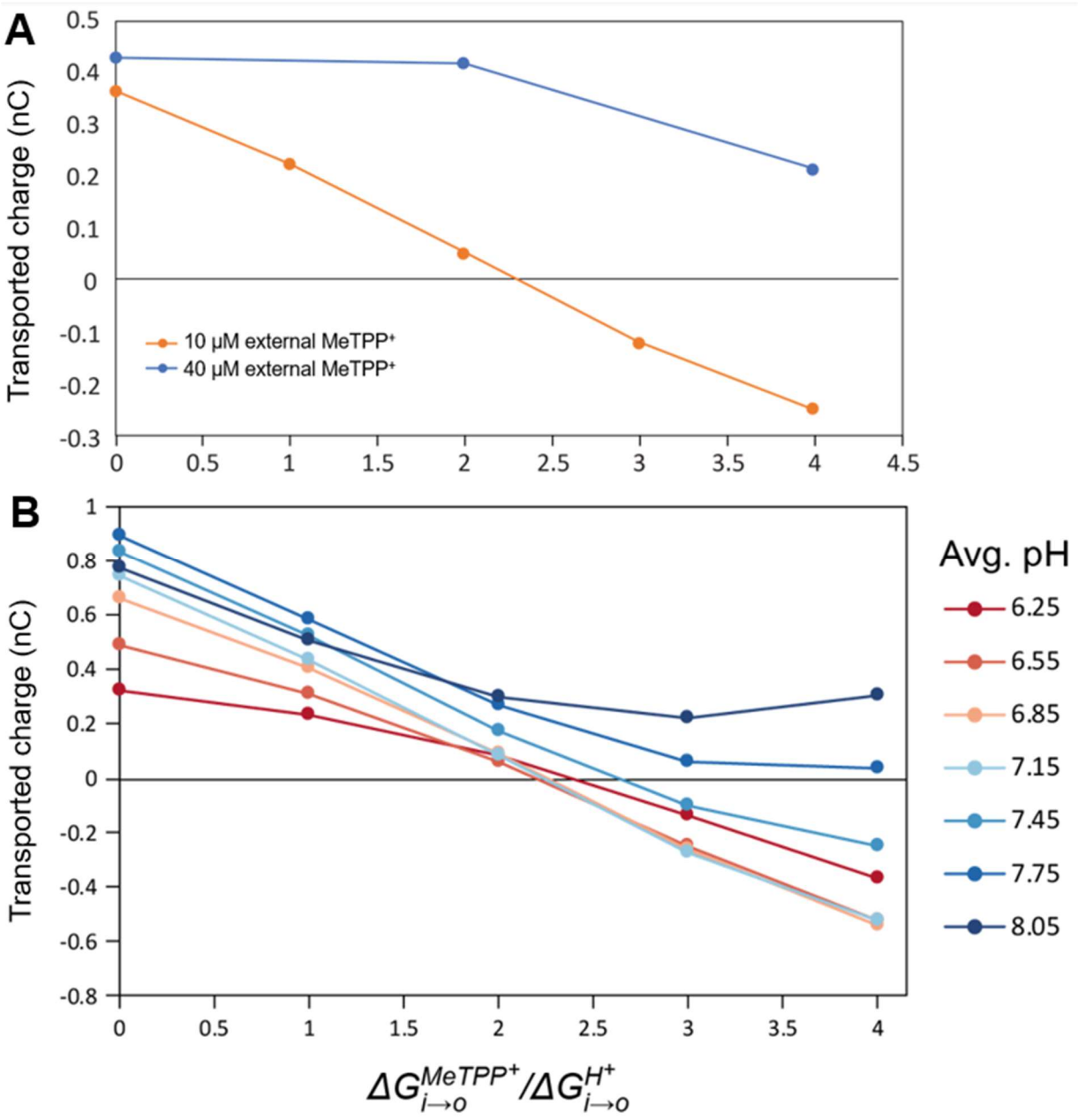

Addendum Figure 1 – *EmrE's transport stoichiometry varies with experimental conditions.* (A) At low MeTPP$^+$ concentrations, the apparent proton:drug coupling stoichiometry is just above 2:1 when the internal pH is 7.3 and the external pH is 7.0. At higher concentrations, transport

becomes less efficient and transport direction fails to reverse, even at gradient ratios corresponding to an apparent stoichiometry of 4:1. (B) At low $MeTPP^+$ concentrations ($[MeTPP^+]_{ext}$ = 16 μM), the apparent proton:drug coupling stoichiometry varies with pH. For all conditions, the internal pH is 0.3 units higher than the external pH. Transport is most efficient near neutral pH and fails to reverse direction at alkaline pH.

References

1. Garibsingh, R.-A. A. & Schlessinger, A. Advances and challenges in rational drug design for SLCs. *Trends Pharmacol Sci* **40**, 790–800 (2019).

2. Lin, L., Yee, S. W., Kim, R. B. & Giacomini, K. M. SLC Transporters as Therapeutic Targets: Emerging Opportunities. *Nat Rev Drug Discov* **14**, 543–560 (2015).

3. Bazzone, A., Zabadne, A. J., Salisowski, A., Madej, M. G. & Fendler, K. A Loose Relationship: Incomplete H+/Sugar Coupling in the MFS Sugar Transporter GlcP. *Biophysical Journal* **113**, 2736–2749 (2017).

4. Burtscher, V., Schicker, K., Freissmuth, M. & Sandtner, W. Kinetic Models of Secondary Active Transporters. *Int J Mol Sci* **20**, (2019).

5. Coady, M. J., Chen, X.-Z. & Lapointe, J.-Y. rBAT is an Amino Acid Exchanger with Variable Stoichiometry. *J. Membrane Biol.* **149**, 1–8 (1996).

6. Hussey, G. A., Thomas, N. E. & Henzler-Wildman, K. A. Highly coupled transport can be achieved in free-exchange transport models. *J. Gen. Physiol.* **152**, (2020).

7. Kang, T. M. & Hilgemann, D. W. Multiple transport modes of the cardiac Na+/Ca2+ exchanger. *Nature* **427**, 544–548 (2004).

8. Sacher, A., Cohen, A. & Nelson, N. Properties of the mammalian and yeast metal-ion transporters DCT1 and Smf1p expressed in Xenopus laevis oocytes. *J. Exp. Biol.* **204**, 1053–1061 (2001).

9. Guskov, A., Jensen, S., Faustino, I., Marrink, S. J. & Slotboom, D. J. Coupled binding mechanism of three sodium ions and aspartate in the glutamate transporter homologue Glt Tk. *Nat Commun* **7**, 1–6 (2016).

10. Li, Z. *et al.* Identification of a Second Substrate-binding Site in Solute-Sodium Symporters. *J. Biol. Chem.* **290**, 127–141 (2015).

11. Piscitelli, C. L., Krishnamurthy, H. & Gouaux, E. Neurotransmitter/sodium symporter orthologue LeuT has a single high–affinity substrate site. *Nature* **468**, 1129–1132 (2010).

12. Schwartz, J. W., Novarino, G., Piston, D. W. & DeFelice, L. J. Substrate binding stoichiometry and kinetics of the norepinephrine transporter. *J. Biol. Chem.* **280**, 19177–19184 (2005).

13. Grabe, M., Zuckerman, D. M. & Rosenberg, J. M. EmrE reminds us to expect the unexpected in membrane transport. *J Gen Physiol* **152**, (2020).

14. Quick, M. *et al.* The LeuT-fold neurotransmitter:sodium symporter MhsT has two substrate sites. *Proc. Natl. Acad. Sci. U.S.A.* **115**, E7924–E7931 (2018).

15. Bozzi, A. T., Bane, L. B., Zimanyi, C. M. & Gaudet, R. Unique structural features in an Nramp metal transporter impart substrate-specific proton cotransport and a kinetic bias to favor import. *J Gen Physiol* **151**, 1413–1429 (2019).

16. Parker, J. L., Mindell, J. A. & Newstead, S. Thermodynamic evidence for a dual transport mechanism in a POT peptide transporter. *eLife* **3**, (2014).

17. Robinson, A. E., Thomas, N. E., Morrison, E. A., Balthazor, B. M. & Henzler-Wildman, K. A. New free-exchange model of EmrE transport. *PNAS* **114**, E10083–E10091 (2017).

18. Fukuhara, Y. & Turner, R. J. The static head method for determining the charge stoichiometry of coupled transport systems. Applications to the sodium-coupled D-glucose transporters of the renal proximal tubule. *Biochim Biophys Acta* **770**, 73–78 (1984).

19. Lapointe, J. Y., Hudson, R. L. & Schultz, S. G. Current-voltage relations of sodium-coupled sugar transport across the apical membrane of Necturus small intestine. *J Membr Biol* **93**, 205–219 (1986).

20. Accardi, A. & Miller, C. Secondary active transport mediated by a prokaryotic homologue of ClC Cl- channels. *Nature* **427**, 803–807 (2004).

21. Nguitragool, W. & Miller, C. Uncoupling of a CLC Cl-/H+ exchange transporter by polyatomic anions. *J. Mol. Biol.* **362**, 682–690 (2006).

22. Fitzgerald, G. A., Mulligan, C. & Mindell, J. A. A general method for determining secondary active transporter substrate stoichiometry. (2017) doi:10.7554/eLife.21016.

23. Ravera, S., Virkki, L. V., Murer, H. & Forster, I. C. Deciphering PiT transport kinetics and substrate specificity using electrophysiology and flux measurements. *Am. J. Physiol., Cell Physiol.* **293**, C606-620 (2007).

24. Shao, X. M., Kao, L. & Kurtz, I. A novel delta current method for transport stoichiometry estimation. *BMC Biophysics* **7**, 14 (2014).

25. Zerangue, N. & Kavanaugh, M. P. Flux coupling in a neuronal glutamate transporter. *Nature* **383**, 634–637 (1996).

26. Groeneveld, M. & Slotboom, D.-J. Na(+):aspartate coupling stoichiometry in the glutamate transporter homologue Glt(Ph). *Biochemistry* **49**, 3511–3513 (2010).

27. Bazzone, A., Barthmes, M. & Fendler, K. SSM-Based Electrophysiology for Transporter Research. *Meth. Enzymol.* **594**, 31–83 (2017).

28. Schulz, P., Garcia-Celma, J. J. & Fendler, K. SSM-based electrophysiology. *Methods* **46**, 97–103 (2008).

29. Kermani, A. A., Macdonald, C. B., Gundepudi, R. & Stockbridge, R. B. Guanidinium export is the primal function of SMR family transporters. *PNAS* **115**, 3060–3065 (2018).

30. Turner, R. J. & Moran, A. Stoichiometric studies of the renal outer cortical brush border membrane D-glucose transporter. *J Membr Biol* **67**, 73–80 (1982).

31. Schulz, P., Dueck, B., Mourot, A., Hatahet, L. & Fendler, K. Measuring Ion Channels on Solid Supported Membranes. *Biophys J* **97**, 388–396 (2009).

32. Garcia-Celma, J., Szydelko, A. & Dutzler, R. Functional characterization of a ClC transporter by solid-supported membrane electrophysiology. *J Gen Physiol* **141**, 479–491 (2013).

33. Walden, M. *et al.* Uncoupling and Turnover in a Cl−/H+ Exchange Transporter. *J Gen Physiol* **129**, 317–329 (2007).

34. Accardi, A., Lobet, S., Williams, C., Miller, C. & Dutzler, R. Synergism between halide binding and proton transport in a CLC-type exchanger. *J Mol Biol* **362**, 691–699 (2006).

35. Jiang, T., Han, W., Maduke, M. & Tajkhorshid, E. Molecular Basis for Differential Anion Binding and Proton Coupling in the Cl(-)/H(+) Exchanger ClC-ec1. *J Am Chem Soc* **138**, 3066–3075 (2016).

36. Wang, Z., Swanson, J. M. J. & Voth, G. A. Modulating the Chemical Transport Properties of a Transmembrane Antiporter via Alternative Anion Flux. *J Am Chem Soc* **140**, 16535–16543 (2018).

37. Henderson, R. K., Fendler, K. & Poolman, B. Coupling efficiency of secondary active transporters. *Current Opinion in Biotechnology* **58**, 62–71 (2019).

38. Paula, S., Volkov, A. G. & Deamer, D. W. Permeation of halide anions through phospholipid bilayers occurs by the solubility-diffusion mechanism. *Biophys J* **74**, 319–327 (1998).

39. Paula, S., Volkov, A. G., Van Hoek, A. N., Haines, T. H. & Deamer, D. W. Permeation of protons, potassium ions, and small polar molecules through phospholipid bilayers as a function of membrane thickness. *Biophys J* **70**, 339–348 (1996).

40. Bazzone, A., Madej, M. G., Kaback, H. R. & Fendler, K. pH Regulation of Electrogenic Sugar/H+ Symport in MFS Sugar Permeases. *PLoS ONE* **11**, e0156392 (2016).

41. Călinescu, O. *et al.* Electrogenic Cation Binding in the Electroneutral Na+/H+ Antiporter of Pyrococcus abyssi. *J. Biol. Chem.* **291**, 26786–26793 (2016).

42. Călinescu, O., Paulino, C., Kühlbrandt, W. & Fendler, K. Keeping it simple, transport mechanism and pH regulation in Na+/H+ exchangers. *J. Biol. Chem.* **289**, 13168–13176 (2014).

43. Mulligan, C., Fitzgerald, G. A., Wang, D.-N. & Mindell, J. A. Functional characterization of a Na+-dependent dicarboxylate transporter from Vibrio cholerae. *J Gen Physiol* **143**, 745–759 (2014).

44. Garcia-Celma, J. J., Smirnova, I. N., Kaback, H. R. & Fendler, K. Electrophysiological characterization of LacY. *PNAS* **106**, 7373–7378 (2009).

45. Morrison, E. A. *et al.* Antiparallel EmrE exports drugs by exchanging between asymmetric structures. *Nature* **481**, 45–50 (2011).

46. Chavan, T. S. *et al.* A CLC-ec1 mutant reveals global conformational change and suggests a unifying mechanism for the CLC Cl–/H+ transport cycle. *eLife* **9**, e53479 (2020).

47. Hille, B. *Ion Channels of Excitable Membranes*. (Oxford University Press, 2001).

48. Hill, T. L. *Free Energy Transduction and Biochemical Cycle Kinetics*. (Academic Press, 1989).

49. Garcia-Celma, J. J., Ploch, J., Smirnova, I., Kaback, H. R. & Fendler, K. Delineating electrogenic reactions during lactose/H+ symport. *Biochemistry* **49**, 6115–6121 (2010).

50. Kelety, B. *et al.* Transporter assays using solid supported membranes: a novel screening platform for drug discovery. *Assay Drug Dev Technol* **4**, 575–582 (2006).

51. Zuber, D. *et al.* Kinetics of charge translocation in the passive downhill uptake mode of the Na+/H+ antiporter NhaA of Escherichia coli. *Biochim. Biophys. Acta* **1709**, 240–250 (2005).

52. Tal, N. & Schuldiner, S. A coordinated network of transporters with overlapping specificities provides a robust survival strategy. *Proceedings of the National Academy of Sciences of the United States of America* **106**, 9051–6 (2009).

Chapter 4

The C terminus of the bacterial multidrug transporter EmrE couples drug binding to proton release

Nathan E. Thomas[1], Chao Wu[2], Emma A. Morrison[2a], Anne E. Robinson[2b], Josephine P. Werner[1], and Katherine A. Henzler-Wildman[1,2c]

[1]Department of Biochemistry, University of Wisconsin-Madison, Madison WI 53706;

[2]Department of Biochemistry and Molecular Biophysics, Washington University School of Medicine in St. Louis, St. Louis MO 63110

Preface

In this paper, we investigate the anomalous behavior of EmrE's highly conserved C-terminal residue, H110. We find that its protonation state is coupled to the occupancy of the central binding site and propose that it could be involved in a secondary gating mechanism to regulate proton transport in the absence of drug. I performed experiments, analyzed data, and wrote, the paper, Chao originally conceived the project and performed some initial NMR experiments, Emma performed ITC, Anne performed the PRE NMR experiments, and Josephine performed one of the NMR pH titrations.

Abstract

Ion-coupled transporters must regulate access of ions and substrates into and out of the binding site to actively transport substrates and minimize dissipative leak of ions. Within the single-site alternating access model, competitive substrate binding forms the foundation of ion-coupled antiport. Strict competition between substrates leads to stoichiometric antiport without slippage. However, recent NMR studies of the bacterial multidrug transporter EmrE have demonstrated that this multidrug transporter can simultaneously bind drug and proton, which will affect the transport stoichiometry and efficiency of coupled antiport. Here we investigated the nature of substrate competition in EmrE using multiple methods to measure proton release upon the addition of saturating concentrations of drug as a function of pH. The resulting proton-release profile confirmed simultaneous binding of drug and proton, but suggested that a residue outside EmrE's Glu-14 binding site may release protons upon drug binding. Using NMR-monitored pH titrations, we trace this drug-induced deprotonation event to His-110, EmrE's C-terminal residue. Further NMR experiments disclosed that the C-terminal tail is strongly coupled to EmrE's drug-binding domain. Consideration of our results alongside those from previous studies of EmrE suggests that this conserved tail participates in secondary gating of EmrE-mediated proton-drug transport, occluding the binding pocket of fully protonated EmrE in the absence of drug to prevent dissipative proton transport.

Introduction

Substrate binding and release is a critical component of the mechanistic cycle for ion-coupled transporters. In single-site alternating access transport, a single binding site is alternately exposed to either side of the membrane, effectively transporting bound substrate across the membrane. Cooperative binding between substrate and ion increases the likelihood of cotransport (symport), while competition between substrate and ion favors antiport. Pure exchange of substrate and ion results when two conditions are met: 1) if binding of substrate excludes stable binding of the ion

and *vice versa,* and 2) if alternating access of the transporter is only permitted when substrate or ion is bound (Fig. 1, left). This simple, attractive model elegantly explains stoichiometric antiport of ion and substrate and excludes alternative pathways that would result in dissipative leak of the driving ion[1,2]. However, the inherent difficulty in performing biochemistry and structural biology on membrane proteins has limited our ability to rigorously test the assumptions of the pure exchange model with a variety of transporters. Our recent studies of the small multidrug resistance transporter EmrE show that this drug/proton antiporter can simultaneous bind both substrates, violating the simplifying assumptions of the pure exchange model.

EmrE effluxes a wide range of aromatic cation antibiotics using the proton motive force (PMF) across the inner membrane of *E. coli*, thus conferring resistance to antibiotics matching this chemical profile[3]. EmrE performs antiport of drug and proton through a classic single-site alternating access mechanism[4]. The common binding site for drug and proton is defined by a pair of glutamates (E14, one from each monomer within the homodimer, Fig. 2) located deep within the membrane[5,6]. This binding site is alternately exposed to the cytoplasm and periplasm through conformational exchange of EmrE during the transport cycle[5,7]. EmrE's ease of purification, broad substrate specificity, and antiparallel topology have led to its adoption as a model system for studying multidrug efflux, membrane protein evolution, and secondary active transport[8–10]. In addition to facilitating genetic analysis, EmrE's small size makes it an ideal candidate for NMR, allowing unprecedented structure-function investigations of an ion-coupled transporter. NMR has been used to confirm EmrE's antiparallel topology[11,12], measure the rates of conformational exchange (alternating access)[13], probe the effects of drug or proton binding on EmrE's structure and dynamics[14,15], and determine pK_a values for both E14 residues[16,17]. Through these studies, it has become clear that EmrE's transport cycle is populated by more states than are included in pure exchange antiport.

Recently, we proposed a new “free exchange” kinetic model for coupled proton/drug transport by EmrE which includes all experimentally observed states and transitions of the transporter (Fig. 1, right)[17]. In this model, there are multiple pathways around the transport cycle leading to different possible transport stoichiometries including symport, antiport, and uniport of both drug and proton. Nevertheless, EmrE does not allow rapid proton leak in the absence of drug[17]. Furthermore, binding of proton and drug to the single site is competitive: drug binding to one E14 lowers the proton affinity (pK_a) of the second E14, promoting proton release[17]; while protonation of the second E14 lowers the drug affinity (raises the K_d) of the first E14, promoting drug release[17,18]. This competition is critical for ensuring that proton/drug antiport is the dominant transport process for common EmrE substrates under physiological conditions, leading to its well-established function as a proton-coupled drug efflux pump[19]. Here, we further investigate this important competition between drug and protons by examining drug-induced proton release from EmrE. The results are generally consistent with the free exchange model but suggest that an additional residue may release protons upon drug binding. We trace this deprotonation event to H110, EmrE’s C-terminal residue and the only residue other than E14 that has a pK_a value near neutral pH[16].

High-resolution structures of EmrE in different states of the transport cycle would shed light on the coupling mechanism between substrate binding and transport. However, the conformational plasticity that enables EmrE to transport diverse substrates also makes it a very challenging system for high resolution structural studies[15,20]. As a result, there are currently only low-resolution cryoEM[21,22] and X-ray structures available[23] for the antiparallel EmrE homodimer (Fig. 2). The one region of EmrE that is not visible in these structures is the C-terminal tail. Terminal regions of proteins are frequently missing from crystal structures due to their dynamic nature and lack of regular structure. However, the NMR spectra of EmrE reveal that the C-terminal region of EmrE is not just a floppy tail. The residues in this region, including 105-110, have very

unique chemical shifts that are not typical of α-helix or random coil and the peaks are not as intense as they would be in an unstructured tail[11,14]. In addition, residues in this tail are sensitive to the occupancy of the binding pocket, with significant chemical shift perturbations upon protonation or drug binding (Fig. S1)[14]. Finally, H110 is highly conserved (Fig. S2)[24–26], indicating that it may be functionally important. Here, we show that the C-terminal tail of EmrE is strongly coupled to the binding domain, suggesting a potential role in secondary gating of EmrE transport.

Results

Modeling drug-induced proton release Since drug and proton compete for binding to EmrE, addition of drug to EmrE triggers the release of protons from E14 that can be directly measured with a pH electrode in a weakly buffered environment. In an earlier study, addition of a constant, low concentration of TPP^+ to EmrE across a range of pH values produced a bell-shaped proton release profile[27]. This provided experimental confirmation of competitive binding between drug and proton for the first time in a solubilized transporter. However, these experimental conditions cannot distinguish between pure exchange and free exchange models. This is because drug and proton compete for binding to E14 in both models, consistent with a weaker $K_D^{apparent}$ for TPP^+ binding to EmrE at low pH when proton concentration is high[5,17]. Thus, addition of a low concentration of drug will not be sufficient to compete with and trigger release of protons from EmrE at low pH under either model.

If sufficient drug is added to saturate EmrE at all pH conditions, then the number of protons released upon drug binding to EmrE as a function of pH has a very different profile for the pure exchange and free exchange models (Fig. 3). Since the pure exchange model forbids simultaneous binding of drug and proton, any protons bound to the EmrE dimer initially will be released upon addition of a saturating concentration of drug. Thus, the number of protons released per EmrE dimer is simply the fraction of EmrE protonated in the drug-free state at the start of the experiment:

$$protons\ released =$$

$$\frac{2 \cdot 10^{pH^2} + 10^{pH \cdot pK_{a1}}}{10^{pH^2} + 10^{pH \cdot pK_a} + 10^{pK_a^2}} \quad (1)$$

We assume cooperative proton binding reflected by a single pK_a of 7.3, in agreement with previous papers suggesting a pure exchange mechanism with a single pK_a for drug-free EmrE[18,28,29]. Allowing asymmetric protonation of drug-free EmrE with two pK_a values for E14, as shown by NMR[16], simply decreases the slope of the curve for proton release as a function of pH. In either case, at low pH where EmrE is fully protonated in the absence of drug, addition of a saturating drug concentration leads to the release of two protons (Fig. 3A, black).

For the free exchange model, the number of protons released upon drug binding can be calculated from the difference in E14 protonation states in the presence and absence of drug.

$$protons\ released = (2EH_2 + EH^-) - EDH \quad (2)$$

The net protonation state of EmrE in each condition is readily calculated using the E14 pKa values (Table 1, Eqns. 3-5). These pKa values were determined from NMR pH titrations of drug-free EmrE at 25 °C and 45 °C[16], TPP^+-bound EmrE at 45 °C[17], and TPP+-bound EmrE at 25 °C (Fig. S3, S4).

$$EH_2 = \frac{10^{pH^2}}{10^{pH^2} + 10^{pH \cdot pK_{a1}} + 10^{pK_{a1} \cdot pK_{a2}}} \quad (3)$$

$$EH^{-} = \frac{10^{pH \cdot pK_{a1}}}{10^{pH^2} + 10^{pH \cdot pK_{a1}} + 10^{pK_{a1} \cdot pK_{a2}}} \quad (4)$$

$$EDH = \frac{10^{-pH}}{10^{-pH} + 10^{-pK_{a3}}} \quad (5)$$

At low pH, the free exchange model allows simultaneous binding of one drug and one proton, so only one proton will be released (Fig. 3A, blue and red) instead of the two protons predicted by the pure exchange model. In order to experimentally distinguish these two models, we first needed to establish the TPP^+ concentration necessary to saturate EmrE across the entire pH range.

Determination of pH-dependent TPP^+ binding affinity We used isothermal titration calorimetry (ITC) to determine the K_D^{app} for TPP^+ binding to EmrE solubilized in isotropic bicelles at pH 5.5, 6.5, 7.5, or 8.5 and 45 °C. The titration profile observed at pH 5.5 with ITC directly confirms that saturation of the binding site with TPP^+ can be achieved even at low pH. Furthermore, the ITC data confirms that one drug binds per asymmetric dimer at all pH values (Table S1) as expected for TPP^+ binding to the single site defined by E14 in EmrE[30]. Using these experimentally determined K_D^{app} values, we calculated the concentration of TPP^+ needed to bind at least 99% of EmrE present in the proton release assay at each pH value.

Measurement of proton release by ITC In addition to the thermodynamics of drug binding, ITC can provide an indirect but robust measurement of proton release[31–33]. The enthalpy observed upon drug binding (ΔH°_{obs}) includes both the heat of reaction for protein-drug binding and consequent proton release, as well as the enthalpy change due to released protons binding to the buffer. By measuring the standard enthalpy change (ΔH°_{obs}) upon drug binding in multiple

buffers with varying heats of ionization (ΔH^i_b), the number of protons released upon drug binding can be determined from the slope of ΔH^i_b vs. ΔH°_{obs}, as described in detail in[17].

We measured ΔH°_{obs} of TPP^+ binding to EmrE solubilized in isotropic bicelles from pH 5.5 to 8.5 at 45°C using at least three buffers at each pH (Table S1, Fig. 3C,E). If drug and proton binding were exclusive, as predicted by pure exchange, we would expect to see the release of two protons per dimer at low pH. Instead, slightly more than one proton is released per dimer at pH 5.5, in agreement with our previous experimental observation that EmrE can simultaneously bind drug and proton. However, the data is not perfectly consistent with the free exchange model: more protons are released than predicted near neutral pH (Fig. 3A, red). The free exchange model considers only E14 protonation and deprotonation events, as previous mutagenesis studies only implicated E14 in drug- and proton-binding by EmrE[5,6,27], and E14 is the only protonatable residue within the transmembrane helices that define the substrate-binding pore in EmrE (Fig. 2). Before considering the possibility that another residue may also participate in coupled binding/release of drug and protons, we first confirmed our experimental observation that the number of protons released upon TPP^+ binding is inconsistent with an E14-only model using a different experimental approach and at a lower temperature (25 °C).

Direct measurement of drug-induced proton release In the original investigation of drug-induced proton release[27], 4μM aliquots of TPP^+ were added to weakly buffered EmrE solubilized in detergent and pH changes were monitored and quantified directly using an electrode. We repeated this experiment using EmrE solubilized in bicelles and with 5 mM TPP^+ (Fig. 3B,D), a concentration sufficient to saturate EmrE at all pH values based on our ITC experiments at 45 °C. We have previously shown that K_D^{app} decreases with temperature[11]. Thus, this TPP^+ concentration will also be sufficient to saturate EmrE at 25°C where the drug binds more tightly. Upon monitoring proton release in this manner, we again found that EmrE releases around one proton per dimer at low pH, but releases more protons than expected near neutral pH (Fig. 3A,

blue). When considered alongside the ITC experiments, this strongly suggests that a second residue, other than E14, releases protons upon binding of drug to EmrE.

Which other residue could be involved in the coupled binding and release of drug and protons? The previous investigation of drug-induced proton release considered E25 and D84[27], and found that they do not contribute to proton release. This is consistent with our more recent NMR-monitored pH titration experiments, which do not show any titration of D25 or E84 near physiological pH. Instead, the only residue other than E14 that titrates near neutral pH in our NMR experiments is H110[16], which has not been previously considered in the proton release mechanism. This C-terminal residue is highly conserved among EmrE-like members of the SMR family (Fig. S2) but has no known role in EmrE function. Could H110 account for the elevated proton release?

Determination of H110 pKa To test this hypothesis, we performed pH titrations of drug-free and TPP^+-bound EmrE using ^1H-^{15}N HMBC NMR experiments to directly observe the histidine side-chain (Fig. S5)[34]. Though HMBC experiments are relatively insensitive, the direct observation of the imidazole ring enables an accurate determination of the histidine side chain pK_a value. Conveniently, EmrE only has a single histidine residue, allowing clean observation of H110 in this experiment.

At 45°C, the rapid rate of alternating access in drug-free EmrE results in intermediate or fast exchange of the $H110^A$ and $H110^B$ peaks such that they are not resolved in the HMBC spectra, preventing accurate determination of the H110 sidechain pK_a values at that temperature. Fortunately, at 25°C the peaks corresponding to H110 from each monomer in the asymmetric homodimer are clearly resolved (Fig. 4, S5, S6, S7), allowing the determination of the pKa for $H110^A$ and $H110^B$ separately (Table 1 and Fig. 5). This reveals a drug-induced pK_a shift of $H110^A$ (Table 1), which is in the C-terminal tail of EmrE located on the open side of the transporter. Interestingly, there is no drug-induced pK_a shift for $H110^B$, which is located on the closed face.

The pK_a shift of $H110^A$ upon TPP^+ binding will result in the release of protons from this C-terminal residue. Including proton release from H110 along with the proton release from E14 in the free exchange model gives a better fit of the experimental proton release data at 25°C (Fig. 6).

Evidence for coupling of the C-terminal tail to the binding pocket The drug-induced pK_a shift of $H110^A$ (Table 1) and sensitivity of the C-terminal tail chemical shifts to the identity of the bound substrate (Fig. S1) could occur through direct interaction with the binding pocket, or indirectly due to large-scale conformational change upon drug binding. To investigate this further, we re-analyzed the effect of pH on the backbone amide groups throughout EmrE as recorded in the ^1H-^{15}N TROSY HSQC pH titration of TPP^+-bound EmrE (Fig. S3). We have previously shown that pH-dependent chemical shift perturbations of core residues in the binding pocket of drug-bound EmrE are the result of protonation of E14[16]. As expected, residues in the tail of monomer B have pH-dependent chemical shift perturbations that are well fit with a pK_a value matching the $H110^B$ side chain pKa value (Table 1, Fig. S4). However, the pH-dependent chemical shifts of residues in the monomer A C-terminal tail have pK_a values that match the pK_a of E14, not $H110^A$. This strong coupling between the C-terminal tail of monomer A and E14 suggests a more direct interaction of this tail with the core binding domain of EmrE, either with the binding pocket itself or with the structured loops surrounding the pocket (Fig. 2).

Assessing solvent accessibility of H110 If the C-terminal tail of monomer A is interacting with the binding pocket in some way, it may be protected from water, since the binding cavity is hydrophobic and poorly hydrated relative to the bulk aqueous solution [35]. To analyze the solvent accessibility of the C-terminus, we recorded spectra with and without a water-soluble paramagnetic ion, Mn^{2+} (Fig. 7). The Mn^{2+} will cause paramagnetic relaxation enhancement (PRE) of nearby nuclei, leading to the disappearance of peaks in the NMR spectra that correspond to residues accessible to water. At high pH, the backbone amides of both $H110^A$ and $H110^B$ are in an aqueous environment since these peaks disappear in the presence of Mn^{2+}. However, at pH

5.2, the H110 signals remain visible in the spectrum even in the presence of Mn^{2+}, indicating that H110 is more protected from water at low pH (Fig. 7).

Evidence for a second state of H110^{A} At elevated pH, the H110^{A} peaks are broadened in the nitrogen dimension, indicative of microsecond to millisecond transitions between different conformational states. This is apparent to a certain extent for drug-free EmrE and is even more pronounced with TPP^{+} bound. While no second state is visible in the HMBC spectra, this pulse sequence is relatively insensitive and may not detect lowly populated states. To address this, we prepared TPP^{+}-bound EmrE selectively labeled with $^{15}N/^{13}C$-histidine and acquired TROSY-HSQC spectra at pH 6 and 8 to observe the backbone amides. Since H110 is the only histidine in EmrE, only peaks corresponding to H110 are visible. The increased sensitivity of this pulse sequence reveals two peaks in addition to the major states of H110, confirming that H110 has multiple conformations when TPP^{+} is bound (Fig. 8). It likely that H110 also exists in multiple conformations for drug-free EmrE, but the highly dynamic nature of EmrE under these conditions makes this difficult to demonstrate conclusively.

Discussion

Ion-coupled transport requires regulated access of ions and substrates into and out of the binding site. Transport will be biased toward symport or antiport depending on whether ion and substrate binding is competitive or cooperative, and how the relative rates of alternating access vary when the transporter is empty or bound to substrate and/or ion. Cartoon models of transporters often exclude states and transitions that would weaken coupling efficiency or lead to leak pathways, but few transporters have been studied in sufficient detail to unambiguously support their exclusion. Recently, it was shown that the H^{+}/sugar symporter GlcP is capable of H^{+}/sugar antiport, in violation of traditional models of symport [36]. Instead, the authors proposed a “universal” kinetic model of transport, that can accommodate symport, antiport, or uniport depending on the rates of the transitions between the various states. This is similar to our free exchange model for

EmrE. In the case of EmrE, the rates of alternating access in different substrate-bound and substrate-free states have previously been studied[14–17,29,35] and do not follow the expected patterns for coupled antiport. Both NMR experiments and MD simulations indicate that apo EmrE is capable of alternating access[13,16,35], and NMR demonstrates that EmrE can simultaneously bind and transport drug and proton near neutral pH[17]. Those results suggest that EmrE should be capable of both symport and antiport of drug and protons, and should rapidly leak protons. Nevertheless, functional assays demonstrate that EmrE does not leak protons in the absence of drug. Furthermore, while liposomal transport assays indicate that EmrE may be capable of both symport and antiport, its well-established drug-resistance activity indicates that antiport is the dominant function under physiological conditions[17]. Here we focus on the competition between drug and proton binding to EmrE to see if this matches the expectations for an ion-coupled antiporter.

The experiments presented here investigate the competitive binding of drug and protons EmrE to better understand how this promiscuous transporter is biased toward net antiport. We identify an additional protonatable residue coupled to drug binding, H110, and demonstrate that the C-terminal tail of EmrE on the open side of the transporter is strongly coupled to the E14 binding pocket within TM 1-3. At first, a role for H110 in EmrE's binding mechanism seems surprising. The C-terminal tail of EmrE extends from TM4, which mediates EmrE dimerization and is set apart from EmrE's core binding domain (TM1-3) (Fig. 2)[25]. Previous Cys-scanning mutagenesis studies of EmrE did not reveal a significant role for the C-terminal tail in substrate binding or transport[6,37,38]. However, H110 is highly conserved across the SMR family (Fig. S2), suggesting an important but as of yet undiscovered functional role. Consideration of our results alongside previous studies of EmrE suggests this conserved tail may participate in secondary gating of EmrE transport, occluding the binding pocket of fully protonated EmrE in the absence of drug and preventing proton leak.

To better understand the functional implications of competition between drug and proton binding to EmrE, we measured drug-induced proton release from EmrE as a function of pH (Fig. 3). At low pH we observed the release of approximately one proton per dimer, which is consistent with the simultaneous binding of drug and proton by EmrE and the free exchange model. Surprisingly, around neutral pH we observed greater proton release than could be explained by consideration of drug and proton-binding at the established “single” binding site defined by E14. Our prior NMR-monitored pH titrations showed that H110 is the only other residue that titrates near neutral pH[16]. We observed a drug-induced pK_a shift for the imidazole side chain of $H110^A$ in the presence and absence of TPP^+. Incorporating the proton release from H110 into the model accounts for the increased proton release near neutral pH.

In addition to the drug-induced pK_a shift of H110, the C-terminus of EmrE is acutely sensitive to drug binding. These effects could be due to direct interaction of the C-terminal tail with the binding site near E14 or indirectly through changes in the overall conformation when EmrE is bound to different drugs. The tail is not resolved in the available crystal and cryo-EM structures of EmrE[23,39], preventing a direct structural analysis. Re-examination of our previous NMR pH titrations monitoring the backbone amides (Fig. S3) revealed that the backbone amides in tail A fit to a pK_a of 6.3, matching the pKa of E14 in the active site of TPP^+-bound EmrE (Table 1). The large pH-dependent chemical shifts displayed by these residues indicate a significant change in chemical environment, which could be consistent with a direct interaction with the binding domain. The poor solvent accessibility of H110 at low pH for TPP^+-bound EmrE further indicates that the tail is located in a less-exposed environment, as would be the case if it folds back toward the active site (Fig. 2, dashed line). Interestingly, in a recent molecular dynamics study using a complete model of EmrE embedded in a lipid bilayer, the tail of monomer A existed in heterogeneous populations, some of which did extend back into the binding pocket for an

extended period during the simulation[35]. Our experimental results, including our observation of multiple states for H110, are consistent with this MD simulation.

If the C-terminal tail can extend into the binding pocket, what is its role in the transport mechanism of EmrE? A possible functional mechanism for the C-terminal tail as a secondary gate in EmrE begins to emerge from consideration of our data and previously published experiments examining the structure and function of EmrE using a variety of experimental approaches.

In recent MD simulations, the binding pocket spontaneously dehydrated when both E14 residues were protonated[35]. This is in agreement with DEER-EPR measurements which showed re-packing of the TM3-4 loop to occlude the binding pocket upon lowering the pH from 8 to 5 for drug-free EmrE[28]. Interestingly, this pH-dependent conformational change was also observed in E14Q-EmrE, demonstrating that it must depend on the protonation of a residue other than E14. The authors proposed protonation of E25 and D84, given the locations of these residues within the structure and the effect of mutations at these positions. While this is a logical conclusion, there is no evidence for protonation of either E25 or D84 in this pH range in our NMR spectra, which provide a more direct probe of electrostatic environments[16]. However, as shown here, H110 does titrate in this pH range and is sensitive to drug binding. Additionally, both co-evolutionary analysis and MD simulations suggest interactions between the C-terminal tail and the TM3-4 loop (Fig. S8). Furthermore, in the MD simulations, interactions were observed between $H110^{A}$ and the TM1-2 loop, where E25 is located. These interactions only occurred when EmrE was fully protonated or in an unstable singly protonated state that is likely physiologically irrelevant.

In consideration of these results, we propose that protonation of $H110^{A}$ at low pH could facilitate electrostatic interactions between positive charges in the C-terminal tail (H110 and R106) and the negatively charged E25 and D84 in the TM1-2 and TM3-4 loops (Fig. 2, dotted line). Formation of such an interaction upon $H110^{A}$ protonation could explain the pH-dependent conformational change of the TM3-4 loop to occlude the E14 binding pocket observed by EPR at

low pH and is consistent with the NMR pH titration data and evolutionary couplings. If the binding pocket is occluded when EmrE is fully protonated, it would prevent proton transport across the membrane in the absence of drug. This could explain the most significant shortcoming of the E14-only free exchange model – the prediction that EmrE should rapidly transport protons across the membrane in the absence of drug, in contrast to results from proton leakage assays that show no significant proton leak[17].

However, in order for EmrE to perform coupled antiport of drug and proton, proton transport must occur in the presence of drug. In an early NMR study of EmrE, TPP^+ binding to EmrE was monitored by ^{31}P NMR, allowing direct observation of the drug[40]. In that study, two distinct populations of EmrE-bound TPP^+ were observed. At low concentrations, TPP^+ bound weakly to E25 and D84 via electrostatic interactions. Binding of TPP^+ to the canonical binding site at E14 only occurred when the TPP^+:EmrE dimer ratio exceeded 1:1, even though this site has a higher affinity. We propose that the binding of TPP^+ to E25 and D84 observed at low drug concentrations[40] disrupts the electrostatic interactions between these residues and the positively charged C-terminal tail. This results in release of the C-terminal tail from interaction with the loops surrounding the transport, opening the secondary gate and allowing proton release from and drug binding to E14 within the transport pore. While speculative, this mechanism is consistent with the experimentally observed behavior of the loop and the tail of EmrE and would explain the tight kinetic correlation of drug on-rates and proton off-rates previously observed by stopped flow[18]. Our proposed model is also analogous to a recently uncovered mechanism in MdfA, a multidrug/proton antiporter from the major facilitator superfamily with a remarkably similar substrate profile to EmrE, in which electrostatic interactions between loop residues around the rim of the binding pocket are essential to proper gating of transport[41].

While gating is a common feature of transporters[2,42], the presence of a secondary gate in EmrE would be remarkable in a such a small transporter. At first glance, distinctions between

secondary gating within a free exchange transport model and the pure exchange model of antiport might seem trivial, since both mechanisms are gated, limiting proton transport in the absence of drug. However, gating EmrE at the fully protonated state, as proposed here, rather than the deprotonated state is a crucial distinction. In the pure exchange model, proton leak is prevented by stipulating that the empty transporter cannot alternate access. If EmrE *can* alternate access when deprotonated, as demonstrated by NMR[15,16] and allowed in the free exchange model, then EmrE should confer drug sensitivity under certain conditions. Indeed, EmrE-mediated sensitivity to methyl viologen, a +2 substrate, has been demonstrated both at high pH[19] and at neutral pH when the E14 pKa is lowered by mutation to aspartate[29]. This is consistent with electrogenic drug uptake. Additionally, this mechanism would explain the ease with which EmrE can be transformed from a proton-coupled efflux pump to a polyamine importer by a single point mutation – W63G[43]. Such a mutation would not need to fundamentally alter the dynamics or mechanism of the transporter; it would merely need to change EmrE's binding specificity. Finally, this mechanism would represent an inversion of the strict competition stipulated by the pure exchange model. Rather than excluding simultaneous drug and proton binding, binding of drug, albeit to a secondary site, would be required for proton release. Competition between drug and proton remains central to antiport, but the mechanism may be very different than proposed by earlier models.

Experimental Procedures

Expression and Purification EmrE was expressed and purified as previously described[44]. ^{15}N-labeled samples were grown in M9 media supplemented with 1g/L $^{15}NH_4Cl$ (for HMBC experiments) or D_2O M9 media supplemented with 0.5g/L ^{15}N isogro (Sigma-Isotec) and 1g/L $^{15}NH_4Cl$ (for HSQC experiments). Histidine-labeled samples were grown in M9 media, with 33 mg/L ^{13}C-^{15}N labeled histidine added one hour prior to induction. EmrE purified in DM was reconstituted into DMPC or DLPC liposomes at a 1:80 EmrE monomer:lipid molar ratio. Detergent

was removed by Amberlite XAD 2 beads, and liposomes were collected by ultracentrifugation. Samples were resuspended in NMR buffer containing DHPC at a 1:3 long chain to short chain lipid ratio to prepare isotropic bicelles.

Isothermal Titration Calorimetry ITC titrations were performed in a TA Instruments Low Volume Nano calorimeter using the ITCRun software (TA Instruments, Lindon, UT) with 2.5 µL injections, stirring at 350 rpm at 45°C. Each buffer condition was run 2-4 times, with a minimum of 3 buffers per pH value between 5.5 and 8.5. At lower pH values, samples contained 20 mM buffer and 20 mM NaCl. At pH 8.5, all samples contained 50 mM buffer to improve buffering capacity and minimize pH drift. Buffer ionization enthalpies were adjusted to 45 °C using the reported standard molar heat capacity change at 25 °C[45]. Each titration was analyzed independently, confirming the 1 TPP^+:EmrE dimer (n=0.5 TPP^+/EmrE monomer) binding stoichiometry under all conditions. ITC experiments in MOPS at pH 7.5 were performed with both 20 and 50 mM MOPS to confirm that observed binding enthalpies were independent of buffer concentration. EmrE in 1:3 DLPC:DHPC isotropic bicelles ranged in concentration from 25 - 835 µM EmrE (monomer concentration) and TPP^+ concentrations varied from 76 µM - 5 mM TPP^+, depending on pH, to keep the c-value for the ITC experiment in an optimal range. Sample pH was checked at 45 °C before and after each experiment. Data is reported in Table S1. The data was fit as previously described[17,46].

Modeling Proton Release. Proton release from E14 was modeled as described in the main text.

Proton release from $H110^A$ was similarly calculated by subtracting the fraction of protonated $H110^A$ in TPP^+-saturated EmrE from the fraction of protonated $H110^A$ in drug-free EmrE, where:

$$fraction\ of\ protonated\ H110^A =$$

$$\frac{10^{-pH}}{10^{-pH} + 10^{-pK_a}}$$

using the relevant pK_a value from Table 1. The pK_a values for $H110^B$ were not significantly different, so no protons are released from $H110^B$.

Direct Measurement of Proton Release EmrE in 1:3 DMPC/DHPC isotropic bicelles with 1 mM bicine, 0.5 mM MOPS, 0.5 mM MES, 0.2 mM acetate, 100mM NaCl was diluted with bicelles (80 mM DMPC, 240 mM DHPC) in the same buffer to create stock solutions ranging from 40-200 μM (monomer concentration) EmrE. 100 μL EmrE stock solutions were diluted with 800 μL 7.5 mM DHPC and 100 mM NaCl, and precise concentrations were determined from the A_{280} (EmrE ε = 38,368 M^{-1} cm^{-1}) of this solution immediately before each experiment. 10 mM NaOH or HCl was used to bring each sample to desired initial pH. 100 μL of 50 mM TPP^+ in 50 mM DHPC and 100 mM NaCl adjusted to the desired pH was added to saturate EmrE and initiate proton release. Proton release was monitored directly with a microelectrode using an HI 2209 analog pH meter from Hanna Instruments digitized with a DataQ data logger. Proton release was quantified by at least five subsequent additions of 20 nM HCl and NaOH per sample, and proton concentration was assumed to be linear within this range. A minimum of five concentrations of EmrE was used to monitor proton release at each pH, and a plot of measured proton release vs. dimer concentration was used to generate reported values of proton release per dimer.

NMR pH Titration All pH titration data were collected using a Bruker Avance III HD 900 MHz spectrometer with a cryogenic probe on 0.6-1.0 mM EmrE samples in q=0.33 DMPC/DHPC isotropic bicelles. Sample buffers contained 100 mM bicine, 50 mM MOPS, 50 mM MES, 20 mM acetate, 20 mM NaCl, 2 mM TCEP, 6% D_2O, and 0.05% NaN_3, with 4 mM TPP^+ added to drug-bound samples. Sample pH was adjusted using a pH electrode and was measured again after each NMR experiment to account for any pH drift. pH drifts during 2D NMR experiments were only observed for titration points above pH 8 and the average pH value was used. TROSY-HSQC spectra were collected as previously described[17]. HMBC spectra were collected using a modified HSQC sequence with delays during INEPT transfer steps adjusted to suppress one-bond J-

coupling and select for long-range coupling. Proton and nitrogen chemical shifts were fit using IgorPro (Wavemetrics, https://www.wavemetrics.com) to the following equation to determine pK_a values:

$$\delta = \frac{\delta_H 10^{-pH} + \delta_D 10^{-pK_A}}{10^{-pH} + 10^{-pK_A}}$$

Where δ_H is the chemical shift of the protonated species at low pH, δ_D is the chemical shift of the deprotonated species at high pH, and pK_A is the pK_a of the titratable group. For drug-bound HMBC spectra of H110, broadening of the monomer A peak in the nitrogen dimension prevented accurate peak position determination above pH 7.8. Proton peak positions above this pH were determined from 1D slices of the 2D HMBC spectra.

Paramagentic relaxation analysis Four separate uniformly labeled NMR samples were prepared as described in 100mM MOPS, 100mM bicine, 20mM acetate, and 20mM NaCl at different pH values. Samples contained 0.7mM EmrE in q=0.33 isotropic bicelles as well as 0.05% NaN_3, 10% D_2O, 2mM TCEP, 2mM TPP^+, and 2mM DSS. Each sample was adjusted to pH at 35°C and pH checked again after data acquisition. To assess paramagnetic relaxation effects, 0.5mM $MnCl_2$ was added to each sample and another, identical ^1H-^{15}N TROSY-HSQC spectrum was collected in the same manner.

Acknowledgements: We thank Geoff Chang for the EmrE expression plasmid. This work was supported by the National Institutes of Health Grant 1R01GM095839, NIH National Research Service Award T32 GM007215 (to N.E.T.), National Science Foundation graduate research Fellowship DGE-1143954 (to E.A.M. and A.E.R.), and a Mr. and Mrs. Spencer T. Olin fellowship for Women in Graduate Study (to A.E.R.).

Conflict of interest: The authors declare that they have no conflicts of interest with the contents of this article.

Footnotes

The abbreviations used are: PMF, proton motive force; TM, transmembrane helix; TPP+, tetraphenylphosphonium; TROSY, transverse relaxation optimized spectroscopy; HSQC, heteronuclear single-quantum coherence; HMBC, heteronuclear multiple bond correlation spectroscopy

Table 1. pK_a values for E14 and H110 determined by NMR

Residue	Drug-free	TPP^+-bound
25°C		
$E14^{\&}$	6.8 +/- 0.1 [16] 8.5 +/- 0.2 [16]	6.32 +/- 0.02*
$H110^A$ $H110^B$	7.05 +/- 0.02# 6.98 +/- 0.01#	6.77 +/- 0.03# 6.97 +/- 0.03#
C-terminal tail A C-terminal tail B	N/A N/A	6.34 +/- 0.04* 7.00 +/- 0.04*
45°C		
$E14^{\&}$	7.0 +/- 0.1 [16] 8.2 +/- 0.3 [16]	6.8 +/- 0.1 [17]

&Drug-free EmrE pKa values are macroscopic pK_a values and cannot be unambiguously assigned to $E14^A$ or $E14^B$. The pKa value for TPP^+-bound EmrE is due to protonation of $E14^B$.

*Determined by TROSY-HSQC monitoring backbone amide chemical shift change with pH (Fig. S3, S4). For the C-terminal tail, chemical shift perturbations of S105, R106, and T108 fit to the reported pK_a values (Fig. S4).

#H110 pKa value of the side chain imidazole determined from a pH titration with HMBC NMR spectra (Fig. 5, S6, S7).

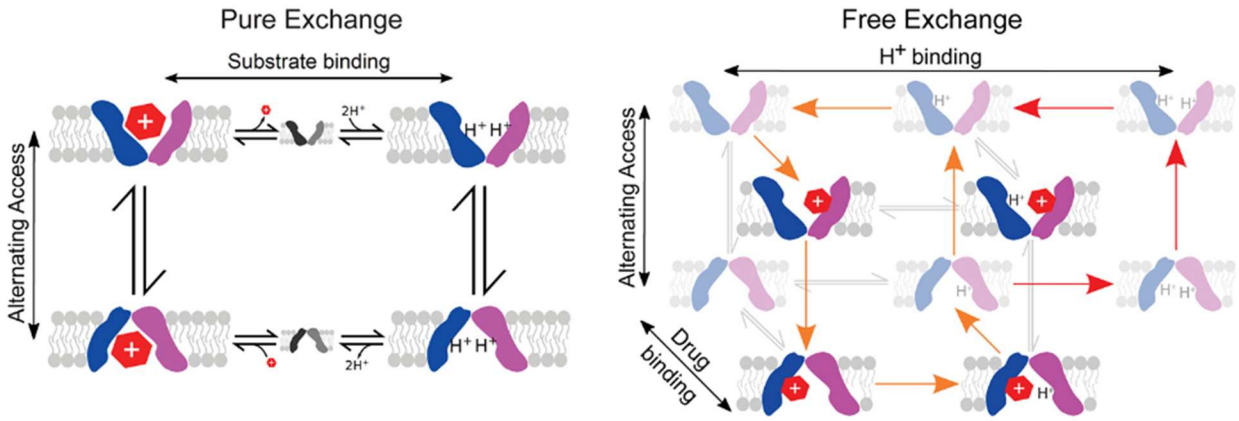

Figure 1. **Two competing models for antiport.** In pure exchange (left), strict competition for the single site between drug and two protons, along with prohibition of alternating access in absence of substrate or ion, leads to tightly coupled stoichiometric antiport of $2H^+$/drug. In free exchange, competition remains but no restrictions are placed on binding or alternating access, allowing both $1H^+$/drug (orange) and $2H^+$/drug (red) antiport.

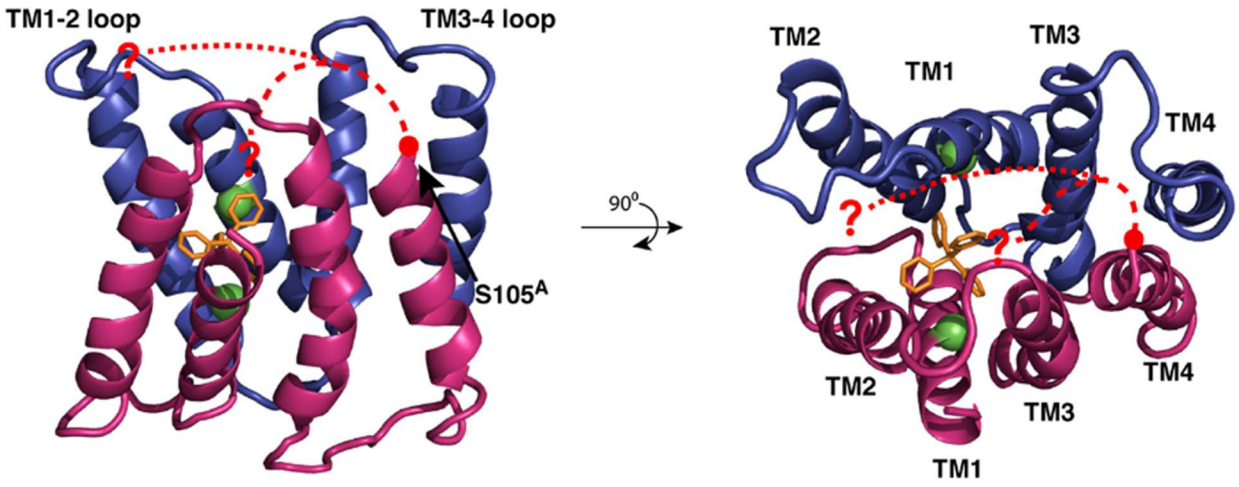

Figure 2. **Structure of TPP^+-bound EmrE.** Crystal structure (3B5D) [23], with monomer A in magenta, monomer B in blue, and TPP^+ in orange. The C^α of E14 is shown as a green sphere. The final residue in the structure, $S105^A$, is indicated by a red dot. The location of the C-terminal tail is unknown, but it could interact with positively-charged residues in the Monomer B loops (dotted line) or fold into the binding pocket itself (dashed line).

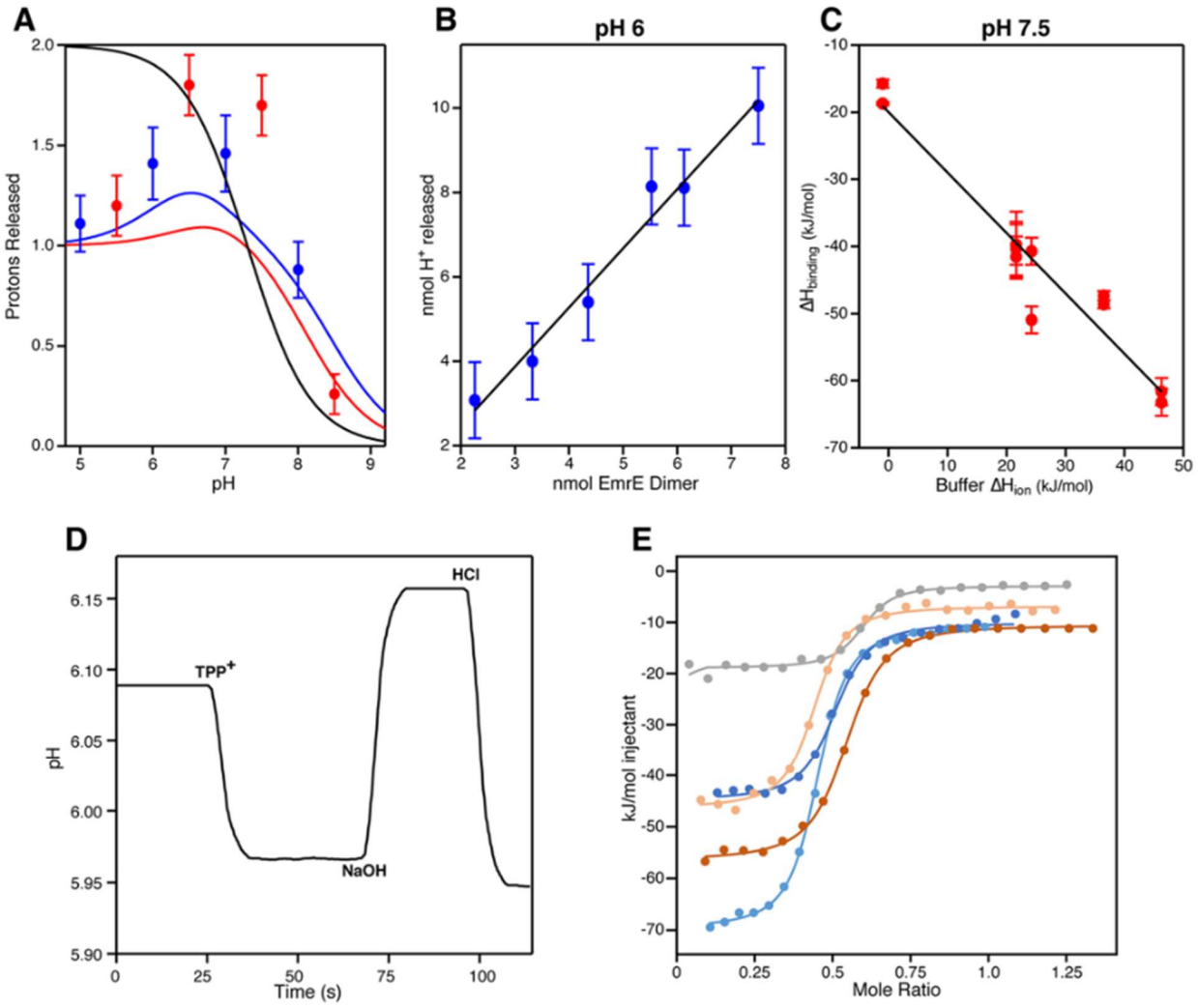

Figure 3. **E14 alone cannot account for drug-induced proton release.** *A,* Proton release per EmrE dimer upon the addition of saturating concentration of TPP^+ as predicted by pure exchange (black line) or free exchange models of transport at 25°C (blue line) or 45°C (red line), assuming E14 is the only residue involved. Experimental proton release, whether measured directly at 25°C (blue circles) or by ITC at 45°C (red circles), is more consistent with the free exchange model at low pH where the two models are most distinct. However, more protons are released upon TPP^+ binding near neutral pH than would be predicted by the E14-only free exchange model. *B,* Fit of proton release measured directly at 25°C and pH 6 by pH electrode as a function of EmrE concentration. The slope indicates the drug-induced proton release per dimer (sample data shown

in panel D). *C,* Fit of enthalpy of TPP^+ binding as a function of buffer ionization enthalpy at 45°C and pH 7.5. The negative slope represents the proton release per monomer (sample data shown in panel E). *D,* Representative trace of TPP^+-induced proton release at pH 6. At the indicated time point, 5 µmol TPP^+ was added to a solution containing 7.5 nmol EmrE dimer causing a release in protons seen by the drop in pH. This pH drop was converted to nmol H^+ by the subsequent addition of known quantities of NaOH and HCl to the solution. Additional aliquots of HCl and NaOH were added to improve quantitation (data not shown). *E,* Overlay of representative ITC binding curves for TPP^+ at 45°C and pH 7.5 in either potassium phosphate (gray), BES (dark blue), MOPS (beige), imidazole (brown), or Tris (light blue) buffer (see Table S1 for complete ITC data).

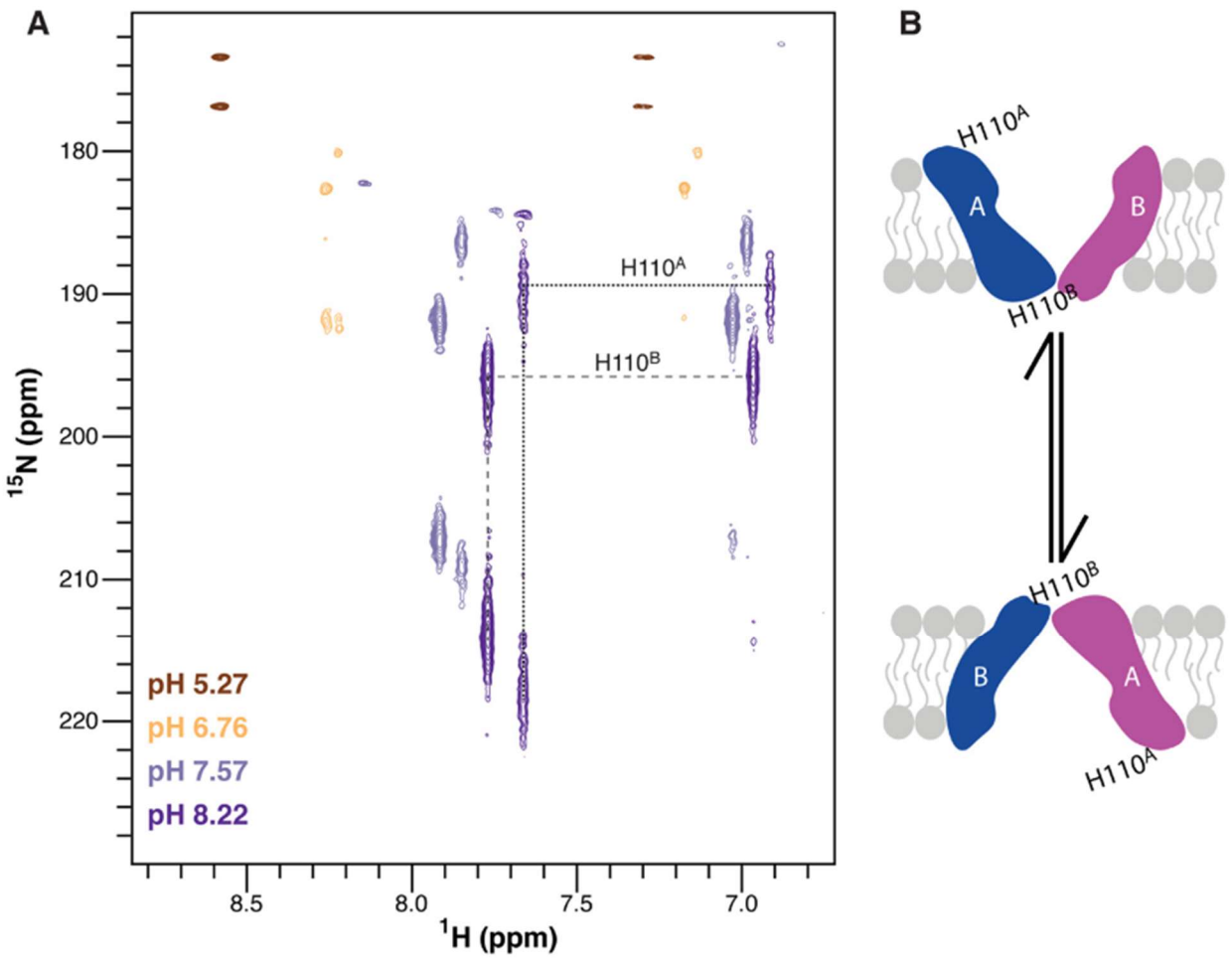

Figure 4. **NMR-monitored pH titration of H110 side chain.** *A*, H110 peaks for each monomer in HMBC NMR spectra of drug-free EmrE in isotropic bicelles are clearly resolved at 25°C. Three or four peaks are observed for each imidazole ring as explained in Fig. S5. As pH changes, the peak positions titrate along a line, consistent with a single protonation event. The peak positions at low pH fall along this line for both monomers, indicating that the peak overlap at low pH is due to similar chemical environments for the two residues, not fast exchange. Thus, the pK_a for each monomer can be determined separately. Representative peaks are shown (see Fig. S6 for full titration). *B*, During alternating access conformational exchange, EmrE's antiparallel protomers swap conformation. Monomer A is defined as the protomer in which the N and C termini (H110^{A})

are facing the same side of the membrane as the binding pocket, regardless of whether EmrE is open-up or open-down.

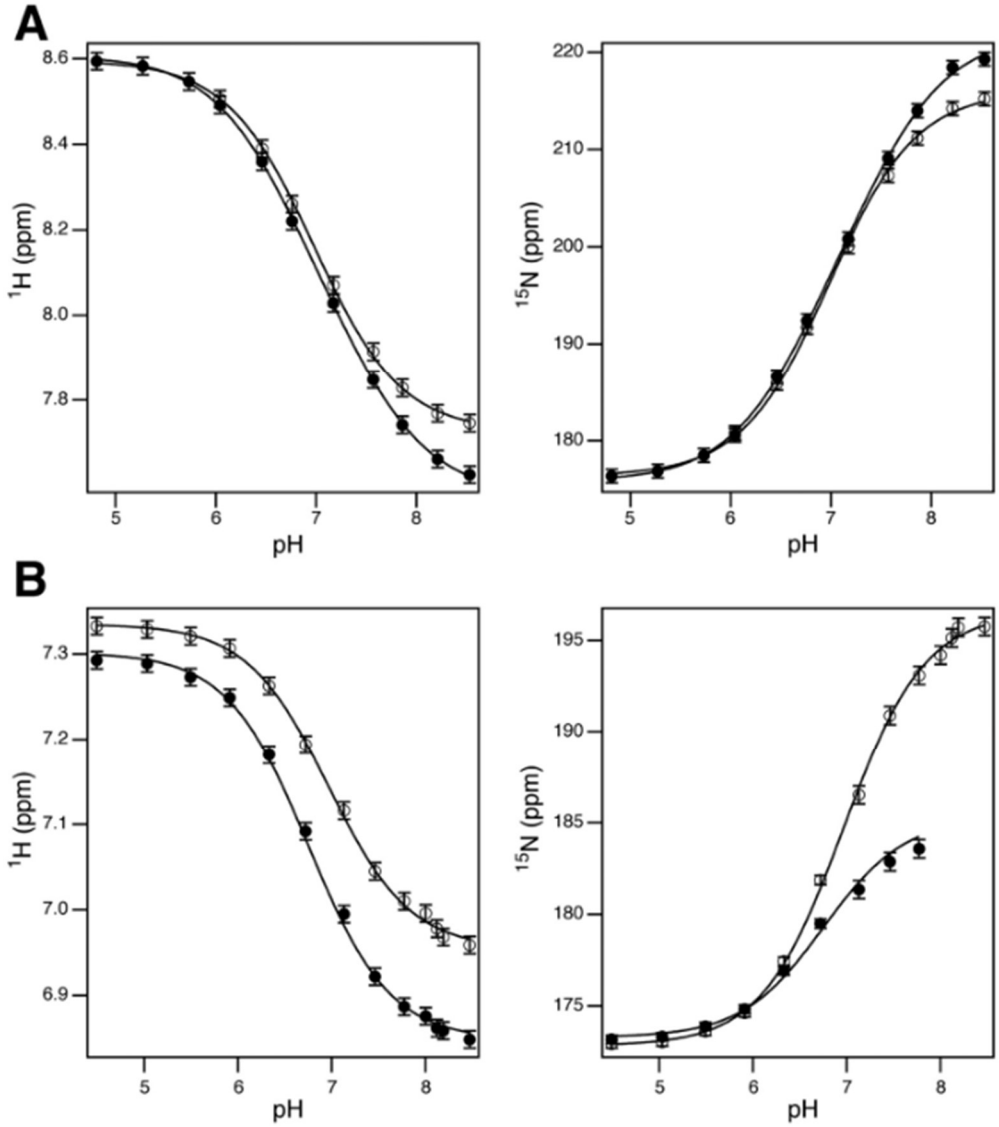

Figure 5. **Determination of the H110 side chain pK$_a$.** *A*, The H$^{\delta 2}$ and N$^{\varepsilon 2}$ chemical shifts of H110^A (filled) and H110^B (open) from the HMBC pH titration of drug-free EmrE are fit to determine the pK$_a$. H$^{\delta 2}$ and N$^{\varepsilon 2}$ data was simultaneously fit to a single pKa for each monomer individually. *B,* Fit of H110^A (filled) and H110^B (open) from HMBC pH titration of TPP$^+$-bound EmrE. Proton and nitrogen were fit together, but due to line broadening at high pH, there is no nitrogen data above pH 7.77 for H110^A. Summary of pK$_a$ values can be found in Table 1.

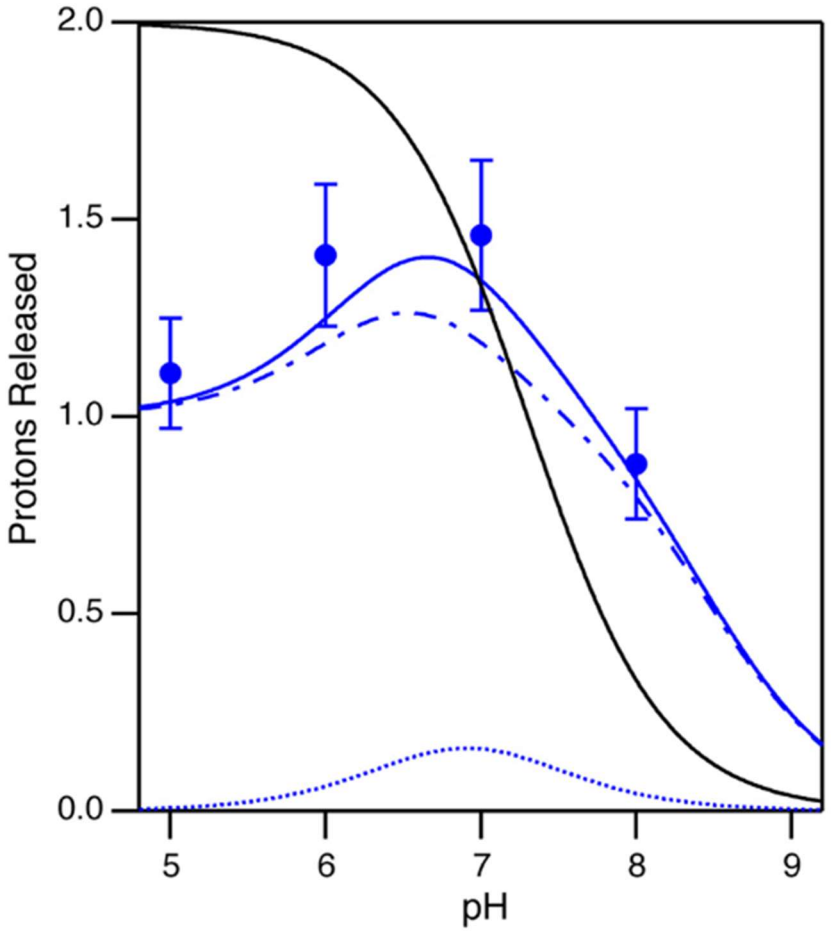

Figure 6. **H110 contributes to drug-induced proton release at 25°C.** Predicted proton release due to the drug-induced pK_a shift of E14 (dashed line) or H110 (dotted line) measured by NMR. Including both E14 and H110 in the proton-release model (solid line) leads to increased proton release near neutral pH and gives a better fit of the data compared to an E14-only model (dashed line).

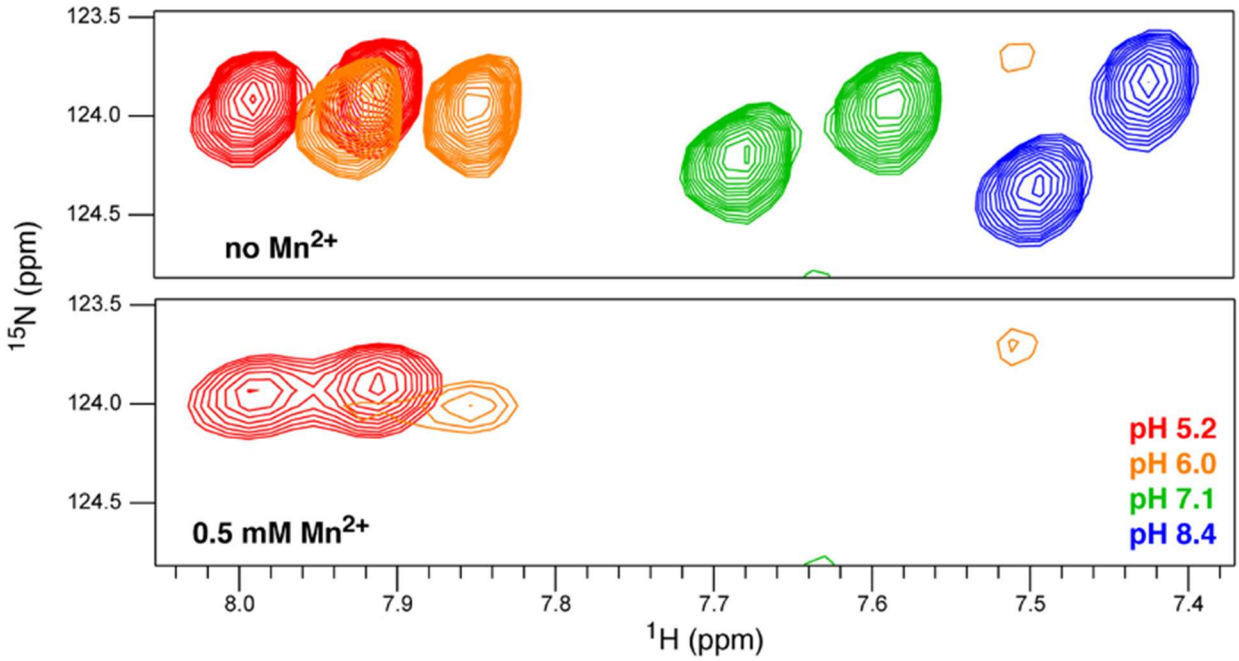

Figure 7. **H110 is protected from solvent at low pH.** TROSY-HSQC NMR spectra of TPP^+-bound EmrE in the absence (top) and presence (bottom) of 0.5 mM of the paramagnetic ion Mn^{2+}. At low pH, the H110 signal is not fully relaxed by Mn^{2+}, indicating that it is at least partially protected from water under these conditions.

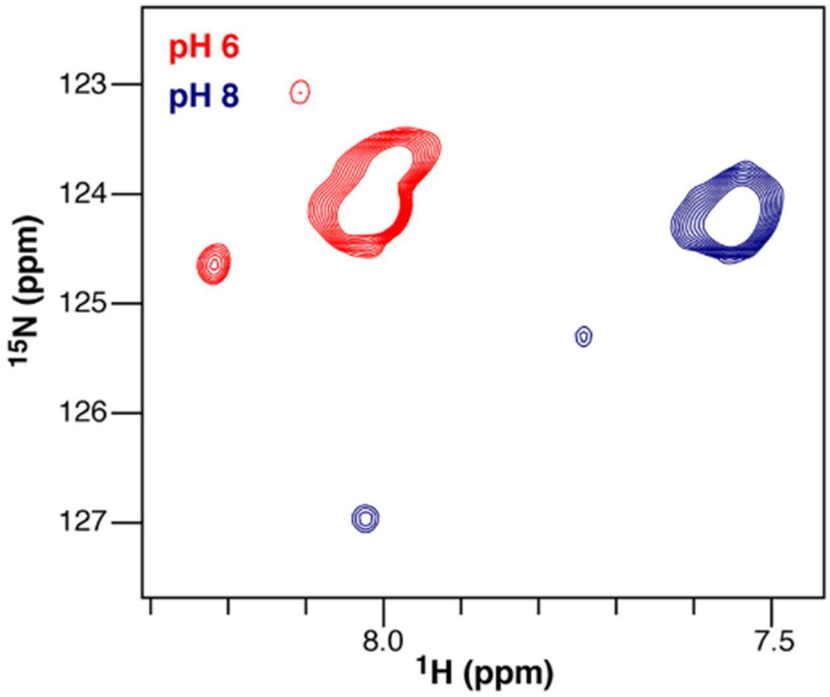

Figure 8. **H110 exists in multiple states when TPP^+ is bound.** TROSY-HSQC spectra of TPP^+-bound EmrE selectively labeled with $^{15}N/^{13}C$-histidine reveal at least two additional histidine peaks at both low and high pH. These could correspond to two additional states of $H110^A$, or one additional state each of both $H110^A$ and $H110^B$.

Supporting Information

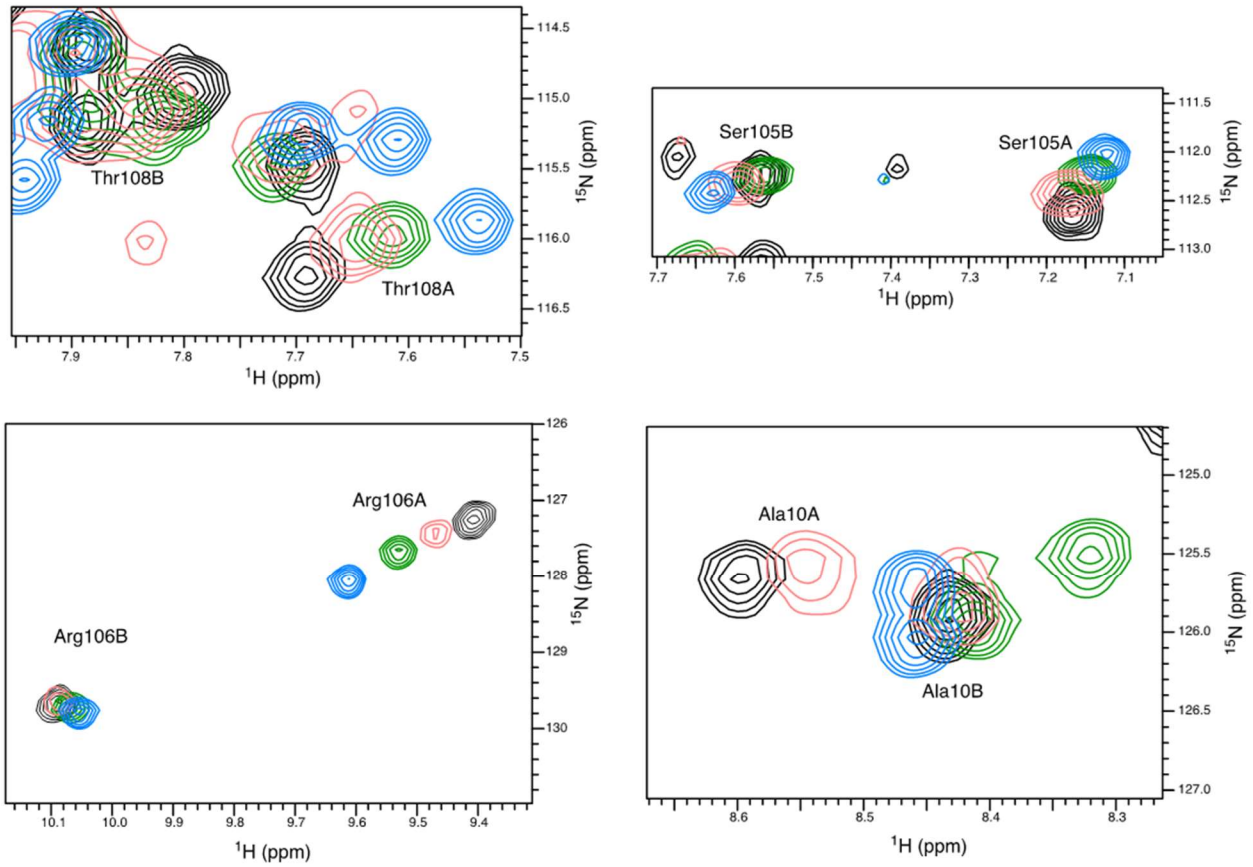

Figure S1 – *Effect of bound drug identity on C-terminal tail.* Spectra of selected residues from EmrE bound to tetraphenylphosphonium (TPP^+, **black**), ethyltriphenylphosphonium ($EtTPP^+$, pink), 2,5-diethoxyphenyltriphenyl-phosphonium ($DPhTPP^+$, **blue**), or methylbenzyltriphenyl-phosphonium ($MBTPP^+$, **green**) at pH 7. Residues in the monomer A C-terminal tail (S105, R106, T108) display significant chemical shift differences when EmrE is bound to different drugs, as we previously reported in [14]. These chemical shift perturbations are comparable to those observed for residues in the active site, such as A10 which is located only one turn away from E14 in TM1.

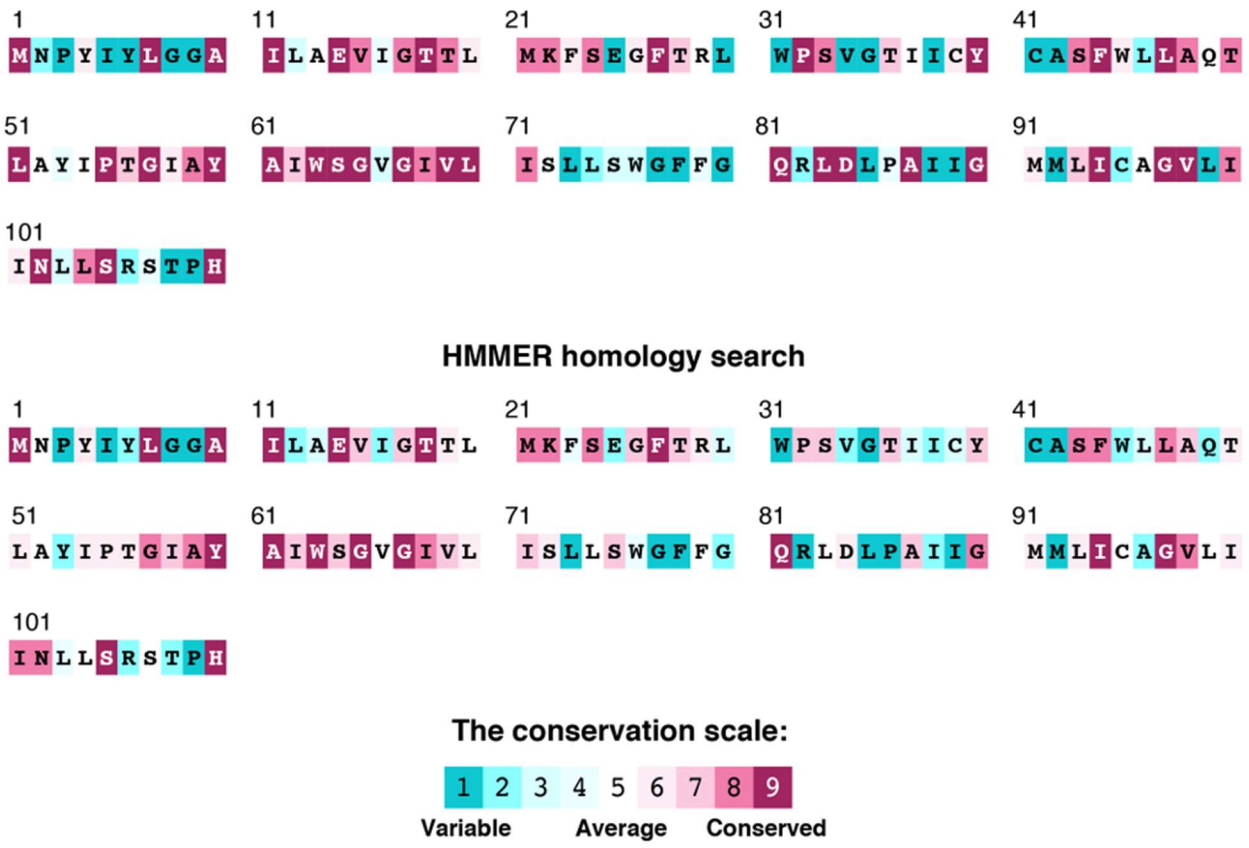

Figure S2 – *Sequence conservation for EmrE.* ConSurf analysis [47–50] was performed on the EmrE amino acid sequence using either five iterations of PSI-BLAST [51] or one iteration of HMMER [52] to search for homologues. Homologous sequences were clustered using CD-HIT with a 90% identity threshold, resulting in 477 results from the PSI-BLAST search and 5979 results from the HMMER search. 300 representative sequences from each search were aligned using MAFFT [53], and calculated conservation scores are shown.

Both homology searches display high conservation of residues that are known to be functionally important, including E14. Additionally, in both searches, H110 was shown to be maximally conserved. However, the PSI-BLAST alignment displayed significantly greater conservation overall. Recent work has shown that the majority of transporters within the SMR family are highly selective guanidinium transporters, and that EmrE is a member of a smaller clade of promiscuous

toxin efflux proteins within this family [54]. 10% of the 300 representative sequences from the HMMER search were annotated as SugE, the prototypical guanidinium exporter, while SugE was not present at all in the results from the PSI-BLAST search, indicating that the PSI-BLAST search returned sequences primarily within the EmrE-like toxin efflux clade while the larger HMMER dataset included sequences across the family. Notably, residues with higher conservation in the PSI-BLAST search include aromatic residues Y40 and F44 known to be important for binding and transport of aromatic cations that are substrates of EmrE [37,55–57]. D84 in the TM3-4 loop is also much more highly conserved within the EmrE-like clade than in the family overall.

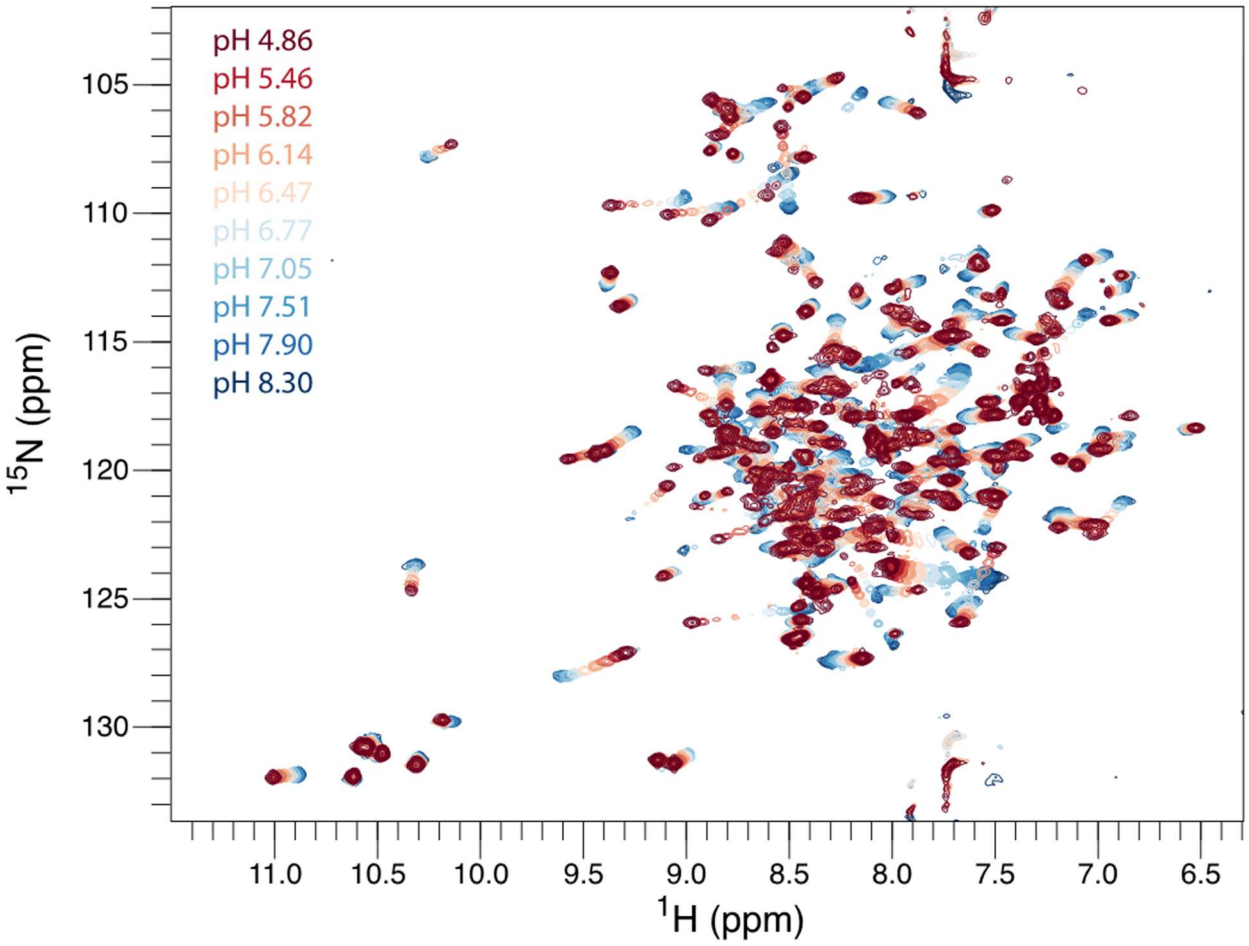

Figure S3 – *TROSY-HSQC pH titration of TPP^+-bound EmrE at 25 °C.* All the peaks change position with pH, reflecting fast proton on-/off- rates and the global conformational change that occurs upon protonation of E14 in EmrE, as we have previously shown at 45 °C [17].

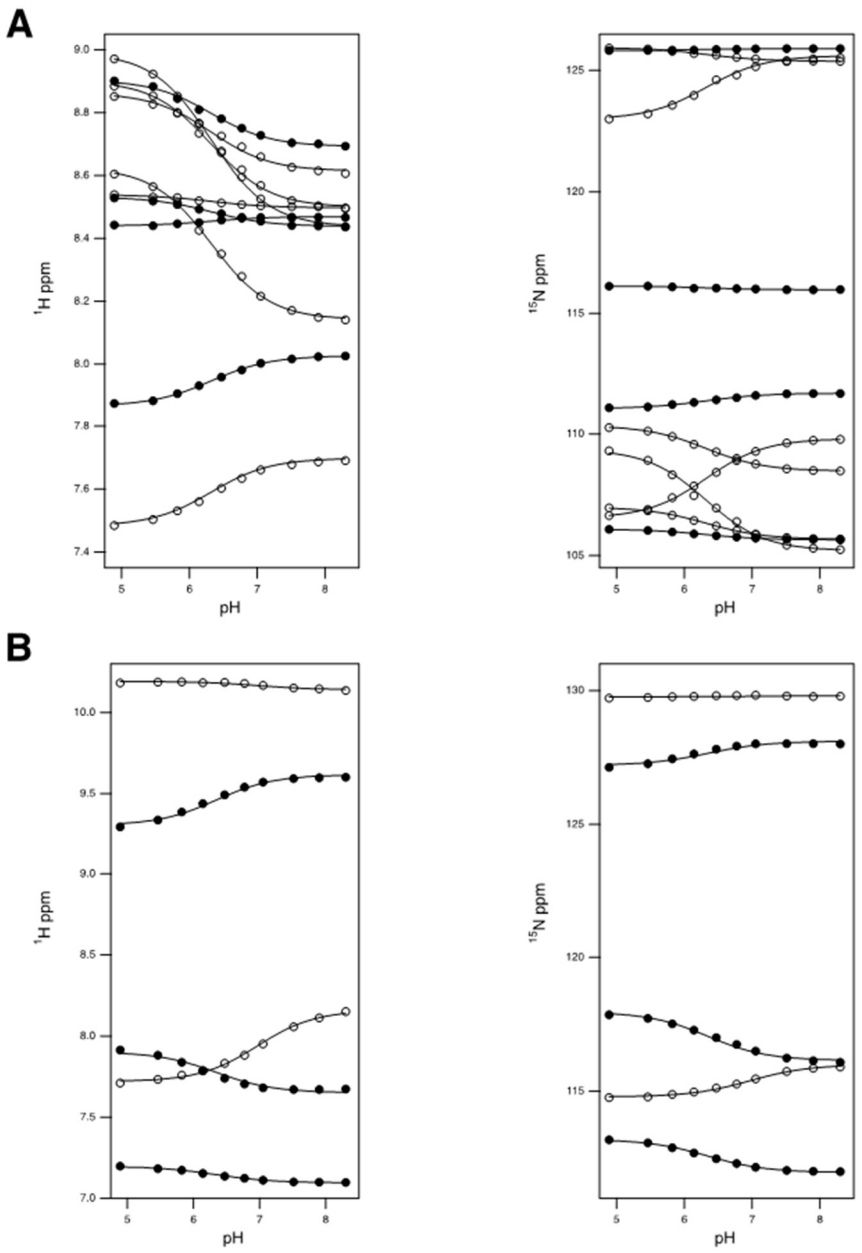

Figure S4 – *pKa determination for residues in TPP$^+$-bound EmrE from TROSY-HSQC NMR pH titration.* A) Global fit of backbone amide chemical shifts for selected core residues for monomer A (filled symbols, residues 10, 17, 44, 65) or monomer B (open symbols, residues 8, 9, 10, 17, 65, 69). B) Global fit of C-terminal tail residues in monomer A (filled symbols, residues 105,106,108) fit to a pK_a of 6.3, indicating strong coupling to the binding site, while chemical shifts

of C-terminal tail residues in monomer B (open symbols, residues 106,108) fit to a pK_a of 7.0, matching the pK_a of the imidazole sidechain of $H110^B$.

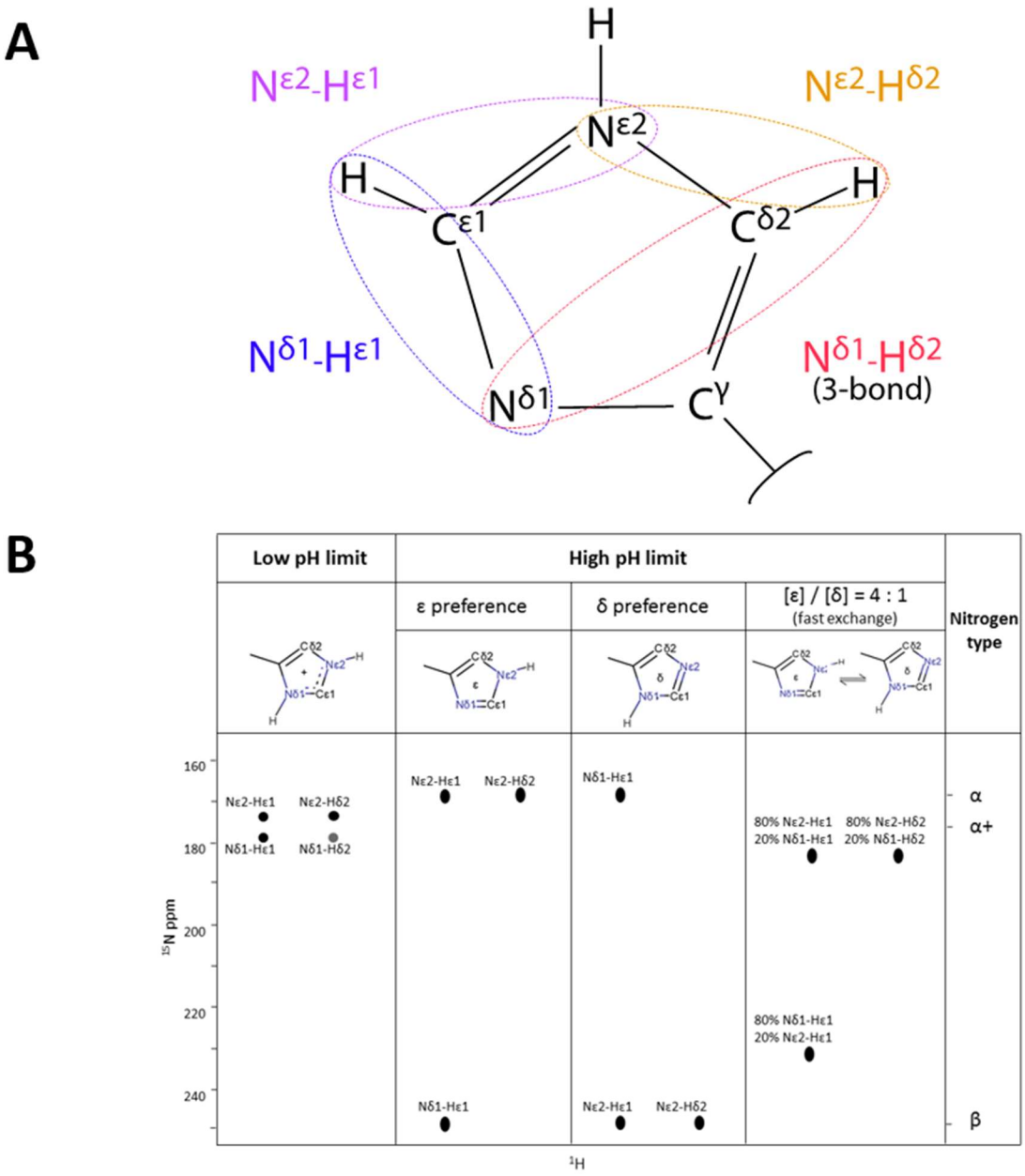

Figure S5 – *Histidine side chain correlations in HMBC spectra.* In this two-dimensional NMR experiment, magnetization is transferred from the $H^{\delta 2}$ and $H^{\varepsilon 1}$ protons to the $N^{\delta 1}$ and $N^{\varepsilon 2}$ on the imidazole side chains. This leads to the appearance of four peaks in the HMBC spectra of cationic histidine, representing the correlation of both protons to both nitrogens. The three-bond $N^{\delta 1}$–$H^{\delta 2}$

correlation (red) weakens for neutral histidine, and often disappears from the spectrum at high pH. The relative position of the three visible peaks at high pH can be used to calculate the tautomer populations of the side chain (4:1 ε/δ for free imidazole).

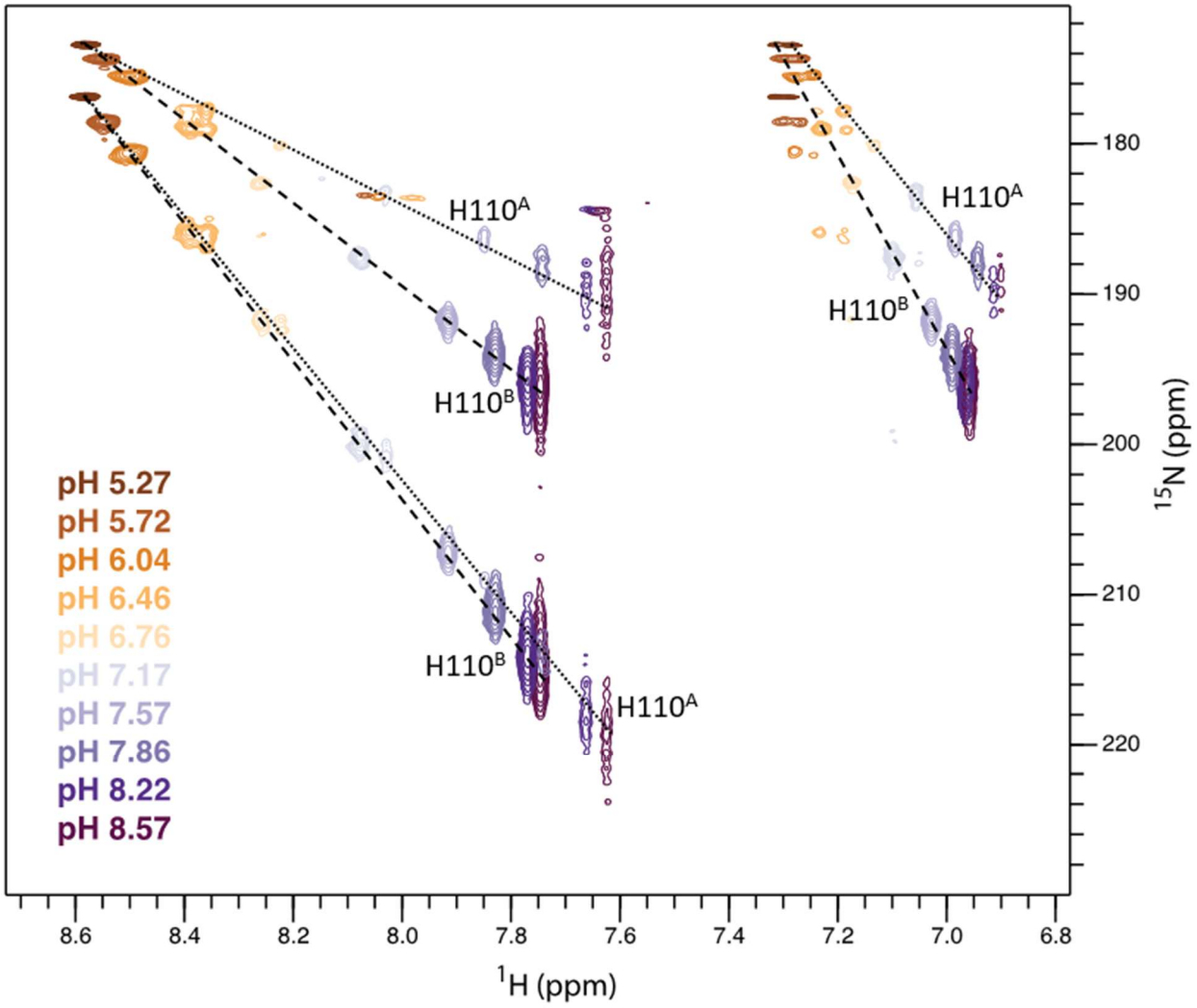

Figure S6 – *Full HMBC NMR-monitored pH titration of H110 for drug-free EmrE.* Spectra of 0.8 mM EmrE in isotropic bicelles at 25°C.

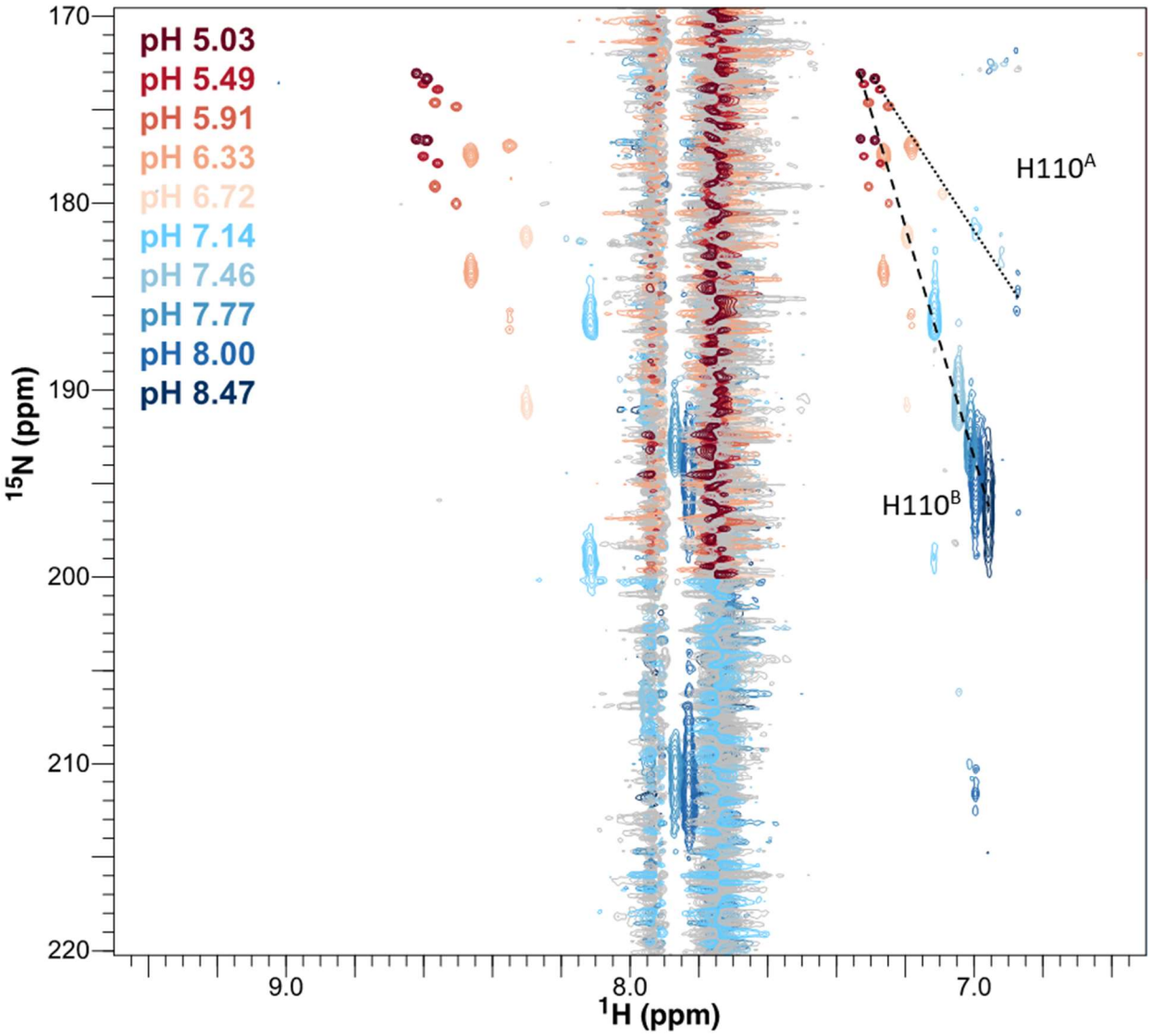

Figure S7 – *HMBC NMR-monitored pH titration of H110 for TPP⁺-bound EmrE.* 0.8 mM EmrE in isotropic bicelles saturated with 5 mM TPP^+ at 25°C. Peaks from monomer A and monomer B are resolved at low and neutral pH. Peaks corresponding to $H110^A$ are greatly broadened in the nitrogen dimension at high pH but can be seen in proton 1D slices (data not shown). Streaking at 7.7 and 7.9 ppm in the proton dimension are due to the large amounts of TPP^+ in the sample.

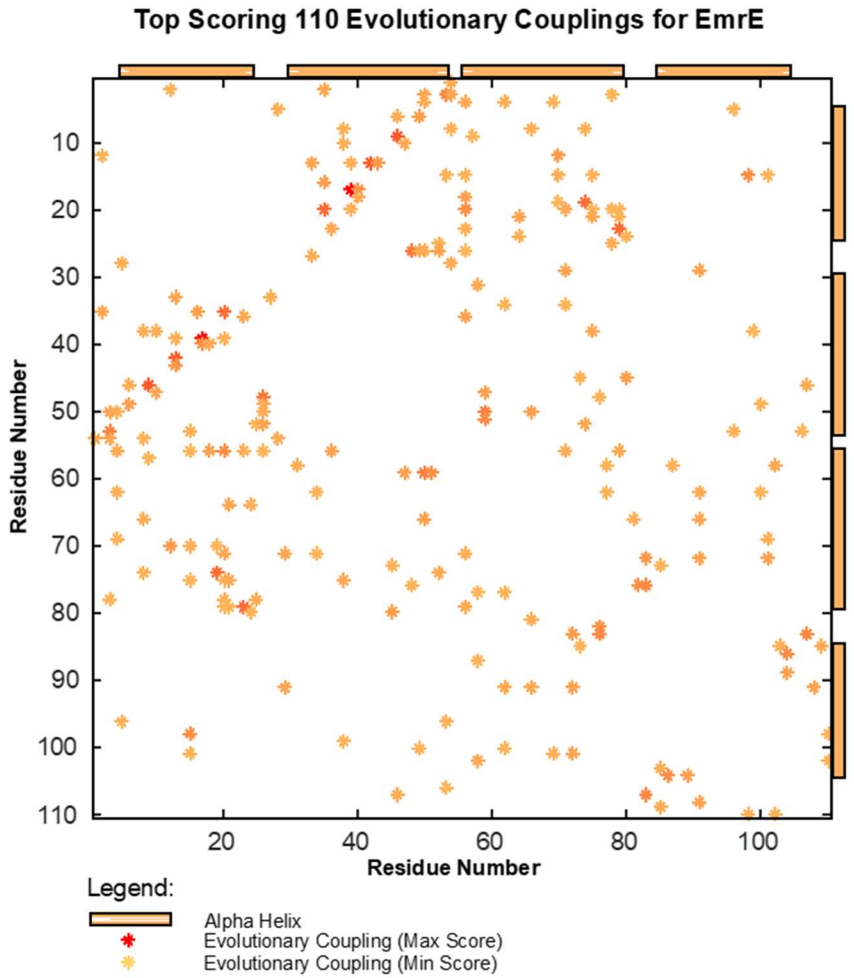

Figure S8 – *Evolutionary couplings for EmrE.* H110 is highly conserved, suggesting it may serve some functional role. To further probe the possibility that the C-terminal tail is coupled to the drug binding pocket, we constructed an alignment of 1408 proteins from the SMR family, each with less than 50% identity with EmrE, and generated an evolutionary coupling map using EVfold. To retrieve EmrE homologues, seven-iterations of PSI-BLAST were performed on June 12, 2018 using the BLOSUM45 scoring matrix[51]. For the first five iterations, 1000 sequences were retrieved, while 4000 sequences were retrieved for the final two iterations. In between each iteration, sequences with greater than 90% identity to EmrE were removed from the Position Specific Score Matrix (PSSM). Sequences with less than 50% identity were aligned using Clustal Omega[58]. Residue positions not found in EmrE were removed from the alignment, and the final

alignment of 1408 sequences were uploaded to the EVFold server to perform the evolutionary coupling analysis[59,60].

The map revealed many couplings that were consistent with the known structure and function of EmrE, such as extensive couplings from TM1 to TM2 and TM3 lining the drug-binding pocket of EmrE. However, the pattern of the couplings is less well defined than for many other helical membrane proteins, possibly because of the highly dynamic nature of EmrE. An inherent drawback with evolutionary coupling analysis is that highly conserved residues that are important for function lack sufficient variation for robust analysis and thus display fewer couplings than moderately conserved residues. H110 is highly conserved, so it only displays two weak couplings, both to TM4. Nevertheless, other residues in the C-terminal tail display strong couplings to several parts of the protein, including TM2 and TM3. Of particular note are couplings from the C-terminal tail to the TM3-4 loop, suggesting a conserved interaction between these regions.

Table S1. ITC Experimental Data

pH	Buffer	Buffer ΔH (kJ/mol)*	[EmrE] (μM)#	[TPP+] (μM)	ΔH (kJ/mol)	*n*#	K_d^{obs} (nM)	Blank (μJ)
5.5	Cacodylate	-4.72	660	2810	-39 ± 1	0.55	67000	-5.8
5.5	Cacodylate	-4.72	840	4890	-36 ± 1	0.53	78000	-3.8
5.5	MES	14.90	810	4560	-48 ± 2	0.56	80000	-10.5
5.5	MES	14.90	800	4610	-48 ± 2	0.57	73000	-13.7
5.5	Piperazine	32.83	800	4870	-61 ± 2	0.57	58000	-12.5
5.5	Piperazine	32.83	800	4980	-61 ± 2	0.56	62000	-12.6
5.5	Average:					0.56 ± 0.02	70 ± 9 x 10^3	
6.5	BES	24.21	84	233	-61 ± 4	0.52	2100	-7.2
6.5	BES	24.21	93	392	-56.4 ± 0.9	0.55	1900	-3.4
6.5	BES	24.21	94	392	-56 ± 1	0.57	1900	-3.3
6.5	Imidazole	36.46	111	254	-60 ± 4	0.48	1700	-12.8
6.5	Imidazole	36.46	92	389	-62 ± 1	0.53	2100	-2.7
6.5	Imidazole	36.46	91	384	-65 ± 2	0.55	2300	-4.1
6.5	KPi	-1.00	93	308	-28.5 ± 0.8	0.57	1800	-1.7
6.5	KPi	-1.00	57	192	-29 ± 1	0.53	1300	-2.6
6.5	KPi	-1.00	94	394	-30.8 ± 0.7	0.54	1900	-1.3
6.5	KPi	-1.00	95	404	-30 ± 1	0.57	1900	-2.7
6.5	Average:					0.54 ± 0.03	1900 ± 300	
7.5	MOPS	21.60	30	133	-40 ± 4	0.42	130	-2.0
7.5	MOPS	21.60	30	117	-40 ± 3	0.45	180	-2.0
7.5	MOPS	21.60	29	117	-40 ± 5	0.48	150	-2.0
7.5	MOPS	21.60	29	119	-42 ± 3	0.49	160	-0.3
7.55	BES	24.21	37	149	-41 ± 2	0.53	210	-2.5
7.55	BES	24.21	37	130	-51 ± 2	0.45	280	-7.6
7.55	Imidazole	36.46	33	141	-47.3 ± 0.7	0.59	270	-1.4
7.55	Imidazole	36.46	34	147	-48.6 ± 0.6	0.57	260	-1.9
7.55	KPi	-1.00	43	307	-15.7 ± 0.6	0.61	120	-1.6
7.55	KPi	-1.00	61	370	-18.7 ± 0.2	0.57	150	-1.1
7.55	Tris	46.27	31	96	-62 ± 2	0.52	250	-0.9

7.55	Tris	46.27	30	97	-63 ± 2	0.48	200	-1.2
7.5	Average:					0.51 ± 0.06	200 ± 60	
8.5	Bicine	26.34	35	141	-31.6 ± 0.8	0.56	40	-2.7
8.5	Bicine	26.34	36	154	-32 ± 1	0.54	40	-2.5
8.5	Bicine	26.34	37	124	-29.3 ± 0.8	0.47	20	0.9
8.5	Bicine	26.34	38	124	-29 ± 1	0.47	20	0.8
8.5	Glycylglycine	43.08	32	124	-38.7 ± 0.7	0.44	30	-0.2
8.5	Glycylglycine	43.08	32	124	-35.1 ± 0.9	0.45	30	-0.1
8.5	Glycylglycine	43.08	30	121	-35.4 ± 0.7	0.40	20	0.0
8.5	Glycylglycine	43.08	32	128	-38 ± 1	0.47	30	-0.9
8.5	Tris	46.27	30	122	-38 ± 2	0.42	50	-2.6
8.5	Tris	46.27	31	133	-43.5 ± 0.7	0.42	50	-1.3
8.5	Average:					0.46 ± 0.05	30 ± 10	

*Buffer data taken from [45] and adjusted for temperature as described in the methods.

#[EmrE] listed is the monomer concentration, *n* is therefore the stoichiometry of TPP^+ bound per EmrE monomer, confirming that 1 TPP^+ binds per dimer.

References

1. Forrest, L. R., Krämer, R. & Ziegler, C. The structural basis of secondary active transport mechanisms. *Biochim. Biophys. Acta BBA - Bioenerg.* **1807**, 167–188 (2011).

2. Boudker, O. & Verdon, G. Structural perspectives on secondary active transporters. *Trends Pharmacol. Sci.* **31**, 418–26 (2010).

3. Yerushalmi, H., Lebendiker, M. & Schuldiner, S. EmrE, an Escherichia coli 12-kDa multidrug transporter, exchanges toxic cations and H+ and is soluble in organic solvents. *J. Biol. Chem.* **270**, 6856–63 (1995).

4. Schuldiner, S. EmrE, a model for studying evolution and mechanism of ion-coupled transporters. *Biochim. Biophys. Acta BBA - Proteins Proteomics* **1794**, 748–762 (2009).

5. Muth, T. R. & Schuldiner, S. A membrane-embedded glutamate is required for ligand binding to the multidrug transporter EmrE. *EMBO J.* **19**, 234–40 (2000).

6. Yerushalmi, H. & Schuldiner, S. A common binding site for substrates and protons in EmrE, an ion-coupled multidrug transporter. *FEBS Lett.* **476**, 93–7 (2000).

7. Yerushalmi, H. An Essential Glutamyl Residue in EmrE, a Multidrug Antiporter from Escherichia coli. *J. Biol. Chem.* **275**, 5264–5269 (2000).

8. Cymer, F., Von Heijne, G. & White, S. H. Mechanisms of integral membrane protein insertion and folding. *Journal of Molecular Biology* vol. 427 (2015).

9. Lloris-Garcerá, P., Seppälä, S., Slusky, J. S. G., Rapp, M. & von Heijne, G. Why Have Small Multidrug Resistance Proteins Not Evolved into Fused, Internally Duplicated Structures? *J. Mol. Biol.* **426**, 2246–2254 (2014).

10. Schuldiner, S. *et al.* Small is mighty: EmrE, a multidrug transporter as an experimental paradigm. *News Physiol. Sci. Int. J. Physiol. Prod. Jointly Int. Union Physiol. Sci. Am. Physiol. Soc.* **16**, 130–4 (2001).

11. Morrison, E. A. *et al.* Antiparallel EmrE exports drugs by exchanging between asymmetric structures. *Nature* **481**, 45–50 (2012).

12. Gayen, A., Banigan, J. R. & Traaseth, N. J. Ligand-Induced Conformational Changes of the Multidrug Resistance Transporter EmrE Probed by Oriented Solid-State NMR Spectroscopy. *Angew. Chem. Int. Ed.* **52**, 10321–10324 (2013).

13. Gayen, A., Leninger, M. & Traaseth, N. J. Protonation of a glutamate residue modulates the dynamics of the drug transporter EmrE. *Nat. Chem. Biol.* **12**, 141–145 (2016).

14. Morrison, E. A. & Henzler-Wildman, K. A. Transported substrate determines exchange rate in the multidrug resistance transporter EmrE. *J. Biol. Chem.* **289**, 6825–36 (2014).

15. Cho, M.-K., Gayen, A., Banigan, J. R., Leninger, M. & Traaseth, N. J. Intrinsic conformational plasticity of native EmrE provides a pathway for multidrug resistance. *J. Am. Chem. Soc.* **136**, 8072–80 (2014).

16. Morrison, E. A., Robinson, A. E., Liu, Y. & Henzler-Wildman, K. A. Asymmetric protonation of EmrE. *J. Gen. Physiol.* **146**, 445–61 (2015).

17. Robinson, A. E., Thomas, N. E., Morrison, E. A., Balthazor, B. M. & Henzler-Wildman, K. A. New free-exchange model of EmrE transport. *Proc. Natl. Acad. Sci.* 201708671 (2017) doi:10.1073/pnas.1708671114.

18. Adam, Y., Tayer, N., Rotem, D., Schreiber, G. & Schuldiner, S. The fast release of sticky protons: kinetics of substrate binding and proton release in a multidrug transporter. *Proc. Natl. Acad. Sci. U. S. A.* **104**, 17989–94 (2007).

19. Rotem, D. & Schuldiner, S. EmrE, a multidrug transporter from Escherichia coli, transports monovalent and divalent substrates with the same stoichiometry. *J. Biol. Chem.* **279**, 48787–93 (2004).

20. Korkhov, V. M. & Tate, C. G. Electron crystallography reveals plasticity within the drug binding site of the small multidrug transporter EmrE. *J. Mol. Biol.* **377**, 1094–103 (2008).

21. Ubarretxena-Belandia, I., Baldwin, J. M., Schuldiner, S. & Tate, C. G. Three-dimensional structure of the bacterial multidrug transporter EmrE shows it is an asymmetric homodimer. *EMBO J.* **22**, 6175–6181 (2003).

22. Fleishman, S. *et al.* Quasi-symmetry in the cryo-EM structure of EmrE provides the key to modeling its transmembrane domain. *J. Mol. Biol.* **364**, 54–67 (2006).

23. Chen, Y.-J. *et al.* X-ray structure of EmrE supports dual topology model. *Proc. Natl. Acad. Sci. U. S. A.* **104**, 18999–9004 (2007).

24. Brill, S., Sade-Falk, O., Elbaz-Alon, Y. & Schuldiner, S. Specificity Determinants in Small Multidrug Transporters. *J. Mol. Biol.* **427**, 468–477 (2015).

25. Elbaz, Y., Salomon, T. & Schuldiner, S. Identification of a Glycine Motif Required for Packing in EmrE, a Multidrug Transporter from *Escherichia coli*. *J. Biol. Chem.* **283**, 12276–12283 (2008).

26. Ninio, S., Rotem, D. & Schuldiner, S. Functional Analysis of Novel Multidrug Transporters from Human Pathogens*. *Publ. JBC Pap. Press* (2001) doi:10.1074/jbc.M108231200.

27. Soskine, M., Adam, Y. & Schuldiner, S. Direct evidence for substrate-induced proton release in detergent-solubilized EmrE, a multidrug transporter. *J. Biol. Chem.* **279**, 9951–5 (2004).

28. Dastvan, R., Fischer, A. W., Mishra, S., Meiler, J. & Mchaourab, H. S. Protonation-dependent conformational dynamics of the multidrug transporter EmrE. *Proc. Natl. Acad. Sci. U. S. A.* **113**, (2016).

29. Gayen, A., Leninger, M. & Traaseth, N. J. Protonation of a glutamate residue modulates the dynamics of the drug transporter EmrE. 1–6 (2016) doi:10.1038/nchembio.1999.

30. Tate, C. G., Ubarretxena-Belandia, I. & Baldwin, J. M. Conformational changes in the multidrug transporter EmrE associated with substrate binding. *J. Mol. Biol.* **332**, 229–42 (2003).

31. Kozlov, A. G. & Lohman, T. M. Large contributions of coupled protonation equilibria to the observed enthalpy and heat capacity changes for ssDNA binding to Escherichia coli SSB protein. *Proteins* **Suppl 4**, 8–22 (2000).

32. Armstrong, K. M. & Baker, B. M. A Comprehensive Calorimetric Investigation of an Entropically Driven T Cell Receptor-Peptide/Major Histocompatibility Complex Interaction. *Biophys. J.* **93**, 597–609 (2007).

33. Baker, B. M. & Murphy, K. P. Evaluation of linked protonation effects in protein binding reactions using isothermal titration calorimetry. *Biophys. J.* **71**, 2049–55 (1996).

34. Pelton, J. G., Torchia, D. A., Meadow, N. D. & Roseman2, A. S. Tautomeric states of the active-site histidines of phosphorylated and unphosphorylated I11 Glc , a signal-transducing protein from Escherichia coli, using two-dimensional heteronuclear NMR techniques. *Protein Sci.* **2**, 543–558 (1993).

35. Vermaas, J. V, Rempe, S. B. & Tajkhorshid, E. Electrostatic lock in the transport cycle of the multidrug resistance transporter EmrE. *Proc. Natl. Acad. Sci. U. S. A.* 201722399 (2018) doi:10.1073/pnas.1722399115.

36. Bazzone, A., Zabadne, A. J., Salisowski, A., Madej, M. G. & Fendler, K. A Loose Relationship: Incomplete H + /Sugar Coupling in the MFS Sugar Transporter GlcP. *Biophys. J.* **113**, 2736–2749 (2017).

37. Mordoch, S. S., Granot, D., Lebendiker, M. & Schuldiner, S. Scanning cysteine accessibility of EmrE, an H+-coupled multidrug transporter from Escherichia coli, reveals a hydrophobic pathway for solutes. *J. Biol. Chem.* **274**, 19480–6 (1999).

38. Amadi, S. T., Koteiche, H. A., Mishra, S. & McHaourab, H. S. Structure, dynamics, and substrate-induced conformational changes of the multidrug transporter EmrE in liposomes. *J. Biol. Chem.* **285**, 26710–8 (2010).

39. Ubarretxena-Belandia, I., Baldwin, J. M., Schuldiner, S. & Tate, C. G. Three-dimensional structure of the bacterial multidrug transporter EmrE shows it is an asymmetric homodimer. *EMBO J.* **22**, 6175–81 (2003).

40. Glaubitz, C. *et al.* ^{31}P-CP-MAS NMR studies on TPP+ bound to the ion-coupled multidrug transport protein EmrE. *FEBS Lett.* **480**, 127–131 (2000).

41. Zomot, E. *et al.* A New Critical Conformational Determinant of Multidrug Efflux by an MFS Transporter. *J. Mol. Biol.* **430**, 1368–1385 (2018).

42. Drew, D. & Boudker, O. Shared Molecular Mechanisms of Membrane Transporters. *Annu. Rev. Biochem.* **85**, (2016).

43. Brill, S., Falk, O. S. & Schuldiner, S. Transforming a drug/H+ antiporter into a polyamine importer by a single mutation. *Proc. Natl. Acad. Sci. U. S. A.* **109**, 16894–9 (2012).

44. Morrison, E. A. & Henzler-Wildman, K. A. Reconstitution of integral membrane proteins into isotropic bicelles with improved sample stability and expanded lipid composition profile. *Biochim. Biophys. Acta* **1818**, 814–20 (2012).

45. Goldberg, R. N., Kishore, N. & Lennen, R. M. Thermodynamic Quantities for the Ionization Reactions of Buffers. *J. Phys. Chem. Ref. Data* **31**, 231–370 (2002).

46. Sigurskjold, B. W. Exact analysis of competition ligand binding by displacement isothermal titration calorimetry. *Anal. Biochem.* **277**, 260–6 (2000).

47. Berezin, C. *et al.* ConSeq: the identification of functionally and structurally important residues in protein sequences. *Bioinformatics* **20**, 1322–1324 (2004).

48. Ashkenazy, H., Erez, E., Martz, E., Pupko, T. & Ben-Tal, N. ConSurf 2010: calculating evolutionary conservation in sequence and structure of proteins and nucleic acids. *Nucleic Acids Res.* **38**, W529–W533 (2010).

49. Celniker, G. *et al.* ConSurf: Using Evolutionary Data to Raise Testable Hypotheses about Protein Function. *Isr. J. Chem.* **53**, 199–206 (2013).

50. Ashkenazy, H. *et al.* ConSurf 2016: an improved methodology to estimate and visualize evolutionary conservation in macromolecules. *Nucleic Acids Res.* **44**, W344–W350 (2016).

51. Altschul, S. F. *et al.* Gapped BLAST and PSI-BLAST: a new generation of protein database search programs. *Nucleic Acids Res.* **25**, 3389–402 (1997).

52. Eddy, S. R. A new generation of homology search tools based on probabilistic inference. *Genome Inform. Int. Conf. Genome Inform.* **23**, 205–11 (2009).

53. Katoh, K., Kuma, K., Toh, H. & Miyata, T. MAFFT version 5: improvement in accuracy of multiple sequence alignment. *Nucleic Acids Res.* **33**, 511–518 (2005).

54. Kermani, A. A., Macdonald, C. B., Gundepudi, R. & Stockbridge, R. B. Guanidinium export is the primal function of SMR family transporters. *Proc. Natl. Acad. Sci. U. S. A.* **115**, 3060–3065 (2018).

55. Rotem, D., Steiner-Mordoch, S. & Schuldiner, S. Identification of tyrosine residues critical for the function of an ion-coupled multidrug transporter. *J. Biol. Chem.* **281**, 18715–22 (2006).

56. Wang, J., Rath, A. & Deber, C. M. Functional response of the small multidrug resistance protein EmrE to mutations in transmembrane helix 2. *FEBS Lett.* **588**, 3720–3725 (2014).

57. Sharoni, M., Steiner-Mordoch, S. & Schuldiner, S. Exploring the Binding Domain of EmrE, the Smallest Multidrug Transporter. *J. Biol. Chem.* **280**, 32849–32855 (2005).

58. Sievers, F. *et al.* Fast, scalable generation of high-quality protein multiple sequence alignments using Clustal Omega. *Mol. Syst. Biol.* **7**, 539 (2011).

59. Marks, D. S. *et al.* Protein 3D structure computed from evolutionary sequence variation. *PloS One* **6**, e28766 (2011).

60. Ekeberg, M., Lövkvist, C., Lan, Y., Weigt, M. & Aurell, E. Improved contact prediction in proteins: Using pseudolikelihoods to infer Potts models. *Phys. Rev. E* **87**, 012707 (2013).

Chapter 5

Novel substrate triggers susceptibility by uncoupling a multidrug resistance efflux pump

Peyton J. Spreacker[1ɣ], Nathan E. Thomas[1ɣ], Will F. Beeninga[1,3], Merissa Brousseau[1], Katherine A. Henzler-Wildman[1,2*]

[1]Department of Biochemistry, University of Wisconsin-Madison, Madison, WI 53703 USA

[2]Nuclear Magnetic Resonance Facility at Madison, University of Wisconsin-Madison, Madison WI 53703, USA

[3]*Current Address*: Mayo Medical Laboratories, Rochester, MN

[ɣ]Equal contribution authors

Preface: This chapter explores an intriguing implication of the free exchange model – that the multiple transport pathways exhibited by EmrE could be exploited to turn this model multidrug efflux pump into an antibiotic target. A manuscript detailing this work is currently being prepared for submission, with Peyton and I as co-first authors. Peyton performed the Biolog screen and acquired the S64V NMR spectra, while I performed the SSME transport assays and acquired and assigned the E14Q spectra. Will performed the growth assays, and Merissa performed binding assays (not included here, but which will appear in the final manuscript).

Introduction:

Antibiotic resistance in bacterial infections is a major global health crisis[1]. Bacteria acquire resistance through many methods, including small multidrug resistance (SMR) transporters which are found throughout the bacterial kingdom[2–5]. EmrE is an SMR transporter found in the inner membrane of *E. coli* that confers resistance to several toxic polyaromatic cations. Active efflux of toxic molecules by EmrE is driven by the proton motive force (PMF) through coupled antiport of substrate and proton as illustrated in Figure 1A. Due to its small size, EmrE has become a model system for studying the structure and mechanism of proton-coupled transporters. However, this minimal transporter has proven to be surprisingly complex, and EmrE has broken many long-held assumptions regarding the mechanism of ion-coupled transport.

Transporters have traditionally been classified as antiporters, uniporters, or symporters. Thus, the discovery that EmrE could perform coupled 2 H^+: 1 substrate antiport of both polyaromatic cations[6] defined its function for many years. More recently, careful exploration of the states and transitions of EmrE using NMR pH titrations and dynamics experiments revealed that many states would be significantly populated under physiological conditions, and that all these states could readily interconvert[7]. These results suggested that the minimal model of pure exchange transport typically used to represent EmrE function[8] was overly simplified. Including all the states and transitions observed by NMR leads to a more complex model where proton/substrate symport, proton uniport, and substrate uniport are all possible in addition to the well-established proton/substrate antiport activity of EmrE (Fig. 1). The biological implications of these alternative pathways are significant – while H^+-driven antiport results in toxin efflux and a resistance phenotype *in vivo*, all the alternative pathways (symport or uniport) result in toxin influx or PMF rundown, and thus would result in a susceptibility phenotype in bacteria.

While $2H^+$: 1 substrate antiport has been shown to be the most common pathway of EmrE[9], substrates may influence EmrE activity by altering the rate of key steps in the transport cycle and biasing flux through different pathways. EmrE functions as an antiparallel homodimer with glutamate 14 (E14) in TM1 playing a critical role in binding both drug and proton [10,11]. Substrate can influence E14's pK_a in the drug bound state – which will impact likelihood to have drug only or drug and proton bound and thus favor antiport or symport[9]. Prior studies with a series of tetraphenylphosphonium (TPP^+) derivatives revealed that the identity of the transported substrate significantly alters the rate of alternating access[12], a critical step in the transport cycle in which EmrE switches between open-in and open-out conformations to move the substrate across the membrane. This raises the question of whether the small molecule substrate itself may not only alter the rate of transport, but also alter the manner or efficiency of proton coupling.

There is precedent for a substrate switching functional behavior of an EmrE mutant. The W63G mutation extends EmrE's substrate profile to erythromycin but also confers susceptibility

to polyamine compounds[13]. Here we explore whether substrate identity can switch the transport phenotype in the wildtype transporter, hypothesizing that EmrE can perform multiple types of proton-coupled and uncoupled transport and that the mode of transport depends on the identity of the transported substrate (Fig. 1). Using an unbiased small molecule phenotyping screen, we identify a new substrate to which EmrE confers susceptibility, harmane, and then use a combination of *in vitro* and *in vivo* assays to confirm direct interaction of harmane with EmrE and determine its mechanism of action. This work opens the possibility that small molecules can be designed that trigger alternative functions of a multidrug transporter, converting a resistance phenotype to a susceptibility phenotype and opening a potential target for antibiotic development.

Results:

An unbiased small molecule screen reveals a new substrate to which EmrE confers resistance.

Many substrate screen have been performed on EmrE, but these screens have focused on quaternary ammonium compounds (QACs) and quaternary cationic compounds (QCCs) and biased the results toward antiport substrates[6,14–16]. We sought to perform an unbiased compound screen on EmrE using the Biolog Phenotypic Microarray assay from Biolog, Inc. This screen has been used to uncover diverse substrates of known proteins[17] by assessing the metabolism of *E. coli* upon treatment with a small set of diverse compounds not biased by a specific motif or mechanism of action. We compared the metabolism of Δ*emrE* MG1655 *E. coli* cells transformed with either wildtype or non-functional EmrE (E14Q-EmrE). Compounds that led to greater metabolic activity when wildtype EmrE was expressed were classified as resistance hits, while compounds that reduced metabolic activity in the presence of wildtype EmrE were classified as susceptibility hits (Figure 2A, Table 1 – see methods for selection criteria). As shown in Figure 1A, the screen found hits in both the resistance and susceptibility categories. The canonical EmrE substrate methyl viologen (MV^{2+}) was the strongest resistance hit with a score of 8, the highest possible. This gave us confidence that the Biolog assay can report on EmrE drug resistance phenotypes. However, we were more interested in whether the assay can report on drug

susceptibility phenotypes. Two compounds scored -6, indicating reduced metabolic activity for wildtype EmrE vs. E14Q for 6 of the 8 concentrations tested: hexachlorophene and harmane. Hexachlorophene is nearly insoluble in aqueous buffer, so we continued on with functional characterization of harmane.

We performed microplate growth assays with MV^{2+} and harmane to determine whether the metabolic phenotypes we observed with Biolog also resulted in bacterial growth phenotypes. As expected, cells expressing wildtype EmrE continued to grow in the presence of MV^{2+} while cells expressing E14Q-EmrE failed to grow at the same concentration of the compound (Figure 2B). In contrast, harmane treatment produced an unprecedented phenotype in EmrE literature. E14Q-EmrE cells grew in the presence of harmane, but those cells expressing wildtype EmrE had a stagnated growth after three to five hours of treatment (Figure 2C). This confirmed that functional EmrE – a multidrug resistance transporter – confers susceptibility to harmane.

Harmane is not transported by EmrE in a coupled manner, but rather induces proton efflux through the transporter.

To better understand the mechanism of this intriguing result, we turned to solid supported membrane electrophysiology (SSME) to monitor the transport activity of EmrE reconstituted into proteoliposomes (Fig. 2)[18]. Proteoliposomes reconstituted with E14Q-EmrE were used as negative controls and produced minimal signals under all conditions. In the presence of a 2-fold inward-facing proton gradient without drug, wildtype EmrE produced a small positive signal, consistent with a small amount of uncoupled proton transport into the liposomes. The addition of either the canonical antiported substrate methyltriphenylphosphonium ($MeTPP^+$) or harmane to both the internal and external buffers greatly increased this signal, consistent with increased transport (Fig. 2A-E, black).

Next, we varied the combination of drug and proton gradients as this should produce predictable results for coupled transport[19]. For antiported substrates, the signal should increase when the drug and proton gradients face opposite directions (favoring exchange) and decrease

when the gradients face the same direction (favoring co-transport). Symported substrates should behave in the opposite manner, with increased transport when the gradients face the same direction and decreased transport when they are opposed. $MeTPP^+$ behaved as expected for an antiported substrate, but harmane function was inconsistent with either antiport or symport. Regardless of the direction of the harmane gradient, the amount of transported charge remained constant – always in the direction of the proton gradient and well above the signal observed in the absence of harmane. This indicates that rather than being transported by EmrE in a proton-coupled manner, harmane induces increased uncoupled proton transport by EmrE.

We then investigated the effect of harmane concentration on the proton transport rate by co-varying the internal and external harmane concentration to maintain zero harmane gradient while maintaining the same 2-fold proton gradient. The peak current increased with increasing harmane concentration and saturated between 32 and 128 μM (Fig. 2F,G). While harmane induces uncoupled transport, the hyperbolic dependence of peak current on the harmane concentration suggests a direct binding interaction between harmane and EmrE is responsible for transport.

Harmane binding induces broad conformational changes in EmrE, like TPP^+.

To understand the nature of the interaction between harmane and EmrE, we analyzed chemical shift perturbations (CSPs) of EmrE by NMR. To maximize the signal-to-noise ratio of the spectra, we used S64V-EmrE. This mutant of EmrE is known to slow the rate of alternating access of EmrE, increasing spectral quality, while binding compounds to similar affinity as wildtype EmrE [20]. We compared the CSPs of apo, harmane-bound, and TPP^+-bound S64V-EmrE to map the conformational changes in EmrE upon compound binding. When S64V-EmrE binds TPP^+, large CSPs occur throughout the protein, with particularly large CSPs in TM1 and TM3 (Fig. 4C,D). While harmane binding also effects changes throughout the spectrum, the CSPs are much smaller (Fig. 4A,B). Additionally, apart from two residues in TM1 ($G17^A$ and $T18^A$), CSPs in the loops and tail are comparable to the CSPs in the transmembrane helices.

This suggested a potential mechanism of action for harmane's uncoupling phenotype. A recent investigation of coupling between EmrE's C-terminal residue H110 and the central binding site E14 led us to propose that proton transport by EmrE is gated by the C-terminal tail in the absence of drug[21]. Drug binding to a secondary site in the loops, originally suggested by drug-monitored ^{31}P NMR studies[22], could unlock this gate and allow transport to proceed. Could harmane binding to this secondary site be responsible for its uncoupling activity?

NMR of E14Q-EmrE reveals a secondary binding site that differs between resistance and susceptibility substrates of EmrE.

To investigate the potential role of a secondary binding site, we performed NMR studies of E14Q-EmrE. This mutation abolishes the central drug binding site and thus, any changes in the spectrum upon the addition of drug must be due to binding to the secondary site. Addition of both harmane (Fig. 5A,B) and TPP^+ (Fig. 5C,D) to E14Q resulted in CSPs throughout the protein. For TPP^+, these changes were much smaller for E14Q than for S64V, with the largest concentration of significant CSPs seen in the C-terminal tail of subunit A. Interestingly, apart from TM1, the harmane CSPs were comparable between E14Q and S64V, suggesting that E14Q retains the functional binding site for harmane.

Discussion:

Recent studies in our lab suggest that the multidrug transporter EmrE may be capable of multiple transport functions, including drug uniport, proton uniport, and even proton-coupled drug symport in addition to its well-characterized proton-coupled drug antiport activity[7,9]. As drug identity dramatically alters the relative rates of EmrE's transport pathways[12], this raises the possibility that certain compounds may be able to bias EmrE toward these additional deleterious pathways and cause this multidrug resistance pump to instead confer drug susceptibility. With this in mind, we performed a metabolic screen of EmrE using a diversity library from Biolog. Despite the small size of the library (238 compounds), we identified several compounds for which EmrE conferred susceptibility, including harmane.

Using SSME transport assays, we found that harmane is not transported by EmrE in a coupled manner but instead, induces uncoupled proton transport. These assays cannot rule out the possibility that harmane is also transported by EmrE, but comparison with the microplate growth assays suggests that the susceptibility phenotype is due to uncoupled proton transport. Growth phenotypes between cells expressing wildtype or E14Q EmrE begin to appear around the 3 hour mark, approximately the point at which fermentable sugars are consumed [23] and cells become more reliant on the PMF for ATP production. NMR studies identified direct interaction between harmane and EmrE, including a peripheral binding site likely responsible for harmane's uncoupling activity. While TPP^+ also interacts with this peripheral site, TPP^+ interactions with the primary binding site are much stronger[22,24], whereas CSPs upon harmane binding are comparable regardless of the presence of the central E14 binding site. Future work to characterize this site and design compounds that preferentially bind to it rather than the central E14 site could yield substrates that cause even greater susceptibility phenotypes.

With the increased threat of antibiotic resistance, it is imperative that we find new ways to combat multidrug efflux and resistance. EmrE's ability to simultaneously confer resistance to some substrates and susceptibility to others is unprecedented, but not necessarily unique. In the absence of drug, the multidrug efflux pump P-glycoprotein exhibits significant levels of basal ATP hydrolysis[25]. In fact, loose coupling between the driving force, whether that consists of ion transport or ATP hydrolysis, and substrate transport may be a requirement of multidrug recognition and efflux, as tight binding generally requires highly specific and selective interactions between the protein and the substrate[26]. If loose coupling is required for multidrug efflux, then targeting dissipative pathways in these transporters may represent a fruitful avenue for combatting antibiotic resistance.

Methods:

Microplate Growth Curves

Cells expressing plasmids of interest were grown in LB media (tryptone, yeast extract, 30mM bistris propane, 100µg/mL ampicillin, pH 7.0) from a single colony to an OD of 0.2. The cells were then diluted to a final OD of 0.01 in microplates (Corning, REF: 351172) containing concentration ranges of harmane or MV^{2+}. The plates were incubated in a microplate reader (BMG-Labtech) at 37°C. OD_{600} (guanidinium and methyl viologen) and OD_{700} (ethidium bromide) were measured every 5 minutes for 20 hours. Experiments were performed in technical and biological triplicate and data was analyzed using Excel and Igor Pro.

Functional Phenotypic MicroArrays

MG1655 Δ*emrE E. coli* cells containing either WT- or E14Q-EmrE constructs were grown on LB-Amp media overnight at 37°C. The phenotype microarray tests followed the established protocols of standard PM procedures for *E. coli* and other gram-negative bacteria (12). PM01-20 plates were used to screen both WT- and E14Q- EmrE expressing cells. Overnight plates were resuspended in IF-0a inoculating fluid (Biolog) to an optical density of 0.37. The cells were diluted by a factor of 6 into IF-0a media plus Redox Dye A and 20mM glucose was added for PM3-8 plates. Cells were diluted to a 1:200 dilution in IF-10a media (Biolog) with Redox Dye A for PM9-20 plates. PM plates were inoculated with 100µL of cell suspensions per well. The microplates were incubated at 37°C and read using the OmniLog instrument every 15min for 24 h. The area under the resulting metabolic curves was determined for cells expressing WT- SMR_{Xx} or E14Q-SMR_{Xx}. The difference was calculated as

$$\text{Delta} = (\text{WT-SMR}_{Xx}\ \text{Area}) - (\text{E14Q-SMR}_{Xx}\ \text{Area}) \quad (1)$$

Resulting in positive values for greater respiration by cell expressing WT-EmrE and negative values for greater respiration by cells expressing non-functional E14Q-EmrE. The 10% trimmed mean was then calculated for each data set (WT replicate 1, WT replicate 2, E14Q replicate 1, E14Q replicate 2) separately for each transporter as variation between replicates can arise due to minor deviations between plate sets or in the exact concentration of dye or OD of cells upon dilution on different days. The standard deviation was then calculated among known non-hits

(selecting at least 50 wells out of the 960 total wells in a single data set) to determine the cut-off values for actual hits. Individual wells were assessed as hits if the calculated Delta value (equation 1) was more than two standard deviations from the 10% trimmed mean. For each hit, a value of +1 was assigned for resistance hits (positive Delta) and a value of -1 was assigned for susceptibility hits (negative Delta). These values were then summed across all eight wells for a single compound (4 wells of the same compound per plate set * 2 replicates, with a max score of ±8. Final resistance or susceptibility hits were assigned if the total score was ≥ +3 (resistance) or ≤ -3 (susceptibility). This definition was chosen since small total hit scores of ±1 or ±2 could arise by chance using the ± 2*SD cutoff to score individual wells. Values of ±3 recognize consistent hits across multiple replicates and/or different concentrations of the same compound. Our cutoff is not set higher since the 4 wells of each compound on a single plate set include different concentrations and some concentrations may not be sufficient to elicit a phenotype.

Protein expression and purification

To obtain purified protein, all EmrE mutants were expressed from a pET15b plasmid in M9 media and purified using an immobilized nickel and size exclusion chromatography as previously described[18].For NMR samples, the M9 media was deuterated and ^{15}N-labeled (and ^{13}C labeled for assignment samples), and supplemented with 0.5g/L ^{2}H-^{15}N or ^{2}H-^{13}C-^{15}N Isogro. Isotopically labeled purified protein was reconstituted into bicelles as previously described for solution NMR experiments[21]. For SSME transport assays, EmrE was reconstituted into 1-palmitoyl-2-oleoyl-glycero-3-phosphocholine (POPC) liposomes at a 400:1 lipid:protomer mol:mol ratio. After adding the detergent solubilized protein, the final lipid concentration was 2.5 mg/mL in a buffer containing 50 mM MES, 50 mM MOPS, 50 mM bicine, 100 mM NaCl, and 2 mM $MgCl_2$ at pH 7. Detergent was removed by Biobeads as previously described[21], and liposome aliquots were flash frozen and stored at -80°C until needed for experiments.

NMR spectroscopy

75% of the backbone resonances of apo E14Q-EmrE was assigned at pH 5.8 by standard triple resonance experiments (TROSY-HNCA, TROSY-HNCO, TROSY-HN(CO)CA). TPP^+-bound E14Q was assigned by titration of TPP^+. 2D TROSY-HSQCs were acquired with a 900 MHz Bruker spectrometer equipped with a cryoprobe using standard pulse sequences with gradient coherence selection.

Solid supported membrane electrophysiology

All SSME data was acquired an a Nanion SURFE^{2}R N1 instrument. Liposome aliquots were thawed, diluted 2-fold, and briefly sonicated. 10 µL of liposomes were added to prepare 3 mm sensors according to a standard protocol (Chapter 3). Prior to experiments, sensor capacitance and conductance values were obtained to ensure sensor quality. For all experiments, buffers contained 50 mM MES, 50 mM MOPS, 50 mM bicine, 100 mM NaCl, and 2 mM $MgCl_2$ with internal pH values of 7.3 and external pH values of 7.0. For inward-facing drug gradients, external drug concentration was 8 µM and internal drug concentration was 0.5 µM. For outward-facing drug gradients, internal drug concentration was 8 µM and external drug concentration was 0.5 µM. Both internal and external drug concentration was 8 µM for the zero gradient data. For data acquisition, sensors were equilibrated with internal buffer and transport was initiated by perfusion of the external buffer before re-equilibration with the internal buffer. Signals were obtained by integrating the current during perfusion of the external buffer, with the final 100 ms of the initial buffer equilibration used as the baseline. Reported data are average values of at least three sensors, with error bars representing the standard error of the mean.

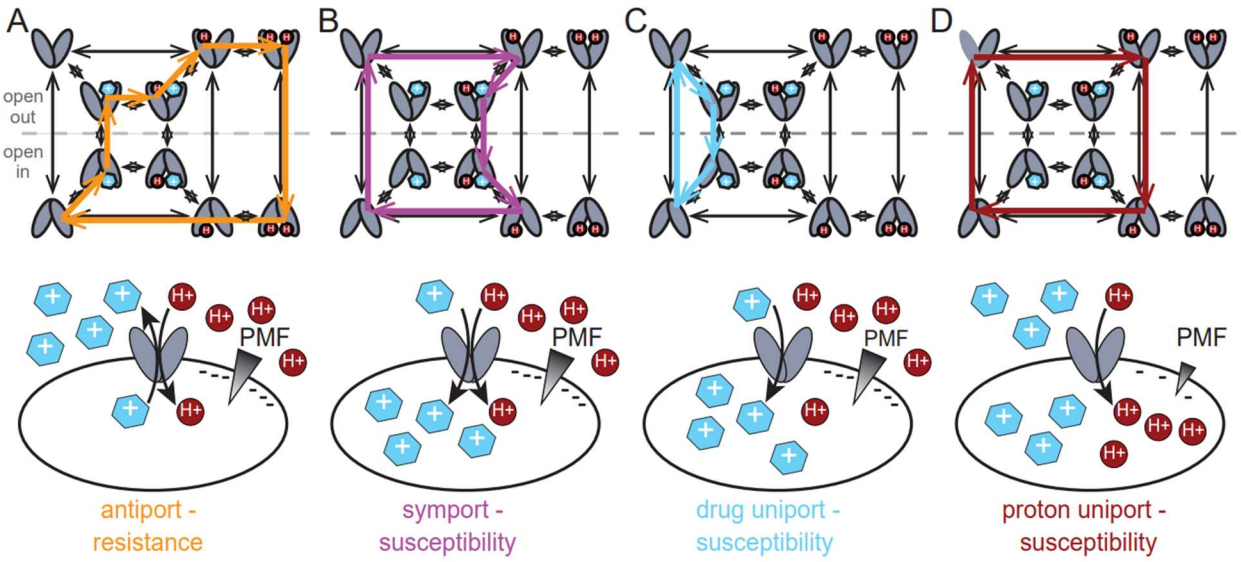

Figure 1 – *Transport pathways in the free exchange model and their expected phenotypes.*

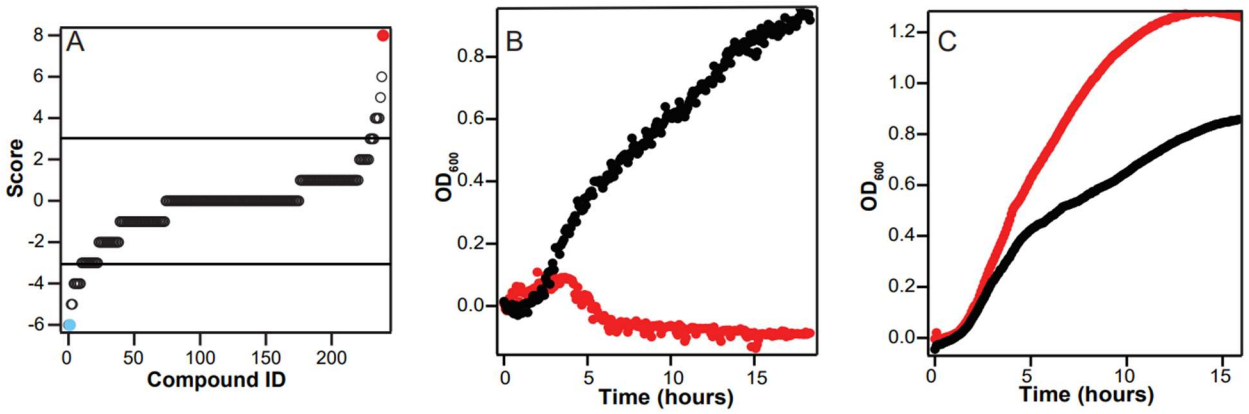

Figure 2 – *Biolog screen results and hit validation*. (A) Plot of hit scores vs. compound number for the Biolog screen (data can be found in Table 1). (B) Growth curves of wildtype (black) or E14Q (red) ΔemrE-MG1655 *E. coli* with 500 μM methyl viologen. (C) Growth curves of wildtype (black) or E14Q (red) ΔemrE-MG1655 *E. coli* with 130 μM harmane.

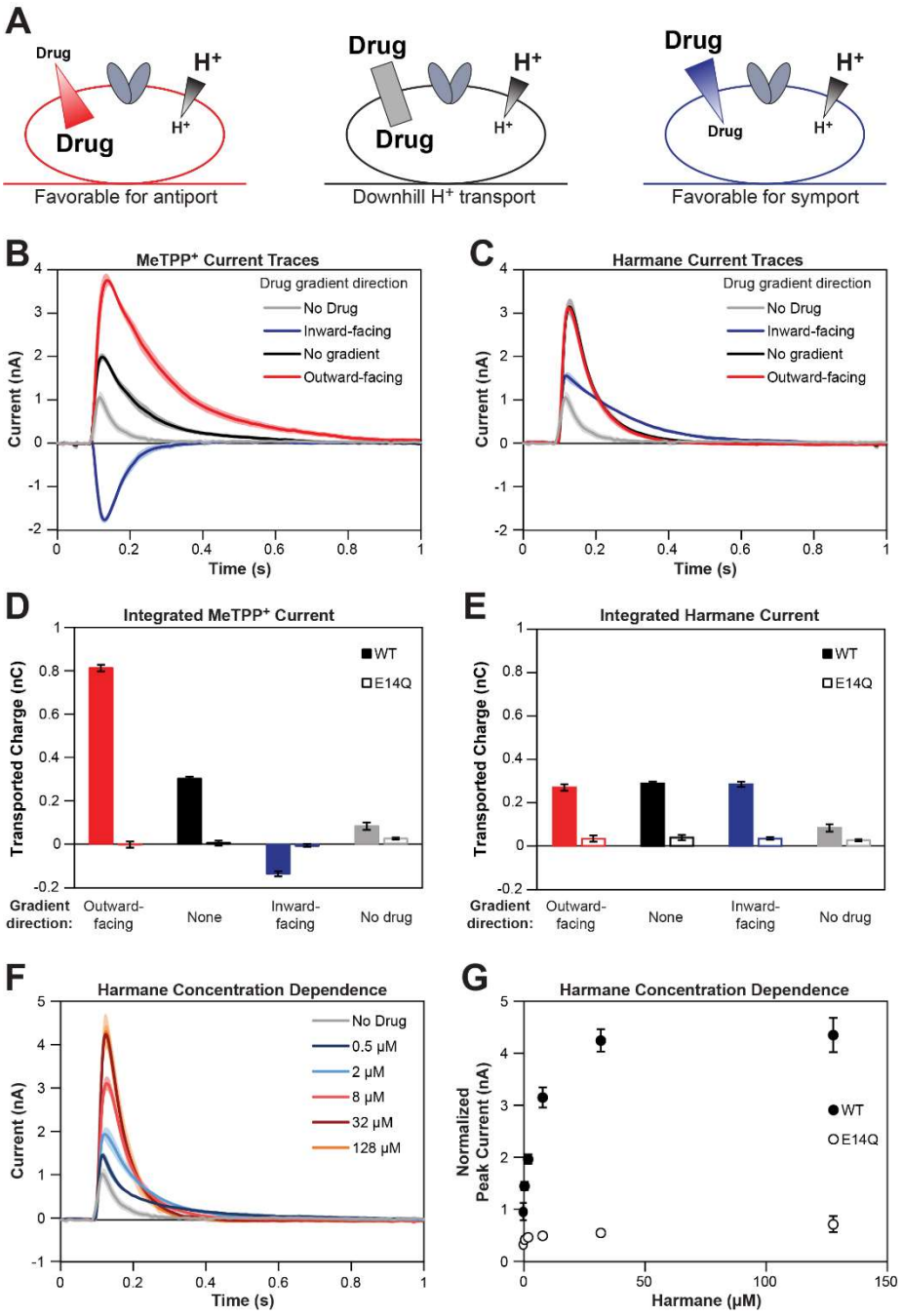

Figure 3 – *SSME characterization of transport behavior.* (A) Cartoon scheme of gradient directions for panels (B-E). MeTPP$^+$ (B and D) behaves as expected for an antiported substrate, with increased signal when the drug and proton gradients are oriented in opposite directions and a reversal of transport direction when the large MeTPP$^+$ gradient is oriented in the same direction as the smaller proton gradient. Harmane (C and E) increases the transport signal compared to a

background without drug. While the direction of the harmane gradient does not affect the amount of observed transport (E), increasing harmane concentrations lead to an increased rate of proton transport (F and G).

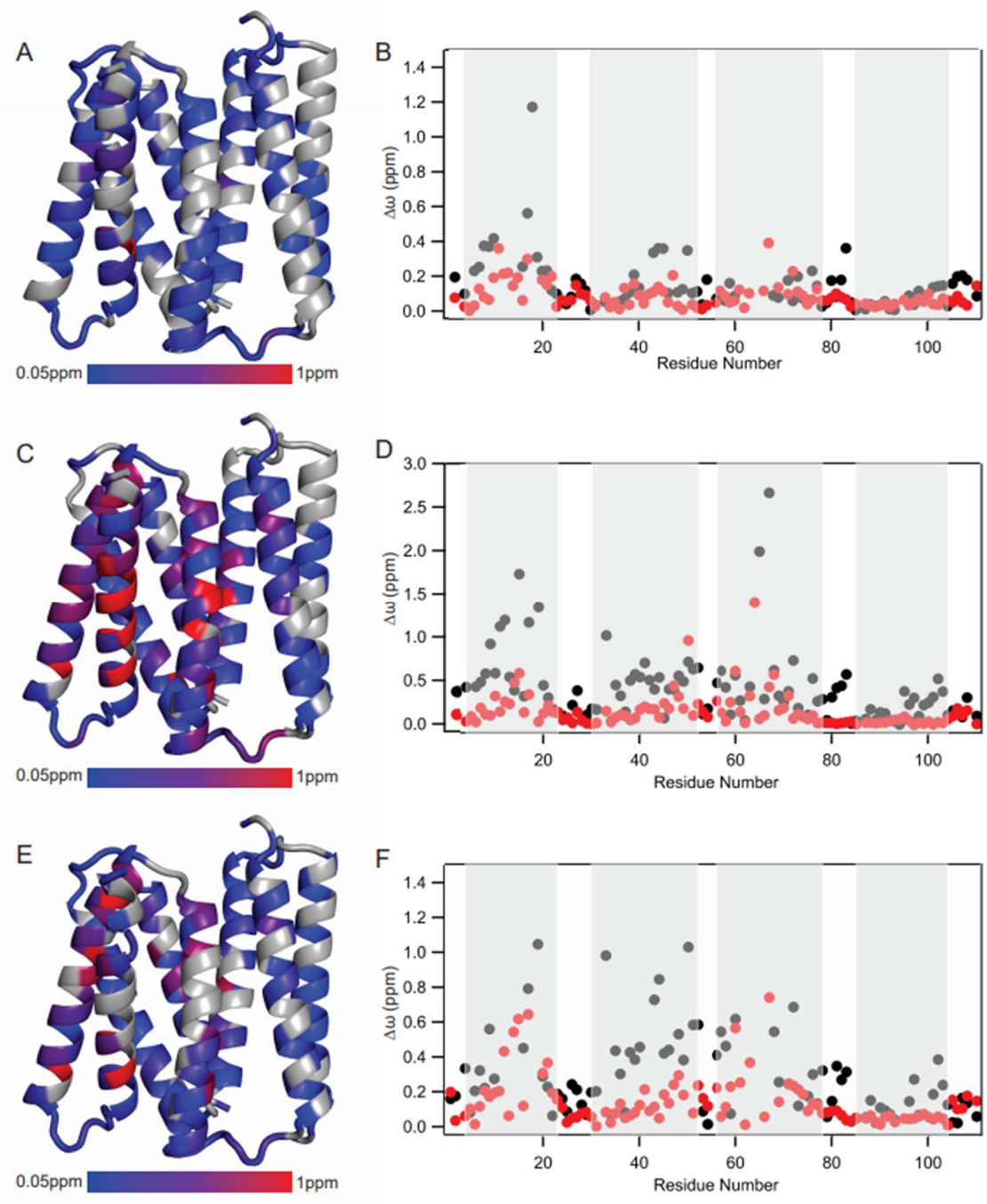

Figure 4 – *CSP analysis of drug binding to S64V-EmrE*. CSPs for harmane-bound vs. drug-free (A and B), TPP^+-bound vs. drug-free (C and D), and harmane-bound vs. TPP^+-bound (E and F). CSPs are plotted onto the full-length MD structure[27] using the indicated color scale, with unassigned residues colored gray.

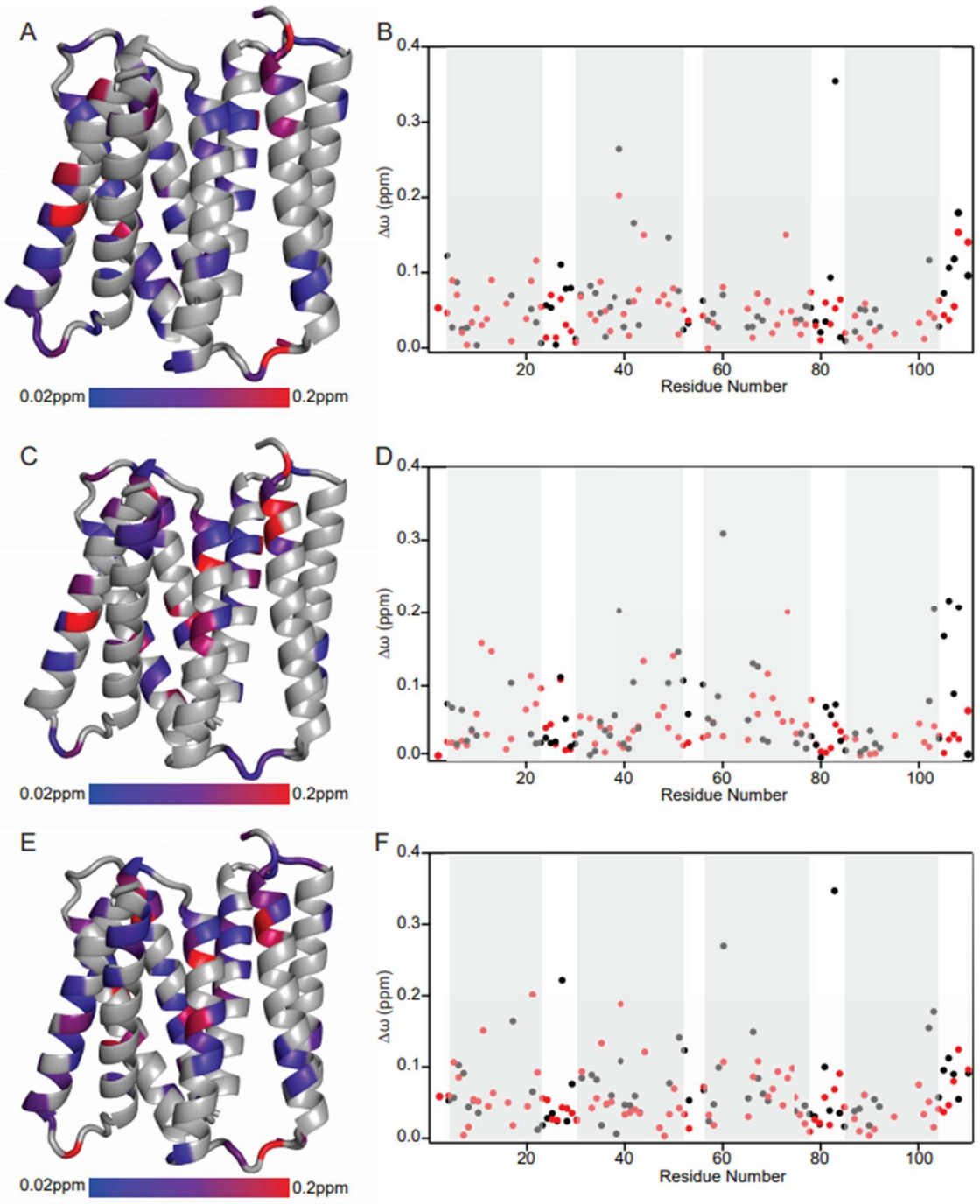

Figure 5 – *CSP analysis of drug binding to E14Q-EmrE*. CSPs for harmane-bound vs. drug-free (A and B), TPP^+-bound vs. drug-free (C and D), and harmane-bound vs. TPP^+-bound (E and F). CSPs are plotted onto the full-length MD structure[27] using the indicated color scale, with unassigned residues colored gray.

Table 1 – Biolog Screen Compound Scores

#	Compound	Score	#	Compound	Score
1	Harmane	-6	*52*	Cytosine-1-beta-D-arabinofuranoside	-1
2	Hexachlorophene	-6	*53*	Bleomycin	-1
3	Menadione, sodium bisulfate	-5	*54*	Oxophenylarsine	-1
4	18-Crown-6 ether	-5	*55*	Cadmium chloride	-1
5	Cefoperazone	-4	*56*	Tetraethylthiuram disulfide	-1
6	Nitrofurazone	-4	*57*	Ciprofloxacin	-1
7	Oxytetracycline	-4	*58*	Doxycycline Hydrochloride	-1
8	Cobalt chloride	-4	*59*	Furaltadone	-1
9	Spectinomycin	-4	*60*	Hygromycin B	-1
10	Ethionamide	-4	*61*	2,4-Diamino-6,7-diisopropylpteridine	-1
11	Rolitetracycline	-3	*62*	Phleomycin	-1
12	Geneticin disulfate (G418)	-3	*63*	3-Amino-1,2,4-triazole	-1
13	Ruthenium red	-3	*64*	Chlorambucil	-1
14	Antimony (III) chloride	-3	*65*	Chromium (III) chloride	-1
15	Troleandomycin	-3	*66*	Sisomicin	-1
16	Cefoxitin	-3	*67*	Rifamycin SV	-1
17	Coumarin	-3	*68*	Streptomycin	-1
18	Nickel chloride	-3	*69*	2-Hydroxy-1,4-Naphthoquinone	-1
19	Oleandomycin, phosphate salt	-3	*70*	L-Glutamic acid g-monohydroxamate	-1
20	Erythromycin	-3	*71*	Gentamicin	-1
21	Dodine	-3	*72*	Phenyl-methylsulfonyl-fluoride	-1
22	Glycine HCl	-3	*73*	Tobramycin	-1
23	Spiramycin	-3	*74*	Oxolinic acid	-1
24	Tylosin tartrate	-2	*75*	Dihydrostreptomycin	-1
25	Trifluoperazine	-2	*76*	Cefmetazole	-1
26	Zinc chloride	-2	*77*	Sulfanilamide	0
27	Aztreonam	-2	*78*	Sodium metavanadate	0
28	Amikacin	-2	*79*	Polymyxin B	0
29	Carbenicillin	-2	*80*	Cefotaxime	0
30	Ornidazole	-2	*81*	Nalidixic acid	0
31	8-Hydroxyquinoline	-2	*82*	3,5-Dinitrobenzoic acid	0
32	Neomycin	-2	*83*	Cefuroxime	0
33	Cefamandole nafate	-2	*84*	4-Hydroxycoumarin	0
34	5- Fluorouracil	-2	*85*	Potassium chromate	0
35	Guanidine hydrochloride	-2	*86*	Atropine	0
36	Puromycin	-2	*87*	3,4-Dimethoxybenzyl alcohol	0
37	Cesium chloride	-2	*88*	Sodium Bromate	0
38	Pyrithione	-2	*89*	Myricetin	0
39	Sodium Azide	-2	*90*	Lomefloxacin	0
40	Lidocaine	-1	*91*	Polymyxin B	0
41	Enoxacin	-1	*92*	Hydroxylamine	0
42	2- Phenylphenol	-1	*93*	Phenethicilllin	0
43	7-Hydroxycoumarin	-1	*94*	Fusidic acid, sodium salt	0
44	2,2`- Dipyridyl	-1	*95*	Sodium Nitrite	0
45	Guanazole	-1	*96*	Josamycin	0
46	Gallic acid	-1	*97*	Lincomycin	0

47	Ampicillin, Sodium salt	-1	*98*	trans-Cinnamic acid	0
48	D-Cycloserine	-1	*99*	Ofloxacin	0
49	Thioridazine	-1	*100*	Captan	0
50	Trimethoprim	0	*101*	Procaine	0
51	Pentachlorophenol	0	*102*	Nordihydroguaiaretic acid	0
	Compound	**Score**	**#**	**Compound**	**Score**
103	Plumbagin	0	*155*	Sulfamonomethoxine	0
104	Blasticidin S	0	*156*	a-Monothioglycerol	0
105	Azlocillin	0	*157*	Lauryl sulfobetaine	0
106	Sodium orthovanadate	0	*158*	Sulfamethazine	0
107	Domiphen bromide	0	*159*	Niaproof	0
108	Nafcillin	0	*160*	Benzethonium Chloride	0
109	Sodium Arsenite	0	*161*	Boric acid	0
110	Orphenadrine	0	*162*	Glycine hydroxamate	0
111	Cefazolin	0	*163*	6-Mercaptopurine monohydrate	0
112	5-Fluoro-5`-deoxyuridine	0	*164*	Ferric chloride	0
113	EGTA	0	*165*	DL-Propanolol	0
114	Chlorhexidine diacetate	0	*166*	Sodium Selenite	0
115	CCCP	0	*167*	5-Azacytidine	0
116	Chlortetracycline	0	*168*	Cinoxacin	0
117	Rifampicin	0	*169*	Sulfathiazole	0
118	Kanamycin	0	*170*	DL-Serine hydroxamate	0
119	Sodium periodate	0	*171*	Diamide	0
120	Cephalothin	0	*172*	Chlorodinitrobenzene	0
121	Demeclocycline	0	*173*	Vancomycin	0
122	Phosphomycin	0	*174*	Chloramphenicol	0
123	Piperacillin	0	*175*	Colistin	0
124	Sulfisoxazole	0	*176*	Benserazide	0
125	Chloramphenicol	0	*177*	5,7-Dichloro-8-hydroxyquinoline	0
126	L-Aspartic-b-hydroxamate	0	*178*	Sodium Caprylate	0
127	Cloxacillin	0	*179*	Protamine sulfate	1
128	Sodium metaborate	0	*180*	Thiamphenicol	1
129	Nitrofurantoin	0	*181*	Paromomycin	1
130	Trifluorothymidine	0	*182*	Patulin	1
131	Sodium pyrophosphate	0	*183*	2-Nitroimidazole	1
132	Ketoprofen	0	*184*	Pridinol	1
133	INT	0	*185*	Penimepicycline	1
134	Cefsulodin	0	*186*	Oxacillin	1
135	Capreomycin	0	*187*	Carbenicillin	1
136	Tannic acid	0	*188*	Apramycin	1
137	Sodium Cyanate	0	*189*	Amitriptyline	1
138	DL-Methionine hydroxamate	0	*190*	1,10-Phenanthroline Monohydrate	1
139	Lithium chloride	0	*191*	DL-Thioctic acid	1
140	Hydroxyurea	0	*192*	Penicillin G	1
141	Chlorpromazine	0	*193*	EDTA	1
142	Sodium Arsenate	0	*194*	Dequalinium chloride	1
143	Fusaric acid	0	*195*	2,4-Dintrophenol	1

144	Sulfachloropyridazine	0	*196*	Aluminum sulfate	1
145	Sulfadiazine	0	*197*	Promethazine	1
146	Hexammine cobalt (III) chloride	0	*198*	Dodecyltrimethyl ammonium	1
147	Minocycline	0	*199*	Triclosan	1
148	Salicylate, sodium	0	*200*	Tinidazole	1
149	Tolylfluanid	0	*201*	Semicarbazide hydrochloride	1
150	Alexidine	0	*202*	Poly-L-lysine	1
151	Sorbic acid	0	*203*	Azathioprine	1
152	Thallium (I) acetate	1	*204*	Amoxicillin	1
153	Pipemidic Acid	1	*205*	Dichlofluanid	1
154	Sulfamethoxazole	1	*206*	Norfloxacin	2
#	**Compound**	**Score**	**#**	**Compound**	**Score**
207	Sodium Dichromate	1	*223*	Sodium metasilicate	2
208	Potassium tellurite	1	*224*	Sodium Tungstate	2
209	Caffeine	1	*225*	9-Aminoacridine	2
210	Iodoacetic acid	1	*226*	Moxalactam, sodium salt	2
211	Compound 48/80	1	*227*	Potassium tellurite	2
212	Oxycarboxin	1	*228*	Tetrazolium violet	3
213	Ceftriaxone	1	*229*	FCCP	3
214	4-Aminopyridine	1	*230*	Methyltrioctylammonium chloride	3
215	Thiosalicylate	1	*231*	Manganese chloride	3
216	b-Chloro-L-alanine	1	*232*	Proflavine	4
217	Novobiocin	1	*233*	Sanguinarine chloride	4
218	D-Serine	1	*234*	Acriflavine	4
219	4-Chloro-3,5-dimethyl-phenol	1	*235*	Cetylpyridinium chloride	4
220	Cupric chloride	1	*236*	Chelerythrine chloride	5
221	Tetracycline	2	*237*	Crystal violet	6
222	5-Chloro-7-iodo-8-hydroxy-quinoline	2	*238*	Methyl viologen	8

References:

1. Morehead, M. S. & Scarbrough, C. Emergence of Global Antibiotic Resistance. *Prim Care* **45**, 467–484 (2018).

2. Brown, M. H. & Skurray, R. A. Staphylococcal multidrug efflux protein QacA. *J Mol Microbiol Biotechnol* **3**, 163–170 (2001).

3. Pérez-Varela, M., Corral, J., Aranda, J. & Barbé, J. Roles of Efflux Pumps from Different Superfamilies in the Surface-Associated Motility and Virulence of Acinetobacter baumannii ATCC 17978. *Antimicrob Agents Chemother* **63**, e02190-18 (2019).

4. Srinivasan, V. B. & Rajamohan, G. KpnEF, a new member of the Klebsiella pneumoniae cell envelope stress response regulon, is an SMR-type efflux pump involved in broad-spectrum antimicrobial resistance. *Antimicrob Agents Chemother* **57**, 4449–4462 (2013).

5. Willsey, G. G. *et al.* Pulmonary Surfactant Promotes Virulence Gene Expression and Biofilm Formation in Klebsiella pneumoniae. *Infect Immun* **86**, e00135-18 (2018).

6. Rotem, D. & Schuldiner, S. EmrE, a multidrug transporter from Escherichia coli, transports monovalent and divalent substrates with the same stoichiometry. *J Biol Chem* **279**, 48787–48793 (2004).

7. Robinson, A. E., Thomas, N. E., Morrison, E. A., Balthazor, B. M. & Henzler-Wildman, K. A. New free-exchange model of EmrE transport. *Proc Natl Acad Sci U S A* **114**, E10083–E10091 (2017).

8. Yerushalmi, H. & Schuldiner, S. A model for coupling of H(+) and substrate fluxes based on ‘time-sharing’ of a common binding site. *Biochemistry* **39**, 14711–14719 (2000).

9. Hussey, G. A., Thomas, N. E. & Henzler-Wildman, K. A. Highly coupled transport can be achieved in free-exchange transport models. *J Gen Physiol* **152**, (2019).

10. Morrison, E. A. *et al.* Antiparallel EmrE exports drugs by exchanging between asymmetric structures. *Nature* **481**, 45–50 (2011).

11. Morrison, E. A., Robinson, A. E., Liu, Y. & Henzler-Wildman, K. A. Asymmetric protonation of EmrE. *J Gen Physiol* **146**, 445–461 (2015).

12. Morrison, E. A. & Henzler-Wildman, K. A. Transported substrate determines exchange rate in the multidrug resistance transporter EmrE. *J Biol Chem* **289**, 6825–6836 (2014).

13. Brill, S., Falk, O. S. & Schuldiner, S. Transforming a drug/H+ antiporter into a polyamine importer by a single mutation. *Proc Natl Acad Sci U S A* **109**, 16894–16899 (2012).

14. Bay, D. C. & Turner, R. J. Small multidrug resistance protein EmrE reduces host pH and osmotic tolerance to metabolic quaternary cation osmoprotectants. *J Bacteriol* **194**, 5941–5948 (2012).

15. Bay, D. C., Stremick, C. A., Slipski, C. J. & Turner, R. J. Secondary multidrug efflux pump mutants alter Escherichia coli biofilm growth in the presence of cationic antimicrobial compounds. *Res Microbiol* **168**, 208–221 (2017).

16. Saleh, M., Bay, D. C. & Turner, R. J. Few Conserved Amino Acids in the Small Multidrug Resistance Transporter EmrE Influence Drug Polyselectivity. *Antimicrob Agents Chemother* **62**, e00461-18 (2018).

17. Blanco, P., Corona, F. & Martínez, J. L. Biolog Phenotype Microarray Is a Tool for the Identification of Multidrug Resistance Efflux Pump Inducers. *Antimicrob Agents Chemother* **62**, e01263-18 (2018).

18. Bazzone, A., Barthmes, M. & Fendler, K. SSM-Based Electrophysiology for Transporter Research. *Meth. Enzymol.* **594**, 31–83 (2017).

19. Shcherbakov, A. A. *et al.* Structure and dynamics of the drug-bound bacterial transporter EmrE in lipid bilayers. *Nat Commun* **12**, 172 (2021).

20. Wu, C. *et al.* Identification of an Alternating-Access Dynamics Mutant of EmrE with Impaired Transport. *J Mol Biol* **431**, 2777–2789 (2019).

21. Thomas, N. E. *et al.* The C terminus of the bacterial multidrug transporter EmrE couples drug binding to proton release. *J. Biol. Chem.* **293**, 19137–19147 (2018).

22. Glaubitz, C. *et al.* 31P-CP-MAS NMR studies on TPP+ bound to the ion-coupled multidrug transport protein EmrE. *FEBS Letters* **480**, 127–131 (2000).

23. Baev, M. V., Baev, D., Radek, A. J. & Campbell, J. W. Growth of Escherichia coli MG1655 on LB medium: monitoring utilization of sugars, alcohols, and organic acids with transcriptional microarrays. *Appl Microbiol Biotechnol* **71**, 310–316 (2006).

24. Ong, Y. S., Lakatos, A., Becker-Baldus, J., Pos, K. M. & Glaubitz, C. Detecting Substrates Bound to the Secondary Multidrug Efflux Pump EmrE by DNP-Enhanced Solid-State NMR. *Journal of the American Chemical Society* **135**, 15754–15762 (2013).

25. Sharom, F. J., Yu, X., Chu, J. W. & Doige, C. A. Characterization of the ATPase activity of P-glycoprotein from multidrug-resistant Chinese hamster ovary cells. *Biochem J* **308**, 381–390 (1995).

26. Krupka, R. M. Uncoupled Active Transport Mechanisms Accounting for Low Selectivity in Multidrug Carriers: P-Glycoprotein and SMR Antiporters. *Journal of Membrane Biology* **172**, 129–143 (1999).

27. Vermaas, J. V., Rempe, S. B. & Tajkhorshid, E. Electrostatic lock in the transport cycle of the multidrug resistance transporter EmrE. *Proceedings of the National Academy of Sciences of the United States of America* 201722399 (2018) doi:10.1073/pnas.1722399115.

Chapter 6

Allosteric regulation of proton transport by the multidrug efflux pump EmrE

Nathan E. Thomas, Merissa Brousseau, and Katherine A. Henzler-Wildman

Preface

Our investigation of EmrE's C-terminal residue H110 led us to propose a role for EmrE's C-terminal tail in gating proton transport by EmrE in the absence of drug (Chapter 4). The evidence for this hypothesis was circumstantial, based on coupling between the highly conserved H110 and the E14 binding site, suggestion of a peripheral binding site in the literature, and the failure of the free exchange model to account for EmrE's behavior in the absence of drug. Here, we directly test this hypothesis by preparing a mutant of EmrE that lacks the C-terminal tail. Consistent with our hypothesis, this mutant exhibits increased proton transport in the absence of drug and surprisingly, displays altered dynamics as well. I designed and supervised experiments, analyzed data, and wrote the chapter, while Merissa performed the majority of the bench work and helped analyze the microplate and SSME transport data.

Introduction

Secondary active transporters utilize the energy stored in electrochemical gradients to power the uphill movement of substrates across the membrane. In the single site, alternating access (SSAA) mechanism, coupled transport is a result of a dynamic regulation mechanism[1]. The transporter is structured such that a substrate binding pocket is exposed to one side of the membrane at a time. Substrate binding to this site induces a conformational change which closes access to the site from one side of the membrane and opens access to the other side, moving bound substrate across the membrane in the process. This strict mechanism, wherein conformational exchange requires substrate binding, prevents dissipative substrate leaks and ensures a high degree of transport coupling between substrates and the electrochemical gradients.

E. coli EmrE is a model system for studying proton-coupled drug efflux[2]. The functional dimer's pair of membrane embedded E14 residues define EmrE's single site in the SSAA paradigm, where competition between drug and proton for binding to E14 forms the basis of the coupling mechanism[3–6]. However, NMR investigations demonstrate that E14 can bind proton and drug in a variety of configurations and that EmrE can alternate access in every configuration[7–10]. To account for the NMR observations, we proposed a kinetically controlled free exchange model of coupled transport[11]. Simulations demonstrate that this model can account for concentrative drug uptake in the presence of a proton gradient[12], but EmrE's ability to alternate access rapidly in the absence of bound substrate breaks the central allosteric regulation mechanism of the SSAA model. Alternating access in the absence of substrate should allow for rapid proton transport in the absence of drug, unnecessarily dissipating the energy stored in the proton motive force (PMF). In contrast, experimental data shows that rapid proton transport by EmrE requires drug[11], indicating that the free exchange model is missing a key regulatory mechanism of EmrE.

In a recent study, we found that protonation of EmrE's C-terminal residue, H110, is coupled to the drug occupancy of the E14 binding site[13]. While the functional effect of this coupling was unclear, we suggested that it could be involved in preventing dissipative proton transport in the absence of substrate. We hypothesized that when both E14 and H110 are fully protonated, the C-terminal tail occludes the central binding pocket to prevent proton release. An early NMR investigation of tetraphenylphosphonium (TPP^+) binding to EmrE identified a weak drug binding site in the loops[14]. We proposed that drug binding to this peripheral site could release the tail, allowing protons to leave the central binding pocket and drugs to enter. Here, we provide functional evidence that EmrE's C-terminal tail gates proton release from the central E14 binding site. Furthermore, we find that alternating access dynamics are controlled not just by the occupancy of the E14 binding site but through coordination between the central binding site, the peripheral site in the loops, andthe tail. This reveals a remarkable allosteric regulation mechanism through which EmrE's

central binding pocket and C-terminal tail work together to bind substrates, alternate access, and couple transport of drugs and protons.

Results

Microplate growth assays demonstrate Δ107-EmrE is functional

To test our hypothesis that EmrE's C-terminal tail is involved in gating proton transport, we prepared a mutant of EmrE lacking the final four residues of the protein (hereafter referred to as Δ107), moving the C-terminus from the highly conserved H110 residue to R106. We then ran microplate growth assays to test the effect of this mutation on EmrE's function in *ΔemrE*-MG1655 *E. coli* cells. If the C-terminal tail is involved in gating proton transport, we might expect the cells expressing Δ107 to grow worse than cells expressing WT in the absence of drug due to dissipation of the PMF. Furthermore, if the primary role of the tail is to regulate proton transport rather than drug transport or a more structural role, then Δ107 should still be able to confer resistance to EmrE's drug substrates.

The results of these experiments are shown in Figure 1. In the absence of drug, cells expressing Δ107 grow worse than cells expressing the non-functional mutant E14Q. The difference in growth between Δ107 and WT is smaller and varies across biological replicates, likely the result of stochastic selection of impaired PMF suppressor mutations[15,16]. Any difference between Δ107 and WT disappears when ethidium is added to the growth media, indicating that Δ107 is capable of conferring resistance to this canonical EmrE drug substrate. While these results are consistent with our hypothesis, the cellular phenotype for removing the C-terminal tail from EmrE is minor. Discerning the functional role of the C-terminal tail requires carefully controlled *in vitro* assays using purified protein.

NMR spectroscopy

We next turned to solution NMR to better understand the effect of the Δ107 mutation on EmrE's structure and function. EmrE's small size makes it an ideal candidate for NMR, which has been used extensively to characterize its structure and dynamics[7–11,13,14,17–20]. We used ^{1}H-^{15}N transverse relaxation optimized heteronuclear single-quantum coherence (TROSY-HSQC) spectroscopy to initially survey the structure and dynamics of Δ107. In the asymmetric antiparallel homodimeric structure of EmrE, each residue exists in two unique environments due to the distinct conformations of subunit A and B, and thus each residue in the protein sequence has two distinct chemical shifts. Alternating access switches the conformations of the subunits, as the subunit initially in conformation A adopts conformation B and vis a versa, resulting in chemical exchange that can be detected by NMR. The rate of this alternating access can fall into three exchange regimes on the NMR timescale. In the slow exchange regime, the chemical shift difference between conformation A and B for a given residue is much larger than the alternating access rate and the two conformations are visible as separate peaks in the spectrum. In the fast exchange regime, the alternating access rate is much larger than the chemical shift difference and single peaks appear at the population weighted average (50:50 for EmrE) of the chemical shifts for each state. Finally, the intermediate exchange regime results when the alternating access rate is similar to the chemical shift difference, producing broadened peaks and poor spectral quality. Thus, the simple appearance of TROSY-HSQC spectra of EmrE can provide great insight into the alternating access dynamics of the protein.

In the absence of drug, the spectral quality of Δ107 is poor (Fig. 2A). Addition of the tight-binding drug substrate tetraphenylphosphonium (TPP^{+}) to the same sample slows down the conformational exchange rate and shifts the spectra into the slow exchange regime (Fig. 2B), demonstrating that the original poor spectral quality is due to conformational exchange on the intermediate to fast timescale or structural heterogeneity in the absence of substrate. For TPP^{+}-bound WT EmrE, this results in the appearance of approximately two peaks for every residue in

the protein, corresponding to the two conformations of the antiparallel, asymmetric dimer[18]. These two conformations are also apparent in the Δ107 spectrum, but many small peaks are also present, indicating the existence of additional minor conformations. The appearance of these minor peaks suggests a role for the C-terminal tail in regulating the conformational dynamics of EmrE.

The loss of spectral quality for TPP^+-bound Δ107 at pH 7.7 provides further evidence for this role. Many peaks broaden, and several peaks disappear entirely, which indicates that at elevated pH, the spectrum of drug-bound Δ107 is moving from the slow exchange regime to the intermediate exchange regime. While multiple chemical exchange events can affect the exchange regime of NMR spectra, including the substrate on-/off-rate or the exchange rate of backbone amide protons with water, the most significant rate for the spectral quality of EmrE is the rate of alternating access. When WT is bound to TPP^+, the alternating access rate is firmly within the slow exchange regime for the vast majority of residues at high field. Protonation of the free E14 residue does not significantly change the rate of alternating access, and if anything, slightly increases this rate (8.9±1.2 s^{-1} when protonated, 7.0±0.6 $s^{-1}$when deprotonated)[11]. The increased dynamics evident in the spectra of TPP^+-bound Δ107 at pH 7.7 suggest that the alternating-access rate of drug-bound EmrE may no longer be independent of pH when the C-terminal tail is removed.

Before assessing the effect of pH on the alternating access rate of TPP^+-bound Δ107, we first performed an NMR pH titration to determine the E14 pK_a in the truncated mutant. While protonation of E14 does not affect the alternating access dynamics of WT, it does cause a conformational change that can be detected by chemical shift perturbations (CSPs) throughout the spectrum. Plotting peak positions as a function of pH reveals that a single pK_a can account for the pH dependent CSPs, allowing the determination of the E14 pK_a for TPP^+-bound WT (6.8±0.5 at 45 °C)[11]. We expected that a similar approach would allow the determination of the E14 pK_a for TPP^+-bound Δ107. Instead, it soon became apparent that many residues in Δ107

sense more than one protonation event. Some peaks moved significantly between pH 5.33 and 6.43, even changing direction during the course of the titration to more alkaline conditions (Fig. 3A), while others barely moved at low pH but titrated significantly at higher pH (Fig. 3B). To minimize the effect of the lower pK_a value, we fit the pKa using only well-resolved residues that primarily sensed the higher pK_a, which gave an estimated pKa of 7.2±0.2.

Dynamic crosstalk between the central binding site and the tail

We then used ZZ-exchange spectroscopy to determine the alternating access rate at two different pH values. In this technique, a delay is inserted in the pulse sequence between the recording of the ^{15}N and ^{1}H chemical shifts. If conformational exchange occurs during this delay, cross-peaks will appear in the spectrum with the ^{15}N chemical shift of the original state and the ^{1}H chemical shift of the new state. Plotting the composite ratio of the cross-peak and the auto-peak intensities as a function of the delay eliminates other parameters to first order, allowing for determination of the exchange rate using a simple equation that depends only on the forward and reverse rate constants (k_f=k_r=k for EmrE) and time (composite peak ratio = k^2t^2)[18]. The results of these experiments are shown in Figure 4. At pH 5.5, the composite peak ratios for three well-resolved residues give an alternating access rate of 6±1 s^{-1} for protonated TPP^+-bound Δ107, somewhat slower than for WT. The reduction in signal quality at pH 7.7 restricted the analysis to a single residue (N81), but the apparent alternating access rate of 12±1 s^{-1} was consistent across three different delays. This elevated rate, more than twice the measured rate of protonated TPP^+-bound Δ107, provides clear evidence that the C-terminal tail plays a role in regulating the conformational dynamics of EmrE.

The effect of removing the C-terminal tail on the alternating access dynamics of EmrE stands in contrast to the canonical SSAA model, which stipulates that alternating access should be regulated only by the occupancy of a single substrate binding site. Analysis of E14Q EmrE provides further evidence that control of alternating access in EmrE is more complicated than

envisioned by the SSAA model. This mutation prevents binding of drug to the central site defined by E14 and is thought to mimic protonation of the active site. However, unlike protonated WT which alternates access rapidly, the spectrum of E14Q is in the slow exchange regime (Chapter 5). Removing the C-terminal tail from E14Q further alters the dynamics and shifts the spectrum into intermediate exchange, with doubled peaks for a few residues, single peaks for others, and many peaks broadened into the noise. This confirms that the C-terminal tail has a profound impact on the structure and dynamics of EmrE whether or not the central E14 binding site is present. Stunningly, addition of TPP^+ to Δ107-E14Q slows the alternating access dynamics and shifts the spectrum towards slow exchange (Fig. 5). Many peaks remain broadened out, but intense peaks such as the C-terminal R106 are visibly doubled. As the E14Q mutation removes the central binding site, TPP^+ can only bind to peripheral sites in the loops. EmrE's alternating access rate must be governed by complex allosteric regulation between the central binding site, peripheral sites in the loops, and the C-terminal tail.

The C-terminal tail gates proton release by EmrE

Finally, we directly assessed the effect of the C-terminal tail on EmrE's transport behavior using solid supported membrane electrophysiology (SSME). In this technique, proteoliposomes are adsorbed onto a membrane bound to a gold electrode sensor. The large number of liposomes adsorbed onto a single sensor allows detection of currents that are too small to measure using traditional electrophysiological methods, such as the currents produced by many secondary active transporters. Transport is initiated by perfusing buffer containing a substrate over the sensor. Current from charge moving into or out of the liposomes can then be measured by capacitive coupling between the membranes and the electrode.

For our experiments, we prepared sensors from liposomes reconstituted with WT or Δ107. "Empty" liposomes which had undergone a simulated reconstitution process were used as a control to account for the background signal. We then ran transport assays by perfusing pH 7.0

buffer over sensors equilibrated at pH 6.5 in the absence of drug. Any uncoupled proton transport down the resulting outward-facing proton gradient should lead to a negative current. While both WT and Δ107 sensors produced negative currents, the signal from the Δ107 was nearly three times larger (Fig. 6A). It is possible that the difference in the amount of transport could be due to a difference in the number of liposomes adsorbed onto the sensors, rather than a functional difference between WT- and Δ107. To account for this possibility, we ran assays with the same proton gradient, but with 16 μM harmane in both the internal and external buffer. Harmane is an uncoupling substrate which causes EmrE to rapidly transport protons without counter transport of drug (Chapter 5). If the difference in transport signal between WT and Δ107 is due to unregulated proton transport, then the addition of harmane should lead to comparable amounts of transport between the two samples. In fact, the integrated current traces for Δ107- and WT are nearly indistinguishable when harmane is present (Fig. 6C). This provides strong evidence that EmrE's C-terminal tail functions to regulate proton transport in the absence of drug.

We then performed a final experiment to investigate the nature of this regulation. According to our hypothesis, the C-terminal tail functions as a secondary gate to occlude the binding pocket when EmrE is fully protonated, thereby preventing proton release and mitigating dissipative proton transport in the absence of drug. At pH 6.5, the sensors were equilibrated below the relevant pK_a values of WT (6.8 and 8.5 for E14, 7.0 for H110). If protonation of these residues is required for the gate to close, then raising the pH should loosen the gate and increase uncoupled proton transport. We equilibrated sensors at pH 7.0 and repeated the assays in the absence of drug with an external pH of 7.5, maintaining the magnitude of the proton gradient but reducing the proton concentration. Consistent with our hypothesis, the signal from the WT sensors increased significantly, while the Δ107 signal remained the same (Fig. 6B). This demonstrates that flux through fully protonated EmrE is gated by the C-terminal tail in the absence of drug.

Conclusions

Previous NMR studies of EmrE have observed behavior that contradicts the canonical single site alternating access model of secondary active transport[8–11]. To account for the NMR data, we proposed a free exchange model of coupled transport, where alternating access is permitted in every proton and/or drug binding state and coupled transport is achieved by kinetic control of the variety of transport pathways. While this model provides a good description of EmrE's behavior in the presence of drug, it predicts that dissipative proton transport in the absence of drug should be much faster than has been observed experimentally.

After observing coupling between the active site and protonation of the C-terminal residue H110, we hypothesized that EmrE's C-terminal tail acts as a secondary gate to inhibit proton transport in the absence of drug. The data reported here provides strong evidence for this hypothesis and reveals complex allosteric coupling between the tail, loops, and the central E14 binding site. Using SSME transport assays, we found that EmrE lacking a C-terminal tail (Δ107) rapidly transports proton in the absence of drug, unlike WT EmrE, but the difference between Δ107 and WT is abolished in the presence of drug. This phenotype is also seen in cells, where Δ107 fully capable of conferring drug resistance but displays impaired growth in the absence of drug. Using NMR, we found that the Δ107 mutation changes the dynamics of EmrE and causes the alternating access rate to be pH sensitive when drug is bound. The dynamic effects of removing the tail are even more evident in the E14Q mutant background. While E14Q spectra are normally in the slow exchange regime, Δ107-E14Q alternates access much faster, shifting the spectra into the intermediate exchange regime. Surprisingly, despite lacking a central binding site, the alternating access dynamics of this mutant are drug sensitive.

Taken together, these results demonstrate that allosteric crosstalk between the C-terminal tail, a drug binding site in the loops, the tail, and the central E14 binding site plays a vital role in EmrE's function. In the absence of drug, EmrE can bind protons, but proton release is inhibited by the C-

terminal tail gate. When drug is introduced, the peripheral binding site in the loops triggers a rapid response[14], opening the gate and allowing proton-coupled drug efflux to proceed.

Methods

Microplate assays

The indicated EmrE mutants were cloned into pWB vectors, low copy number plasmid vectors with a p15A origin and pTrc promoter, and transformed into *ΔemrE*-MG1655 *E. coli*. For experiments, LB plates were streaked and grown overnight at 37°C. In the morning, single colonies were picked to inoculate liquid LB cultures at 37°C. Once liquid cultures reached log phase growth, they were diluted back to an OD_{600} of 0.2 and further diluted 20-fold into microplates with LB media containing the indicated amount of ethidium. Growth in microplates at 37°C was monitored for 15 hours using a TECAN Spark microplate reader at OD_{700} to prevent interference from ethidium absorbance at 600 nm. Reported growth curves and final ODs are mean values of technical triplicates, with errors calculated using the standard error of the mean.

Protein expression and purification

To obtain purified protein, all EmrE mutants were expressed from a pET15b plasmid in M9 media and purified using an immobilized nickel and size exclusion chromatography as previously described[18].

For NMR samples, the M9 media was deuterated and ^{15}N-labeled (and ^{13}C labeled for assignment samples), and supplemented with 0.5g/L ^{2}H-^{15}N or ^{2}H-^{13}C-^{15}N Isogro. Isotopically labeled purified protein was reconstituted into bicelles as previously described for solution NMR experiments[21].

For SSME transport assays, EmrE was reconstituted into 1-palmitoyl-2-oleoyl-glycero-3-phosphocholine (POPC) liposomes at a 400:1 lipid:protomer mol:mol ratio. After adding the detergent solubilized protein, the final lipid concentration was 2.5 mg/mL in a buffer containing 50

mM MES, 50 mM MOPS, 50 mM bicine, 100 mM NaCl, and 2 mM $MgCl_2$ at pH 7. Detergent was removed by Biobeads as previously described[21], and liposome aliquots were flash frozen and stored at -80°C until needed for experiments.

NMR spectroscopy

70% of the backbone resonances of TPP^+-bound Δ107-EmrE was assigned at pH 5.5 by combining standard triple resonance experiments (TROSY-HNCA, TROSY-HNCACB, TROSY-HNCO, TROSY-HN(CO)CA) with ZZ-exchange data. 2D TROSY-HSQC or TROSY-selected ZZ-exchange spectra were acquired on an 800 MHz Varian spectrometer equipped with a cryoprobe using standard pulse sequences with gradient coherence selection. For NMR pH titrations, samples were prepared at the extreme pH values measured, with intermediate pH values obtained by mixing the initial two samples.

Solid supported membrane electrophysiology

All SSME data was acquired an a Nanion SURFE^{2}R N1 instrument. Liposome aliquots were thawed, diluted 4-fold, and briefly sonicated. 10 µL of liposomes were added to prepare 3 mm sensors according to a standard protocol (Chapter 3). Prior to experiments, sensor capacitance and conductance values were obtained to ensure sensor quality. For all experiments, buffers contained 50 mM MES, 50 mM MOPS, 50 mM bicine, 100 mM NaCl, and 2 mM $MgCl_2$ at the indicated pH value and indicated drug concentration. For data acquisition, sensors were equilibrated with internal buffer and transport was initiated by perfusion of the external buffer before re-equilibration with the internal buffer. Signals were obtained by integrating the current during perfusion of the external buffer, with the final 100 ms of the initial buffer equilibration used as the baseline. Reported data are average values of at least three sensors, with error bars representing the standard error of the mean.

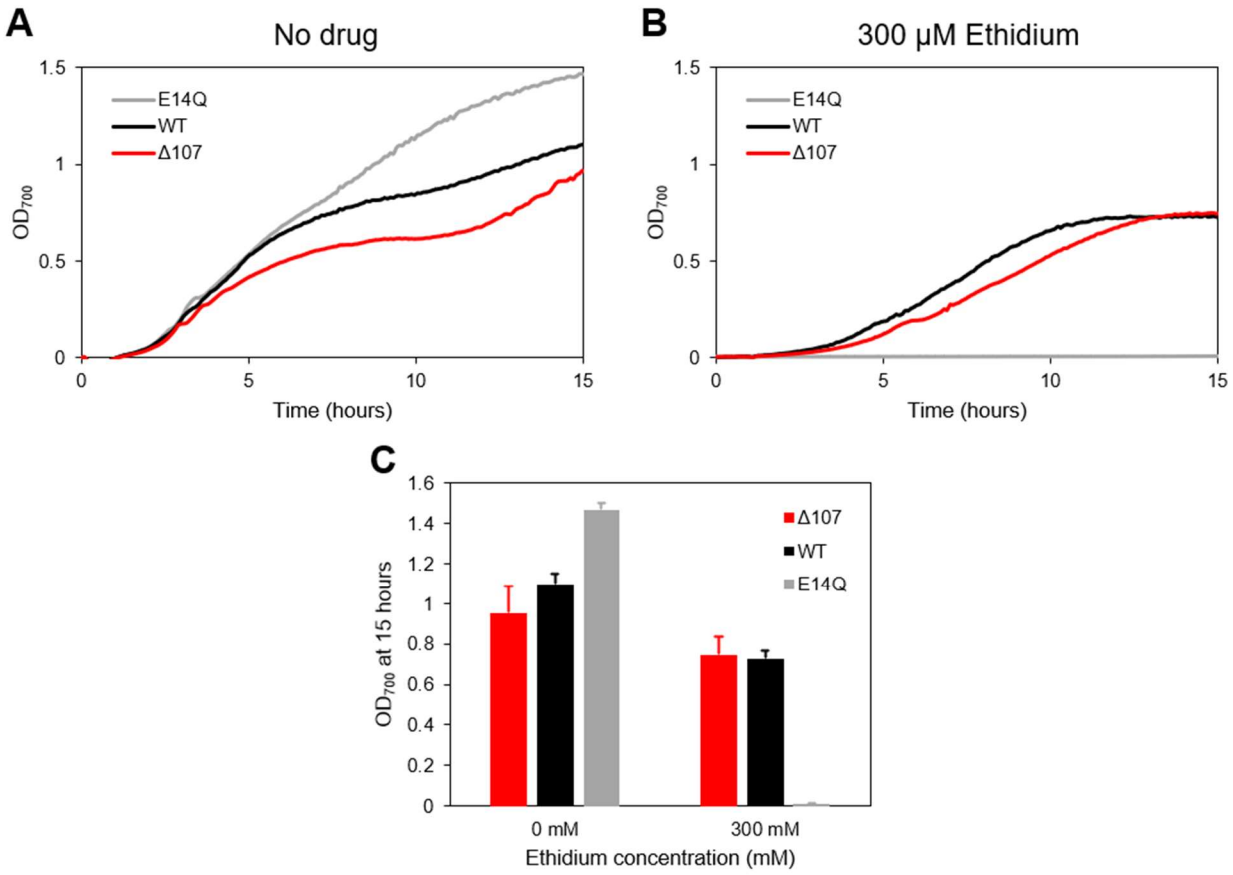

Figure 1 – *Microplate growth assays. E. coli* expressing WT, E14Q, or Δ107 were grown in MHB media in microplates. Growth was monitored by following the OD reading at 700nm, due to the absorbance of ethidium at 600 nm. *(A)* In the absence of drug, cells expressing Δ107 grow worse than cells expressing the non-functional mutant E14Q. The difference between cells expressing WT and Δ107 was smaller and varied between biological replicates. *(B)* Both WT and Δ107 expressing cells were able to grow in the presence of 300 μM ethidium, while cells expressing E14Q were not. *(C)* Comparison of OD_{700} values after 15 hours of growth.

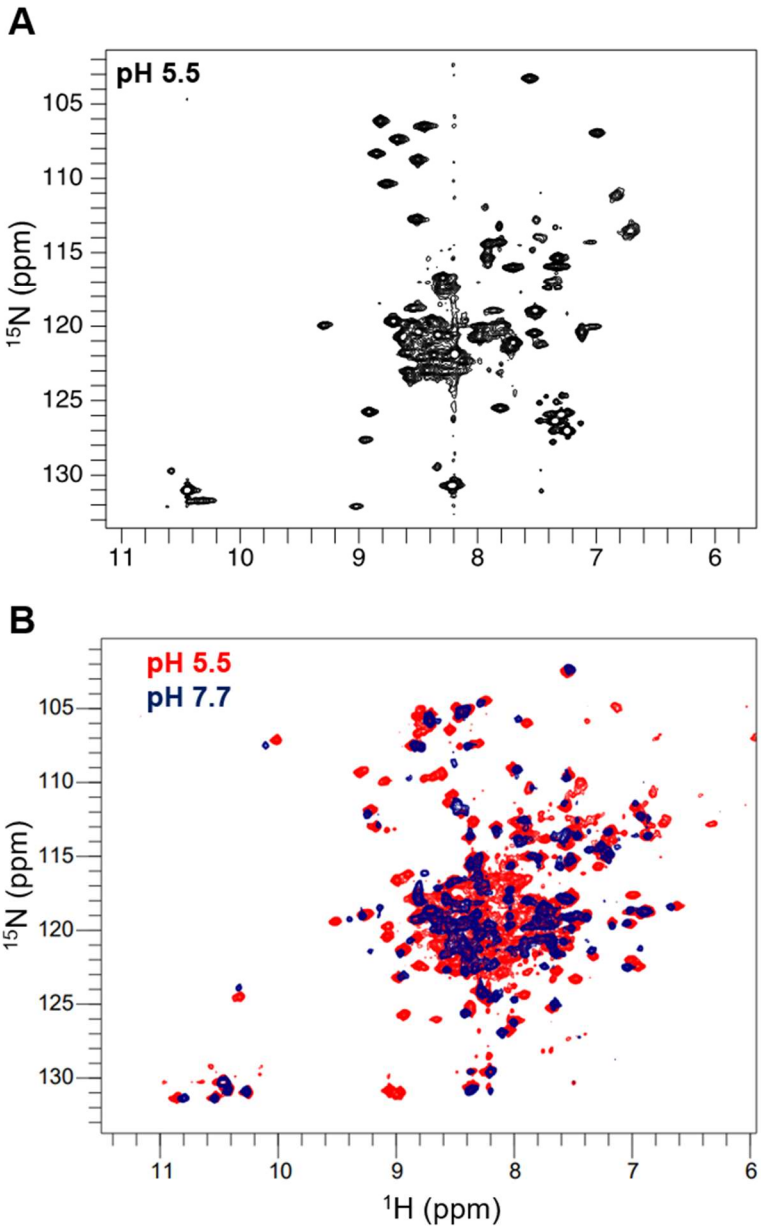

Figure 2 – *^{1}H-^{15}N TROSY-HSQC spectra of Δ107. (A)* In the absence of drug at low pH, the spectrum is in the fast to intermediate exchange regime as the result of rapid alternating access. *(B)* Addition of 5mM TPP^{+} at low pH shifts the spectrum into the slow exchange regime, with peaks for both conformations for each residue within the asymmetric antiparallel dimer. Weak peaks indicating additional minor states are also visible throughout the spectrum. Raising the pH to 7.7 reduces the spectral quality, as peaks broaden or disappear entirely.

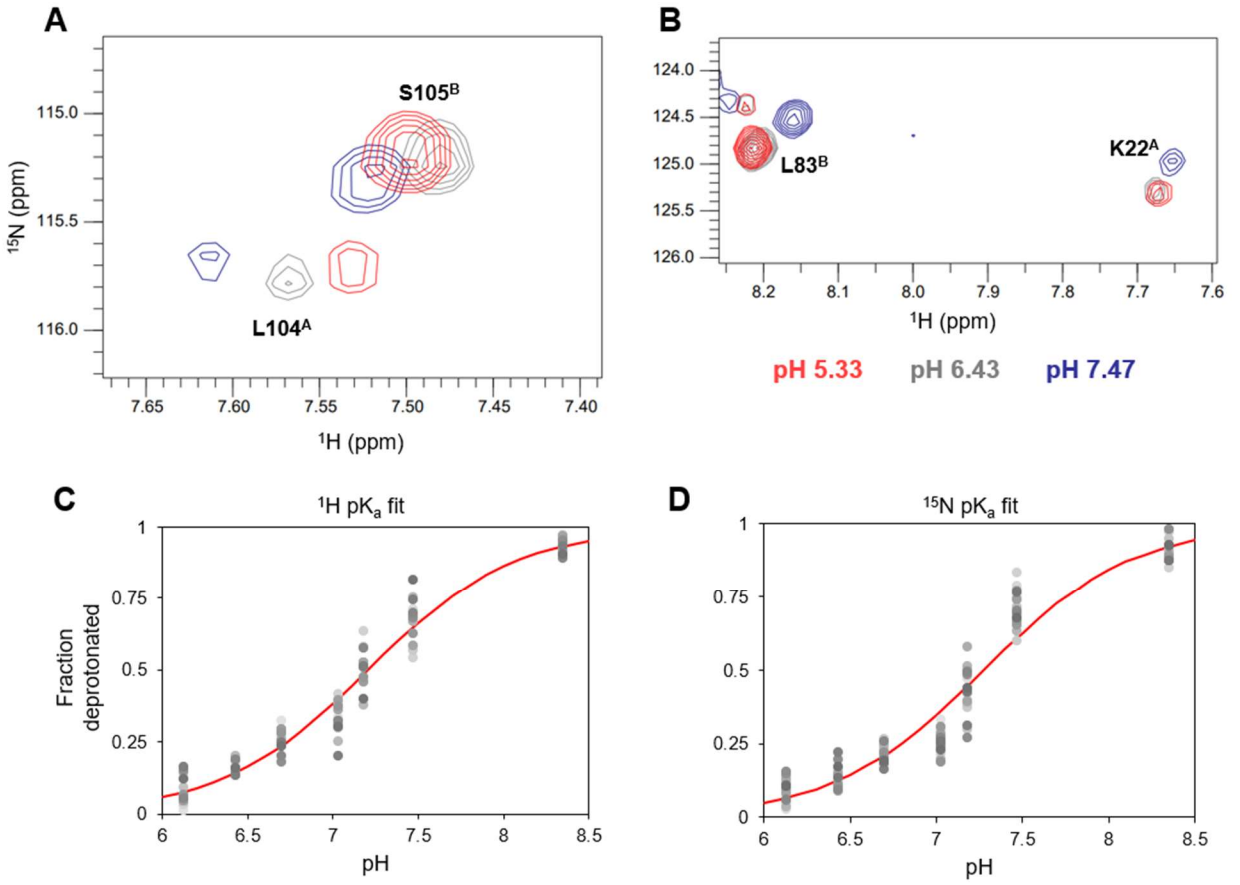

Figure 3 – *pH titration of TPP⁺-bound Δ107.* In an NMR pH titration, the peak position is a population weighted average of the chemical shifts of the different protonation states. Peaks sensing a single pKa should titrate along a straight line. *(A)* Several peaks in Δ107 exhibit curved titration paths and move significantly between both pH 5.33 and 6.43, and between 6.43 and 7.47. *(B)* Other peaks do not titrate at lower pH but do titrate near neutral pH. Well-resolved peaks that primarily sensed the protonation event around neutral pH were fit to a single pK_a using both the *(C)* ^{1}H and *(D)* ^{15}N chemical shifts, yielding an apparent pK_a of 7.2±0.2.

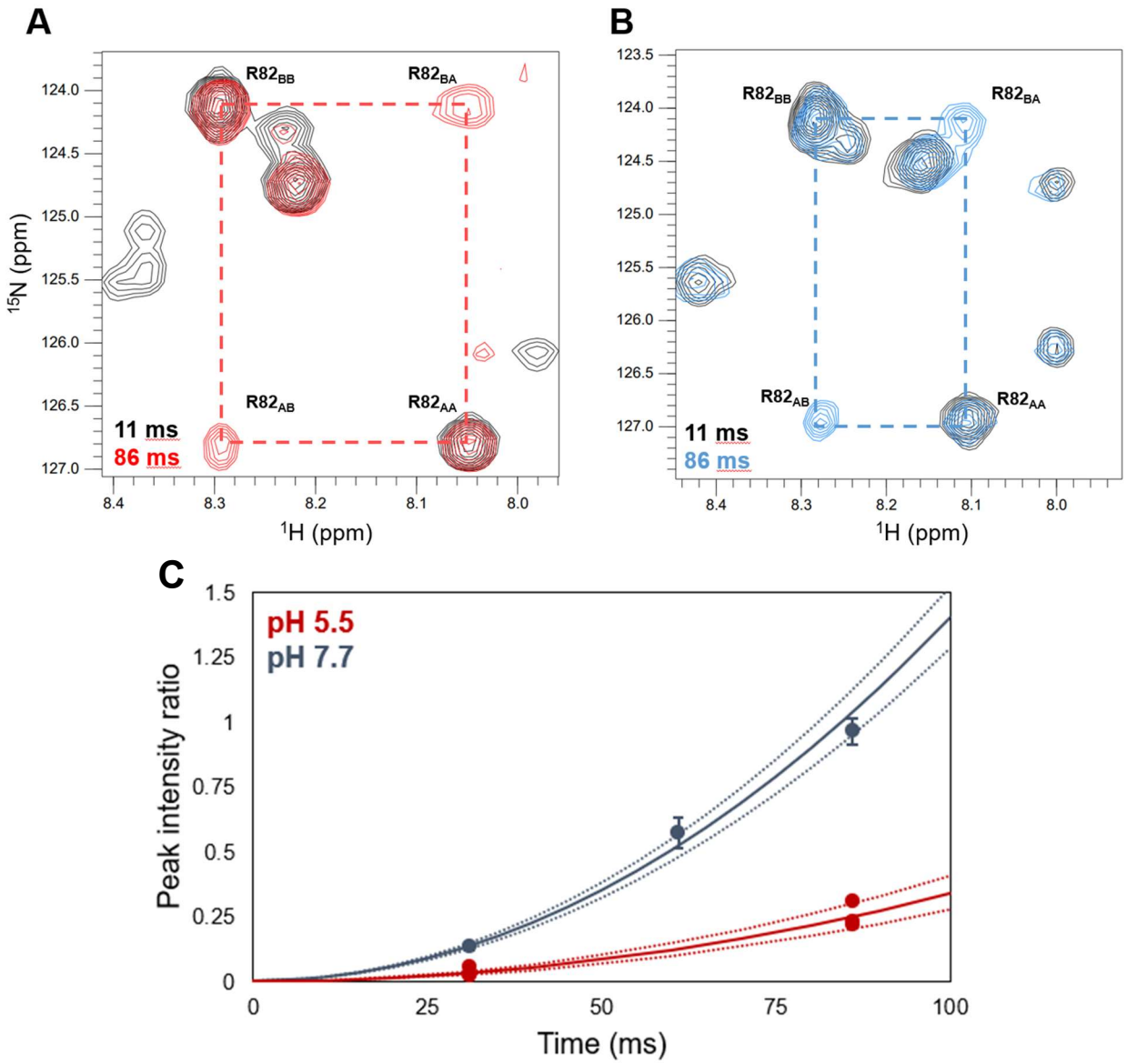

Figure 4 – *ZZ-exchange of TPP$^+$-bound Δ107.* ZZ-exchange spectra with the indicated delays are shown for *(A)* pH 5.5 and *(B)* pH 7.7. *(C)* The composite peak intensity ratios for G80, N81, and L83 fit to an exchange rate of 6±1 s^{-1} at pH 5.5. At pH 7.7, only N81 had a full set of well-resolved auto- and cross-peaks, which fit to an exchange rate of 12±1 s^{-1}.

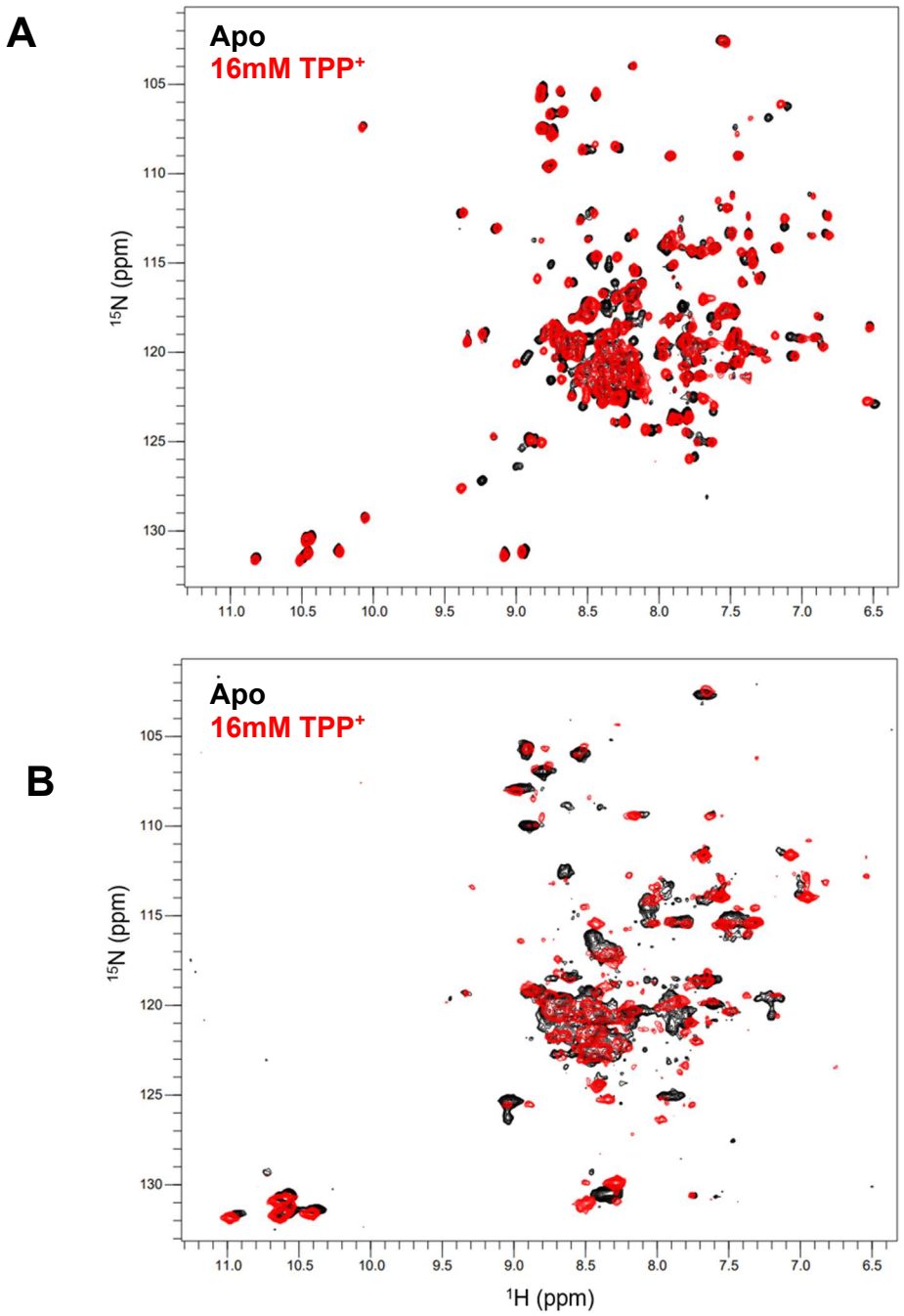

Figure 5 – *^{1}H-^{15}N TROSY-HSQC spectra of EmrE lacking a central binding site.* (A) E14Q spectra are in the slow exchange regime, both in the presence and absence of drug. Figure is reproduced from Chapter 5. (B) The combined Δ107-E14Q mutant has drug-dependent dynamics. Without drug, the spectrum is in the fast to intermediate exchange regime, while the addition of 16mM TPP^{+} shifts the spectrum into the intermediate to slow exchange regime.

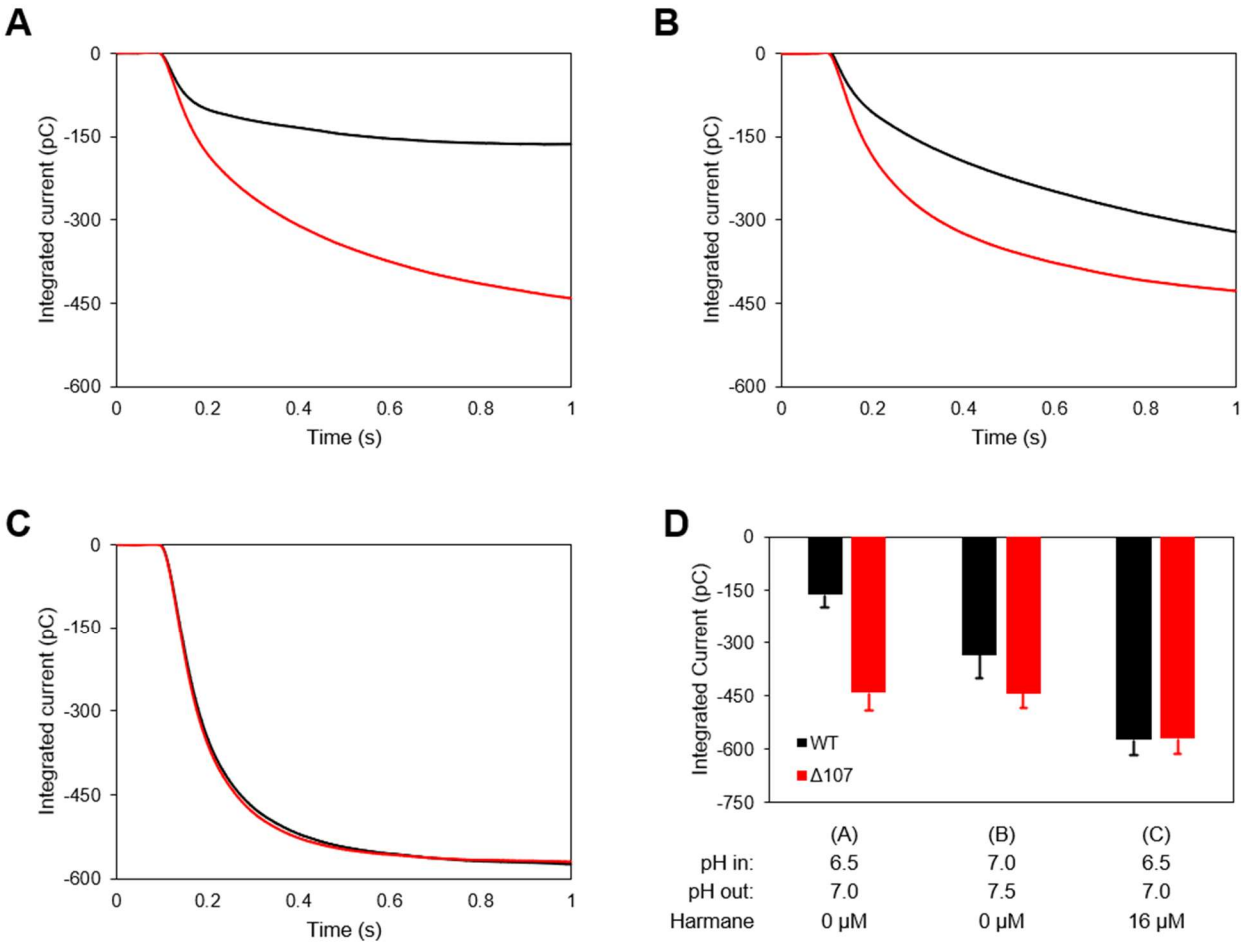

Figure 6 – *SSME transport assays. (A-C)* Integrated current traces for the experimental conditions shown in *(D)*. Proton transport in the absence of drug is greater for Δ107 vs. WT at both low pH *(A)* and higher pH *(B)*, but proton transport by WT is increased at higher pH, consistent with a model that requires EmrE to be fully protonated in order for the C-terminal gate to close. *(C)* The addition of the uncoupler substrate harmane unlocks the gate and abolishes the difference in proton transport between WT and Δ107.

References

1. Jardetzky, O. Simple Allosteric Model for Membrane Pumps. *Nature* **211**, 969–970 (1966).

2. Schuldiner, S. EmrE, a model for studying evolution and mechanism of ion-coupled transporters. *Biochimica et Biophysica Acta (BBA) - Proteins and Proteomics* **1794**, 748–762 (2009).

3. Muth, T. R. & Schuldiner, S. A membrane-embedded glutamate is required for ligand binding to the multidrug transporter EmrE. *The EMBO journal* **19**, 234–40 (2000).

4. Yerushalmi, H. & Schuldiner, S. A common binding site for substrates and protons in EmrE, an ion-coupled multidrug transporter. *FEBS Letters* **476**, 93–97 (2000).

5. Yerushalmi, H. & Schuldiner, S. *A model for coupling of H+ and substrate fluxes based on 'time-sharing' of a common binding site*. vol. 39 (2000).

6. Schuldiner, S. Competition as a way of life for H(+)-coupled antiporters. *Journal of molecular biology* **426**, 2539–46 (2014).

7. Cho, M.-K., Gayen, A., Banigan, J. R., Leninger, M. & Traaseth, N. J. Intrinsic conformational plasticity of native EmrE provides a pathway for multidrug resistance. *J. Am. Chem. Soc.* **136**, 8072–8080 (2014).

8. Gayen, A., Leninger, M. & Traaseth, N. J. Protonation of a Glutamate Residue Modulates the Dynamics of the Drug Transporter EmrE. *Nat Chem Biol* **12**, 141–145 (2016).

9. Leninger, M., Sae Her, A. & Traaseth, N. J. Inducing conformational preference of the membrane protein transporter EmrE through conservative mutations. *Elife* **8**, e48909 (2019).

10. Morrison, E. A., Robinson, A. E., Liu, Y. & Henzler-Wildman, K. A. Asymmetric protonation of EmrE. *The Journal of General Physiology* **146**, 445–461 (2015).

11. Robinson, A. E., Thomas, N. E., Morrison, E. A., Balthazor, B. M. & Henzler-Wildman, K. A. New free-exchange model of EmrE transport. *PNAS* **114**, E10083–E10091 (2017).

12. Hussey, G. A., Thomas, N. E. & Henzler-Wildman, K. A. Highly coupled transport can be achieved in free-exchange transport models. *J. Gen. Physiol.* **152**, (2020).

13. Thomas, N. E. *et al.* The C terminus of the bacterial multidrug transporter EmrE couples drug binding to proton release. *J. Biol. Chem.* **293**, 19137–19147 (2018).

14. Glaubitz, C. *et al.* 31P-CP-MAS NMR studies on TPP+ bound to the ion-coupled multidrug transport protein EmrE. *FEBS Letters* **480**, 127–131 (2000).

15. Creamer, K. E. *et al.* Benzoate- and Salicylate-Tolerant Strains of Escherichia coli K-12 Lose Antibiotic Resistance during Laboratory Evolution. *Appl Environ Microbiol* **83**, e02736-16 (2017).

16. Griffith, J. M. *et al.* Experimental Evolution of Escherichia coli K-12 in the Presence of Proton Motive Force (PMF) Uncoupler Carbonyl Cyanide m-Chlorophenylhydrazone Selects for Mutations Affecting PMF-Driven Drug Efflux Pumps. *Appl Environ Microbiol* **85**, e02792-18 (2019).

17. Schwaiger, M. *et al.* NMR investigation of the multidrug transporter EmrE, an integral membrane protein. *European Journal of Biochemistry* **254**, 610–619 (1998).

18. Morrison, E. A. *et al.* Antiparallel EmrE exports drugs by exchanging between asymmetric structures. *Nature* **481**, 45–50 (2011).

19. Gayen, A., Banigan, J. R. & Traaseth, N. J. Ligand-Induced Conformational Changes of the Multidrug Resistance Transporter EmrE Probed by Oriented Solid-State NMR Spectroscopy. *Angewandte Chemie International Edition* **52**, 10321–10324 (2013).

20. Morrison, E. A. & Henzler-Wildman, K. A. Transported Substrate Determines Exchange Rate in the Multidrug Resistance Transporter EmrE. *J. Biol. Chem.* **289**, 6825–6836 (2014).

21. Morrison, E. A. & Henzler-Wildman, K. A. Reconstitution of integral membrane proteins into isotropic bicelles with improved sample stability and expanded lipid composition profile. *Biochimica et biophysica acta* **1818**, 814–20 (2012).

Conclusions and Future Directions

We now have a nearly complete picture of the proton/drug coupling mechanism of EmrE. Instead of a tightly coupled mechanism with a single transport cycle and a single transport stoichiometry, the loosely coupled free exchange model allows EmrE to utilize multiple transport pathways and multiple transport stoichiometries. The existence of these additional pathways is supported by transport assay data using both traditional liposomes (Chapter 1) and solid supported membrane electrophysiology (Chapter 3). Kinetic simulations demonstrate that the free exchange model can effectively describe proton-coupled active transport of drug (Chapter 2). In the absence of drug, EmrE does not rapidly transport protons despite rapid conformational exchange between the subunits (Chapter 1). This is explained by a secondary gating mechanism involving coupling between the C-terminal tail, an allosteric site in the loops, and the central E14 binging site (Chapters 4 and 6). When EmrE is fully protonated, the C-terminal tail occludes the binding pocket to prevent proton release. Drug binding to the allosteric site in the loops releases the tail, allowing protons to release and transport to proceed.

This picture of EmrE's transport mechanism may be nearly complete, but many portions of the picture remain blurry. A central limitation of our current understanding of EmrE is our lack of a high-resolution structure of the protein. While it played a vital role in our understanding of EmrE's antiparallel topology, the original crystal structure was solved to just 3.8 Å, only contains coordinates for the alpha carbons, and is missing the C-terminal tail[1]. A more recent full-length MD model of the structure provides additional insight, but this structure's treatment of a critical residue, S64, may limit its accuracy[2]. Experimental determination of EmrE's structure has been hindered by its highly dynamic nature. To address this, we screened for EmrE mutants that retained drug binding ability but lost function (Appendix A). One mutant, S64V, exhibits slow dynamics in all binding states and produces high quality NMR spectra. Using this mutant bound to a fluorinated tetraphenylphosphonium derivative, we were able to solve a high-resolution structure of the binding pocket using ^{19}F REDOR NMR[3] (Appendix B). However, this structure

lacks sufficient restraints in the loops or tail regions, which limits its usefulness in understanding EmrE's allosteric regulation mechanism.

Our understanding of this allosteric regulation mechanism and the relationship of EmrE's behavior with and without drug is still in its infancy. We know that an allosteric site exists, but the exact location of this site, which residues are involved, and its structure is still unclear. It seems likely that one or both of the loop carboxylate residues are involved – E25 and D84[4,5]. Mutating these residues does not appear to be critical for EmrE's function[6,7], though there is a report that the E24D mutation changes the drug specificity of a different SMR transporter[8]. The ability of these mutagenesis studies to uncover subtle phenotypes related to proton leak is unclear, as the authors were more interested in drug resistance phenotypes. In addition, two of these studies were performed very early in the history of SMR research before it was even established that E14 was the central shared binding site for drug and proton.

Our increased understanding of EmrE's mechanism in the intervening twenty years should allow us to perform more carefully controlled mutagenesis studies of the loop regions of EmrE in the future, for example, by combining mutations to the loop residues with mutations to the central binding site or the tail. NMR will be useful for tracking perturbations to EmrE's structure upon the addition of drug and for investigating the effects of binding to this site on the alternating access dynamics and dynamics of the tail. Stopped-flow experiments could be used to directly measure the proton-off rate under a variety of experimental conditions, which would allow us to expand the kinetic description of the free exchange model to include the allosteric gating mechanism. Future small molecule screens may identify substrates that bind preferentially to the allosteric site, which would enable further studies on the impact of this site on EmrE's transport in the absence of a traditional drug substrate. Ultimately, successfully characterization of the allosteric gating mechanism will require creative synthesis of a variety of approaches. If EmrE has taught us anything, it is to always expect the unexpected.

References

1. Chen, Y.-J. *et al.* X-ray structure of EmrE supports dual topology model. *PNAS* **104**, 18999–19004 (2007).

2. Vermaas, J. V., Rempe, S. B. & Tajkhorshid, E. Electrostatic lock in the transport cycle of the multidrug resistance transporter EmrE. *Proceedings of the National Academy of Sciences of the United States of America* 201722399 (2018) doi:10.1073/pnas.1722399115.

3. Shcherbakov, A. A., Mandala, V. S. & Hong, M. High-Sensitivity Detection of Nanometer 1H–19F Distances for Protein Structure Determination by 1H-Detected Fast MAS NMR. *J. Phys. Chem. B* **123**, 4387–4391 (2019).

4. Glaubitz, C. *et al.* 31P-CP-MAS NMR studies on TPP+ bound to the ion-coupled multidrug transport protein EmrE. *FEBS Letters* **480**, 127–131 (2000).

5. Ong, Y. S., Lakatos, A., Becker-Baldus, J., Pos, K. M. & Glaubitz, C. Detecting Substrates Bound to the Secondary Multidrug Efflux Pump EmrE by DNP-Enhanced Solid-State NMR. *Journal of the American Chemical Society* **135**, 15754–15762 (2013).

6. Yerushalmi, H. An Essential Glutamyl Residue in EmrE, a Multidrug Antiporter from Escherichia coli. *Journal of Biological Chemistry* **275**, 5264–5269 (2000).

7. Amadi, S. T., Koteiche, H. A., Mishra, S. & McHaourab, H. S. Structure, dynamics, and substrate-induced conformational changes of the multidrug transporter EmrE in liposomes. *J. Biol. Chem.* **285**, 26710–26718 (2010).

8. Grinius, L. L. & Goldberg, E. B. Bacterial multidrug resistance is due to a single membrane protein which functions as a drug pump. *The Journal of biological chemistry* **269**, 29998–30004 (1994).

Appendix A

Identification of an alternating-access dynamics mutant of EmrE with impaired transport

Chao Wu[1a], Samantha A. Wynne[2b], Nathan E. Thomas[3], Eva-Maria Uhlemann[3c], Christopher G. Tate[2], Katherine A. Henzler-Wildman[1,3]

[1] Department of Biochemistry and Molecular Biophysics, Washington University School of Medicine in St. Louis, MO 63110

[2] MRC Laboratory of Molecular Biology, Cambridge CB2 0QH, UK

[3] Department of Biochemistry, University of Wisconsin-Madison, Madison WI 53706

[a] Present address: Department of Pathology and Immunology, Washington University School of Medicine in St. Louis, MO 63110

[b] Present address: Wellcome Sanger Institute, Hinxton, Cambridge CB10 1SA

[c] Present address: Department of Biochemistry, Microbiology and Immunology, University of Saskatchewan, Saskatoon, SK, S7N5E5, Canada

Preface: In this paper, we report our attempts to find an EmrE mutant with impaired dynamics that would be aid determination of a high-resolution EmrE structure. Chao performed NMR experiments, analyzed data, and wrote the first draft, Samantha created the mutant library and ran the resistance assays, I wrote the final draft, and Eva performed the in-cell transport experiments.

Abstract: Proteins that perform active transport must alternate the access of a binding site, first to one side of a membrane and then to the other, resulting in the transport of bound substrates across the membrane. To better understand this process, we sought to identify mutants of the small multidrug resistance transporter EmrE with reduced rates of alternating access. We performed extensive scanning mutagenesis by changing every amino acid residue either to Val,

Ala or Gly, and then screening the drug resistance phenotypes of the resulting mutants. We identified EmrE mutants that had impaired transport activity but retained the ability to bind substrate and further tested their alternating access rates using NMR. Ultimately, we were able to identify a single mutation, S64V, which significantly reduced the rate of alternating access but did not impair substrate binding. Six other transport-impaired mutants did not have reduced alternating access rates, highlighting the importance of other aspects of the transport cycle to achieve drug resistance activity *in vivo.* To better understand the transport cycle of EmrE, efforts are now underway to determine a high-resolution structure using the S64V mutant identified here.

Introduction

The small multidrug resistance transporter EmrE harnesses the energy of the proton motive force (PMF) to confer resistance to a wide array of toxic cations [1]. EmrE functions as an antiparallel homodimer, with a shared binding site for both protons and drug-substrates [2–5]. The dynamic process of switching conformations so that this binding site alternates between inward-facing and outward-facing is the key step in moving substrates across the membrane (Fig. 1). When this alternating access process is prevented by specific cross-linking, EmrE is rendered nonfunctional, providing experimental confirmation that alternating access is required for transport [6].

Multiple labs have investigated the impact of individual mutations on EmrE function. Several common themes emerged from these studies, such as the importance of Glu14 as a shared binding site both for drugs and protons, the role of transmembrane helices 1, 2 and 3 (TMs 1-3) as the core substrate binding domain, and the role of TM4 as a dimerization domain. These studies identified specific residues critical for drug binding, drug specificity, proton-drug coupling, and dimerization [2,7–17]. However, no individual sites have previously been identified as critical for alternating access.

EmrE is the most studied member of the Small Multidrug Resistance (SMR) family and is the only SMR for which even modest resolution structures are available [3,4,18]. These structures provided crucial insight into the surprising asymmetric, antiparallel topology of EmrE, but the lack of side chain information hinders a deeper understanding of the transport mechanism. More recently, two models of the EmrE structure have been published [19,20] based on molecular dynamics simulations of EmrE embedded in lipid bilayers. While these models provide useful information on the transport cycle [19] and dimerization [20] of EmrE, they are ultimately based on the earlier low-resolution experimental structures. There are several potential reasons why a high-resolution structure has proven elusive. First, EmrE is quite small, with short loops connecting four transmembrane helices in only 110 total amino acids. The lack of soluble domains hampers three-dimensional crystallization, and strategies that have proven useful for solving the structure of other integral membrane proteins have been unsuccessful for EmrE. Second, EmrE is inherently dynamic. In fact, there is no known condition under which wild type EmrE is not dynamic; alternating access occurs even when neither proton nor drug is bound [21–24]. This natural plasticity is proposed to be an important property enabling its very broad multidrug binding capability [23] but is problematic for the determination of high-resolution structures. Therefore, we have a second motivation in identifying a mutant that suppresses the inherently dynamic nature of EmrE in order to determine a higher resolution structure and better understand how this small protein interacts with such a broad class of substrates.

Here, we identify a critical residue in EmrE, S64V, which alters the rate of alternating access but does not significantly change the affinity for substrate binding.

Results

Identification of Functionally Important Residues in EmrE

To screen for potential dynamics mutants, we sought to identify EmrE point mutations that inhibited transport, but which did not significantly affect substrate binding. First, wild type EmrE was mutated at every residue (except the N-terminal Met) to the amino acids Ala, Gly or Val as described in the Methods. In a few positions Leu was introduced if the native amino acid was already Ala, Gly, or Val. Previous scanning mutagenesis of EmrE used Cys or Trp substitutions to probe residue accessibility, identify the dimer interface, and to insert spin labels for EPR studies [8,9,11,13,16,25,26]. However, Ala, Gly and Val are more common in transmembrane helical regions than Cys or Trp [27,28]. Substitutions with these three amino acids are well tolerated throughout a membrane protein and have been used previously to isolate conformational specific mutants of the tetracycline carrier TetA(B) [29]. After two rounds of mutagenesis, all but five mutants were made (F44A, W63V, F79G, D84A, I88G). The EmrE mutants were then tested for their ability to confer resistance to three canonical EmrE substrates: methyl viologen, acriflavine, and ethidium bromide (Fig. S1-S3, Supplementary Data Table 1). Two concentrations of each substrate (see Methods) were chosen for testing. These concentrations were selected so that *E. coli* strain JM109 containing the plasmid pKK223-3 was unable to grow even at the lower concentration and leaky expression of wild type *emrE* from the same plasmid was still able to confer resistance and permit growth of JM109 at the higher concentration. Growth was scored as robust at both concentrations of a given substrate (++), growth at both substrate concentrations but notably reduced relative to WT at the higher concentration (+), growth only at the lower substrate concentration (+/-) or no growth at either substrate concentration (-) for each of the three different substrates.

Mapping the transport activity of the EmrE mutants onto the recent all-atom model [19] of EmrE (Fig. 2A) highlights the similarity between the functionally important residues identified experimentally and regions of high sequence conservation as identified using ConSurf (Fig. 2B). The screen identified residues in TM1-3 lining the substrate binding pocket known to be

important for drug- and proton-binding (for example, Glu14, Leu47, and Trp63) [2,11,12], as well as residues in the TM4 dimerization interface (Gly90, Ile94, and Gly97) [10,13,20]. As expected, many locations were sensitive to the identity of the substituted amino acid (Fig. 3A). For example, mutation of Ala10 – located just one helical turn away from the Glu14 binding site – to the bulkier valine abolished resistance to all three substrates, while mutation to glycine did not impair the resistance phenotype. In addition, by testing growth on three different EmrE substrates, our scan highlights residues where mutation has a potential effect on drug selectivity (Fig. 3B). Many residues thought to interact with substrates, such as Leu7 and Phe44 [8], conferred varying levels of resistance to different drugs. This supports the hypothesis that substrates with widely variant structures do not necessarily interact with identical amino acid residues and could affect the EmrE structural intermediates differently [30]. Interestingly, a number of residues from the TM2-3 loop and from TM4 had an effect on substrate selectivity, even though these regions are not part of the previously-identified substrate binding site [2–5].

Identification of potential EmrE dynamics mutants

Alternating access between outward-open and inward-open states is essential for EmrE to confer drug resistance [6] but is not necessary for drug binding. Therefore, in order to identify mutants of EmrE with impaired alternating access rates, we first identified mutants with impaired resistance phenotypes that were not thought to be involved in direct interactions with substrates. The mutants chosen were M21G, A59L, S64V, G67A, G90V, G97V, I101G, N102A and N102V. We then tested the ^{3}H-TPP^{+}-binding affinity of the selected mutants (Table 1). G67A and G97V were excluded at this stage because expression was very low, and they did not give good saturation binding curves, suggesting they would not be able to be purified for structure determination. Four mutants showed affinities of ^{3}H-TPP similar to wild type EmrE (S64V, I101G, N102A, N102V), two mutants had affinities 2-3 fold lower (M21G, G90V) and one was 10-fold lower (A59L). The location of all seven mutations is shown on the recently published

refined atomic model of the complete structure of EmrE (Fig. 4A). M21G and A59L are located near the ends of the first and second TM helices, respectively. S64V is close to the ^{65}GVG^{67} TM3 kink region, which is important for inward-open/outward-open interconversion and multidrug recognition according to cryo-EM and NMR studies [4,5,30–32]. G90V is located in the established G90/G97 TM4 dimerization motif [10,13]. Finally, I101G, N102A, and N102V are located in TM4, but have not been directly implicated in dimerization.

Mutants with altered dynamics inhibit EmrE–mediated drug efflux

To confirm the impaired transport phenotype, the M21G, A59L, S64V, I101G, and N102A mutations were further characterized using an ethidium efflux assay in *E. coli* (Fig. 4B). This assay provided a kinetic assessment of EmrE activity, compared to the plate assay that simply reflected whether drug efflux was sufficient to enable survival over 24 hours. The results confirmed that efflux of ethidium from *E. coli* was indeed slower for each of the EmrE mutants than for wild type EmrE, and the slower efflux is not a result of decreased EmrE expression (Fig. 4C). This is consistent with the hypothesis that the impaired drug resistance activity of these EmrE mutants is due to a reduced rate of alternating access.

The effect of the mutations upon EmrE dynamics was then assessed using NMR spectroscopy, a technique that is uniquely suited to provide information simultaneously about both protein structure and dynamics. We acquired ^{1}H-^{15}N TROSY HSQC spectra of each mutant in q=0.33 DMPC/DHPC bicelles bound to TPP^{+} and compared them to TPP^{+}-bound WT EmrE under the same conditions (Fig. 5 and S4). In the WT spectrum, two peaks are visible for each residue, reflecting the distinct chemical environments for each protomer in the asymmetric dimer. Peak doubling is still visible in the spectra for at least some residues in six mutants, indicating that the asymmetric EmrE dimer remains intact. The only exception is G90V-EmrE, which has fewer peaks and a poorly resolved spectrum, suggesting a loss of its unique tertiary

structure of the asymmetric dimer. This is consistent with previous demonstrations that the dimer is destabilized when G90 or G97 is mutated [10,13].

The ^{1}H-^{15}N TROSY spectra also provide substantial insight into protein dynamics. While each protomer in the asymmetric dimer of EmrE is in a unique chemical environment, the protomers swap conformations during alternating access [5]. The presence of pairs of relatively sharp peaks for each amino acid in the WT EmrE spectrum indicates that this alternating access rate is slow on the NMR timescale ($k_{ex} < \Delta\omega$, where $\Delta\omega$ is the chemical shift difference between the two exchanging states) when TPP^{+} is bound. If this process were fast on the NMR timescale ($k_{ex} > \Delta\omega$), then the spectrum would reflect an average of the two chemical environments and only a single peak per amino acid would be visible. Dynamics on intermediate timescales result in significant broadening of the peaks in the NMR spectrum. Despite our expectations that impaired transport would arise from reduced dynamics, five mutants displayed *enhanced* dynamics. The ^{1}H-^{15}N TROSY spectra of I101G, A59L, N102A, and N102V (Fig. 5 and S4) displayed progressively increased line broadening and each pair of peaks shifted toward each other, eventually coalescing into a broad single peak for many residues. It is important to note that the effect of dynamics on peak widths and intensities is not limited to alternating access conformational exchange. The enhanced line broadening may also reflect greater structural heterogeneity or increased motion within the “ground-state” structure. This is a more likely explanation for M21G, which has significant loss of peak intensity while still having well-resolved peak doubling.

Importance of the TM3 kink for alternating access and drug transport by EmrE

In contrast to all other mutants, S64V-EmrE displayed pairs of sharp, well-resolved peaks throughout the spectrum. The ^{1}H-^{15}N TROSY spectrum of this mutant was similar to WT EmrE, indicating that it has a very similar asymmetric dimer structure. Indeed, chemical shift changes were greatest in the immediate vicinity of the mutation, as shown on the three-

dimensional structure in Figure 6. Since the chemical shifts reflect the unique environment of each nucleus, these data indicated that the three-dimensional structure of the asymmetric EmrE homodimer was very similar in WT EmrE and S64V-EmrE.

To determine whether S64V exhibited slower dynamics, NMR exchange spectroscopy was used to directly determine the alternating access rate. For a static structure, the ZZ-exchange spectrum will be identical to the ^{1}H-^{15}N TROSY spectrum. However, if alternating access occurs during the delay period in the ZZ-exchange experiment, additional cross-peaks appear in the spectrum (Fig. 7A-C). By varying the mixing time, the build-up of cross-peaks and decay of autopeaks can be fit to quantitatively determine the kinetics of alternating access (Fig. 7D), as we have previously shown for WT EmrE [5]. The S64V alternating access rate measured with these experiments is 0.6 ± 0.1 s^{-1}, 8-fold slower than WT EmrE under the same conditions (4.7 ± 0.6 s^{-1}) [32]. In addition, the individual peaks in the spectra are even more intense and uniform in shape, suggesting less structural plasticity in this mutant on all timescales.

Finally, we used isothermal titration calorimetry data to determine the affinity of S64V for several different drug substrates. The data show that S64V-EmrE binds TPP^{+}, $MeTPP^{+}$, and $EtTPP^{+}$ with affinities nearly identical to WT EmrE (Table 2, S1, S2, and Fig. S6). This is consistent with the NMR chemical shift data indicating very little difference in the structure of this mutant and confirms that impaired transport is not due to difference in drug binding affinity. Thus, we have successfully discovered a dynamics mutant that has a reduced rate of alternating access without disrupting the structure or substrate affinity of EmrE.

Discussion

In this study, we aimed to identify mutations that suppressed the ability of EmrE to exchange between conformations open to either side of the membrane. To this end, we performed the single most extensive mutagenesis scan of EmrE to date, testing the effect of

mutations to one of three amino acids (alanine, glycine, or valine) at each position on resistance to three canonical EmrE substrates (ethidium, acriflavine, or methyl viologen). From this screen, we selected several mutants that exhibited impaired drug resistance but normal drug binding for further dynamics study. In a kinetic assay, all of the mutants had reduced rates of PMF-driven drug efflux in *E. coli*. Alternating access in the drug-bound state is the rate limiting step in the transport cycle of TPP^+ by wild-type EmrE [21,33]. Thus, we hypothesized that the reduced rate of drug efflux by these mutants was due to a decrease in the rate of this critical step. Surprisingly, the rate of net drug efflux from *E. coli* for our mutants does not correlate simply with the rate of alternating access observed by NMR.

How might the rate of drug efflux be reduced despite an increased rate of alternating access? EmrE's transport mechanism is complex [21,34,35], so it is possible that the mutations drastically reduced the rates of steps other than alternating access, thereby changing which step is rate-limiting. However, in light of the overall increased dynamics displayed by the mutant spectra, it is important to note that decreased transporter dynamics are not required for a decreased rate of transport. Efficient drug efflux requires allosteric communication between various regions of the protein, such that large-scale dynamic motions, including the loop and helix rearrangements necessary for alternating access, are properly coordinated to binding of drug and proton. Loss of this coordination could increase the rate of drug or proton leak pathways, reducing the efficiency of transport even when alternating access is fast [36].

Unfortunately, the lack of a high-resolution EmrE structure precludes a deep understanding of its allosteric couplings. Nevertheless, there are several examples of known allosteric mechanisms that are essential for proper transport. The first and most important is the relationship between the alternating access rate of EmrE and the occupancy of the E14 binding site. This rate varies over several orders of magnitude depending on the identity of bound drug, while in the absence of drug it increases upon protonation [22,32,37]. A second allosteric

coupling involves the TM2-3 loop, which exhibits increased dynamics upon protonation of E14. This loop is proposed to be involved in a latching mechanism, wrapping around TM1 to stabilize the closure of the transport pore on one side of the membrane and prevent proton leak. Mutation of this loop to destabilize the latch can abolish drug resistance (I54G, repeated here in Table S1) and increase the alternating access rate (I54L) [37]. A final set of couplings involve the TM1-2 and TM3-4 loops. In an electron paramagnetic resonance (EPR) study, it was shown that these loops close to form an occluded state upon protonation of a residue apart from E14 [35], which our NMR data suggests is H110 [22,34]. Recently, we demonstrated further coupling between the C-terminal tail, which includes H110, and the occupancy of the E14 binding site. Consideration of these couplings led to our proposal of an allosteric gating mechanism to prevent futile proton transport in the absence of drug [34].

It seems likely that mutations that increase the alternating access rate of EmrE disrupt one or more of these mechanisms, resulting in the impaired drug resistance phenotype. A59L is located at the beginning of TM3, possibly disrupting stable closure of the TM2-3 loop. Similarly, M21G is located at the end of TM1 and could disturb EmrE gating by disrupting the coupling of TM1, which contains the critical E14 residue, with the rest of the transporter. Previous comparison of the NMR chemical shifts of TPP^+-bound EmrE showed very little difference between TM1 and TM2 in the two protomers of the asymmetric homodimer [31], suggesting that the first few helices move together as the protein switches between open-in and open-out conformations. Loss of this coordinated movement could disrupt the transition and gating of EmrE.

It is more difficult to rationalize the effects of I101G, N102A, and N102V within our current understanding of EmrE structure and function. The primary role of TM4 is thought to be dimerization [10,38], holding the small EmrE homodimer together while it undergoes the large-scale conformational changes needed to alternate access. However, mutations at positions 101

and 102 did not disrupt the EmrE dimer in previous mutagenesis studies and do not disrupt dimerization in the mutants examined here [13].

The answer could lie in the importance of the ^{65}GVG^{67} motif, which forms a hinge point in TM3 [10]. In the available moderate resolution structures, this kink is only found in monomer A of the EmrE homodimer [3,4,18]. The NMR chemical shift data confirms this difference in TM3 structure between the two halves of the dimer [5]. Thus, the TM3 helices must alternately kink and straighten as EmrE transitions between open-in and open-out conformations during each transport cycle. It is perhaps not surprising then that the one slow dynamics mutant of EmrE we identified, S64V, is adjacent to this motif. Interestingly, residues 101 and 102 also pack against this region. Re-examining our previous studies of WT EmrE bound to diverse substrates confirms the coupling between TM3 and this segment of TM4: large chemical shift changes are observed for TM4 residues at the level of the TM3 kink when EmrE is bound to different substrates [32]. We previously attributed this to indirect effects from structural changes in the TM3 kink that are necessary for EmrE to accommodate diverse substrates. However, the dramatic phenotypes of I101G, N102A, and N102V presented here suggest that mutation of these residues may instead disrupt a critical function of the TM3 kink. We are currently exploring the effects of additional substitutions at position 64 and the effect of the S64V mutation on each step in the transport cycle. Ultimately, a deep understanding of the importance of this region, and of EmrE's broader transport mechanism, will require a high-resolution structure. This effort is underway, facilitated by the slow dynamics of the S64V mutant presented here.

Materials and Methods

Screening for putative dynamics mutants

Every codon in the gene encoding EmrE was mutated using degenerate oligonucleotides that converted a given codon to GBN, where B either is T, C or G and N is any

base. Thus, every amino acid residue was changed either to Val, Ala or Gly [29]. The mutagenic reactions (QuikChange II, Agilent) were performed on the wild type *EmrE* gene inserted under the control of the *tac* promoter in plasmid pKK223-3 (making plasmid pKK56 [1]), transformed into *E. coli* strain JM109 and colonies grown on 2xTY agar plates containing 100 μg/ml ampicillin. Eight colonies were picked from each mutagenic reaction, grown overnight at 37˚C in 1 ml 2xTY in a deep-well block, and then this culture was diluted 1000-fold. The ability of each EmrE mutant to transport substrates out of *E. coli* was then assessed by spotting 5 □l of the diluted culture onto 2xTY agar plates either containing methyl viologen (50 μM or 200 μM), acriflavine (116 μM or 463 μM), ethidium bromide (400 μM or 1500 μM) or control plates containing no substrate. DNA sequencing was performed in parallel to determine which mutations were present in each EmrE mutant. In the first round of mutagenesis, 109 amino acid residues corresponding to residues 2-110 of EmrE were mutated and 276 of the possible 327 mutants were obtained (Fig S1, S2). The remaining 51 mutants were made using oligonucleotides designed specifically to introduce a single amino acid residue, sequenced and then tested for their growth phenotype on the three substrates (Fig S3). Five mutants were not made (F44A, W63V, F79G, D84A, I88G). Growth was scored as robust at both concentrations of a given substrate (++), growth at both substrate concentrations but notably reduced relative to WT at the higher concentration (+), growth only at the lower substrate concentration (+/-) or no growth at either substrate concentration (-) for each of the three different substrates. Neither JM109 or JM109(pKK56) grew in the presence of any of the substrate concentrations tested. Selected mutants with impaired transport, as indicated by severe defects in the growth assays were then checked for substrate binding using [^{3}H]-TPP^{+} binding assays performed with the selected EmrE mutants purified in DDM detergent using previously published methods [39]. Data were gathered from a single experiment performed in triplicate. Reported errors are standard error of mean (SEM).

ConSurf analysis Sequence conservation analysis using ConSurf [40–42] was performed on the EmrE amino acid sequence using one iteration of HMMER to search for homologues with E-value cutoff of 0.0001 against protein database of UNIREF-90. A total of 300 sequences with that sample the list of homologues to reference sequence were selected out of homology search. These sequences were aligned using MAFFT. Calculated Bayesian conservation scores were mapped on the structure.

Sample preparation

WT and mutant EmrE was expressed, purified, and reconstituted into DLPC or DMPC liposomes as previously described [5,32]. Detergent was removed by Amberlite® XAD®-2 resin, and 6:0 DHPC was added to form isotropic bicelles as described in [43]. Single point mutants were constructed using QuikChange (Stratagene).

In-cell assay

These assays were carried out using BL21(DE3) *E. coli* transformed with empty pET15b vector or pET15b-EmrE with the specified WT or mutant sequence. The cells were grown in M9 minimal media with 100 μg/ml of ampicillin at 37 ˚C until the OD_{600} reached 0.4. Then cells were induced with 0.33 mM isopropyl 1-thio-β-D-galactopyranoside (IPTG) at the same temperature for 30 minutes. After induction, cell density was adjusted to OD_{600} = 0.4 followed by incubation with 2.5 μM ethidium bromide and 40 μM carbonyl cyanide p-chlorophenylhydrazone (CCCP) for an hour to load ethidium bromide into the cells. The cell cultures were then stored on ice until assays were complete. For each experiment, 2 ml of cell culture was spun down and immediately resuspended in 1 ml fresh M9 media with 2.5 μM ethidium bromide. Fluorescence of ethidium bromide was monitored with an excitation wavelength at 545 nm and emission wavelength at 610 nm. The time course of fluorescence was plotted after normalization to the initial value of each run.

Western Blot analysis of EmrE expression levels

Cells prepared for the in-cell transport assay as described above were induced and adjusted to OD_{600nm} =0.4. A 1 ml aliquot of this cell suspension was pelleted by centrifugation and resuspended in 40 µl of SDS-PAGE sample buffer. A 5 µl sample was loaded on a 4-12% Bis-Tris NuPAGE gel (Thermo Fisher) and, following electrophoresis, transferred onto Immobilon PVDF membrane (EMD-Millipore). The blot was probed with anti-His_6-HRP conjugated antibody (QIAGEN) at 1:10,000 dilution, following manufacturer's instructions. Bands were visualized with ECL Prime Western blotting kit (GE) according to the standard protocol. HyBlot Films (Denville) were exposed for 3 min and captured with EZ doc imaging system (BioRad).

NMR spectroscopy and data analysis

NMR data were collected using samples with 0.8-1.5 mM $^{2}H,^{15}N$ EmrE in DMPC/DHPC bicelles (q = 0.33, with a protein to DMPC molar ratio of 1:50) and 100 mM MOPS, 10-30 mM NaCl, 2 mM TCEP, 8-10 % D_2O, pH 7 at 45 ˚C on a Varian 700 MHz spectrometer with a room temperature probe unless otherwise noted. All NMR spectra were processed with NMRPipe [44] and analyzed in CcpNmr Analysis [45]. For the TPP^+-bound EmrE, 2 mM TPP^+ was added to ensure EmrE saturation. 2D $^{1}H,^{15}N$ TROSY-HSQC and TROSY-selected ZZ-exchange experiments [46] with a lipid flip-back pulse [5] were carried out with a recycle delay of 2 s and 128-144 increments.

Chemical shift differences ($\Delta\delta$), between TPP^+-bound WT and S64V EmrE were calculated as a weighted average of the differences in amide proton ($\Delta\delta_H$) and nitrogen ($\Delta\delta_N$) chemical shifts according to:

$$\Delta\delta = \sqrt{\Delta\delta_H{}^2 + (0.154\,\Delta\delta_N)^2}\,. \quad (1)$$

The conformational interconversion rate, k_{conf}, were analyzed from the ZZ-exchange data as previously described[47] using the composite peak ratio method with an 11.1 ms offset time, t_0, to account for the back-transfer time in the pulse sequence[22]. The composite peak ratios of

intensities of the auto-peaks (I_{AA}, I_{BB}) and cross-peaks (I_{AB}, I_{BA}) were fit to the following equation as a function of the delay time, t,:

$$\Xi(t) = \frac{I_{AB}(t)I_{BA}(t)}{I_{AA}(t)I_{BB}(t) - I_{AB}(t)I_{BA}(t)} \cong k_{conf}^2(t - t_0)^2. \qquad (2)$$

For TPP^+-bound EmrE, at least two planes were collected with different mixing times and the mixing times were adjusted according to the conformational interconversion rate of each mutant. For S64V, the slow rate of alternating access requires long mixing times in order for measurable cross-peak build up and the large size of bicelle-solubilized EmrE leads to relatively fast relaxation, which limits the total possible mixing time. Thus, for TPP^+-bound S64V-EmrE, mixing times of 100 ms and 200 ms were used in DLPC bicelles and 200 ms and 225 ms in DMPC bicelles. For TPP^+-bound WT-EmrE in DMPC bicelles, conformational exchange is faster and 4 planes with mixing times of 20 ms, 50 ms, 90 ms, and 125 ms were used to quantify the rate of alternating access. The rate was determined by global fitting of all residues with resolved auto- and cross-peaks in the spectra, and the standard deviation of the rates determined by separately fitting individual residues was used to estimate the error of the rates.

Isothermal titration calorimetry All isothermal titration calorimetry (ITC) experiments were performed on a TA instruments Nano-ITC calorimeter as previously described [32]. Data were fit to a model of ligand binding to *n* independent and identical sites plus a constant baseline due to mixing using the NanoAnalyze software EmrE was reconstituted into DMPC/DHPC (q = 0.33) isotropic bicelles in 20 mM potassium phosphate, 20 mM NaCl, pH 7, 45 ºC and loaded into the cell at 40-60 μM for tetraphenylphophonium (TPP^+) titrations and 500 μM for titration with methyltriphenylphophonium ($MeTPP^+$) or ethyltriphenylphosphonium ($EtTPP^+$). TPP^+ concentration in the syringe was 150-200 μM. $MeTPP^+$ and $EtTPP^+$ concentrations were 2-4 mM with buffer and bicelle conditions that exactly matched the protein solution in the cell. Titrations replicates are listed in Table S1 and S2. Reported errors are standard error of mean (SEM).

NMR Assignment Deposition

NMR assignments were deposited to the Biological Magnetic Resonance Database (BMRB) under accession number 27902.

Acknowledgements

NMR data was collected both at Washington University in St. Louis and at the National Magnetic Resonance Facility at Madison. NMRFAM is supported by NIH grant P41GM103399 (NIGMS), old number: P41RR002301. Equipment was purchased with funds from the University of Wisconsin-Madison, the NIH P41GM103399, S10RR02781, S10RR08438, S10RR023438, S10RR025062, S10RR029220), the NSF (DMB-8415048, OIA-9977486, BIR-9214394), and the USDA. We thank Changguo Tang and Greg DeKoster at Washington University in St. Louis and Marco Tonelli at NMRFAM for assistance in implementing NMR pulse sequences. Some of the ITC replicates were obtained at the University of Wisconsin-Madison Biophysics Instrumentation Facility, which was established with support from the University of Wisconsin-Madison and grants BIR-9512577 (NSF) and S10RR13790 (NIH).

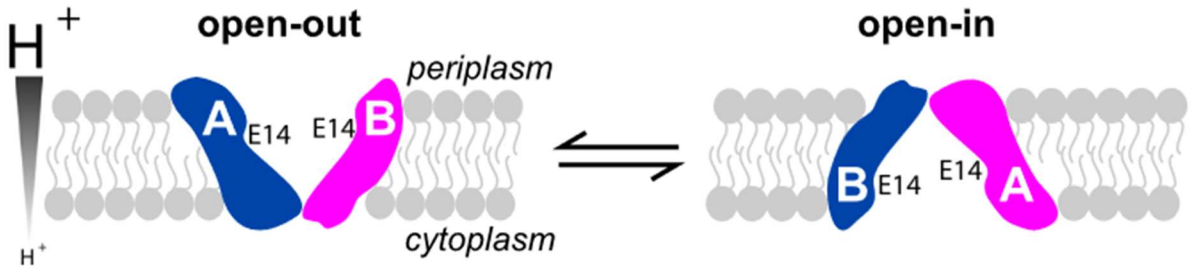

Figure 1 *Alternating-access of EmrE.* EmrE binds both protons and polyaromatic cation substrates at a shared binding site defined by the two E14 residues from the two protomers of the functional homodimer. Alternating accessibility of this binding site to either side of the membrane occurs when the two protomers in the antiparallel homodimer swap conformational states (illustrated by the different shapes drawn for each protomer). EmrE couples proton import to export of toxic substrates, conferring resistance to these compounds to *E. coli*.

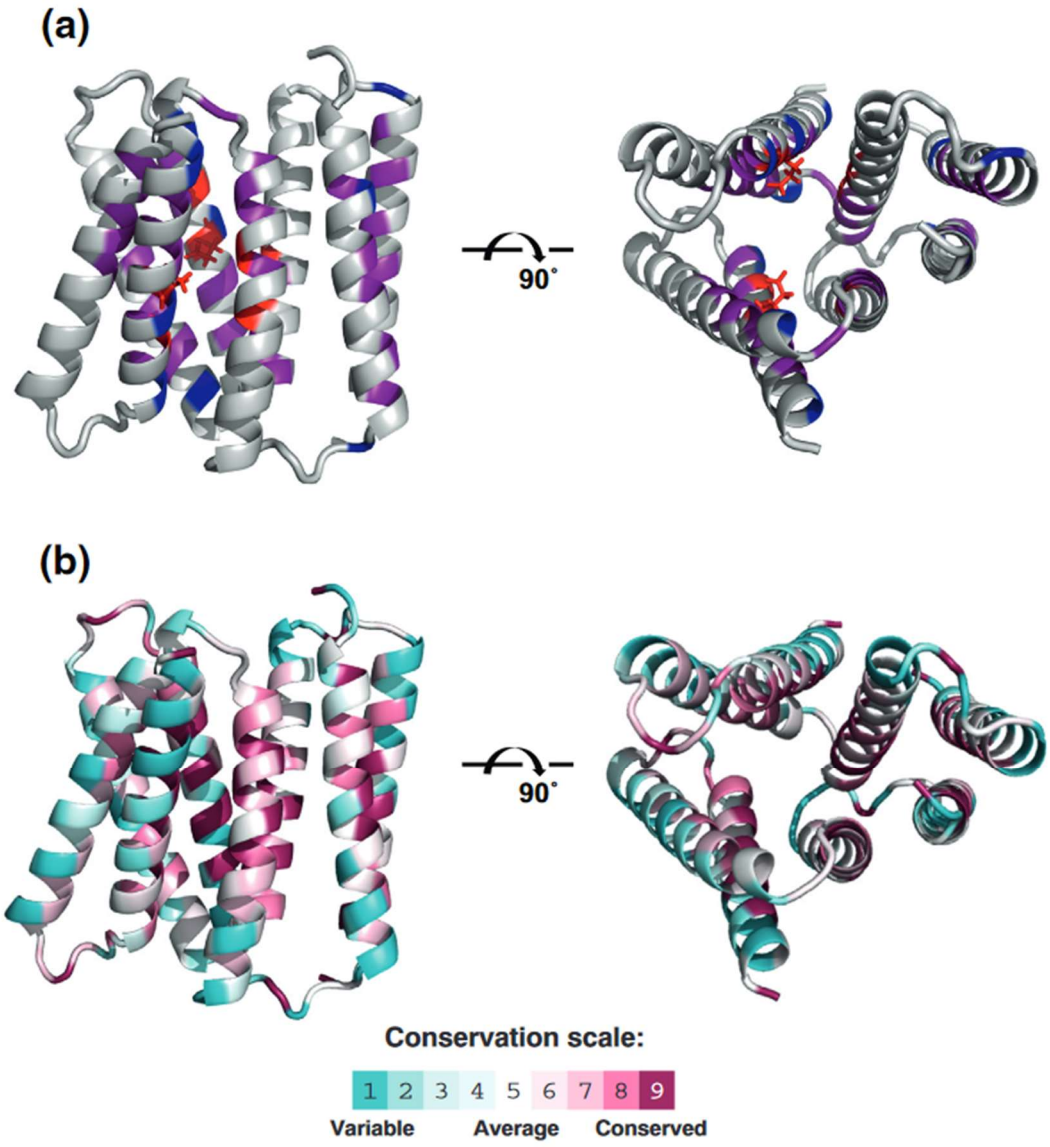

Figure 2 *Functionally critical residues in EmrE identified from screening are evolutionarily conserved. A*, Summary of plate assay results from Supplementary Data Table 1 mapped on to the complete structural model of EmrE [19]. Gray, no effect (++) of mutation to V, A, or G at that position on resistance to any of the tested compounds. Blue, modest effect (+) of mutation on resistance profile. Magenta, significant effect (+/-) of mutation on resistance profile. Red, severe defect (-) in growth or resistance to all tested compounds upon mutation of that position to any other amino acid. *B*, Evolutionary conservation profile calculated using ConSurf.

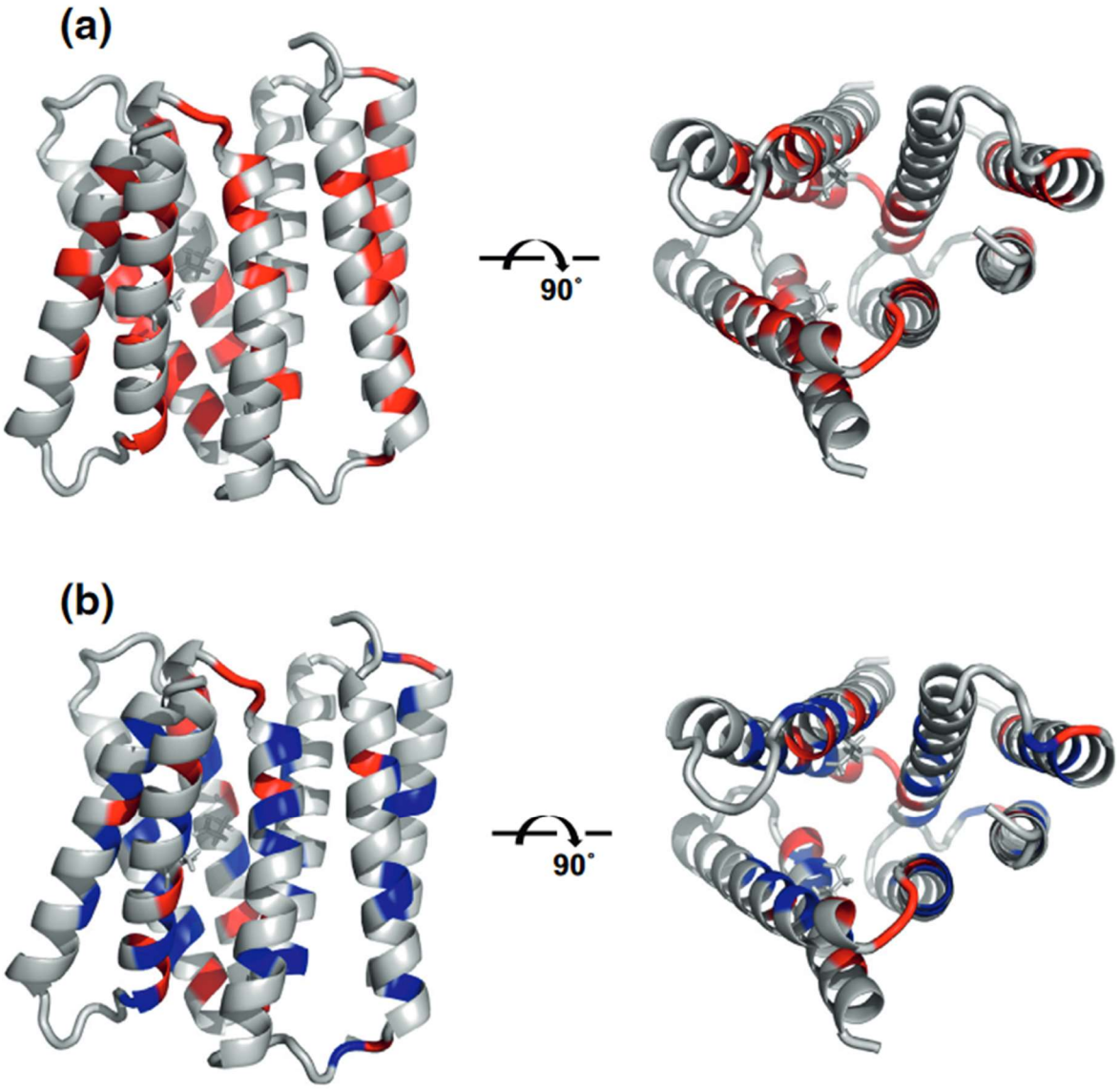

Figure 3 *Locations critical for function depend on identity of substituted amino acid and identity of drug. A*, locations where the identity of the substituted amino acid affects the ethidium bromide resistance phenotype highlighted in red. *B*, locations where different drug substrates led to different growth phenotypes for one of the substituted amino acids (blue) or multiple amino acids (red).

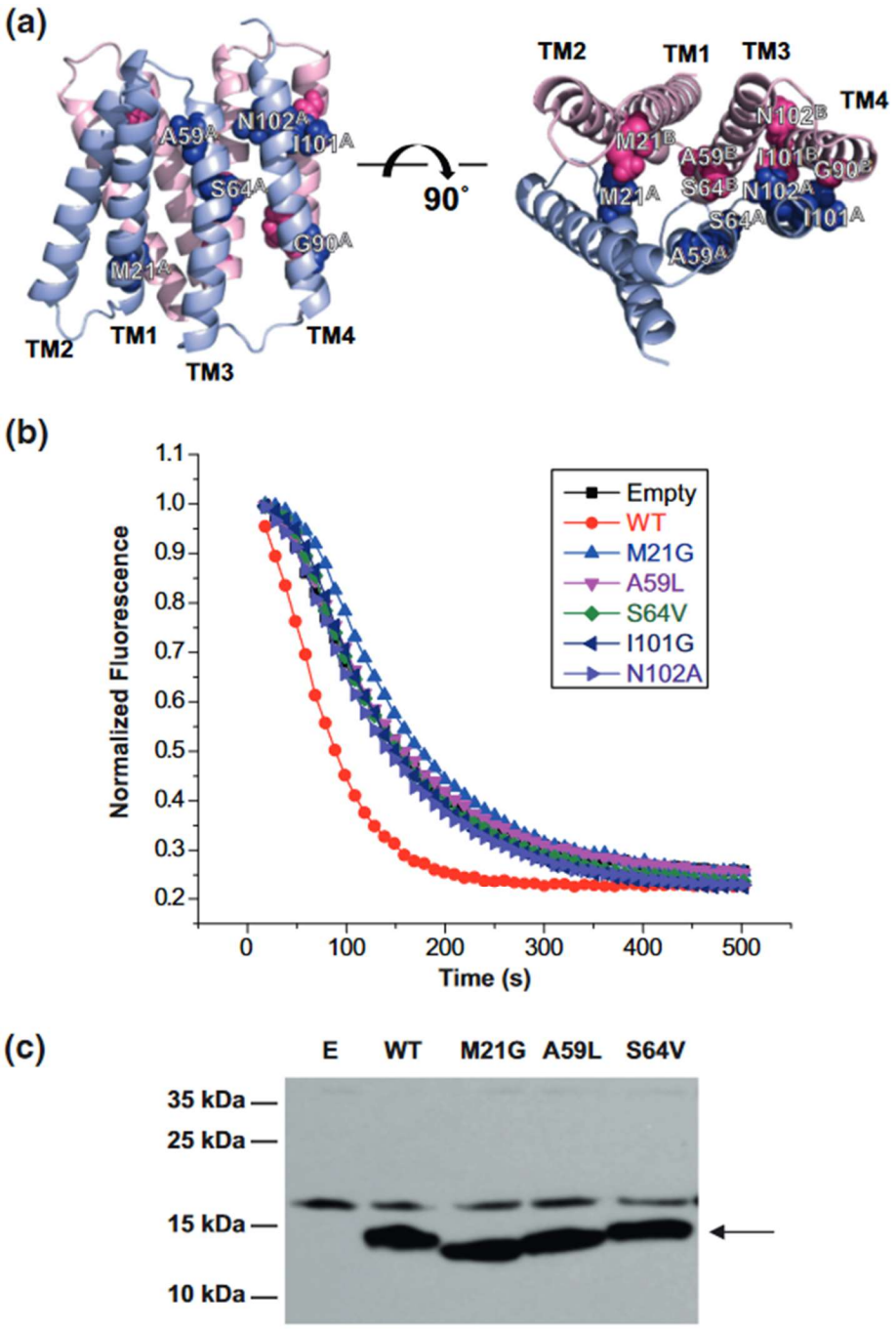

Figure 4 *In-cell transport data confirm impaired transport phenotype. A,* position of putative dynamics mutants on the structure, with wild-type residue identities indicated. *B*, efflux of ethidium from BL21 (DE3) E. coli cells transformed with either empty vector or the indicated EmrE mutant results in a decrease in fluorescence. *C*, Western blot of selected EmrE mutants demonstrates that expression levels are similar to WT-EmrE.

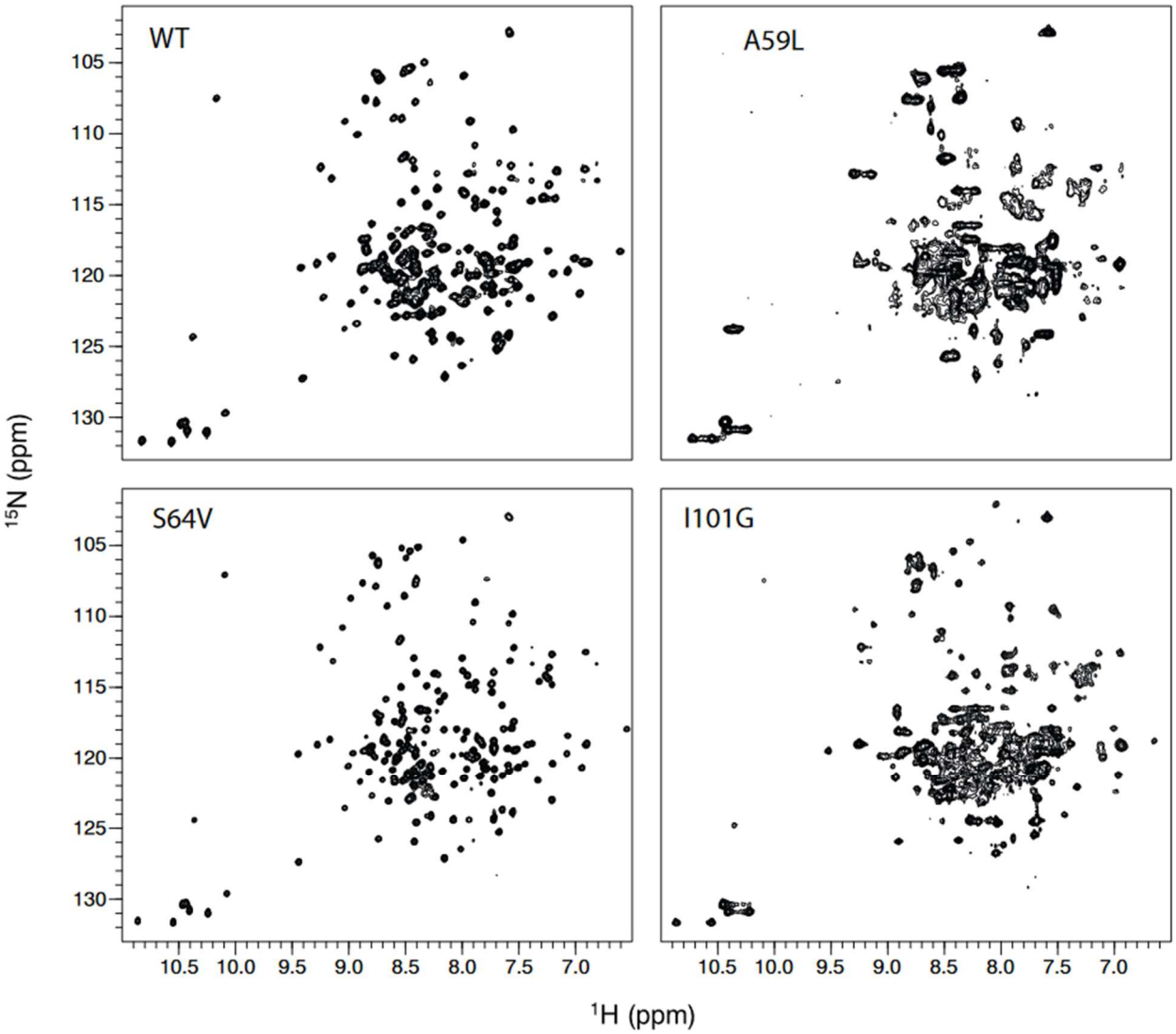

Figure 5 *TROSY-HSQC spectra for TPP^{+}-bound WT-EmrE and selected mutants.* The S64V spectrum has sharper peaks than the WT spectrum, suggesting that this mutation decreases the dynamics of EmrE. A59L and I101G both exhibit significant line broadening, indicative of increased dynamics. Interestingly, peak doubling is still evident in the I101G spectrum, indicating that this TM4 mutation alters EmrE's dynamics without disturbing dimerization. The spectrum of all seven mutants can be found in Fig. S4.

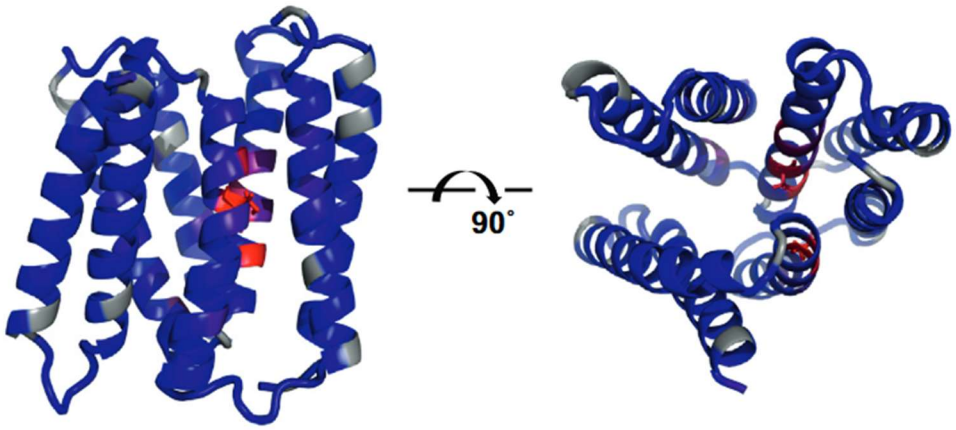

Figure 6 *S64V mutation perturbs TM3 kink region locally.* Chemical shift differences between WT- and S64V-EmrE were plotted onto structure. The largest perturbations are seen in the immediate vicinity of the TM3 kink. Nevertheless, several smaller changes are seen throughout the protein, suggesting several long-range allosteric effects of the S64V mutation.

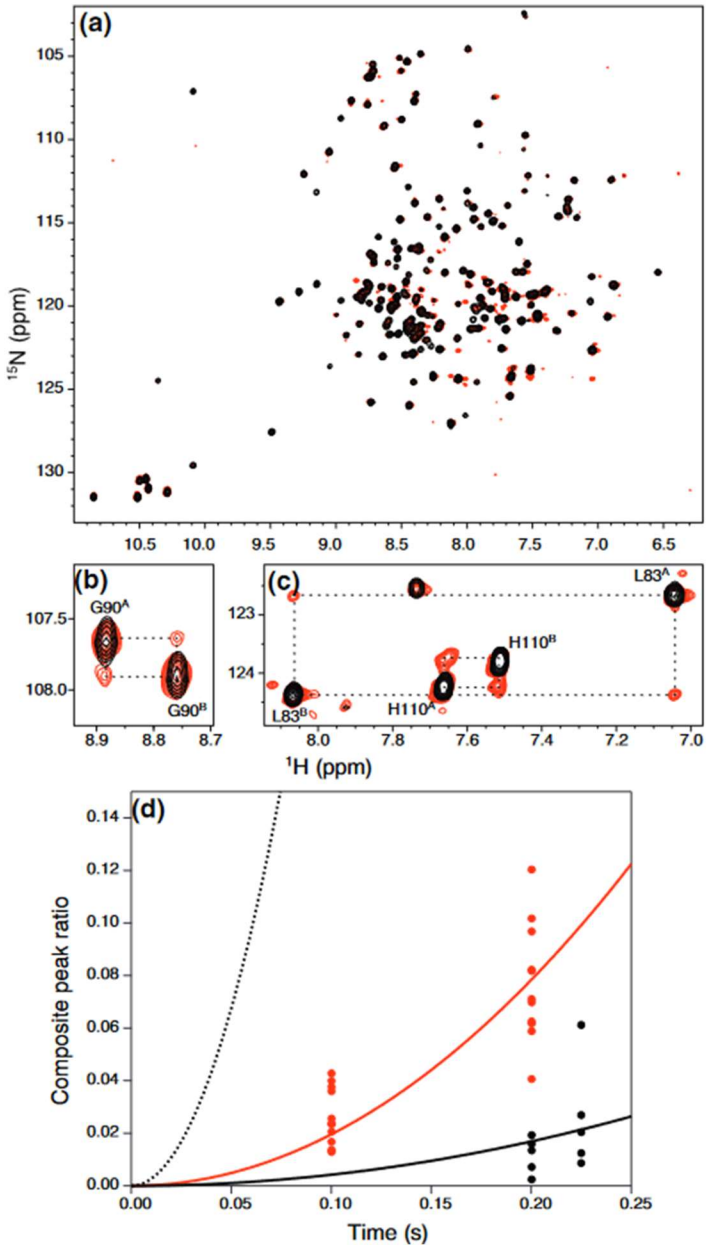

Figure 7 *S64V mutation slows down conformational interconversion rate of EmrE. A*, TROSY-HSQC (black) overlay with a ZZ-exchange plane with a mixing time of 200 ms (red) for TPP^{+}-bound S64V-EmrE. *B*, detail showing the pair of G90 peaks, and their cross-peaks in the ZZ-exchange spectrum. *B*, detail showing the pairs of L83 and H110 peaks, and their cross-peaks in the ZZ-exchange spectrum. *D*, composite peak ratio fitting as a function of mixing time for

TPP^+-bound S64V-EmrE in DMPC (solid black) or DLPC (solid red) bicelles. The dotted line indicates the fit of TPP^+-bound WT EmrE (data in Fig. S5).

Supporting Information

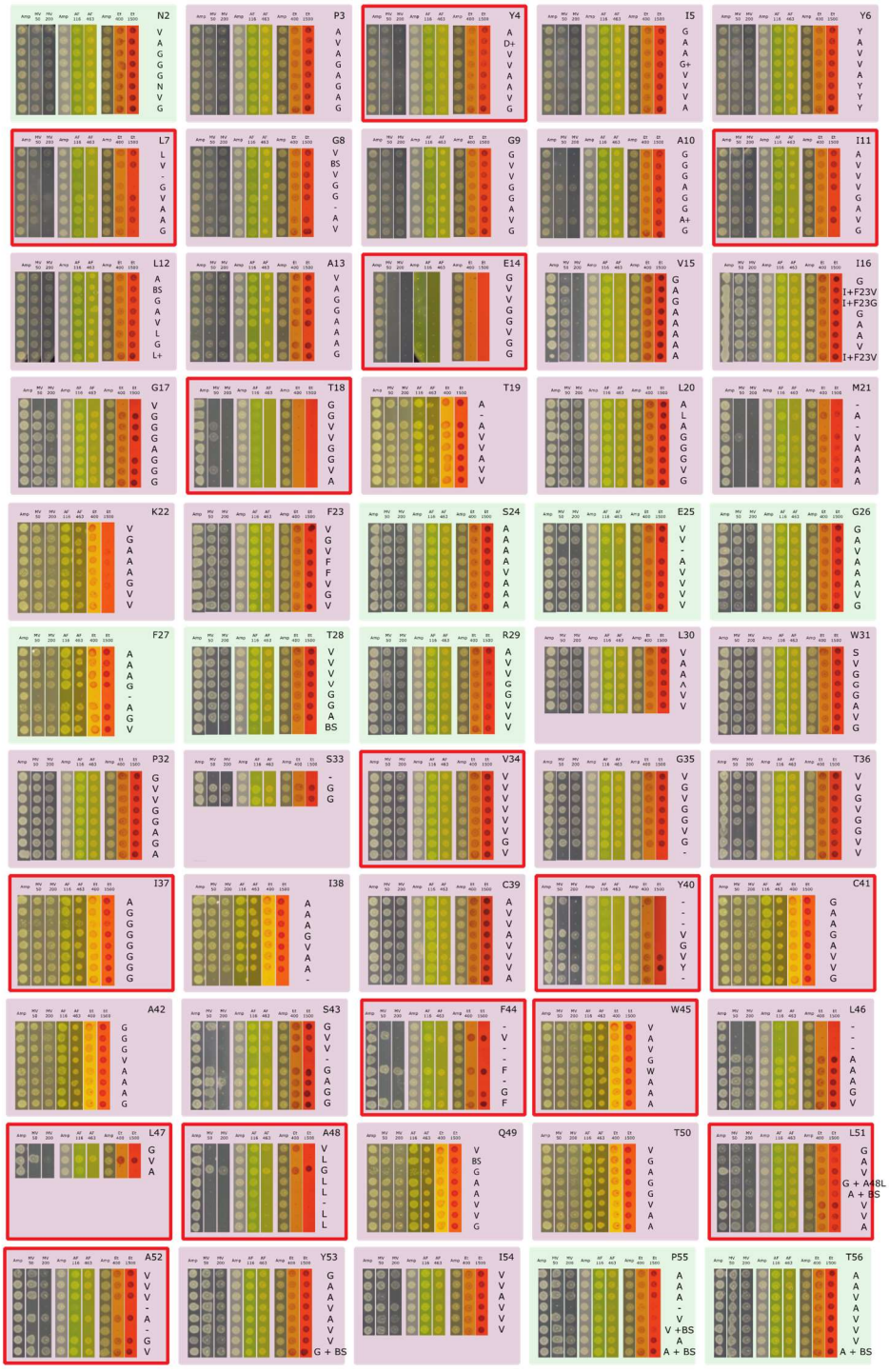

Figure S1 Resistance screen of substitutions at positions 2-56 Mutations were made with degenerate primers, and sequencing was performed in parallel with resistance screen

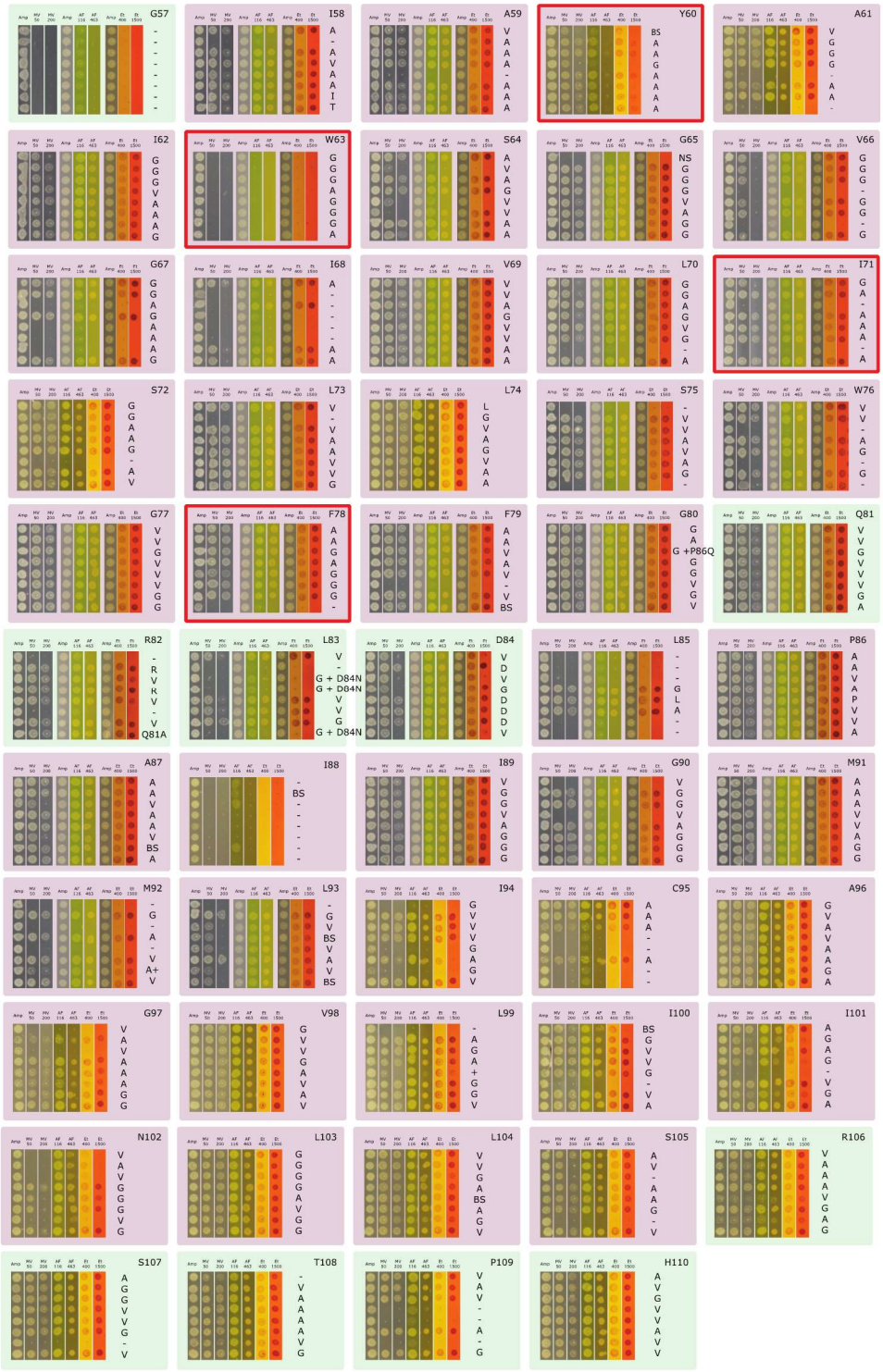

Figure S2 Resistance screen of substitutions at positions 57-110 Mutations were made with degenerate primers, and sequencing was performed in parallel with resistance screen

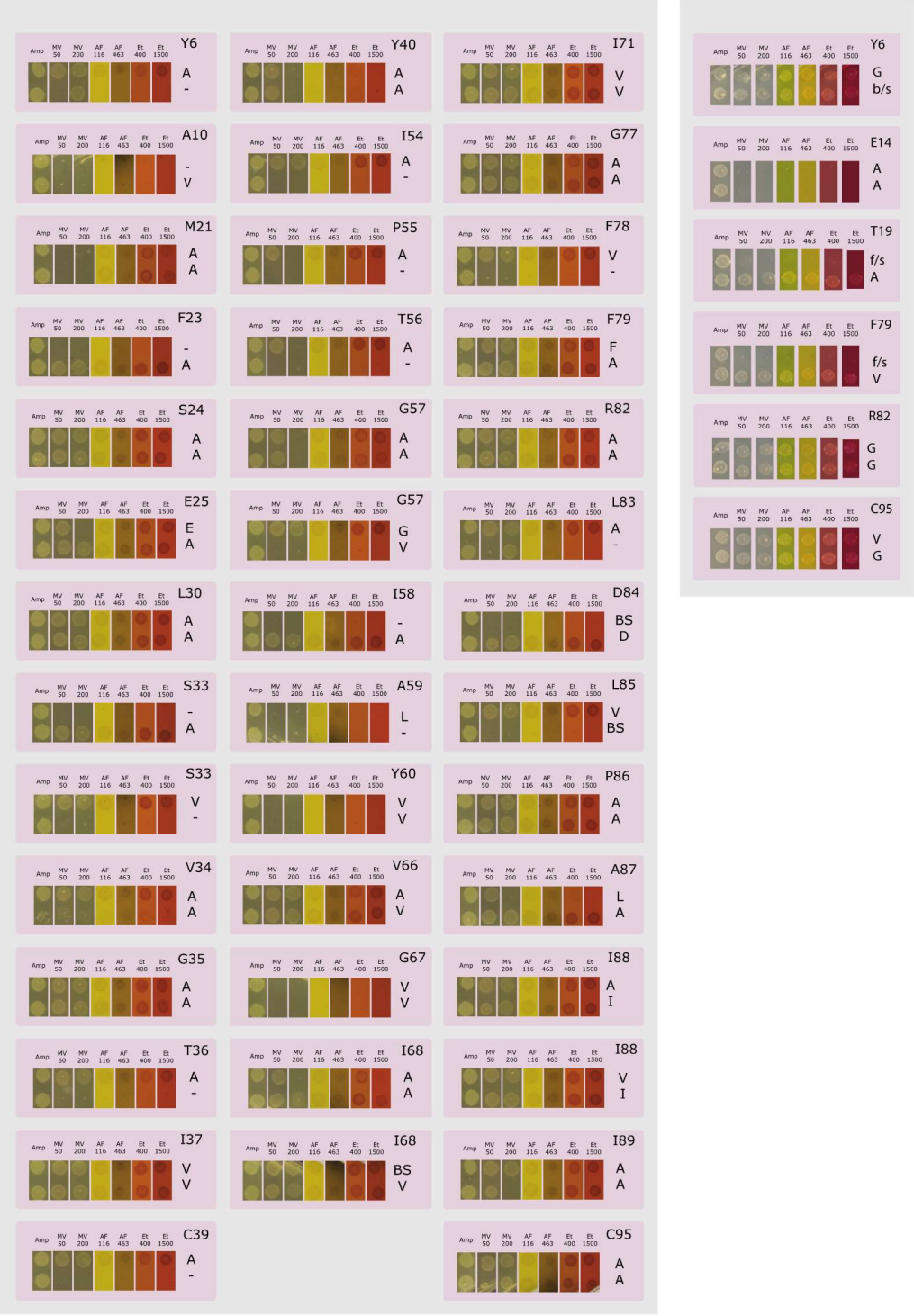

Figure S3 Resistance screen of remaining substitutions Mutations were made using QuikChange

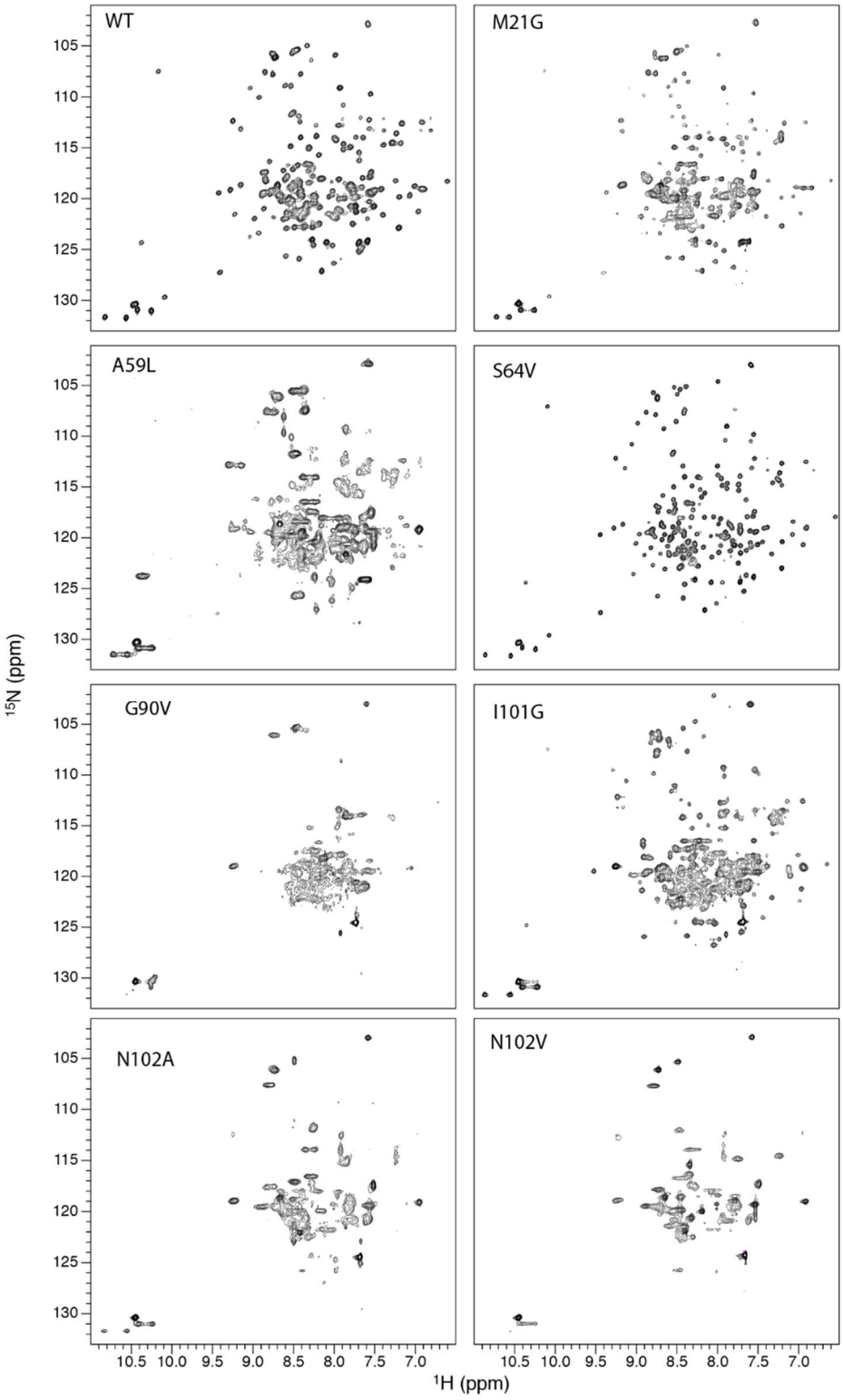

Figure S4 TROSY-HSQC spectra for TPP^{+}-bound WT-EmrE and mutants

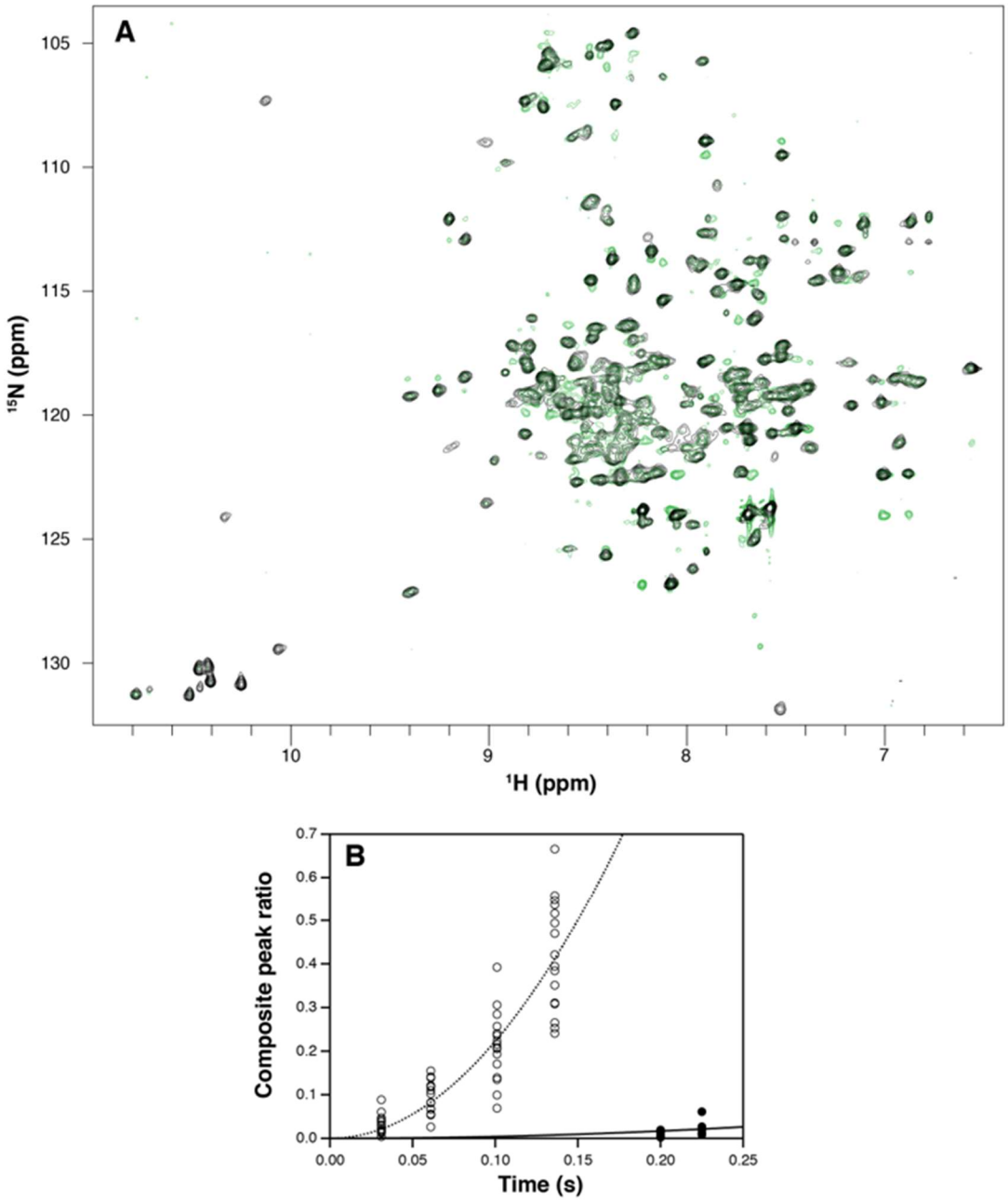

Figure S5. Alternating access rate of TPP$^+$-bound WT and S64V-EmrE in DMPC/DHPC isotropic bicelles. *A*, TROSY-HSQC (black) overlay with a ZZ-exchange plane with a mixing time of 90 ms (green) for TPP$^+$-bound WT EmrE in DMPC bicelles. *B*, composite peak ratio fitting as a function of mixing time for TPP$^+$-bound WT EmrE in DMPC bicelles (open circles, dotted line) and S64V-EmrE in DMPC bicelles (filled circles, solid line). The data is shown for multiple residues from across the protein, and the fitted line is a global fit.

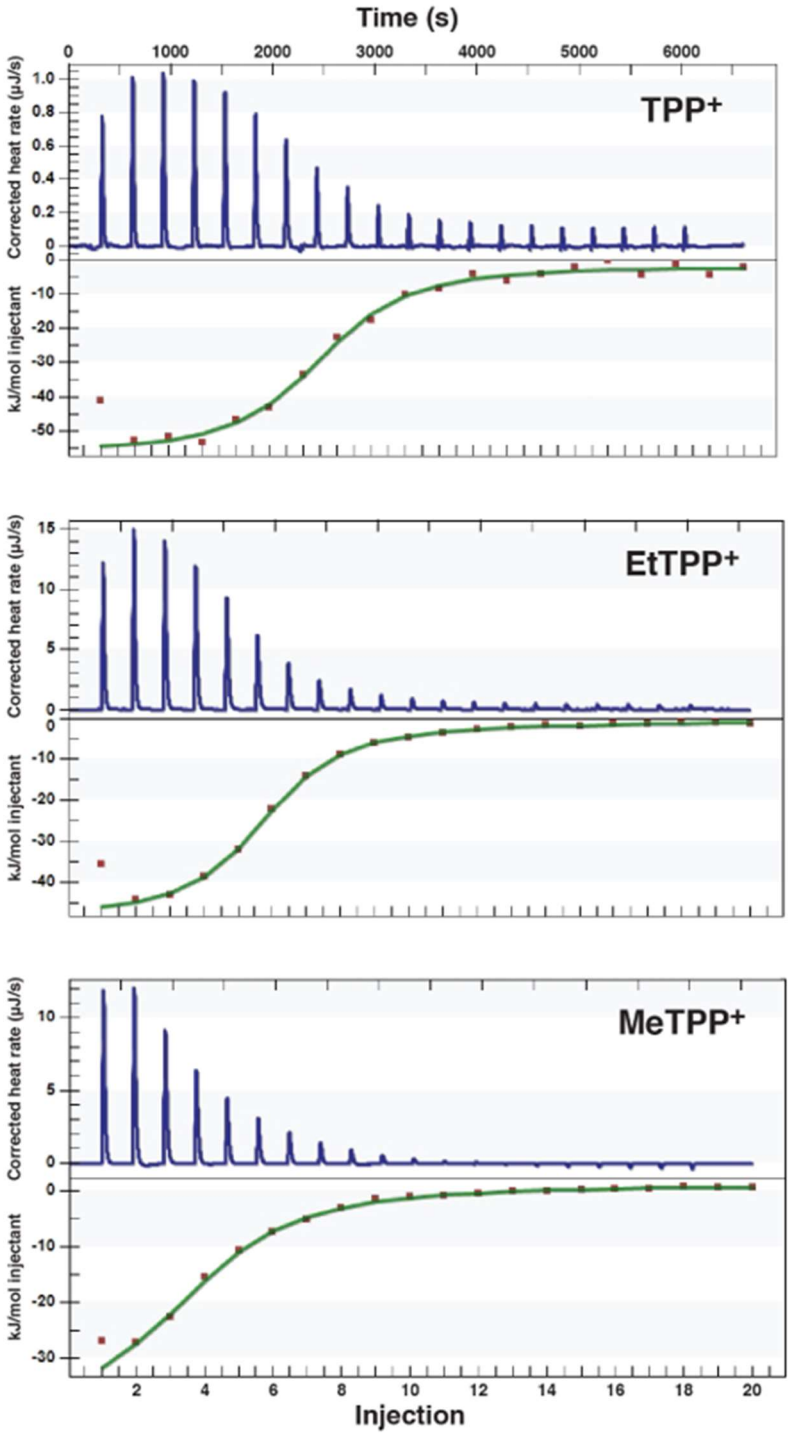

Figure S6 *S64V-EmrE binds a variety of ligands* Representative traces of isothermal titration calorimetry experiments for S64V binding to tetraphenylphosphonium (TPP^+), methyltriphenyl-phosphonium ($MeTPP^+$), and ethyltriphenyl-phosphonium ($EtTPP^+$).

Table S1. ITC Data for TPP^+ Binding to EmrE in Isotropic Bicelles*

	K_d (μM)	ΔH (kJ/mol)	n
S64V-EmrE	0.628	-56.0	0.465
	0.483	-51.6	0.535
	0.500	-50.9	0.526
	0.680	-50.9	0.503
	0.686	-53.0	0.469
WT-EmrE	0.589	-34.3	0.455
	0.325	-28.7	0.506
	0.395	-27.8	0.477
	0.569	-23.6	0.531

*q=0.33 DMPC/DHPC isotropic bicelles at pH 7

Table S2. ITC Data for Different Ligands Binding S64V-EmrE*

	K_d (μM)	ΔH (kJ/mol)	n
$EtTPP^+$	12.9	-46.8	0.474
	20.5	-62.7	0.568
$MeTPP^+$	56.2	-41.9	0.474
	46.3	-34.5	0.481

*q=0.33 DMPC/DHPC isotropic bicelles at pH 7

References

[1] H. Yerushalmi, M. Lebendiker, S. Schuldiner, EmrE, an Escherichia coli 12-kDa multidrug transporter, exchanges toxic cations and H+ and is soluble in organic solvents., J. Biol. Chem. 270 (1995) 6856–63. doi:10.1074/JBC.270.12.6856.

[2] H. Yerushalmi, S. Schuldiner, A common binding site for substrates and protons in EmrE, an ion-coupled multidrug transporter., FEBS Lett. 476 (2000) 93–7.

[3] Y.-J. Chen, O. Pornillos, S. Lieu, C. Ma, A.P. Chen, G. Chang, X-ray structure of EmrE supports dual topology model., Proc. Natl. Acad. Sci. U. S. A. 104 (2007) 18999–9004. doi:10.1073/pnas.0709387104.

[4] S. Fleishman, S. Harrington, A. Enosh, D. Halperin, C. Tate, N. Ben-Tal, Quasi-symmetry in the cryo-EM structure of EmrE provides the key to modeling its transmembrane domain., J. Mol. Biol. 364 (2006) 54–67. doi:10.1016/j.jmb.2006.08.072.

[5] E.A. Morrison, G.T. DeKoster, S. Dutta, R. Vafabakhsh, M.W. Clarkson, A. Bahl, D. Kern, T. Ha, K.A. Henzler-Wildman, Antiparallel EmrE exports drugs by exchanging between asymmetric structures., Nature. 481 (2012) 45–50. doi:10.1038/nature10703.

[6] S. Dutta, E.A. Morrison, K.A. Henzler-Wildman, Blocking dynamics of the SMR transporter EmrE impairs efflux activity., Biophys. J. 107 (2014) 613–20. doi:10.1016/j.bpj.2014.06.030.

[7] H. Yerushalmi, S.S. Mordoch, S. Schuldiner, A Single Carboxyl Mutant of the Multidrug Transporter EmrE Is Fully Functional, J. Biol. Chem. 276 (2001) 12744–12748. doi:10.1074/jbc.M010979200.

[8] M. Sharoni, S. Steiner-Mordoch, S. Schuldiner, Exploring the Binding Domain of EmrE, the Smallest Multidrug Transporter, J. Biol. Chem. 280 (2005) 32849–32855. doi:10.1074/jbc.M504910200.

[9] D. Rotem, S. Steiner-Mordoch, S. Schuldiner, Identification of tyrosine residues critical for the function of an ion-coupled multidrug transporter., J. Biol. Chem. 281 (2006) 18715–22. doi:10.1074/jbc.M602088200.

[10] Y. Elbaz, T. Salomon, S. Schuldiner, Identification of a Glycine Motif Required for Packing in EmrE, a Multidrug Transporter from *Escherichia coli*, J. Biol. Chem. 283 (2008) 12276–12283. doi:10.1074/jbc.M710338200.

[11] S.T. Amadi, H.A. Koteiche, S. Mishra, H.S. McHaourab, Structure, dynamics, and substrate-induced conformational changes of the multidrug transporter EmrE in liposomes., J. Biol. Chem. 285 (2010) 26710–8. doi:10.1074/jbc.M110.132621.

[12] S. Brill, O.S. Falk, S. Schuldiner, Transforming a drug/H+ antiporter into a polyamine importer by a single mutation., Proc. Natl. Acad. Sci. U. S. A. 109 (2012) 16894–9. doi:10.1073/pnas.1211831109.

[13] P. Lloris-Garcerá, J.S.G. Slusky, S. Seppälä, M. Prieß, L. V. Schäfer, G. Von Heijne, In vivo trp scanning of the small multidrug resistance protein EmrE confirms 3D structure models', J. Mol. Biol. (2013). doi:10.1016/j.jmb.2013.07.039.

[14] J. Wang, A. Rath, C.M. Deber, Functional response of the small multidrug resistance protein EmrE to mutations in transmembrane helix 2, FEBS Lett. 588 (2014) 3720–3725.

doi:10.1016/j.febslet.2014.08.018.

[15] S. Brill, O. Sade-Falk, Y. Elbaz-Alon, S. Schuldiner, Specificity Determinants in Small Multidrug Transporters, J. Mol. Biol. 427 (2015) 468–477. doi:10.1016/j.jmb.2014.11.015.

[16] N. Gutman, S. Steiner-Mordoch, S. Schuldiner, An Amino Acid Cluster around the Essential Glu-14 Is Part of the Substrate- and Proton-binding Domain of EmrE, a Multidrug Transporter from *Escherichia coli*, J. Biol. Chem. 278 (2003) 16082–16087. doi:10.1074/jbc.M213120200.

[17] M. Saleh, D.C. Bay, R.J. Turner, Few Conserved Amino Acids in the Small Multidrug Resistance Transporter EmrE Influence Drug Polyselectivity, Antimicrob. Agents Chemother. 62 (2018). doi:10.1128/AAC.00461-18.

[18] I. Ubarretxena-Belandia, J.M. Baldwin, S. Schuldiner, C.G. Tate, Three-dimensional structure of the bacterial multidrug transporter EmrE shows it is an asymmetric homodimer, EMBO J. 22 (2003) 6175–6181. doi:10.1093/emboj/cdg611.

[19] J. V Vermaas, S.B. Rempe, E. Tajkhorshid, Electrostatic lock in the transport cycle of the multidrug resistance transporter EmrE., Proc. Natl. Acad. Sci. U. S. A. (2018) 201722399. doi:10.1073/pnas.1722399115.

[20] V. Ovchinnikov, T.A. Stone, C.M. Deber, M. Karplus, Structure of the EmrE multidrug transporter and its use for inhibitor peptide design., Proc. Natl. Acad. Sci. U. S. A. 115 (2018) E7932–E7941. doi:10.1073/pnas.1802177115.

[21] A.E. Robinson, N.E. Thomas, E.A. Morrison, B.M. Balthazor, K.A. Henzler-Wildman, New free-exchange model of EmrE transport, Proc. Natl. Acad. Sci. (2017) 201708671. doi:10.1073/pnas.1708671114.

[22] E.A. Morrison, A.E. Robinson, Y. Liu, K.A. Henzler-Wildman, Asymmetric protonation of EmrE., J. Gen. Physiol. 146 (2015) 445–61. doi:10.1085/jgp.201511404.

[23] M.-K. Cho, A. Gayen, J.R. Banigan, M. Leninger, N.J. Traaseth, Intrinsic conformational plasticity of native EmrE provides a pathway for multidrug resistance., J. Am. Chem. Soc. 136 (2014) 8072–80. doi:10.1021/ja503145x.

[24] A. Gayen, M. Leninger, N.J. Traaseth, Protonation of a glutamate residue modulates the dynamics of the drug transporter EmrE, Nat. Chem. Biol. 12 (2016) 141–145. doi:10.1038/nchembio.1999.

[25] S.S. Mordoch, D. Granot, M. Lebendiker, S. Schuldiner, Scanning cysteine accessibility of EmrE, an H+-coupled multidrug transporter from Escherichia coli, reveals a hydrophobic pathway for solutes., J. Biol. Chem. 274 (1999) 19480–6.

[26] S. Ninio, Y. Elbaz, S. Schuldiner, The membrane topology of EmrE ^ a small multidrug transporter from Escherichia coli, (2004). doi:10.1016/S0014-5793(04)00240-6.

[27] M.B. Ulmschneider, M.S. Sansom, Amino acid distributions in integral membrane protein structures., Biochim. Biophys. Acta. 1512 (2001) 1–14.

[28] M. Saidijam, S. Azizpour, S.G. Patching, Comprehensive analysis of the numbers, lengths and amino acid compositions of transmembrane helices in prokaryotic, eukaryotic and viral integral membrane proteins of high-resolution structure, J. Biomol. Struct. Dyn. 36 (2018) 443–464. doi:10.1080/07391102.2017.1285725.

[29] D.J. Wright, C.G. Tate, Isolation and characterisation of transport-defective substrate-binding mutants of the tetracycline antiporter TetA(B), Biochim. Biophys. Acta - Biomembr. 1848 (2015) 2261–2270. doi:10.1016/j.bbamem.2015.06.026.

[30] V.M. Korkhov, C.G. Tate, Electron crystallography reveals plasticity within the drug binding site of the small multidrug transporter EmrE., J. Mol. Biol. 377 (2008) 1094–103. doi:10.1016/j.jmb.2008.01.056.

[31] A. Gayen, J.R. Banigan, N.J. Traaseth, Ligand-Induced Conformational Changes of the Multidrug Resistance Transporter EmrE Probed by Oriented Solid-State NMR Spectroscopy, Angew. Chemie Int. Ed. 52 (2013) 10321–10324. doi:10.1002/anie.201303091.

[32] E.A. Morrison, K.A. Henzler-Wildman, Transported substrate determines exchange rate in the multidrug resistance transporter EmrE., J. Biol. Chem. 289 (2014) 6825–36. doi:10.1074/jbc.M113.535328.

[33] Y. Adam, N. Tayer, D. Rotem, G. Schreiber, S. Schuldiner, The fast release of sticky protons: kinetics of substrate binding and proton release in a multidrug transporter., Proc. Natl. Acad. Sci. U. S. A. 104 (2007) 17989–94. doi:10.1073/pnas.0704425104.

[34] N.E. Thomas, C. Wu, E.A. Morrison, A.E. Robinson, J.P. Werner, K. Henzler-Wildman, The C terminus of the bacterial multidrug transporter EmrE couples drug binding to proton release, J. Biol. Chem. (2018) jbc.RA118.005430. doi:10.1074/jbc.RA118.005430.

[35] R. Dastvan, A.W. Fischer, S. Mishra, J. Meiler, H.S. Mchaourab, Protonation-dependent conformational dynamics of the multidrug transporter EmrE., Proc. Natl. Acad. Sci. U. S. A. 113 (2016). doi:10.1073/pnas.1520431113.

[36] M. V. LeVine, M.A. Cuendet, G. Khelashvili, H. Weinstein, Allosteric Mechanisms of Molecular Machines at the Membrane: Transport by Sodium-Coupled Symporters, Chem. Rev. 116 (2016) 6552–6587. doi:10.1021/acs.chemrev.5b00627.

[37] A. Gayen, M. Leninger, N.J. Traaseth, Protonation of a glutamate residue modulates the dynamics of the drug transporter EmrE, (2016) 1–6. doi:10.1038/nchembio.1999.

[38] B.E. Poulsen, A. Rath, C.M. Deber, The assembly motif of a bacterial small multidrug resistance protein., J. Biol. Chem. 284 (2009) 9870–5. doi:10.1074/jbc.M900182200.

[39] C.G. Tate, I. Ubarretxena-Belandia, J.M. Baldwin, Conformational changes in the multidrug transporter EmrE associated with substrate binding., J. Mol. Biol. 332 (2003) 229–42.

[40] H. Ashkenazy, E. Erez, E. Martz, T. Pupko, N. Ben-Tal, ConSurf 2010: calculating evolutionary conservation in sequence and structure of proteins and nucleic acids, Nucleic Acids Res. 38 (2010) W529–W533. doi:10.1093/nar/gkq399.

[41] H. Ashkenazy, S. Abadi, E. Martz, O. Chay, I. Mayrose, T. Pupko, N. Ben-Tal, ConSurf 2016: an improved methodology to estimate and visualize evolutionary conservation in macromolecules, Nucleic Acids Res. 44 (2016) W344–W350. doi:10.1093/nar/gkw408.

[42] G. Celniker, G. Nimrod, H. Ashkenazy, F. Glaser, E. Martz, I. Mayrose, T. Pupko, N. Ben-Tal, ConSurf: Using Evolutionary Data to Raise Testable Hypotheses about Protein Function, Isr. J. Chem. 53 (2013) 199–206. doi:10.1002/ijch.201200096.

[43] E.A. Morrison, K.A. Henzler-Wildman, Reconstitution of integral membrane proteins into

isotropic bicelles with improved sample stability and expanded lipid composition profile., Biochim. Biophys. Acta. 1818 (2012) 814–20. doi:10.1016/j.bbamem.2011.12.020.

[44] F. Delaglio, S. Grzesiek, G.W. Vuister, G. Zhu, J. Pfeifer, A. Bax, NMRPipe: a multidimensional spectral processing system based on UNIX pipes., J. Biomol. NMR. 6 (1995) 277–93.

[45] W.F. Vranken, W. Boucher, T.J. Stevens, R.H. Fogh, A. Pajon, M. Llinas, E.L. Ulrich, J.L. Markley, J. Ionides, E.D. Laue, The CCPN data model for NMR spectroscopy: Development of a software pipeline, Proteins Struct. Funct. Bioinforma. 59 (2005) 687–696. doi:10.1002/prot.20449.

[46] Y. Li, A.G. Palmer, TROSY-selected ZZ-exchange experiment for characterizing slow chemical exchange in large proteins., J. Biomol. NMR. 45 (2009) 357–60. doi:10.1007/s10858-009-9385-0.

[47] V.Z. Miloushev, F. Bahna, C. Ciatto, G. Ahlsen, B. Honig, L. Shapiro, A.G. Palmer, Dynamic properties of a type II cadherin adhesive domain: implications for the mechanism of strand-swapping of classical cadherins., Structure. 16 (2008) 1195–205. doi:10.1016/j.str.2008.05.009.

Appendix B

Drug-Binding Structure and Drug Dynamics of the Bacterial Transporter EmrE in Lipid Bilayers

Alexander A. Shcherbakov[1], Grant Hisao[2], Venkata S. Mandala[1], Nathan E. Thomas[2], Mohammad Soltani[3], E. A. Salter[3], James H. Davis Jr[3], Katherine A. Henzler-Wildman[2]*, and Mei Hong[1]*

[1]Department of Chemistry, Massachusetts Institute of Technology, 170 Albany Street, Cambridge, MA 02139

[2]Department of Biochemistry, University of Wisconsin at Madison, Madison, WI 53706

[3]Department of Chemistry, University of South Alabama, Mobile, AL 36688

* Co-corresponding authors:

Katherine A. Henzler-Wildman: henzlerwildm@wisc.edu

Mei Hong: meihong@mit.edu

Preface Here, we use the S64V dynamics mutant along with a fluorinated ligand to solve the structure of the EmrE binding pocket with ^{1}H-^{19}F REDOR NMR. Alexander and Venkata performed the NMR experiments and MD simulations, Grant prepared and purified the protein, I performed the SSME assays, and Mohammad and E. A. synthesized the ligand.

Abstract

The dimeric transporter, EmrE, effluxes polyaromatic cationic drugs in a proton-coupled manner to confer multidrug resistance in bacteria. Although the protein is known to adopt an antiparallel asymmetric topology, its high-resolution drug-bound structure is so far unknown, limiting our understanding of the molecular basis for promiscuous transport. Here we report a 2.1 Å structure of drug-bound EmrE in phospholipid bilayers, determined using ^{19}F and ^{1}H solid-state NMR and a fluorinated substrate tetra(4-fluorophenyl) phosphonium (F_4-TPP^+). The drug-binding site, constrained by 213 protein-substrate distances, is dominated by aromatic residues such as W63

and Y60, but is sufficiently spacious for the tetrahedral drug to reorient at physiological temperature. F_4-TPP^+ lies closer to the proton-binding residue E14 in subunit A than in subunit B, explaining the asymmetric protonation of the protein. The structure establishes a molecular basis for multidrug recognition by EmrE and for future design of substrate inhibitors to combat antibiotic resistance.

Introduction

Antibiotic resistance is a rising public health crisis. Active drug efflux by multidrug resistance (MDR) transporters is of particular concern because it allows bacteria to mount rapid defense against toxic compounds. Active efflux of harmful metabolites, antiseptics, antibiotics, and toxins that either naturally occur in the environment or are produced by competing bacteria or by host organisms allow bacteria to survive these challenging conditions. The broad substrate specificities of MDR transporters provide redundancy and can lead to unexpected outcomes with inhibition of individual transporters. To effectively curb this antibiotic resistance mechanism requires a molecular understanding of the mechanism of substrate recognition and specificity. Here we present atomic-level experimental distance restraints that define the location of a substrate in the transport pathway of EmrE. EmrE is a member of the Small Multidrug Resistance (SMR) transporter family in *E. coli. In vivo*, it has been implicated in pH and osmotic stress response [1], biofilm formation [2], and resistance to many quaternary cationic compounds, including the topical antiseptic acriflavine [3, 4]. Many SMR transporters have been implicated in resistance to clinically relevant drugs in pathogenic organisms such as *mycobacterium tuberculosis* [5, 6] and *Acinetobacter baumanii* [7]. Although EmrE has not been directly involved in resistance to clinical antibiotics by pathogenic *E. coli,* resistance is readily selected for *in vitro*, by mutation of only 1-3 residues [8]. Thus, structure determination of the EmrE-substrate complexes is relevant for elucidating the mechanism of action of the SMR family of transporters. In addition, EmrE is one of the smallest known proton-coupled transporters and thus serves as a model for understanding proton-coupled transport [9].

To date, the available EmrE structural models have modest resolution and lack details for understanding how multiple substrates are recognized by the protein. EmrE transports a wide array of polyaromatic cations *in vitro*, including ethidium, methyl viologen, acriflavine, dequalinium, and tetraphenylphosphonium [10-12]. Low-resolution cryo-electron microscopy (EM) maps and NMR chemical shift changes suggest that the protein's transmembrane (TM) helices undergo large-scale reorientation to accommodate these diverse substrates, but these data do not indicate how the substrates interact with specific residues in the protein [13, 14]. Biophysical and mechanistic studies have revealed unexpected complexity in the transport process [15-21], giving evidence that EmrE may function not only as a proton-coupled antiporter, pumping toxic polyaromatic cations out of *E. coli* (**Fig. 1A**), but also as a proton-coupled symporter or uncoupled uniporter [15, 17]. Either symport or uniport has the potential to confer *susceptibility* rather than resistance because the inward proton motive force and negative-inside membrane potential in bacteria would lead to concentrative *uptake* of toxic cations. To elucidate how EmrE interacts with and transports diverse substrates with divergent biological outcomes, high-resolution structural information of the substrate-EmrE complex is essential.

The functional unit of EmrE is an antiparallel, asymmetric homodimer. Cryo-EM, X-ray crystallography, and EPR studies have established the global topology and asymmetry of the dimer. Cryo-EM maps of EmrE in 2D crystals formed in lipid bilayers [22] gave the first indication that the dimeric protein had no obvious two-fold symmetry. This surprising result was later confirmed in moderate resolution (7.5 Å in-plane, 16 Å perpendicular to the membrane) 3D cryo-EM structures with and without the tight-binding substrate tetraphenylphosphonium (TPP^+) [23]. These 2D maps and 3D structures [13, 24] also indicated that the substrates bind at the homodimer interface, but asymmetrically between the two subunits. A subsequent 3.8 Å crystal structure of the backbone of TPP^+-bound EmrE [25] showed an antiparallel topology for the homodimer, which

was controversial because it was the first example of a dual topology integral membrane protein. However, subsequent NMR and single-molecule FRET experiments on wild-type EmrE in lipid bicelles demonstrated that the asymmetric antiparallel dimer was capable of undergoing alternating access (**Fig. 1A**) [26], and crosslinking that blocked this process also blocked transport *in vivo* [19]. Dual topology was further supported by mutagenesis [27-29], DEER EPR [30, 31], and studies of the EmrE homolog Gdx [32]. The recent discovery of a second family of antiparallel homodimeric bacterial membrane proteins, the Fluc channels [33], further established dual topology. Orientational data from solid-state NMR confirmed the asymmetry of the EmrE dimer [20, 21, 34], and showed that the glutamate residue (E14) [35], which binds both protons and substrates, differs between the two subunits. Despite the well-established dual topology and asymmetry of EmrE, no atomic structure of the substrate-binding site is known.

The lack of higher-resolution structural information for EmrE is not surprising, because the protein is small and lacks large soluble domains that are usually required to obtain high-quality crystals or particle alignment for cryo-EM studies. The protein is also flexible and dynamic, as evidenced by NMR [17-20, 26, 34], EPR [30, 31], and cryo-EM [13, 24] data. These dynamics are important for multidrug transport and recognition but pose challenges for structure determination. NMR is one of the best techniques for determining the structure of small and dynamic proteins, but the plastic nature of the substrate-free EmrE still leads to significant line broadening in the spectra. Even with substrate-bound protein, the rate of alternating access is faster than the cross-peak buildup rates in 2D correlation spectra.

Recently, we discovered a point mutant of EmrE, S64V-EmrE, which has the same affinity for TPP^+ and related substrates but slower internal dynamics and alternating-access rates [36]. The reduced dynamics allowed us to determine an experimental high-resolution structure of the substrate-bound protein using magic-angle-spinning (MAS) solid-state NMR spectroscopy. We

exploit a fluorinated TPP^+ derivative, tetra(4-fluorophenyl) phosphonium (F_4-TPP^+) (**Fig. 1A**), which resembles TPP^+ in the transport activity, and employ a multidimensional ^{19}F NMR technique [37] to measure a large number of protein-substrate distances. The resulting binding-site structure and the observed drug dynamics provide atomic insights into the mechanism of promiscuous substrate recognition and transport by this protein.

Results

Our structure determination of the EmrE-TPP^+ complex is enabled by three experimental advances: a recently developed long-range ^1H-^{19}F distance measurement NMR technique [37], synthesis of fluorinated TPP^+, and the slow-exchanging S64V-EmrE [36]. Because of the large magnetic dipole moments of ^1H and ^{19}F spins, ^1H-^{19}F distances up to ~2 nm can be measured using a two-dimensional rotational-echo-double-resonance (REDOR) NMR technique [37]. To utilize this technique, we synthesized F_4-TPP^+ (**Fig. S1A, B**), which has the same three-dimensional structure as TPP^+ but slightly larger cationic charge of the central phosphorous due to the electronegative fluorines (**Fig. S1C**). To assess whether fluorination affects the protein conformation, we measured the chemical shifts of S64V-EmrE bound to F_4-TPP^+ versus TPP^+ under identical conditions in DMPC/DHPC bicelles (q=0.33, pH 5.8, 45°C) using solution NMR. The amide chemical shift difference between proteins with bound F_4-TPP^+ versus TPP^+ (**Fig. 1B**) is small, and is less than the chemical shift difference between the two subunits of the dimer (**Fig. 1C**). The chemical shift differences between F_4-TPP^+- and TPP^+-bound protein mainly localize to residues in TM1–3 helices that are known from mutagenesis to interact with the substrate [31, 38-42]. 2D ZZ-exchange spectrum of F_4-TPP^+ bound protein shows no conformational dynamics within 200 ms (**Fig. S2**), indicating that alternating access is slower for S64V-EmrE bound to F_4-TPP^+ than to TPP^+ [36]. The slower alternating-access rate with bound F_4-TPP^+ facilitate the measurement of protein-substrate distances. But given the lack of observable alternating access, we first verified that F_4-TPP^+ is indeed transported by EmrE.

F_4-TPP$^+$ is an antiported substrate of EmrE

We used solid-supported membrane electrophysiology to monitor liposomal transport of F_4-TPP$^+$ by wild-type (WT) EmrE (**Fig. 1D, Fig. S3**). The assay starts with equal concentrations of both proton and substrate on either side of the liposome. Changing the external buffer creates an inward-facing pH gradient triggering transport, and net charge movement is recorded by the sensor. Combining this pH gradient with varying F_4-TPP$^+$ gradients allows for investigation of the proton/substrate coupling behavior of EmrE. In the absence of a drug gradient, protons are transported down their gradient into the liposome, creating a positive signal for transported charge. This signal is increased by an outward-facing F_4-TPP$^+$ gradient (favoring antiport). However, a large inward-facing F_4-TPP$^+$ gradient reverses the transport direction, driving protons against their concentration gradient out of the liposomes. This reversal of current is indicative of coupled transport and demonstrates that F_4-TPP$^+$ is antiported by EmrE. Although the timescale of transport differs between transporters, similar reversal of current is observed for proton/guanidinium antiport by the EmrE homolog Gdx.

The substrate is dynamic in the binding pocket of membrane-bound EmrE

The four fluorines of F_4-TPP$^+$ provide a direct probe of substrate dynamics and interaction with the protein. The ^{19}F NMR spectra of F_4-TPP$^+$ bound to S64V-EmrE in DMPC bilayers show strongly temperature-dependent spinning sideband intensities and linewidths (**Fig. 2A**). At a sample temperature (T_{eff}) of 245 K, the ^{19}F linewidth is about 5.7 ppm, and the sideband intensity envelope fits to a rigid-limit chemical shift anisotropy (CSA) of 60.1 ppm and an asymmetry parameter of 0.8, indicating that the drug is immobilized.[43] At 285 K, most sideband intensities remain, but each peak in the sideband manifold resolves into multiple components, indicating that the fluorines experience a heterogeneous environment. At 308 K, in the liquid-crystalline phase of the DMPC bilayer, the ^{19}F spectrum collapses into a narrow isotropic peak at -106 ppm,

indicating that the ligand undergoes near-isotropic motion at rates faster than the ^{19}F CSA of ~34 kHz. These substrate dynamics coincide with the onset of the protein dynamics, as seen in the ^{13}C NMR spectra, which exhibit lower intensities above the membrane phase transition temperature (**Fig. 2C**).

To further understand the heterogeneous environment of F_4-TPP^+, we measured the ^{19}F direct-polarization (DP) spectrum under 35 kHz MAS to detect only the isotropic peaks. The spectral lineshape is complex, and can be deconvoluted into five components (**Fig. 2B)**. A small sharp peak (0.2 ppm linewidth) at -105.7 ppm can be attributed to free F_4-TPP^+ in solution. Three broad peaks with linewidths of 1.9 – 4.2 ppm are observed from -102 to -108 ppm. Most interestingly, we observed a sharp peak at -110 ppm with a linewidth of 1.0 ppm. These four components vary in intensity from 6% to 50% of the full spectral intensity, thus cannot be simply assigned to each of four fluorines. When the ^{19}F intensity was cross-polarized (CP) from protein carbons [44, 45], the -103 ppm, -105 ppm, and -110 ppm peaks are preferentially enhanced, indicating that these resonances arise from fluorines that are in close contact with protein carbons. The -110 ppm signal exhibits the largest intensity increase, indicating that this peak results from a fluorine that is both structurally ordered and the closest to the protein. In contrast, the -106 ppm peak is preferentially suppressed in the ^{13}C-^{19}F CP spectrum, indicating that this fluorine is the furthest from the protein. We attribute this peak partly to lipid-bound F_4-TPP^+, consistent with previously reported ^{31}P and ^{13}C spectra of TPP^+ [46], which also detected nonspecific lipid-bound ligand in addition to EmrE-bound ligand.

The partially resolved ^{19}F isotropic chemical shifts allow us to probe millisecond-timescale ligand dynamics using a 2D ^{19}F-^{19}F exchange experiment (**Fig. 2D**). With a fast MAS frequency of 38 kHz and a short mixing time of 10 ms, we measured motional exchange, with minimal spin-diffusion effects [47]. No cross peaks were observed at 265 K, consistent with the absence of ^{19}F-

^{19}F spin diffusion under this condition. In contrast, at 285 K, cross peaks between -110 ppm and other peaks are observed, indicating that F_4-TPP$^+$ reorients on the 10 ms timescale. Cross-peak intensity buildup (**Fig. 2E**) indicates a time constant of 16±2 ms for the exchange, indicating that F_4-TPP$^+$ reorients, possibly by tetrahedral jumps, in the binding pocket with a rate of ~50 s^{-1} at ambient temperature.

Conformation of the EmrE dimer in DMPC bilayers

To investigate the conformation of EmrE in lipid bilayers and to obtain the amide ^{1}H chemical shifts that are required for measuring protein-substrate distances, we recorded four ^{1}H-detected 3D correlation spectra of CDN-labeled EmrE that was back-exchanged in protonated buffer. The hCANH and hCO(CA)NH spectra correlate intra-residue chemical shifts whereas the hCA(CO)NH and hCONH spectra correlate inter-residue chemical shifts [48] (**Fig. S4**). At 55 kHz MAS, the DMPC-bound protein exhibits narrow linewidths of 0.2 ppm for ^{1}H, 0.8 ppm for ^{15}N, and 0.5 ppm for ^{13}C, indicating high conformational homogeneity. **Fig. 3** and **Fig. S5A** show representative 3D strips to illustrate resonance assignment. Overall, monomer A peaks display higher intensities than monomer B (**Fig. S6B**), indicating that monomer B of the dimer is more dynamic, except for residues C-terminal to TM3, where the trend is reversed [17]. Additional sidechain ^{13}C chemical shifts were obtained from a 3D NCACX spectrum (**Fig. S5B**). Altogether, we assigned the H^N, ^{15}N, and $^{13}C\alpha$ and ^{13}CO chemical shifts of 72 residues in monomer A and 54 residues in monomer B (**Table S1**). The Cα and CO chemical shifts confirm that the protein is predominantly □-helical [49], with inter-helical loops at residues 25-35, 50-55, and 75-85, in good agreement with the secondary structure determined in solution (**Fig. S7**) and with low-resolution cryo-EM and crystal structures [8, 25]. The two subunits exhibit small average chemical shift differences: 0.47 ppm for Cα and CO, 0.30 ppm for $^1H^N$, and 1.0 ppm for ^{15}N. Among the four TM helices, TM3 displays the largest conformational asymmetry: for example, V64 CO, I68 Cα, and I71 Cα exhibit ^{13}C chemical

shift differences of 2.9 ppm, 5.4 ppm, and 3.3 ppm, respectively (**Fig. S6A**). The chemical shifts show excellent agreement between bilayers and bicelles (**Fig. S8**), with average ^{13}C, H^N and ^{15}N chemical shift differences of 0.23 ppm, 0.29 ppm, and 0.78 ppm, respectively, indicating that the substrate-bound EmrE conformation is similar between these two environments.

^{1}H–^{19}F distances restrain the structure of the substrate-binding pocket

With the ^{15}N and ^{1}H chemical shifts assigned, we turned to the ^{1}H-^{19}F REDOR experiment [37] to measure protein-substrate distances. We detected REDOR dephasing in 2D hNH spectra, which exhibit both backbone H^N signals and the sidechain indole Hε signals of the important residue W63 (**Fig. 4A**). Two REDOR spectra were measured at each mixing time, one without ^{19}F pulses (S_0) and one with (S) to induce distance-dependent dipolar dephasing. The difference spectrum selectively exhibits the signals of H^N sites that are in close proximity to the substrate fluorines. Thus, the difference spectra not only encode distance information but also have enhanced site resolution, allowing the assignment of substrate-proximal H^N sites based on the 3D experiments. At a mixing time of 1.68 ms, the ΔS spectrum already exhibits signals from aromatic residues such as W63 and Y60 in TM3 and from aliphatic residues such as E14 and S43A. Increasing the REDOR mixing time yielded more ΔS peaks, indicating the detection of additional residues that are further away from the substrate. The largest number of ΔS signals is observed for TM3 residues, spanning residues A59 to S72 (**Fig. 4C**). Difference intensities are also observed for TM1 residues A13 to T18 in subunit A and TM2 residues such as Y40 and S43. In comparison, no difference intensities are detected C-terminal to the TM3 helix, indicating that the substrate-binding pocket is comprised solely of TM1-3 helices.

We quantified ^{1}H–^{19}F distances by fitting the mixing-time dependent S/S_0 ratios (**Fig. 4B**): faster decays indicate shorter H^N-F distances. Residues such as W63A show rapid dipolar oscillations,

indicating that they lie immediately adjacent to the substrate. The S/S_0 ratios decay to about 0, indicating that all binding sites are saturated with TPP^+. In comparison, some residues such as R82A show minimal decay, indicating that they are far from the fluorines. Best-fit distances were obtained by minimizing the root-mean-square deviation (RMSD) between the measured and simulated S/S_0 ratios (**Fig. S9**). Many TM1-3 residues show significant dipolar dephasing that is fit to distances of less than 10 Å (**Fig. 4C, D**), whereas residues in TM4, the TM1-TM2 loop and the TM3-TM4 loop display minimal dephasing and are more than ~10 Å from the fluorines. These distances constitute the basis for constraining the structure of the protein-substrate complex.

Structure of the EmrE-TPP^+ complex in lipid bilayers: an aromatic-rich binding pocket

We combined 213 protein-substrate H-F distances with 186 pairs of chemical-shift derived (ϕ, ψ) torsion angles and 95 X_1 torsion angles (**Table 1**) to calculate the structure of the EmrE-TPP^+ complex. Because the solution-state chemical shifts are very similar to the solid-state values and are more extensively assigned, we used the solution NMR chemical shifts in the final structure calculation. The use of solid-state NMR chemical shifts did not cause any qualitative difference. The structure calculation consisted of two stages: docking of F_4-TPP^+ into previous molecular dynamics (MD) simulated apo structural models in DMSO, followed by all-atom MD refinement of the docked protein-ligand complexes in explicit DMPC bilayers. Both stages used the measured distance restraints and torsion angles, but the ^1H–^{19}F distances were input with four-fold ambiguity at the docking step (**Table S2**) while structurally assigned at the second step (**Table S3**). Two MD apo structural models were used for docking [50, 51]. The substrate clustered to a single position in one model [50] (**Fig. S10A**) but diverged to four positions in the second model [51] (**Fig. S10B**), only one of which lies at the dimer interface. Thus we removed the outcome of the second model from further analysis. In the uniquely docked model, TPP^+ is surrounded by TM1–3 helices of subunit A and TM3 of subunit B. Among the 20 lowest-energy docked structures, the phosphorus and its directly bonded carbons in TPP^+ have an RMSD of 2.3±0.6 Å, while the protein shows an

all-atom RMSD of 0.5±0.1 Å. Importantly, docking allowed the assignment of the specific phenylene Hζ atoms, replaced by fluorine here, that dephase each protein H^N (**Table S3**). With the H^N-F pairs thus assigned and the overall ligand position constrained, we then refined the protein structure in DMPC bilayers (**Fig. S10C**), again restrained by ^1H–^{19}F distances and (ϕ, ψ, X_1) torsion angles.

We used two of the four lowest-energy HADDOCK models to refine the structure of the complex in two independent MD runs, in order to assess the consistency of structure calculation. The two ensembles (**Fig S10D**) are each well clustered but show modest differences from each other. The protein heavy-atom RMSD was 1.43±0.12 Å for the run 1 ensemble and 1.52±0.21 Å for the run 2 ensemble (**Fig. S10D, F**), and increases to 2.12 Å between the two lowest-violation structures from each ensemble. The structural differences between the two runs are manifested more in subunit B than subunit A, with TM1B and TM2B helices becoming less tilted in run 2 than in run 1. The position of the C-terminal ends of TM3A and TM3B also deviate between the two runs (**Fig. S10D**). These differences are consistent with the aforementioned experimental data that the B monomer is more dynamic than the A monomer, and the chemical shifts are most asymmetric in the C-terminal end of TM3. TPP^+ has the same orientation between the two ensembles (**Fig. S10F)** but its center is shifted slightly closer to subunit A in run 2 than run 1. The RMSD between the two runs for the TPP^+ center, defined as the phosphorous atom and its four directly bonded carbons, is 2.56 Å. Despite these differences, the two ensembles are sufficiently similar (**Fig. S10G**) that they can be combined into a single structural ensemble. We chose ten conformers from the two runs with the lowest violations with the experimental distance restraints to constitute the final NMR structure ensemble (**Fig. S10D,H**).

The NMR structural ensemble of the EmrE F_4-TPP^+ complex shows TM1-3 residues to interact with the substrate while the two TM4 helices associate to stabilize the dimer (**Fig. 5A, Fig. S10D, H**). This architecture is in good agreement with low-resolution cryo-EM and X-ray data [25, 52]. In each monomer, E14 in TM1 and Y40 in TM2 approach the substrate from one side, while Y60 and W63 of TM3 approach the substrate from another side at an angle of ~100˚ from the E14/Y40 pair (**Fig. 5B**). Among these four residues, Y40 is the furthest away from the substrate (**Table 2**). The relative proximities of these aromatic and polar residues to F_4-TPP^+ are in good agreement with biochemical data that W63 and Y60 are essential for substrate binding and transport, whereas Y40 regulates substrate specificity [9]. Between the A and B subunits, the two E14 sidechains are approximately colinear and lie on two opposite sides of TPP^+. However, E14's displacement relative to the substrate is asymmetric. The distances from the phosphorous to the two E14 C□ atoms, averaged over the structural ensemble, are 5.4 Å to monomer A and 7.1 Å to monomer B. The four phenylene Hζ corners of the substrate are also asymmetrically positioned relative to E14: the nearest Hζ lies 4.8 Å away from E14A Cδ while the nearest Hζ lies 6.0 Å from E14B Cδ. Taken together, these structural features suggest that monomer A provides more stabilization to the substrate. This is consistent with the weaker intensities of monomer B peaks than monomer A, suggesting that monomer B is more dynamic. Importantly, one of the four phenylene Hζ atoms, designated as F3 (**Fig. 5B**), is held by a cage of four functional residues: W63A, W63B, Y60A and E14B, with distances of 4.7 Å, 4.8 Å, 5.2 Å, and 6.1 Å to W63A Nε, W63B Nε, Y60A Oζ, and E14B Cδ□□respectively (**Table 2**). Thus, the F3-bearing phenylene ring is well constrained by multiple π-π, CH-π, and electrostatic interactions, making this fluorine most likely responsible for the narrow -110 ppm peak in the ^{19}F NMR spectrum (**Fig. 2B**). This binding-site geometry indicates that multivalent aromatic and polar interactions play the dominant role for TPP^+ binding by EmrE. The aromatic-rich binding pocket is further supported by ^{13}C-^{19}F REDOR

spectra (**Fig. 4E**), which show difference intensities at the ^{13}C chemical shifts of binding-site residues such as W63, Y60, F44, E14, G65, G67, S43, and V64.

This NMR structure of the EmrE-TPP^+ complex shows TPP^+ at a similar location as the MD model (**Fig. 5C, Fig. S10I**), but differs significantly in terms of the substrate orientation and the positions and orientations of the protein residues. In the NMR structure, the two W63 indoles are roughly perpendicular to each other, with the W63A indole plane aligned with the nearest TPP^+ phenylene plane. In comparison, the MD model puts the two W63 indole rings roughly parallel to each other, and both are perpendicular to the closest TPP^+ ring. In the MD model, the two E14 residues approach the substrate at different angles and displacement compared to those of the NMR structure. Finally, the shape of the binding pocket is more elongated in the experimental structure than in the MD model: the inter-protomer distances between the two E14 Cδ carbons and between the two W63 Nε atoms are ~11 Å and ~7 Å in the NMR structure, whereas the corresponding distances in the MD model are 10.5 Å and 9.4 Å. The residues in the NMR structure model are more loosely packed compared to the MD model. For example, the E14B-Y60A-W63B triad show distances of 3.9–5.5 Å among the C_α, Oζ, and Nε atoms in the NMR structure (**Fig. 5B**), while the corresponding distances in the MD structural model are much shorter, to 3.2 – 3.8 Å, suggesting hydrogen-bonding. On the other side of TPP^+, the equivalent triad of E14A-Y60B-W63A is even looser, with inter-atomic distances of 6-11 Å.

Discussion

The results shown here provide the first precise experimental definition of the geometry of the substrate-binding pocket of EmrE. The large number of protein-substrate ^1H-^{19}F distances (**Fig. S10E**) [37], measured in bilayer-bound EmrE, indicates the relative proximities of residues at the binding pocket. The inequivalent substrate position between the two subunits [48] gives insight into

the asymmetric protonation of the two E14 residues [17, 18]. In our structure, E14A Cδ is closer to the TPP^+ phosphorus and the nearest fluorine than E14B Cδ (**Table 2**), suggesting that E14A is negatively charged to have favorable electrostatic attraction with the positively charged F_4-TPP^+. E14A is also further away from W63A and Y60B than E14B is from W63B and Y60A (**Fig. 5B**). These structural differences are consistent with the distinct chemical shifts of E14A and E14B, with E14A exhibiting larger Cα, Cβ and Cγ chemical shifts than E14B (**Table S1**). A previous NMR study of E14-labeled EmrE bound to ethidium bromide reported similar aliphatic chemical shift differences as seen here [35], but in addition measured the carboxyl chemical shifts at a low temperature of 200 K. E14A and E14B were found to have Cδ chemical shifts of 180.9 ppm and 178.3 ppm, respectively. Since protonated carboxyl groups have smaller isotropic chemical shifts on average than deprotonated ones [53], this Cδ chemical shift difference suggests that E14B is protonated while E14A is deprotonated in the presence of ethidium. Therefore, this result is consistent with our assignment of E14A to be negatively charged and in closer proximity to the positively charged TPP^+. In addition, solution NMR pH and TPP^+ titrations with bicelle-bound EmrE also suggested asymmetric binding of TPP^+: only E14B remained titratable, with a pK_a of 6.8, implying that TPP^+ is closer to E14A, preventing its protonation [17]. These data, taken together, indicate that TPP^+, as well as other EmrE ligands, bind the dimer asymmetrically, closer to subunit A than to subunit B,

The present data also report the first direct observation of substrate dynamics in the EmrE binding pocket, coupled with protein dynamics. These dynamics are manifested by the ^{19}F NMR spectra of the substrate at physiological temperature and the temperature-dependent ^{13}C spectra of the protein (**Fig. 2**). It is also hinted at by the TM2 and TM3 helix orientational changes between the two MD runs (**Fig. S10**). How does the structure of the complex, solved at low temperature, explain these substrate and protein motions, and how do these motions relate to promiscuous

substrate binding and transport? The present structure shows that the binding pocket is established by many aromatic and polar residues, which provide multivalent interactions with the substrate that are not easily perturbed by a single mutation at residue 64. At the same time, the binding pocket is spacious: the inter-residue distances are in general much longer than the hydrogen-bond length, and the protein-drug distances are also sufficiently large to allow drug reorientation. This spacious and multivalent binding pocket is fully consistent with the similar binding affinities of TPP^+ for the mutant and WT EmrE, and is also consistent with the ability of the protein to bind multiple drugs indiscriminately. However, binding is not equal to transport. Efficient translocation of the drug requires coordinated motion of the protein between the outward-facing and inward-facing conformations. Although S64V-EmrE binds substrates with nearly identical, sub-micromolar, affinity as wild-type EmrE, it has a slower transport rate and an 8-fold slower alternating-access rate than the WT protein [36]. This slower transport rate implies a reduced ability of the mutant to undergo coordinated conformational motions. We observed less helical chemical shifts for V64 in monomer B than in monomer A, suggesting helix disorder in TM3 of monomer B [13, 52]. The fact that this TM3 disorder is observed in the more dynamic monomer (**Fig. S6**) suggests that the local motion of monomer B might regulate the ability of the dimer to undergo conformational interconversion, which is required for drug efflux. Direct comparison of the mutant with the WT structure and dynamics will be necessary in the future to determine whether increased dynamics of monomer B facilitates or impedes the alternating-access motion.

Between different members of the tetrahedral ligands, higher binding affinity is correlated with slower transport [14]. When the same ligand binds different mutants, then the anti-correlation between binding affinity and protein dynamics decreases [36]. These data suggest that the ligand geometry and protein structure both affect the binding-site structure and alternating-access rate, but in a partially independent manner. Future studies to determine how the EmrE binding-site

structure changes with the ligand, pH, and protein mutation, will be informative to define the conformational landscape of this promiscuous SMR transporter.

The contribution of MDR transporters to bacterial virulence and antibiotic resistance has led to significant interest in developing efflux pump inhibitors. The goal is to block transport activity in order to reduce bacterial virulence, restore antibiotic efficacy, and provide tools to understand the complex toxin efflux network in bacteria [54-59]. These inhibitors often resemble substrates and compete for substrate binding or prevent the protein from undergoing the conformational changes that are required for transport [60, 61]. The structure presented here provides an initial guide for structure-based design of EmrE inhibitors to probe EmrE function within the *E. coli* MDR efflux network *in vivo.* As a model system, EmrE has provided rich insight into the complexity of proton-coupled transport. Biophysical studies have revealed its ability to perform different types of coupled transport that would lead to either resistance or susceptibility *in vivo* [15, 17]. Mutagenesis of EmrE and other SMR homologs demonstrate the ease with which SMR transporters may be converted between these two phenotypes and confirm that a single transporter can confer resistance to some substrates and susceptibility to others [8, 62]. Application of the approach used here to additional substrates will provide a foundation for understanding the multidrug poly-specificity of EmrE and how different substrates can interact with EmrE to trigger opposing biological outcomes of resistance or susceptibility.

Acknowledgements

This work is supported by NIH grants GM095839 to K.A. H-W, GM066976 to M.H., and the MIT School of Science Sloan Fund to A.A.S. and M.H. The study made use of NMR spectrometers at the National Magnetic Resonance Facility at Madison, supported by NIH grant P41 GM103399 and P41 RR002301; the Center for Magnetic Resonance, supported by P41 GM132079; and the NMRbox, supported by P41 GM111135. Equipment was purchased with funds from the University

of Wisconsin-Madison, NIH (S10RR02781, S10RR08438, S10RR023438, S10RR025062, S10RR029220), the NSF (DMB-8415048, OIA-9977486, BIR-9214394), and the USDA. This study also made use of the Alabama Supercomputing Center. The authors thank Jochem Struppe for help in setting up two of the H^N-detected 3D experiments, Albert Donkoh for assistance with probe repairs, Peyton Spreacker for S64V-EmrE sample preparation, and Marco Tonelli for assistance with acquisition of solution NMR assignment experiments.

Author contributions

A.A.S. conducted all solid-state NMR experiments, data analysis and structure calculation; V.S.M. contributed to the solid-state NMR experiments, resonance assignment, and structure calculation. G.H. purified the protein, prepared the membrane samples, and conducted the solution NMR experiments; G.H. and K.A.H.-W. analyzed the solution NMR data; J.H.D. devised the F_4-TPP^+ design and synthetic approach; M.S. carried out F_4-TPP^+ synthesis, purification, and characterization; E.A.S. performed the electrostatic surface calculations; N.T. performed and analyzed the liposomal transport assays; K.A.H-W and M.H. designed the experiments. All authors discussed the results and analysis and wrote the paper.

Competing interests

The authors declare no competing financial interests.

Data availability

Solid-state NMR chemical shifts and distance restraints have been deposited in the Biological Magnetic Resonance Bank (BMRB) with ID number 50411. The structural coordinates have been deposited in the Protein Data Bank with accession code 7JK8.

Table 1. NMR and refinement statistics for F_4-TPP^+ bound S64V-EmrE structure in lipid bilayers.

	Monomer A	Monomer B
NMR distance and dihedral constraints		
Dipolar Coupling Measurements	42	30
Distance Constraints	119	94
Total dihedral-angle restraints		
ϕ	99	86
ψ	99	87
χ_1	53	42
Structure statistics		
Violations (mean ± s.d.)		
Distance constraints (Å)	0.012 ± 0.082	0.015 ± 0.059
Max. distance-constraint violation (Å)	1.32	1.17
ϕ Dihedral-angle constraints (°)	0.096 ± 1.402	0.294 ± 2.428
ψ Dihedral-angle constraints (°)	0.071 ± 0.667	0.417 ± 3.279
Max. ϕ dihedral-angle violation (°)	33.4	29.1
Max. ψ dihedral-angle violation (°)	10.5	43.1
Average pairwise r.m.s.d (Å)[a]		
Protein Heavy atom for TM helices	2.05 ± 0.55	
Protein Backbone for TM helices	1.67 ± 0.52	
Ligand Heavy	1.98 ± 0.64	
Ligand Center [b]	1.58 ± 0.68	

[a] Pairwise r.m.s.d. was calculated among 10 lowest-violation structures between the two independent MD runs after the refinement had equilibrated.
[b] Ligand center is defined as phosphorus and the four directly bonded carbon atoms of F_4-TPP^+.

Table 2. Protein-substrate distances extracted from the NMR-refined structural models. The average distances and standard deviations are from the ensemble of 10 minimum constraint-violation structures in the final 150 ns of the two MD trajectories.

	Monomer A	Monomer B
P – E14 Cδ	5.4 ± 0.6 Å	7.1 ± 0.7 Å
P – Y40 Oζ	6.9 ± 0.8 Å	14.5 ± 2.1 Å
P – Y60 Oζ	8.3 ± 0.6 Å	6.7 ± 0.7 Å
P – W63 Nε	5.7 ± 0.8 Å	5.0 ± 0.5 Å
Min. F [a] – E14 Cδ	4.8 ± 0.6 Å	6.0 ± 0.5 Å
Min. F [a] – Y40 Oζ	5.7 ± 0.4 Å	10.7 ± 1.4 Å
Min. F [a] – Y60 Oζ	5.2 ± 1.3 Å	5.5 ± 0.9 Å
Min. F – W63 Nε	4.7 ± 0.6 Å	4.8 ± 0.5 Å
A.B.F [b] – E14 Cδ	9.0 ± 1.4 Å	6.1 ± 0.5 Å
A.B.F [b] – Y60 Oζ	5.2 ± 1.3 Å	9.9 ± 2.6 Å
A.B.F [b] – W63 Nε	4.7 ± 0.6 Å	4.8 ± 0.5 Å

[a] Distance of the nearest fluorine to the specified protein atom.

[b] Distance from the fluorine atom (annotated as F3) that interacts within the aromatic box of W63 and Y60 to the specified protein atom.

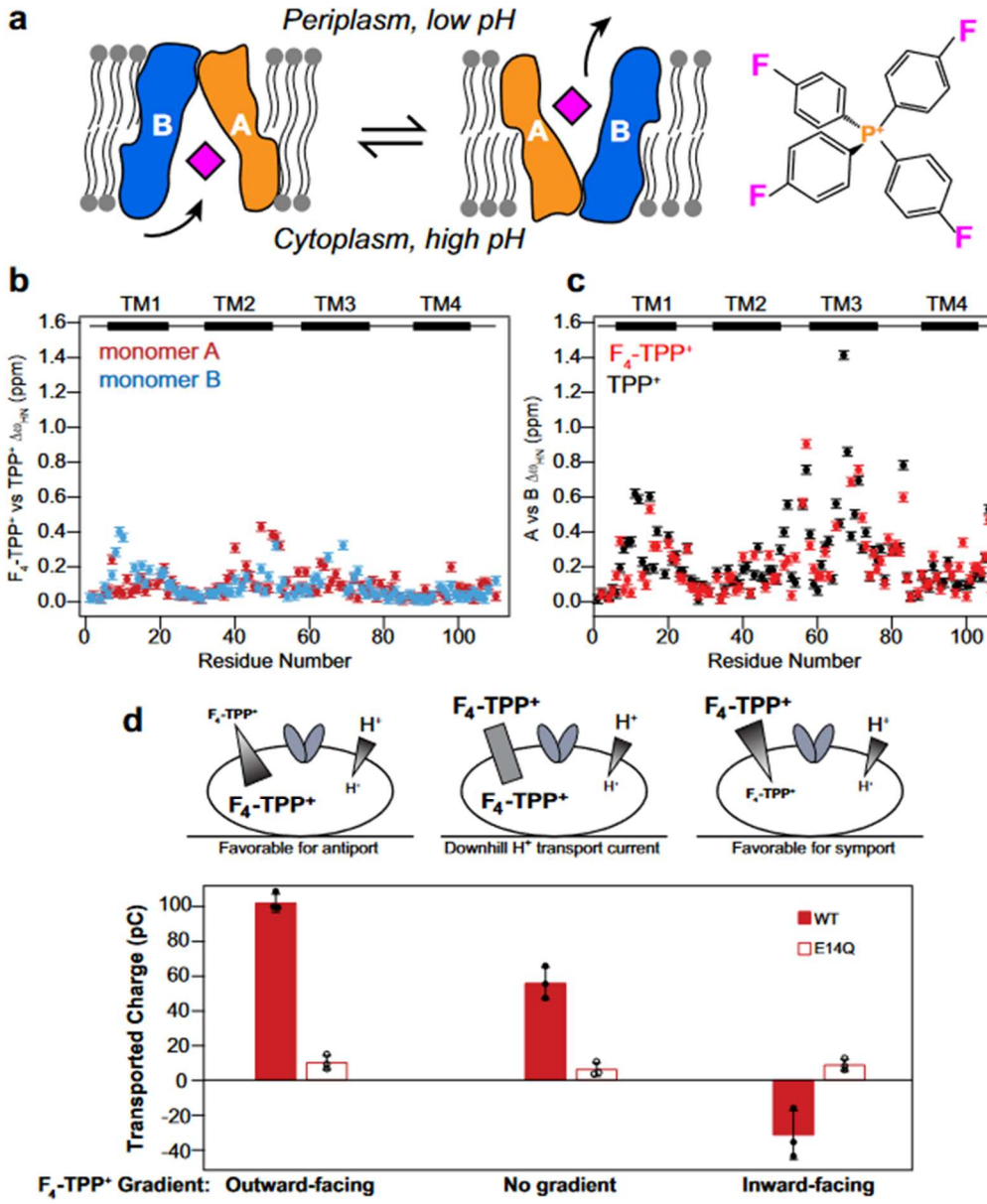

Figure 1. EmrE binds and transports F_4-TPP$^+$ in a similar fashion to TPP$^+$. (**A**) Schematic model of the alternating-access mechanism of the asymmetric EmrE homodimer to export polyaromatic substrates out of bacterial cells. The F_4-TPP$^+$ structure is shown on the right. (**B**) Amide H^N and ^{15}N chemical shift difference between F_4TPP$^+$- and TPP$^+$-bound S64V-EmrE in lipid bicelles. Red: subunit A; Blue, subunit B. The small chemical shift differences indicate that substrate fluorination has little effect on the protein structure. (**C**) Amide H^N and ^{15}N chemical shift difference between subunits A and B of bicelle-bound S64V-EmrE. Red: F_4-TPP$^+$ bound protein data; Black: TPP$^+$-

bound protein data. Similar structural asymmetry between the two subunits is observed for the two substrates. (**D**) ΔpH-driven liposomal transport assays of F_4-TPP^+ using solid-supported membrane electrophysiology. When the proton and F_4-TPP^+ gradients are in opposite directions, net current increases, but when they are in the same direction, net current decreases, indicating that F_4-TPP^+ is a canonical antiport substrate of EmrE. The E14Q data serve as controls. Raw current traces and additional details are shown in **Figure S3**.

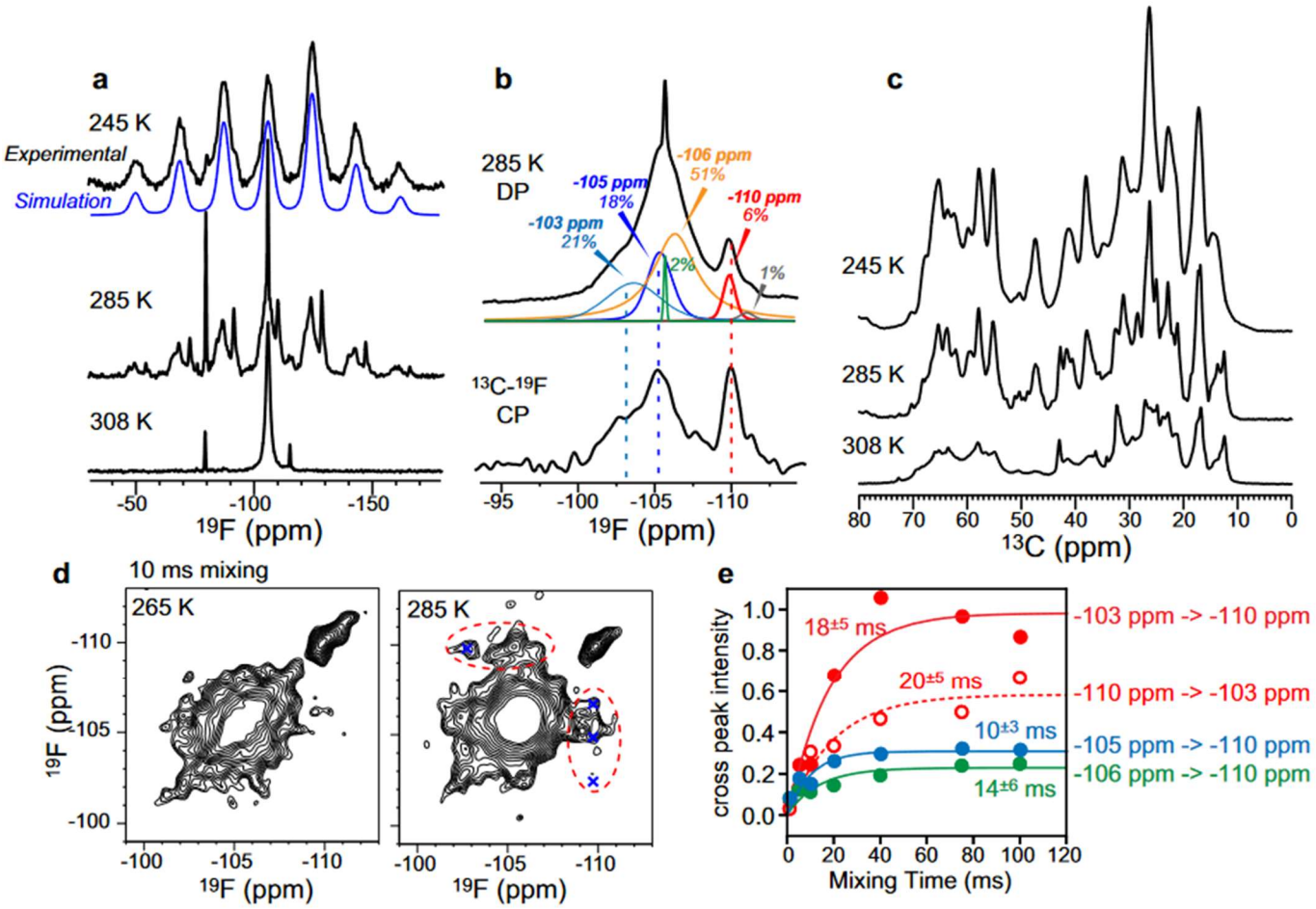

Figure 2. ^{19}F MAS NMR spectra of F_4-TPP$^+$ bound to S64V-EmrE in DMPC bilayers. (**A**) Variable-temperature ^{19}F DP spectra measured under 10.5 kHz MAS. The substrate has an isotropic ^{19}F chemical shift of -106 ppm. The ^{19}F linewidths and spinning sideband intensities are strongly dependent on temperature. At 245 K, the substrate is immobilized, whereas at 308 K, the substrate is nearly isotropically mobile. The minor sharp peaks at -80 ppm and -116 ppm in the high-temperature spectrum are attributed to residual 4-fluoroiodobenzene and tris(4-fluorophenyl)phosphine from the F_4-TPP$^+$ synthesis. (**B**) ^{19}F DP spectrum measured at 285 K under 35 kHz MAS. Spectral deconvolution gives five components, indicating that the ligand experiences a heterogeneous structural environment. ^{13}C-^{19}F cross-polarization (CP) spectrum enhanced three out of the five components, indicating that these species are closest to the ^{13}C-labeled protein. (**C**) Variable-temperature ^{13}C CP MAS spectra of DMPC-bound S64V-EmrE. The

spectral intensity decreases with increasing temperature, indicating that the protein becomes more dynamic at higher temperatures. (**D**) 2D ^{19}F-^{19}F correlation spectrum of F_4-TPP^+ with 10 ms mixing. The spectra were measured under 38 kHz MAS. Exchange peaks are observed at 285 K but not at 265 K, indicating that the exchange is due to substrate reorientation. (**E**) Intensity buildup curves of cross peaks (shown as blue crosses in **D**) give an average exchange time constant of 16 ± 2 ms.

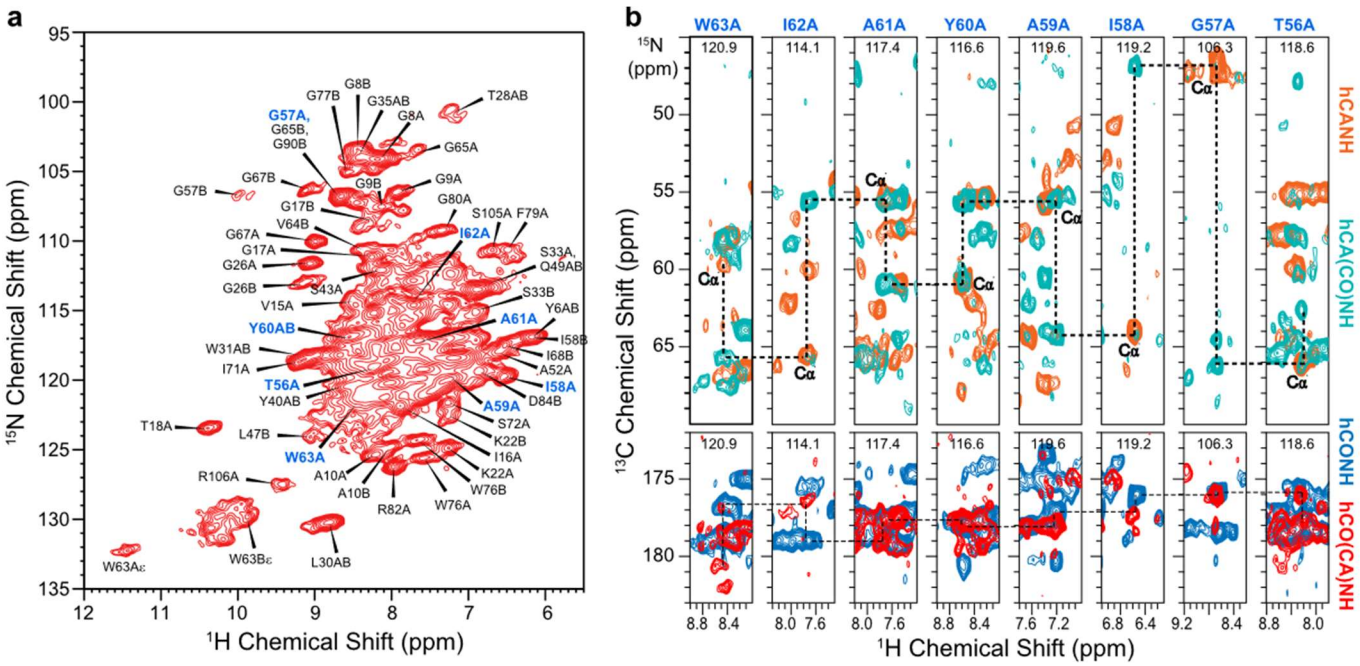

Figure 3. ^{1}H-detected 2D and 3D correlation MAS NMR spectra of F_4-TPP^{+} bound S64V-EmrE in DMPC bilayers. (**A**) ^{1}H-^{15}N 2D correlation spectrum measured under 55 kHz MAS. Selected resonances are assigned based on 3D correlation spectra. (**B**) Representative strips, for residues T56–W63 in subunit A, of the four 3D ^{1}H-detected correlation spectra for resonance assignment. Aliphatic ^{13}C chemical shifts were assigned using hCANH and hCA(CO)NH experiments, while CO chemical shifts were assigned using the hCO(CA)NH and hCONH experiments. All spectra were measured under 55 kHz MAS on CDN-labeled protein at a sample temperature of 285 K.

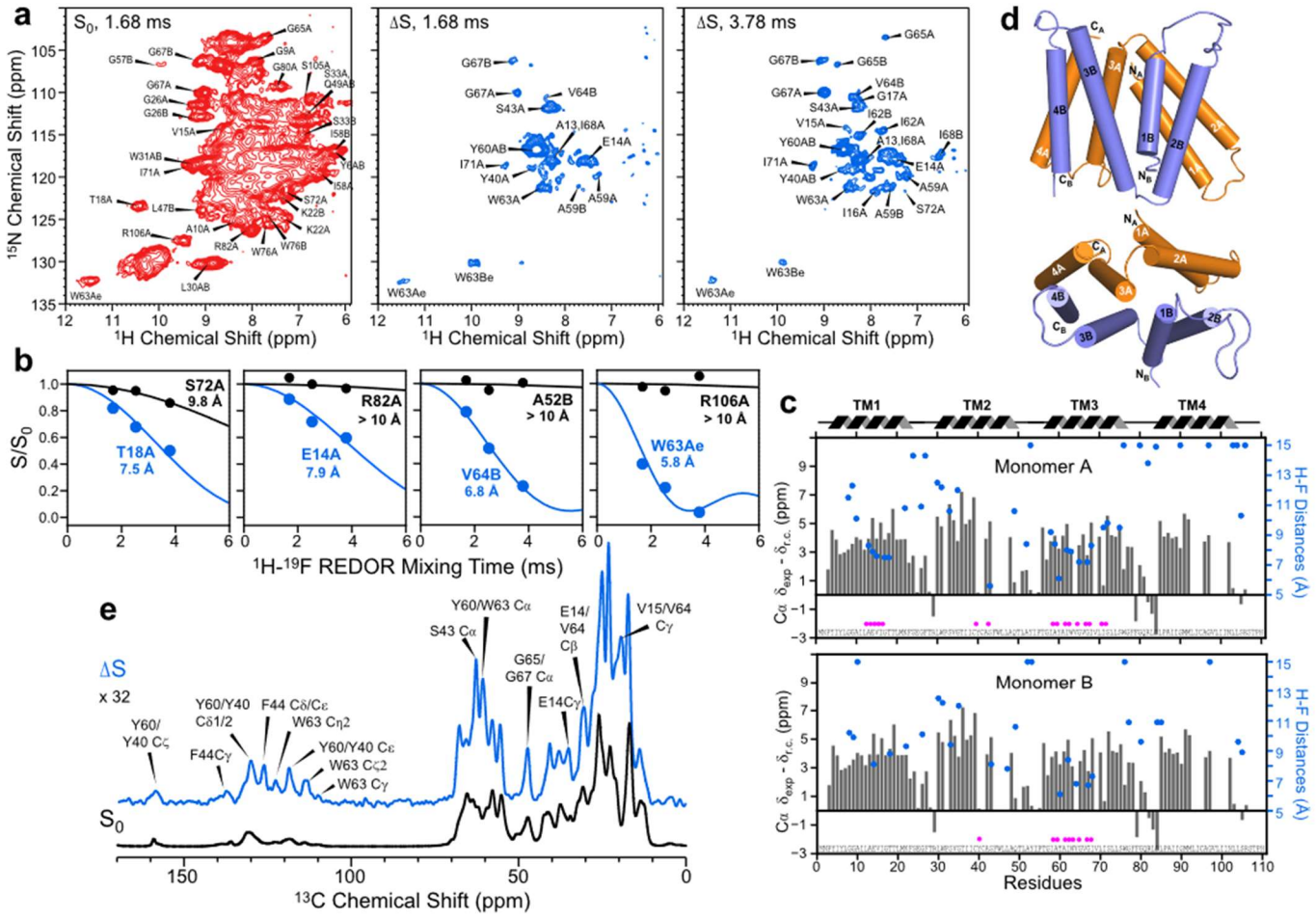

Figure 4. EmrE to F_4-TPP$^+$ distances measured using ^{1}H-^{19}F and ^{13}C-^{19}F REDOR experiments. (**A**) Representative S_0 (red) and ΔS (blue) 2D REDOR-hNH correlation spectra, measured with mixing times of 1.68 ms and 3.78 ms. Assignment is shown for selected resolved peaks in the S_0 spectrum. More difference peaks are observed in the 3.78 ms ΔS spectrum than in the 1.68 ms ΔS spectrum, as expected. (**B**) Representative ^{1}H-^{19}F REDOR S/S_0 dephasing curves with best-fit simulations. Fast and slow dephasing, corresponding to short and long distances, are shown in blue and black, respectively. (**C**) Cα secondary chemical shifts (grey bars) of F_4-TPP$^+$ bound EmrE, indicating four TM α-helices separated by short loops. Residues whose H^N atoms show difference signals in the 2D REDOR spectra are indicated by magenta circles at the bottom. Best-fit H^N-F distances are indicated by blue circles. Residues in TM3A, TM3B, and TM1A display short

distances to F_4-TPP^+. (**D**) Topology of the eight TM helices in the dimeric EmrE, with monomer A helices shown in orange and monomer B helices shown in blue. (**E**) ^{13}C-^{19}F REDOR S_0 and ΔS spectra, coadded from spectra recorded with mixing times of 0.92, 2.0, 3.0, and 4.5 ms. The ΔS spectrum is plotted to be 32 x scaled up relative to the S_0 spectrum to better show the signals of ^{13}C sites that are close to the substrate. Note the preferential increase of aromatic ^{13}C intensities in the 100-160 ppm region in the ΔS spectrum compared to the control S_0 spectrum. This is consistent with the predominance of aromatic residues at the binding site. Selected peaks are assigned based on the chemical shifts known from the 3D correlation spectra (Table S1).

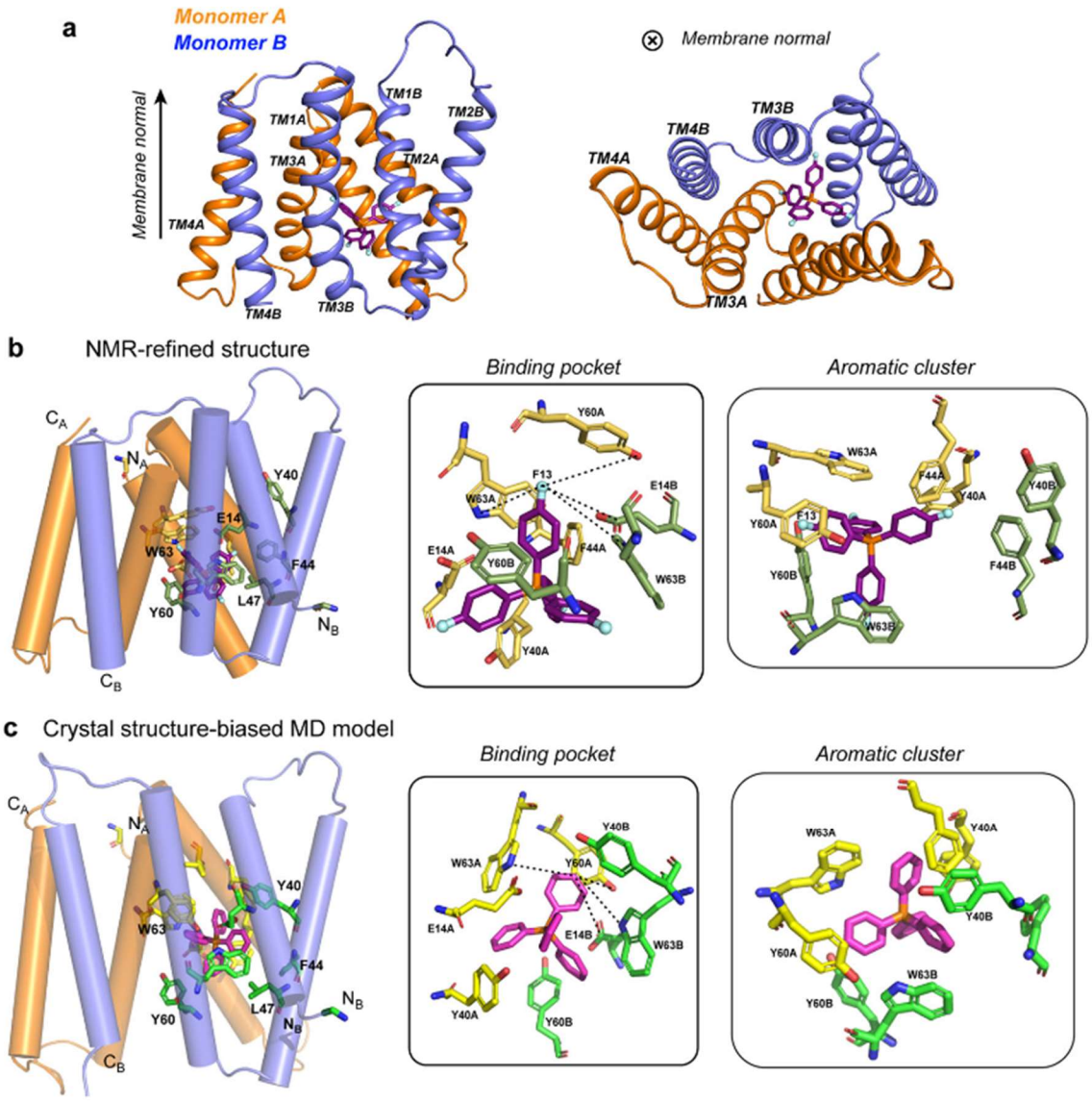

Figure 5. Experimentally constrained structure model of the EmrE-TPP$^+$ complex in DMPC bilayers at low pH. (**A**) Side view (left) and bottom view (right) of the topology of the complex. The ligand (purple) lies closer to monomer A (orange) than monomer B (blue). (**B**) Distance-constrained NMR structure model of the binding site. Key residues, including E14, Y40, Y60 and W63, surround the substrate. One of the four phenylene Hζ atoms, marked as F3, is tightly coordinated by residues from both monomer A (yellow) and monomer B (green). The right side shows a bottom view of all aromatic residues (W63, Y60, F44, and Y40) near the substrate. (**C**) MD simulated structure model biased to the low-resolution crystal structure. The substrate and

key binding-site residues show various differences in position and orientations compared to the experimental NMR structure.

References

1. Bay DC, Stremick CA, Slipski CJ, Turner RJ. Secondary multidrug efflux pump mutants alter Escherichia coli biofilm growth in the presence of cationic antimicrobial compounds. *Res Microbiol* **168**, 208-221 (2017).

2. Matsumura K, Furukawa S, Ogihara H, Morinaga Y. Roles of multidrug efflux pumps on the biofilm formation of Escherichia coli K-12. *Biocontrol Sci* **16**, 69-72 (2011).

3. Sulavik MC*, et al.* Antibiotic Susceptibility Profiles of Escherichia coli Strains Lacking Multidrug Efflux Pump Genes. *Antimicrobial Agents Chemo* **45**, 1126-1136 (2001).

4. Nishino K, Nikaido E, Yamaguchi A. Regulation and physiological function of multidrug efflux pumps in Escherichia coli and Salmonella. *Biochim Biophys Acta* **1794**, 834-843 (2009).

5. Gupta AK*, et al.* Microarray analysis of efflux pump genes in multidrug-resistant Mycobacterium tuberculosis during stress induced by common anti-tuberculous drugs. *Microb Drug Resist* **16**, 21-28 (2010).

6. De Rossi E, Branzoni M, Cantoni R, Milano A, Riccardi G, Ciferri O. mmr, a Mycobacterium tuberculosis gene conferring resistance to small cationic dyes and inhibitors. *J Bacteriol* **180**, 6068-6071 (1998).

7. Srinivasan VB, Rajamohan G, Gebreyes WA. Role of AbeS, a novel efflux pump of the SMR family of transporters, in resistance to antimicrobial agents in Acinetobacter baumannii. *Antimicrobial Agents Chemo* **53**, 5312-5316 (2009).

8. Brill S, Falk OS, Schuldiner S. Transforming a drug/H+ antiporter into a polyamine importer by a single mutation. *Proc Natl Acad Sci U S A* **109**, 16894-16899 (2012).

9. Schuldiner S. EmrE, a model for studying evolution and mechanism of ion-coupled transporters. *Biochim Biophys Acta* **1794**, 748-762 (2009).

10. Yerushalmi H, Lebendiker M, Schuldiner S. EmrE, an Escherichia coli 12-kDa multidrug transporter, exchanges toxic cations and H+ and is soluble in organic solvents. *J Biol Chem* **270**, 6856-6863 (1995).

11. Rotem D, Schuldiner S. EmrE, a multidrug transporter from Escherichia coli, transports monovalent and divalent substrates with the same stoichiometry. *J Biol Chem* **279**, 48787-48793 (2004).

12. Bay DC, Rommens KL, Turner RJ. Small multidrug resistance proteins: a multidrug transporter family that continues to grow. *Biochim Biophys Acta* **1778**, 1814-1838 (2008).

13. Korkhov VM, Tate CG. Electron crystallography reveals plasticity within the drug binding site of the small multidrug transporter EmrE. *J Mol Biol* **377**, 1094-1103 (2008).

14. Morrison EA, Henzler-Wildman KA. Transported substrate determines exchange rate in the multidrug resistance transporter EmrE. *J Biol Chem* **289**, 6825-6836 (2014).

15. Hussey GA, Thomas NE, Henzler-Wildman KA. Highly coupled transport can be achieved in free-exchange transport models. *J Gen Physiol* **152**, (2020).

16. Thomas NE, Wu C, Morrison EA, Robinson AE, Werner JP, Henzler-Wildman KA. The C terminus of the bacterial multidrug transporter EmrE couples drug binding to proton release. *J Biol Chem* **293**, 19137-19147 (2018).

17. Robinson AE, Thomas NE, Morrison EA, Balthazor BM, Henzler-Wildman KA. New free-exchange model of EmrE transport. *Proc Natl Acad Sci U S A* **114**, E10083 (2017).

18. Morrison EA, Robinson AE, Liu Y, Henzler-Wildman KA. Asymmetric protonation of EmrE. *J Gen Physiol* **146**, 445-461 (2015).

19. Dutta S, Morrison EA, Henzler-Wildman KA. Blocking Dynamics of the SMR Transporter EmrE Impairs Efflux Activity. *Biophys J* **107**, 613-620 (2014).

20. Gayen A, Leninger M, Traaseth NJ. Protonation of a glutamate residue modulates the dynamics of the drug transporter EmrE. *Nat Chem Biol* **12**, 141 (2016).

21. Cho M-K, Gayen A, Banigan JR, Leninger M, Traaseth NJ. Intrinsic Conformational Plasticity of Native EmrE Provides a Pathway for Multidrug Resistance. *J Am Chem Soc* **136**, 8072-8080 (2014).

22. Tate CG, Kunji ER, Lebendiker M, Schuldiner S. The projection structure of EmrE, a proton-linked multidrug transporter from Escherichia coli, at 7 A resolution. *EMBO J* **20**, 77-81 (2001).

23. Ubarretxena-Belandia I, Baldwin JM, Schuldiner S, Tate CG. Three-dimensional structure of the bacterial multidrug transporter EmrE shows it is an asymmetric homodimer. *EMBO J* **22**, 6175-6181 (2003).

24. Tate CG, Ubarretxena-Belandia I, Baldwin JM. Conformational changes in the multidrug transporter EmrE associated with substrate binding. *J Mol Biol* **332**, 229-242 (2003).

25. Chen Y-J, Pornillos O, Lieu S, Ma C, Chen AP, Chang G. X-ray structure of EmrE supports dual topology model. *Proc Natl Acad Sci U S A* **104**, 18999 (2007).

26. Morrison EA*, et al.* Antiparallel EmrE exports drugs by exchanging between asymmetric structures. *Nature* **481**, 45 (2011).

27. Lloris-Garcerá P, Slusky JSG, Seppälä S, Prieß M, Schäfer LV, von Heijne G. In Vivo Trp Scanning of the Small Multidrug Resistance Protein EmrE Confirms 3D Structure Models. *J Mol Biol* **425**, 4642-4651 (2013).

28. Lloris-Garcerá PP, Bianchi FF, Slusky JSGJ, Seppälä SS, Daley DOD, von Heijne GG. Antiparallel dimers of the small multidrug resistance protein EmrE are more stable than parallel dimers. *J Biol Chem* **287**, 26052-26059 (2012).

29. Rapp M, Granseth E, Seppälä S, von Heijne G. Identification and evolution of dual-topology membrane proteins. *Nat Struct Mol Biol* **13**, 112-116 (2006).

30. Dastvan R, Fischer AW, Mishra S, Meiler J, McHaourab HS. Protonation-dependent conformational dynamics of the multidrug transporter EmrE. *Proc Natl Acad Sci U S A* **113**, 1220-1225 (2016).

31. Amadi ST, Koteiche HA, Mishra S, McHaourab HS. Structure, dynamics, and substrate-induced conformational changes of the multidrug transporter EmrE in liposomes. *J Biol Chem* **285**, 26710-26718 (2010).

32. Kermani AA, Macdonald CB, Gundepudi R, Stockbridge RB. Guanidinium export is the primal function of SMR family transporters. *Proc Natl Acad Sci U S A* **115**, 3060-3065 (2018).

33. Stockbridge RB, Koide A, Miller C, Koide S. Proof of dual-topology architecture of Fluc F- channels with monobody blockers. *Nat Commun* **5**, 5120 (2014).

34. Gayen A, Banigan JR, Traaseth NJ. Ligand-Induced Conformational Changes of the Multidrug Resistance Transporter EmrE Probed by Oriented Solid-State NMR Spectroscopy. *Angew Chem Int Ed* **52**, 10321-10324 (2013).

35. Lehner I*, et al.* The key residue for substrate transport (Glu14) in the EmrE dimer is asymmetric. *J Biol Chem* **283**, 3281-3288 (2008).

36. Wu C, Wynne SA, Thomas NE, Uhlemann EM, Tate CG, Henzler-Wildman KA. Identification of an Alternating-Access Dynamics Mutant of EmrE with Impaired Transport. *J Mol Biol* **431**, 2777-2789 (2019).

37. Shcherbakov AA, Mandala VS, Hong M. High-Sensitivity Detection of Nanometer 1H–19F Distances for Protein Structure Determination by 1H-Detected Fast MAS NMR. *J Phys Chem B* **123**, 4387-4391 (2019).

38. Sharoni M, Steiner-Mordoch S, Schuldiner S. Exploring the binding domain of EmrE, the smallest multidrug transporter. *J Biol Chem* **280**, 32849-32855 (2005).

39. Elbaz Y, Tayer N, Steinfels E, Steiner-Mordoch S, Schuldiner S. Substrate-induced tryptophan fluorescence changes in EmrE, the smallest ion-coupled multidrug transporter. *Biochemistry* **44**, 7369-7377 (2005).

40. Gutman N, Steiner-Mordoch S, Schuldiner S. An amino acid cluster around the essential Glu-14 is part of the substrate- and proton-binding domain of EmrE, a multidrug transporter from Escherichia coli. *The Journal of biological chemistry* **278**, 16082-16087 (2003).

41. Rotem D, Steiner-Mordoch S, Schuldiner S. Identification of tyrosine residues critical for the function of an ion-coupled multidrug transporter. *The Journal of biological chemistry* **281**, 18715-18722 (2006).

42. Wang J, Rath A, Deber CM. Functional response of the small multidrug resistance protein EmrE to mutations in transmembrane helix 2. *FEBS letters* **588**, 3720-3725 (2014).

43. Duncan TM. *Principal Components of Chemical Shift Tensors: A Compilation*, Second Edition edn. The Farragut Press (1997).

44. Shcherbakov AA, Roos M, Kwon B, Hong M. Two-dimensional 19F–13C correlation NMR for 19F resonance assignment of fluorinated proteins. *J Biomol NMR* **74**, 193-204 (2020).

45. Lu M*, et al.* 19F Dynamic Nuclear Polarization at Fast Magic Angle Spinning for NMR of HIV-1 Capsid Protein Assemblies. *J Am Chem Soc* **141**, 5681-5691 (2019).

46. Ong YS, Lakatos A, Becker-Baldus J, Pos KM, Glaubitz C. Detecting Substrates Bound to the Secondary Multidrug Efflux Pump EmrE by DNP-Enhanced Solid-State NMR. *J Am Chem Soc* **135**, 15754-15762 (2013).

47. Roos M, Wang T, Shcherbakov AA, Hong M. Fast Magic-Angle-Spinning F-19 Spin Exchange NMR for Determining Nanometer Distances in Proteins and Pharmaceutical Compounds. *J Phys Chem B* **122**, 2900–2911 (2018).

48. Barbet-Massin E*, et al.* Rapid Proton-Detected NMR Assignment for Proteins with Fast Magic Angle Spinning. *J Am Chem Soc* **136**, 12489-12497 (2014).

49. Shen Y, Bax A. Protein backbone and sidechain torsion angles predicted from NMR chemical shifts using artificial neural networks. *J Biomol NMR* **56**, 227-241 (2013).

50. Ovchinnikov V, Stone TA, Deber CM, Karplus M. Structure of the EmrE multidrug transporter and its use for inhibitor peptide design. *Proc Natl Acad Sci U S A* **115**, E7932 (2018).

51. Vermaas JV, Rempe SB, Tajkhorshid E. Electrostatic lock in the transport cycle of the multidrug resistance transporter EmrE. *Proc Natl Acad Sci U S A* **115**, E7502 (2018).

52. Fleishman SJ, Harrington SE, Enosh A, Halperin D, Tate CG, Ben-Tal N. Quasi-symmetry in the cryo-EM structure of EmrE provides the key to modeling its transmembrane domain. *J Mol Biol* **364**, 54-67 (2006).

53. Platzer G, Okon M, McIntosh LP. pH-dependent random coil (1)H, (13)C, and (15)N chemical shifts of the ionizable amino acids: a guide for protein pK a measurements. *J Biomol NMR* **60**, 109-129 (2014).

54. Willers C, Wentzel JF, du Plessis LH, Gouws C, Hamman JH. Efflux as a mechanism of antimicrobial drug resistance in clinical relevant microorganisms: the role of efflux inhibitors. *Expert Opin Ther Targets* **21**, 23-36 (2017).

55. Shriram V, Khare T, Bhagwat R, Shukla R, Kumar V. Inhibiting Bacterial Drug Efflux Pumps via Phyto-Therapeutics to Combat Threatening Antimicrobial Resistance. *Front Microbiol* **9**, 2990 (2018).

56. Reens AL*, et al.* A cell-based infection assay identifies efflux pump modulators that reduce bacterial intracellular load. *PLoS Pathog* **14**, e1007115 (2018).

57. Kabra R, Chauhan N, Kumar A, Ingale P, Singh S. Efflux pumps and antimicrobial resistance: Paradoxical components in systems genomics. *Progress in biophysics and molecular biology*, (2018).

58. Handzlik J, Matys A, Kieć-Kononowicz K. Recent Advances in Multi-Drug Resistance (MDR) Efflux Pump Inhibitors of Gram-Positive Bacteria S. aureus. *Antibiotics* **2**, 28-45 (2013).

59. Baugh S, Phillips CR, Ekanayaka AS, Piddock LJ, Webber MA. Inhibition of multidrug efflux as a strategy to prevent biofilm formation. *J Antimicrob Chemother* **69**, 673-681 (2014).

60. Blanco P, Sanz-Garcia F, Hernando-Amado S, Martinez JL, Alcalde-Rico M. The development of efflux pump inhibitors to treat Gram-negative infections. *Expert Opin Drug Discov* **13**, 919-931 (2018).

61. Wang Y, Venter H, Ma S. Efflux Pump Inhibitors: A Novel Approach to Combat Efflux-Mediated Drug Resistance in Bacteria. *Curr Drug Targets* **17**, 702-719 (2016).

62. Son MS, Del Castilho C, Duncalf KA, Carney D, Weiner JH, Turner RJ. Mutagenesis of SugE, a small multidrug resistance protein. *Biochim Biophys Res Comm* **312**, 914-921 (2003).

Methods

Synthesis of tetra(4-fluorophenyl) phosphonium iodide

Into a 50 ml heavy-wall pressure vessel with a PTFE internal-thread cap with a magnetic stir bar, 4-fluoroiodobenzene (1.4g, 1.0 equiv), tris(4-fluorophenyl)phosphine (2.0g, 1.0 equiv), $Pd(OAc)_2$ (0.021g, 1.5 mol%), and mixed xylenes (15 mL) were added. The tube was flushed with nitrogen, capped, and the reaction mixture stirred at 140°C for 2 hours. The product, tetra(4-fluorophenyl) phosphonium iodide, precipitates during the course of the reaction. Once cooled, the product was isolated by filtration, washed with small portions of fresh xylenes, and air-dried. The pure tetra(4-fluorophenyl) phosphonium iodide product was isolated as a pale ivory solid (3.2 g, 95% yield).

S64V-EmrE Expression and Purification

S64V-EmrE was expressed and purified as previously described [36], using the same procedure as for WT EmrE [63]. For $^{13}C,^{15}N$-labeled S64V-EmrE, the protein was expressed using media containing 2.5 g/L U-^{13}C glucose, 1 g/L $^{15}NH_4Cl$, 0.5 g/L $^{13}C,^{15}N$-labled ISOGRO (Millipore-Sigma). $^{2}H,^{13}C,^{15}N$ (CDN) S64V-EmrE was expressed in $^{2}H_2O$ media containing 2.5 g/L U-$^{2}H,^{13}C$ glucose, 1 g/L $^{15}NH_4Cl$, 0.5 g/L $^{2}H,^{13}C,^{15}N$-labled ISOGRO. $^{2}H,^{15}N$ (DN)-labeled S64V-EmrE was expressed in $^{2}H_2O$ media containing 1 g/L $^{15}NH_4Cl$ and 0.5 g/L $^{2}H,^{13}C,^{15}N$-labled ISOGRO. Lysis and purification were performed as previously reported [14, 63] using Ni-NTA affinity column followed by thrombin cleavage of the His-tag and size exclusion chromatography on a S200 column in buffer containing 50 mM MES, 20 mM NaCl, 10 mM decyl-maltoside, 5 mM BME, pH 5.8.

Solid-Supported Membrane-based Electrophysiology Experiments

WT EmrE and E14Q EmrE was expressed and purified as previously described [17]. To minimize solution exchange artifacts, the buffers used for size exclusion chromatography, reconstitution, and electrophysiology steps had the same salt composition: 50 mM MES, 50 mM MOPS, 50 mM

bicine, 100 mM NaCl, and 2 mM $MgCl_2$. Buffer pH values were carefully adjusted using only NaOH to ensure that internal and external Cl^- concentrations were identical for all measurements. Protein was reconstituted into POPC liposomes at a 1:400 protomer : lipid molar ratio, and detergent was removed with Amberlite XAD-2. Liposomes were collected, aliquoted, and flash frozen. Immediately prior to measurements, liposomes were thawed, diluted 2-fold with pH 7.3 buffer, and briefly sonicated.

All electrophysiology measurements were recorded and analyzed using a Surf2er N1 solid-supported membrane-based electrophysiology (SSME) instrument from Nanion Technologies. Prior to measurements, sensors were equilibrated on the instrument with multiple washes with pH 7.30 buffer containing 0.5 μM F_4-TPP^+ while recording currents. Washes were performed until successive washes produced no observable current. Transport was initiated by perfusion of pH 7.00 buffer containing 10 μM F_4-TPP^+ to simultaneously set inward-facing proton and drug gradients. Transport currents were recorded during 1.5 seconds of perfusion of the external buffer and integrated to obtain transported charge. After these measurements, sensors were washed with pH 7.30 buffer containing 10 μM F_4-TPP^+ while recording currents. Washes were again performed until successive washes produced no observable current. (0.5 μM F_4-TPP^+ for outward-facing gradient, 10 μM F_4-TPP^+ for inward-facing or no gradient). Transport was initiated by perfusion of pH 7.00 buffer containing 0.5 or 10 μM F_4-TPP^+ to simultaneously set inward-facing drug and/or proton gradients. Reported values are the average of replicates on three different sensors, and error bars are the standard error of the mean.

Reconstitution and Preparation of Solid-State NMR samples

^{13}C,^{15}N-labeled S64V-EmrE was reconstituted into DMPC (Avanti Polar Lipids) liposomes at a EmrE monomer to lipid molar ratio (P : L) of 1 : 50 or 1 : 25. DMPC was resuspended in 50 mM MES, 20 mM NaCl, pH 5.8 buffer at 20 mg/mL. The lipid mixture was incubated at 45 ºC for 1 h

to hydrate, then bath-sonicated for 1 min before addition of 0.5% octyl-glucoside (OG) followed by 30 s bath sonication. The lipid mixture was incubated at 45ºC for an addition 15 min before mixing with purified S64V-EmrE solution. After 20 min room temperature (RT) incubation, Amberlite (Supelco) was added (3 x 30mg Amberlite per mg total detergent) to remove the detergent. The amberlite was removed after 16-24 hours by simple filtration. Liposomes were collected by ultracentrifugation (165,000 xg, 6 ºC, 2 h.) and resuspended in a small volume (~20 mg/mL lipid conc.) of buffer. To ensure complete detergent removal, the sample was dialyzed against 1 L of the same buffer (50 mM MES, 20 mM NaCl, pH 5.8) with buffer change every 24 hours over a 72 hour period. The sample was then incubated with excess solid F_4-TPP+$^+$ at RT with end-to-end mixing for at least 16 hours. Excess F_4-TPP+$^+$ was removed using microcentrifugation (10,000 rpm., 5 min). Proteoliposomes were then pelleted at 100,000 *g*, 4 ºC, 2 h in an ultracentrifuge. A similar method was used to prepare the CDN-S64V-EmrE sample, except that the protein was reconstituted into DMPC-d_{54} liposomes at a P : L of 1 : 25 . Proteoliposomes were dried to ~40% hydration by mass in a desiccator. Samples were centrifuged into 3.2, 1.9, and 1.3 mm MAS rotors. Three 1.9 mm rotors were packed: 1) a CDN-EmrE sample containing 3.6 mg protein in 16.0 mg proteoliposomes, 2) a CN-labeled EmrE sample (P : L = 1 : 25) containing 3.4 mg protein in 14.9 mg proteoliposomes, and 3) a CN-labeled EmrE sample (P : L = 1 : 50) containing 1.9 mg protein in 15.0 mg proteoliposomes. A 1.3 mm MAS rotor was packed with 0.9 mg CDN-EmrE in 3.9 mg proteoliposomes. The 3.2 mm Revolution NMR rotor was packed with 5 mg CN-EmrE in 39 mg proteoliposomes (P : L=1 : 50).

Reconstitution and Preparation of Solution NMR Samples

All solution NMR samples were reconstituted into DMPC/DHPC isotropic bicelles (q=3) at a 75:1 lipid to EmrE monomer ratio. The reconstitution was performed similarly to the solid-state NMR sample up to the point where liposomes were pelleted at (165,000 g, 6 ºC, 2 h). Once pelleted, the sample was resuspended in buffer containing 3-fold higher concentration of 1,2-dihexanoyl-

sn-glycero-3-phosphocholine (DHPC-6). Samples were then subjected to 3 cycles of freeze-thaw. The pH of the final samples was adjusted to 5.8 at 45ºC using a Hamilton biotrode microelectrode. The sample was then incubated with excess solid F_4-TPP+$^+$ at 45ºC overnight. Excess F_4-TPP+$^+$ was removed using microcentrifugation prior to transferring solution to NMR tubes.

Solid-state NMR Experiments

The MAS NMR experiments were conducted at 600, 700, and 800 MHz Bruker NMR spectrometers. ^{1}H-^{19}F REDOR distance measurements were conducted under 38 kHz MAS at an effective sample temperature (T_{eff}) of 285 K on a Bruker Avance III HD 600 MHz (14.1 T) spectrometer at MIT using a 1.9 mm HFX probe. ^{1}H-detected 3D correlation experiments for resonance assignment were conducted on 1.3 mm HCN probes under 55 kHz MAS between 280 and 285 K on the 600 MHz spectrometer and an Avance NEO 700 MHz (16.5 T) spectrometer at Bruker Biospin (Billerica, MA). ^{13}C-detected 3D correlation experiments were conducted under 14 kHz MAS using a 3.2 mm BlackFox HCN probe on an 800 MHz spectrometer.[64]. The effective sample temperatures were estimated from the water ^{1}H chemical shifts using the equation T_{eff} (K) = 96.9(7.83 – δ_{H2O}) where δ_{H2O} is the observed chemical shift of water [65]. The corresponding thermocouple-reported set temperature (T_{set}) is given in **Table S4**. There is no chemical shift difference between fast and slow MAS, and the samples were maintained at similar near ambient temperature by choosing appropriate bearing temperatures. Thus, the protein conformation is unchanged by fast MAS compared to slow MAS.

Pulse sequences for the ^{1}H-detected experiments and ^{19}F solid-state NMR experiments are shown in **Fig. S4**, with experimental parameters given in **Table S4**. In general, N-C correlation experiments used specific CP for polarization transfer [66]. ^{13}C-^{13}C correlation was achieved using the CORD spin diffusion sequence [67] under slow MAS (14 kHz) and the DREAM sequence for one-bond ^{13}C–^{13}C transfer under fast MAS (55 kHz).[68] High-power ^{1}H decoupling used either

continuous wave (CW) or TPPM [69] schemes, and low-power ^{1}H decoupling was achieved with the WALTZ-16 scheme.[70] Proton-detected MAS NMR experiments employed MISSISPPI to suppress the water signal.[71] Four ^{1}H-detected 3D correlation experiments were used to assign the ^{1}H, ^{15}N and ^{13}C chemical shifts of bilayer-bound S64V-EmrE. The hCANH and hCO(CA)NH experiments allow intra-residue assignment while the hCA(CO)NH and hCONH experiment allow inter-residue assignment.

^{19}F chemical shifts were externally referenced to the -122.1 ppm signal of 5F-tryptophan on the CF_3Cl scale [72] and ^{15}N chemical shifts were externally referenced to the ^{15}N peak of N-acetylvaline at 122.0 ppm on the liquid ammonia scale. ^{1}H and ^{13}C chemical shifts were internally referenced to match the DSS-referenced chemical shifts of the solution-state ^{1}H and ^{13}C values. The solids 2D ^{13}C-^{13}C correlation spectrum was calibrated by referencing the T28AB Cβ peak to 70.3 ppm. For the hNH, hCANH, hCONH, and hCA(CO)NH spectra, we chose G67A as the reference signal, setting the ^{1}H chemical shift to 9.0 ppm, $^{13}C\alpha$ to 47.1 ppm, the V66 ^{13}CO to 178.1 ppm, and V66Cα to 67.1 ppm (**Table S1**). The hCO(CA)NH spectrum was referenced similarly by reference to solution-state chemical shifts. However we noticed temperature-induced perturbations between redundant ^{13}CO shifts in the hCONH and hCO(CA)NH spectra; as a result, we calculated the average perturbation in the hCO(CA)NH spectrum relative to the hCONH spectrum for 10 ^{13}CO shifts, and applied an additional +0.4 ppm correction change to the ^{13}C dimension of the hCO(CA)NH spectrum.

Solution NMR Experiments

TROSY-selected ZZ exchange [73] spectra were collected on an 800 MHz Varian VNMRS DD spectrometer equipped with a 5 mm cold probe ($^{1}H/^{13}C/^{15}N$) using VnmrJ 4.0. The VT setpoint was set at 45ºC and data were collected with 200 ms mixing for ~5 days, yielding no discernable

exchange cross peaks. Data were processed using NMRPipe [74] and NMRFAM-Sparky [75] was used to analyze spectrum.

Solid-state NMR Spectral Analysis and Distance Extraction

1D and 2D MAS NMR spectra were processed in the Bruker Topspin software package. Frequency-domain addition of 3D correlation spectra was performed using a Python script that made use of NMRGlue and NumPy Python packages.[76, 77] Chemical shift assignment and plotting of 3D strip spectra were performed in NMRFAM-Sparky [78]. Comparisons of solid-state and solution NMR chemical shifts and monomer A and B chemical shifts were computed in Python and plotted with Matplotlib.[79] Protein backbone torsion angles were predicted using the TALOS-N software [49] from measured chemical shifts, excluding all ^{1}H chemical shifts and applying a deuterium isotope correction to the Cα and Cβ chemical shifts.

REDOR H^{N}-^{19}F distance restraints were extracted as described before.[37, 80] Briefly, peak volumes in the 2D ^{1}H–^{19}F REDOR-edited hNH S_0 and S spectra were integrated to obtain the intensity ratios S/S_0 for all mixing times. We then simulated the two-spin REDOR dephasing curves for distances of 3.0 – 15.0 Å in 0.1 Å increments using the SIMPSON software package [81]. These numerical simulations included the magnitude (δ) and asymmetry (η) of ^{19}F CSA, but left the tensor orientations unknown (i.e. Euler angles of 0, 0, 0). Finite-pulse effects were explicitly encoded in the NMR parameters. RF inhomogeneity was accounted for by simulating for pulse flip angles of 180˚ to 145˚ in 5˚ increments, weighted by a half-Gaussian function centered at 180˚.[37, 80] The REPULSION168 scheme with 32 gamma angles was used for powder averaging [82]. The best-fit ^{1}H–^{19}F distance was extracted by minimizing the RMSD between the simulated and measured S/S_0 values. The uncertainty in the best-fit distance was set by an RMSD threshold of 0.2, as this was the maximum scatter observed for sites that do not dephase; distances below this RMSD

value were considered significant (**Fig. S9**). In cases where little to no dephasing was observed, we set the distance upper uncertainty to 40 Å, which is approximately the longest possible distance in the dimer. For residues whose signals overlap in the 2D hNH spectrum, the lower-limit distance uncertainty was increased.

Solution NMR Assignment Spectra

Solution chemical shift assignments were assigned using the following suite of three-dimensional NMR spectra with non-uniform sampling (NUS): TROSY-HNCA and TROSY-HNCACB spectra were recorded on a 900 MHz Bruker Avance III HD equipped with a 5 mm triple resonance cryoprobe (^{1}H/^{13}C/^{15}N) running Topspin NMR 3.5. Temperature was set to 45ºC. The TROSY-HNCA[83-85] (Bruker trhncaetgp2h3d) was acquired with 1024 complex points in the direct dimension (^{1}H) and 604 non-uniformly sampled complex points in the indirect dimensions (max increments 36 (^{15}N) and 48 (^{13}C)) for 35% sampling. 64 scans were acquired per increment with a 2s delay. Spectral widths were 16.34 ppm centered at 4.58 ppm (^{1}H), 31.3 ppm centered at 116.5 ppm (^{15}N) and 29.5 ppm centered at 55.6 ppm (^{13}C). The TROSY-HNCACB [83-85] (Bruker trhncacbetgp2h3d) was acquired with 1024 complex points acquired in the direct dimension (^{1}H) and 740 non-uniformly sampled complex points in the indirect dimensions (max increments 36 (^{15}N) and 64 (^{13}C)) for 32% sampling. 128 scans were acquired per increment with a 2s delay. Spectral widths were the same as the HNCA except for ^{13}C, which was 63.1 ppm centered at 43.6 ppm.

The TROSY-HN(CO)CA, TROSY-HNCO (BioPack ghnco_trosy_3DA), and TROSY-HN(CA)CO [86-90] spectra were collected on a 600 MHz Varian VNMRS DD console equipped with a 5 mm cold probe (^{1}H/^{13}C/^{15}N) using VnmrJ 4.0. The TROSY-HNCO was acquired with 1024 complex points in the direct dimension (^{1}H) and 900 non-uniformly sampled complex points in the indirect dimensions (max increments 48 (^{15}N) and 48 (^{13}C)) for 39% sampling. 32 scans were acquired

per increment with a 2 s delay. Spectral widths were 20.03 ppm centered at 4.58 ppm (^{1}H), 35.4 ppm centered at 117.8 ppm (^{15}N) and 11.9 ppm centered at 177.4 ppm (^{13}C). The TROSY-HN(CA)CO was acquired with 1024 complex points in the direct dimension (^{1}H) and 380 non-uniformly sampled complex points in the indirect dimensions (max increments 32 (^{15}N) and 34 (^{13}C)) for 38% sampling. 144 scans were acquired per increment with a 2s delay. Spectral widths were the same as for the HNCO. The TROSY-HN(CO)CA was acquired with 1024 complex points in the direct dimension (^{1}H) and 598 non-uniformly sampled complex points in the indirect dimensions (max increments 36 (^{15}N) and 48 (^{13}C)) for 35% sampling. 64 scans were acquired per increment with a 2s delay. Spectral widths were the same as for the HNCO except for ^{13}C, which was 29.8 ppm centered at 55.9 ppm.

All data were processed using NMRPipe [74] and SMILE [91] for NUS reconstruction. Spectral analysis and assignments were performed using CcpNmr Analysis [92].

Electrostatic Surface Calculation

The electrostatic surface of the EmrE substrates $TPP+^{+}$ and F_4-$TPP+^{+}$ were calculated assuming S_4 symmetry. Gaussian16 optimization was used with B3LYP/6-31G(d) intially, and then re-optimized using B3LYP/6-311+G(d,p). Single point B3LYP/6-311+G(d,p) calculations were performed using Spartan'08 to generate the elstat figures.

Structure Calculation of F_4-TPP^{+}-bound EmrE

Structure calculation of the TPP^{+}-EmrE complex consists of two stages: *de-novo* docking to determine the location and orientation of F_4-TPP^{+} within the apo protein structure, and to structurally assign which fluorine dephases each protein H^{N}, and MD simulations in explicit lipid bilayers to equilibrate and refine the structure of the complex. The docking used the MD-simulated apo EmrE structure [25, 50] as input. Both E14 residues are protonated, and a S64V mutation with

the lowest energy rotamer was introduced. The coordinate of F_4-TPP^+ was generated by replacing the *para*-hydrogens of TPP^+ [50] with fluorines. To assign the two sets of protein chemical shifts to monomers A and B, we used the V64 Cα chemical shift. A resolved Val Cα signal is observed at 64.1 ppm, which is upfield from the more ideal α-helical Cα chemical shift (~66 ppm) of all other valines. In the apo EmrE structural model, TM3 of monomer A is a relatively ideal α-helix while TM3 of monomer B has a significant kink around V64. Thus, we assigned the less helical 64.1 ppm V64 Cα chemical shift to monomer B and the more ideal helical chemical shifts to monomer A. The N- and C-termini of the protein were set as charged, and the "active" residue list, from which the HADDOCK Ambiguous Interaction Restraints (AIRs) were generated, was set to a minimal subset of residues that are well known to be involved in binding based on biochemical data [38] and the current REDOR data. The ^1H–^{19}F distance restraints for REDOR RMSD values below 0.2 (**Fig. S9**) were uploaded as unambiguous constraints, for which energy penalties were always enforced. Backbone (ϕ, ψ) torsion angles and sidechain χ_1 torsion angles predicted based on solution-NMR chemical shifts were input as restraints with an uncertainty of 20˚. Docking was performed in DMSO and started with 1000 structures, from which 200 lowest energy structures were refined. These 200 structures were aligned and analyzed in Pymol with an integrated Python-Pymol script for reporting the protein and ligand RMSD's.[77, 93]

The lowest energy structure from docking was used to resolve the ambiguity of which ^{19}F atom(s) dephase which ^1H atoms of the protein by a structure-based assignment algorithm. We read the PDB coordinates into dataframe structures using an in-house written Python script that employed the Biopandas package [77, 93-95]. We calculated the distances between all fluorine atoms and each protein H^N to identify the nearest fluorine. The distances to the three other fluorine atoms were checked against the shortest distance; if any of the three other fluorines had a distance within 1.5 Å of the nearest F, then this fluorine atom was also flagged. In total, we assigned each protein H^N

to one of three categories: 1) those H^N atoms with a single nearest F, a positive constraint; 2) those H^N atoms with two similarly proximal (within 1.5 Å of each other) F atoms, or two positive constraints, and 3) those H^N atoms that are far from all fluorine atoms, or four "negative" constraints. In case 2), we increased both upper-bound distance uncertainty by 2 Å, to account for the fact that the REDOR fitting assumed a single-distance two-spin model, so that the individual distance in the three-spin situation is longer than the two-spin fit. This algorithm converted the ambiguous HADDOCK distance restraints to a list of pairwise distance restraints to be input into the GROMACS simulation. In total, from the 72 dipolar coupling measurements, we obtained 213 unique distance restraints for all-atom MD simulations.

We inserted the docked EmrE-TPP^+ complexes into an explicit hydrated DMPC bilayer using the CHARMM-GUI [96, 97] membrane builder tool [98, 99]. The DMPC bilayer contains 100 lower leaflet lipids and 104 upper leaflet lipids, and hydrated on both faces with a TIP3P water layer of ~2.5 nm in thickness [100]. A total of 6 chloride ions and 4 sodium ions were included in the system to match the experimental 20 mM NaCl condition. The complex was aligned to the membrane normal using the OPM web-service.[101] The ligand force fields were parameterized from the ligand coordinates. MD simulation was conducted in GROMACS [102] using the NMRbox virtual servers [103]. The simulation was conducted at 310 K, and CHARMM36 force fields [104-107], including the WYF parameter for cation-pi interactions, [108] were used. Backbone (ϕ, ψ) angles and sidechain χ_1 torsion angles from solution-NMR chemical shifts were applied as constraints with an angle uncertainty of ±20˚. The protein-ligand H-F distance restraints (**Table S3**) were applied with the piecewise linear restoring force in GROMACS [109]. Simulation started with a 5000-step energy minimization with position and dihedral restraints on the protein backbone, sidechain, and lipid atoms. The position and dihedral restraints were progressively weakened and removed over 1.875 ns of equilibration. The production stage involved 400 ns in 2 fs steps to equilibrate the

structure. GROMACS periodic boundary condition commands were used to remove jumps across the box boundary, and the MDAnalysis Python package [110] was used to align each successive MD step to the initial state for calculating root-mean-square deviations (**Fig. S10C**) and to keep the protein position immobilized throughout the trajectory. Final structures were subjected to a similar 5000-step energy minimization to remove improper bond angles. Ensembles from both trajectories were created taking 16 time points between 250 and 400 ns. The models from both trajectories were scored based on the original 4-fold ambiguous set of distance restraints. In the 32 structures from the two runs, the average number of violations was 7.1 ± 1.2 (min, max = 5, 9), the average violation magnitude is 1.7 ± 0.2 Å (min, max = 1.3 Å, 2.1 Å), and the total violations ('violation score') is 11.6 ± 0.8 Å (min, max = 9.5 Å, 13.2 Å). The final reported ensemble consisted of the 10 lowest-violation conformers from the two runs, with six structures from run 1 and four from run 2.

Methods References

63. Morrison EA, Henzler-Wildman KA. Reconstitution of integral membrane proteins into isotropic bicelles with improved sample stability and expanded lipid composition profile. *Biochim Biophys Acta* **1818**, 814-820 (2012).

64. McNeill SA, Gor'kov PL, Shetty K, Brey WW, Long JR. A low-E magic angle spinning probe for biological solid state NMR at 750MHz. *J Magn Reson* **197**, 135-144 (2009).

65. Cavanagh J, Fairbrother WJ, III AGP, Skelton NJ. *Protein NMR spectroscopy: principles and practice*. Academic Press (1996).

66. Baldus M, Petkova AT, Herzfeld J, Griffin RG. Cross polarization in the tilted frame: assignment and spectral simplification in heteronuclear spin systems. *Molecular Physics* **95**, 1197-1207 (1998).

67. Hou G, Yan S, Trébosc J, Amoureux J-P, Polenova T. Broadband homonuclear correlation spectroscopy driven by combined R2nv sequences under fast magic angle spinning for NMR structural analysis of organic and biological solids. *J Magn Reson* **232**, 18-30 (2013).

68. Verel R, Ernst M, Meier BH. Adiabatic Dipolar Recoupling in Solid-State NMR: The DREAM Scheme. *J Magn Reson* **150**, 81-99 (2001).

69. Bennett AE, Rienstra CM, Auger M, Lakshmi KV, Griffin RG. Heteronuclear decoupling in rotating solids. *J Chem Phys* **103**, 6951-6958 (1995).

70. Shaka AJ, Keeler J, Frenkiel T, Freeman R. An improved sequence for broadband decoupling: WALTZ-16. *J Magn Reson* **52**, 335-338 (1983).

71. Zhou DH, Rienstra CM. High-performance solvent suppression for proton detected solid-state NMR. *J Magn Reson* **192**, 167-172 (2008).

72. Dürr HN, Grage SL, Witter R, Ulrich AS. Solid state ^{19}F NMR parameters of fluorine-labeled amino acids. Part I: Aromatic substituents. *J Magn Reson* **191**, 7-15 (2008).

73. Li Y, Palmer AG. TROSY-selected ZZ-exchange experiment for characterizing slow chemical exchange in large proteins. *J Biomol NMR* **45**, 357-360 (2009).

74. Delaglio F, Grzesiek S, Vuister GW, Zhu G, Pfeifer J, Bax A. NMRPipe: a multidimensional spectral processing system based on UNIX pipes. *J Biomol NMR* **6**, 277-293 (1995).

75. Lee W, Tonelli M, Markley JL. NMRFAM-SPARKY: enhanced software for biomolecular NMR spectroscopy. *Bioinformatics* **31**, 1325-1327 (2015).

76. Helmus JJ, Jaroniec CP. Nmrglue: an open source Python package for the analysis of multidimensional NMR data. *J Biomol NMR* **55**, 355-367 (2013).

77. Walt Svd, Colbert SC, Varoquaux G. The NumPy Array: A Structure for Efficient Numerical Computation. *Computing in Science & Engineering* **13**, 22-30 (2011).

78. Lee W, Tonelli M, Markley JL. NMRFAM-SPARKY: enhanced software for biomolecular NMR spectroscopy. *Bioinformatics* **31**, 1325-1327 (2014).

79. Hunter JD. Matplotlib: A 2D Graphics Environment. *Computing in Science & Engineering* **9**, 90-95 (2007).

80. Shcherbakov AA, Hong M. Rapid Measurement of Long-Range Distances in Proteins by Multidimensional ^{13}C-^{19}F REDOR NMR Under Fast Magic-Angle Spinning. *J Biomol NMR* **71**, 31-43 (2018).

81. Bak M, Rasmussen JT, Nielsen NC. SIMPSON: A general simulation program for solid-state NMR spectroscopy. *J Magn Reson* **147**, 296-330 (2000).

82. Bak M, Nielsen NC. REPULSION, A Novel Approach to Efficient Powder Averaging in Solid-State NMR. *J Magn Reson* **125**, 132-139 (1997).

83. Schulte-Herbrüggen T, Sørensen OW. Clean TROSY: Compensation for Relaxation-Induced Artifacts. *J Magn Reson* **144**, 123-128 (2000).

84. Eletsky A, Kienhöfer A, Pervushin K. TROSY NMR with partially deuterated proteins. *J Biomol NMR* **20**, 177-180 (2001).

85. Salzmann M, Wider G, Pervushin K, Senn H, Wuthrich K. TROSY-type Triple-Resonance Experiments for Sequential NMR Assignments of Large Proteins. *J Am Chem Soc,* **121**, 844-848 (1999).

86. Pervushin KV, Wider G, Wuthrich K. Single Transition-to-single Transition Polarization Transfer (ST2-PT) in [15N,1H]-TROSY. *J Biomol NMR* **12**, 345-348 (1998).

87. Pervushin K, Riek R, Wider G, Wüthrich K. Attenuated T2 relaxation by mutual cancellation of dipole-dipole coupling and chemical shift anisotropy indicates an avenue to NMR structures of very large biological macromolecules in solution. *Proc Natl Acad Sci U S A* **94**, 12366-12371 (1997).

88. Yang D, Kay LE. Improved 1HN-detected triple resonance TROSY-based experiments. *J Biomol NMR* **13**, 3-10 (1999).

89. Yamazaki T, Lee W, Arrowsmith CH, Muhandiram DR, Kay LE. A Suite of Triple Resonance NMR Experiments for the Backbone Assignment of 15N, 13C, 2H Labeled Proteins with High Sensitivity. *J Am Chem Soc* **116**, 11655-11666 (1994).

90. Yamazaki T*, et al.* An HNCA Pulse Scheme for the Backbone Assignment of N-15,C-13,H-2-Labeled Proteins - Application to a 37-Kda Trp Repressor DNA Complex. *J Am Chem Soc* **116**, 6464-6465 (1994).

91. Ying J, Delaglio F, Torchia DA, Bax A. Sparse multidimensional iterative lineshape-enhanced (SMILE) reconstruction of both non-uniformly sampled and conventional NMR data. *J Biomol NMR* **68**, 101-118 (2017).

92. Vranken WF*, et al.* The CCPN data model for NMR spectroscopy: development of a software pipeline. *Proteins: Structure, Function, and Bioinformatics* **59**, 687-696 (2005).

93. Virtanen P*, et al.* SciPy 1.0: fundamental algorithms for scientific computing in Python. *Nature Methods* **17**, 261-272 (2020).

94. Raschka S. BioPandas: Working with molecular structures in pandas DataFrames. *J Open Source Software* **2**, 279-279 (2017).

95. McKinney W. Data Structures for Statistical Computing in Python. *Proc 9th Python Sci Conf* **1697900**, 51-56 (2010).

96. Lee J*, et al.* CHARMM-GUI Input Generator for NAMD, GROMACS, AMBER, OpenMM, and CHARMM/OpenMM Simulations Using the CHARMM36 Additive Force Field. *J Chem Theo Comput* **12**, 405-413 (2016).

97. Jo S, Kim T, Iyer VG, Im W. CHARMM-GUI: A web-based graphical user interface for CHARMM. *J Comput Chem* **29**, 1859-1865 (2008).

98. Wu EL*, et al.* CHARMM-GUI Membrane Builder toward realistic biological membrane simulations. *J Comput Chem* **35**, 1997-2004 (2014).

99. Jo S, Kim T, Im W. Automated Builder and Database of Protein/Membrane Complexes for Molecular Dynamics Simulations. *PLOS ONE* **2**, e880 (2007).

100. Mark P, Nilsson L. Structure and Dynamics of the TIP3P, SPC, and SPC/E Water Models at 298 K. *J Phys Chem A* **105**, 9954-9960 (2001).

101. Lomize MA, Pogozheva ID, Joo H, Mosberg HI, Lomize AL. OPM database and PPM web server: resources for positioning of proteins in membranes. *Nuc Acids Res* **40**, D370-D376 (2012).

102. Berendsen HJC, van der Spoel D, van Drunen R. GROMACS: A message-passing parallel molecular dynamics implementation. *Computer Physics Communications* **91**, 43-56 (1995).

103. Maciejewski MW*, et al.* NMRbox: A Resource for Biomolecular NMR Computation. *Biophys J* **112**, 1529-1534 (2017).

104. Huang J*, et al.* CHARMM36m: an improved force field for folded and intrinsically disordered proteins. *Nature Methods* **14**, 71-73 (2017).

105. Jorgensen WL, Chandrasekhar J, Madura JD, Impey RW, Klein ML. Comparison of simple potential functions for simulating liquid water. *J Chem Phys* **79**, 926-935 (1983).

106. Klauda JB*, et al.* Update of the CHARMM All-Atom Additive Force Field for Lipids: Validation on Six Lipid Types. *J Phys Chem B* **114**, 7830-7843 (2010).

107. MacKerell AD*, et al.* All-Atom Empirical Potential for Molecular Modeling and Dynamics Studies of Proteins. *J Phys Chem B* **102**, 3586-3616 (1998).

108. Khan HM, MacKerell AD, Reuter N. Cation-π Interactions between Methylated Ammonium Groups and Tryptophan in the CHARMM36 Additive Force Field. *J Chem Theo Comput* **15**, 7-12 (2019).

109. Abraham MJ, Spoel Dvd, Lindahl E, Hess B, team atGd. GROMACS User Manual version 2019.).

110. Gowers R*, et al.* MDAnalysis: A Python Package for the Rapid Analysis of Molecular Dynamics Simulations. *Proc 15th Python Sci Conf*, 98-105 (2016).